

# **THE TIMING OF VOLCANO-ICE INTERACTIONS AND DEGLACIATION IN ICELAND**

---

A thesis submitted to the University of Manchester for the degree of  
Doctor of Philosophy in the Faculty of Engineering and Physical  
Sciences

**By Kathryn M. Street**

**School of Earth and Environmental Sciences  
The University of Manchester  
2016**

# **Contents**

List of figures	5
List of tables	9
Abstract	10
Declaration	11
Copyright statement	11
Acknowledgements	12

## **Chapter One: Introduction**

1.1 Introduction	13
1.2 Aims of the study	14
1.3 Outline of thesis	15

## **Chapter Two: Literature Review**

2.1 Geological setting of Iceland	16
2.1.1 Geological history and tectonics	16
2.1.2 Rift zones of Iceland	18
2.1.3 Geological History	21
2.2 Glacial history of Iceland	22
2.2.1 Weichselian Timeline	24
2.2.2 Ice dynamics during the Weichselian	28
2.2.3 Decompression Mantle Melting	30
2.3 Volcano-ice interactions	33
2.3.1 Subglacial volcanic edifices	35
2.3.2 Past dating of subglacial formations	44

## **Chapter Three: Helium Dating Techniques**

3.1 Introduction	47
3.2 Cosmogenic ${}^3\text{He}$ exposure age dating	48
3.2.1 The nature of cosmic rays and their origin	48
3.2.2 Interactions with Earth's magnetic field	51
3.2.3 Interactions with the Earth's atmosphere	55
3.2.4 Interactions with the Earth's surface	58
3.2.5 Principles of cosmogenic nuclide surface exposure dating	61

3.2.6 Generation of ${}^3\text{He}_c$ in surface rocks	62
3.2.7 Spallation generated ${}^3\text{He}_c$ production rates	64
3.2.8 Production rate scaling methods	67
3.2.9 Factors affecting production rates	70
3.2.10 Temporal variations	71
3.2.11 Factors affecting $\text{He}$ exposure age dating specific to Iceland and this study	73
3.3 (U-Th)/He dating	78
3.3.1 Why use (U-Th)/He dating?	78
3.3.2 U-series radioactive decay	79
3.3.3 Factors affecting (U-Th)/He dating specific to Iceland and this study	85
3.4 Separating multiple sources of He	86
3.4.1 Sources of ${}^4\text{He}$ in (U-Th)/He dating	86
3.4.2 Sources of ${}^3\text{He}$ for cosmogenic exposure dating	87
3.4.3 Sample Heterogeneity	88

## **Chapter Four: Fieldwork and sample preparation**

4.1 Introduction	89
4.2 Sample collection and field protocol	89
4.2.1 Basal pillow samples for eruption ages	91
4.2.2 Capping lava samples for cosmic-ray exposure dating	93
4.3 Sample Preparation	97

## **Chapter Five: Experimental Methods**

5.1 Theoretical basis of mass spectrometry	99
5.1.1 Ionisation	99
5.1.2 Mass Analyzer	100
5.1.3 Detectors	100
5.2 VG5400 noble gas mass spectrometer	102
5.2.1 Trapped helium analysis (sample crushing)	103
5.2.2 VG5400 extraction line	105
5.2.3 Purification and separation of noble gases	107
5.2.4 Isotopic analysis	108

5.3 Helix MC Plus noble gas mass spectrometer	110
5.3.1 Radiogenic and cosmogenic helium analysis (sample fusion)	113
5.3.2 Helix extraction line	119
5.3.3 Purification and separation of noble gases	121
5.3.4 Isotopic analysis	122
5.4 Line blanks and air calibrations	122
5.5 Analysis of uranium and thorium isotopes	127
5.5.1 Sample Digestion	127

## **Chapter Six: Trapped components**

6.1 Introduction	129
6.2 Results	130
6.2.1 ${}^3\text{He}/{}^4\text{He}$	130
6.2.2 Mantle reservoir	134
6.2.3 ${}^{40}\text{Ar}/{}^{36}\text{Ar}$	137
6.3 Discussion	138
6.3.1 ${}^3\text{He}/{}^4\text{He}$	138
6.3.2 Mantle source	140
6.3.3 Basaltic glass vs. olivine	142
6.4 Conclusions	143

## **Chapter Seven: Cosmogenic helium**

7.1 Introduction	144
7.2 Results	147
7.2.1 Production rates	148
7.2.2 Scaling factor	148
7.2.3 Surface categories	148
7.2.4 ${}^3\text{He}$ cosmogenic ages	149
7.3 Discussion	150
7.3.1 Olivine fusion	150
7.3.2 Erosion	151
7.3.3. Geochemical links	152
7.3.4 Passage zones	153
7.3.5 High ${}^3\text{He}$ exposure ages	153

7.4 Conclusions	154
-----------------	-----

## **Chapter Eight: Radiogenic helium**

8.1 Introduction	156
8.2 Results	157
8.3 Discussion	161
8.3.1 Concentration variation in different minerals	161
8.3.2 Radiogenic ${}^4\text{He}$	161
8.3.3 Parentless ${}^4\text{He}$	165
8.4 Conclusions	165

## **Chapter Nine: Conclusions and further work**

9.1 Conclusions	167
9.2 Further Work	169

<b>Appendix A: Error Propagation</b>	172
--------------------------------------	-----

## **Appendix B: Sampling Context**

B1 Hlöðufell (KS88A, KS88B and KS97)	174
B2 Bláfell (KS91 and KS94)	179
B2 Gaesafjöll (KS104 and KS106)	183

<b>References</b>	187
-------------------	-----

# **Contents**

## **List of Figures**

### **Chapter One: Introduction**

Figure 1.1	Suggested mantle model	14
------------	------------------------	----

### **Chapter Two: Literature Review**

Figure 2.1	Aerial map of Iceland	16
Figure 2.2	Bathymetry map of Iceland	17
Figure 2.3A	Rift zones of Iceland	18
Figure 2.3B	Central volcano and fissure swarms	19
Figure 2.4	Geological map of Iceland	21
Figure 2.5	Oxygen isotope curve	23
Figure 2.6	A 3D thermomechanical model showing Iceland's glaciers at LGM	26
Figure 2.7	Icelandic ice sheet at its maximum during the Younger Dryas	27
Figure 2.8	Icelandic glacial directional features used to reconstruct ice flows	29
Figure 2.9	Ice sheet flow patterns and ice divides	30
Figure 2.10	Iceland map featuring locations of subglacial formations	34
Figure 2.11	Photo of tuya, Herðubreið	35
Figure 2.12	Illustration of tuya formation with photo examples	39
Figure 2.13	Photo of tindar, ridge south of Askja	40
Figure 2.14	Illustrations comparing the components of a tindar and tuya	41

### **Chapter Three: Dating Techniques**

Figure 3.1	Three main components of cosmic ray flux	49
Figure 3.2	Cut-off rigidity values with varying geomagnetic latitudes	52
Figure 3.3	Global magnetic cut-off rigidities	53
Figure 3.4	Nuclear disintegration rates with varying geomagnetic latitudes	54
Figure 3.5	Nuclear cascade diagram	55
Figure 3.6	Attenuation length variation as a function of cut-off rigidity	57
Figure 3.7	A: Neutron flux below the Earth's surface. B: Neutron flux with varying water content	60
Figure 3.8	Effect of erosion on cosmogenic exposure age	72

Figure 3.9	Schematic of the decay chain of uranium and thorium	79
Figure 3.10	Plot of U/He vs age illustrating progression of non-steady state decay of U into steady-state decay	80
Figure 3.11	Illustration of olivine phenocryst illustrating various sources of He	86
Figure 3.12	Flowchart of sources of He in olivine phenocryst and what needed to calculate eruption and exposure ages	88

## **Chapter Four: Fieldwork and sample preparation**

Figure 4.1	Map of sample locations	90
Figure 4.2	Photo of melt-water channel of Ðórólfssfell exposing shielded pillow basalts	93

## **Chapter Five: Experimental methods**

Figure 5.1	Illustration of electron multiplier with dynode plates	101
Figure 5.2	Fully resolved peaks of HD and $^3\text{He}$ on VG5400	103
Figure 5.3	Schematic of solenoid crushers used to extract noble gases	105
Figure 5.4	Schematic of VG5400 extraction line	106
Figure 5.5	Regression tool used in Origin to regress $^3\text{He}$ data taken from VG5400	109
Figure 5.6	Annotated photo of Helix-MC Plus	110
Figure 5.7	Fully resolved peaks of $^3\text{He}$ from HD and partially resolved $^3\text{He}$ from HD on Helix-MC Plus	111
Figure 5.8	Annotated photo of multi-detector on Helix-MC Plus	112
Figure 5.9	Annotated pictures of molybdenum crucibles	113
Figure 5.10	Illustration of hook system used to lower and lift crucibles in and out of furnace	114
Figure 5.11	Illustration of furnace crucible and sample holder tray	114
Figure 5.12	Annotated picture of sample introduction system on the resistance furnace	117
Figure 5.13	Schematic of Helix-MC Plus extraction line	119
Figure 5.14	Illustration of inside of Helix-MC Plus multicollector cup holders	120
Figure 5.15	Mass spectrum showing multi-collection of argon isotopes	121
Figure 5.16	$^3\text{He}/^4\text{He}$ ratios in spiked air calibration bottle on VG5400	124
Figure 5.17	$^{40}\text{Ar}/^{36}\text{Ar}$ ratios in spiked air calibration bottle on VG5400	124
Figure 5.18	$^{40}\text{Ar}/^{36}\text{Ar}$ ratios in non-spiked air calibration bottle on VG5400	125

Figure 5.19	$^4\text{He}$ concentration in a non-spiked air calibration bottle on Helix-MC	125
Figure 5.20	$^{40}\text{Ar}/^{36}\text{Ar}$ ratios in non-spiked air calibration bottle on Helix-MC	126
Figure 5.21	A logarithmic plot of $^4\text{He}/^3\text{He}$ vs. $^{36}\text{Ar}/^3\text{He}$ of crushed samples	126

## Chapter Six: Trapped components

Figure 6.1	Iceland map presenting $^3\text{He}/^4\text{He}$ ratios analysed here from crushing and other published data	133
Figure 6.2	Two graphs plotting $^3\text{He}/^{40*}\text{Ar}$ vs. $^4\text{He}/^{40*}\text{Ar}$ . Graph A illustrating difference seen between type of edifice and graph B illustrating difference seen between volcanic zones.	135
Figure 6.3	$^{40}\text{Ar}/^{36}\text{Ar}$ vs. $^3\text{He}/^{36}\text{Ar}$ of crushed samples	138
Figure 6.4	Proposed centre of mantle plume under Iceland	141
Figure 6.5	Model illustrating mantle plume sourcing both WVZ and EVZ	142

## Chapter Seven: Cosmogenic helium

Figure 7.1	Photo of tuya Hlöðufell	145
Figure 7.2	Photo on the summit of Bláfell	145
Figure 7.3	Google Earth image of Gaesafjöll	145
Figure 7.4	Photo of surface texture at summit of Gaesafjöll	146
Figure 7.5	Photo of olivine for cosmogenic $^3\text{He}$ samples post-fusion	151

## Chapter Eight: Radiogenic helium

Figure 8.1	A: Concentration of radiogenic $^4\text{He}$ expected for edifice samples in WVZ B: Concentration of radiogenic $^4\text{He}$ expected for edifice samples in NVZ	163
Figure 8.2	Difference in radiogenic $^4\text{He}$ analysed and expected for Herðabréiðatögl	163

## Appendix A: Error Propagation

Figure A1	$^3\text{He}$ regression to calculate relevant error for measurement	172
Figure A2	$^{40}\text{Ar}$ regression to calculate relevant error for measurement	173

## **Appendix B: Sampling Context**

Figure B	Map showing tuyas that were sampled for both exposure and eruption ages	174
Figure B1	Images of Hlöðufell sample sites for both eruption and exposure age dating. Both summit and basal sample areas are shown, as well as various stages of sample preparation	174-
Figure B2	Images of Bláfell sample sites for both eruption and exposure age dating. Both summit and basal sample areas are shown, as well as various stages of sample preparation	179
Figure B3	Images of Gaesafjöll sample sites for both eruption and exposure age dating. Both summit and basal sample areas are shown, as well as various stages of sample preparation	183

## **List of Tables**

### **Chapter Two: Literature Review**

Table 2.1	Geological timeline of Iceland	25
-----------	--------------------------------	----

### **Chapter Three: Dating Techniques**

Table 3.1	Nuclear disintegration rates in the atmosphere	65
Table 3.2	Summary of $^3\text{He}$ production rates gathered from previous research	66
Table 3.3	Scaling methods used for spallation produced cosmogenic nuclides	67
Table 3.4	Reference $^3\text{He}$ production rates for pyroxene and olivine data	70
Table 3.5	Radionuclides with their noble gas daughters and atomic production	81

### **Chapter Four: Fieldwork and sample preparation**

Table 4.1	Helium concentrations demonstrating importance to sample shielded locations	92
Table 4.2	Samples analysed	95

### **Chapter Five: Experimental methods**

Table 5.1	Different components of both noble gas mass spectrometers used	101
Table 5.2	Percentage fractions below and above 100 $\mu\text{m}$ post crushing	104

### **Chapter Six: Trapped components**

Table 6.1	Concentrations of helium and argon isotopes released from crushing	131
-----------	--	-----

### **Chapter Seven: Cosmogenic helium**

Table 7.1	Data of cosmogenic helium analysis	147
-----------	------------------------------------	-----

### **Chapter Eight: Radiogenic helium**

Table 8.1	Uranium, thorium and helium data analysed from melted olivine samples	159
-----------	---	-----

## Abstract

# THE TIMING OF VOLCANO-ICE INTERACTIONS AND DEGLACIATION IN ICELAND

*Submitted to The University of Manchester for the degree of Doctor of Philosophy,  
by Kathryn M. Street, September 2016*

Iceland possesses numerous subglacial volcanoes (tuyas and tindars) that act as geological records of the thick ice sheets that once spanned across the country. Flat topped volcanic summits, which were able to penetrate through the covering ice, provide an estimate of the ice sheet's minimum thickness at the time the volcano was in its final eruptive stage. Iceland not only provides a large number of potential subglacial edifices to sample but is geologically interesting as it sits above a magmatic hotspot and spreading ridge, providing a long term record of volcanism during considerable climate variability. However, it is unknown exactly in which glacial cycle these volcanic edifices formed, due to the lack of accurate and reliable eruption ages.

Helium isotopes are valuable tracers of the mantle source for the origin of volcanic rocks. Helium isotopes are comprised of a mixture of magmatic helium trapped whilst in the mantle, cosmogenic helium built up by interaction with cosmic rays during surface exposure and radiogenic helium produced from the in situ decay of U and Th. These helium components yield invaluable information on the mantle source, time of eruption and length of exposure respectively. The principle aim of this study is to determine whether reliable and accurate eruption ages of basaltic subglacial volcanoes in Iceland are possible, by applying a relatively new geochronological tool: U-Th/He dating. These eruption ages combined with cosmogenic derived  ${}^3\text{He}$  surface exposure ages of the summits helps to establish ice surface elevation and thickness fluctuations over time.

Olivine bearing basalt samples were acquired from 14 tuyas, 4 tindars and 1 shield volcano across the Western and Northern Volcanic Zones in Iceland (WVZ and NVZ). Samples were collected from the base of each edifice for U-Th/He dating and the summits of 3 tuyas for cosmogenic  ${}^3\text{He}$  surface exposure dating. Olivine phenocrysts were hand-picked and analysed on two noble gas mass spectrometers (VG5400 and Helix-MC instruments). As part of the analytical procedure for these techniques, magmatic helium trapped in the olivine grains is also analysed.

The mantle helium isotope ratios indicate that nearly all edifices sampled obtain a MORB-like source ( $1\text{-}18\text{R}_\text{A}$ ) except for an OIB-like ( $24\text{R}_\text{A}$ ) centrally located tuya, Bláfell. The helium ratios acquired in the NVZ are lower ( $4\text{-}11\text{R}_\text{A}$ ) than those in the WVZ ( $8\text{-}20\text{R}_\text{A}$ ). There are no significant differences seen in the mantle components between the different types of edifice sampled. Mantle helium isotope ratios confirm the heterogeneity of the mantle beneath Iceland. The cosmogenic  ${}^3\text{He}$  exposure ages of Hlöðufell and Bláfell in the WVZ and Gaesafjöll in the NVZ are determined as  $0.5\pm7.4\text{ka}$ ,  $67\pm0.7\text{ka}$  and  $108\pm46\text{ka}$  respectively. This study presents the first  ${}^3\text{He}$  cosmogenic exposure age determined to be over 20ka in Iceland. The low concentrations of U and Th observed in Icelandic olivines (0.002-0.04 nmol/g and 0.01-0.1 nmol/g respectively) prevent any reliable disequilibrium ages to be established. Minimum secular equilibrium U-Th/He ages are determined and provide a range of erroneously large eruption ages (0.4 - 80.4 Ma), due to potential helium implantation and under-detection of  ${}^3\text{He}$  released during sample analysis. Progress can be made towards determining accurate eruption ages for Icelandic basalts if certain factors are adhered to and various sources of helium are separated effectively.

## **Declaration**

No portion of the work referred to in this thesis has been submitted in support of an application for another degree or qualification of this or any other university or other institute of learning.

## **Copyright statement**

- 1) The author of this thesis (including any appendices and/or schedules to this thesis) owns certain copyright or related rights in it (the “Copyright”) and s/he has given The University of Manchester certain rights to use such Copyright, including for administrative purposes.
- 2) Copies of this thesis, either in full or in extracts and whether in hard or electronic copy, may be made only in accordance with the Copyright, Designs and Patents Act 1988 (as amended) and regulations issued under it or, where appropriate, in accordance with licensing agreements which the University has from time to time. This page must form part of any such copies made.
- 3) The ownership of certain Copyright, patents, designs, trade-marks and other intellectual property (the “Intellectual Property”) and any reproductions of copyright works in the thesis, for example graphs and tables (“Reproductions”), which may be described in this thesis, may not be owned by the author and may be owned by third parties. Such Intellectual Property and Reproductions cannot and must not be made available for use without the prior written permission of the owner(s) of the relevant Intellectual Property and/or Reproductions.
- 4) Further information on the conditions under which disclosure, publication and exploitation of this thesis, the Copyright and any Intellectual Property and/or Reproductions described in it may take place is available in the University IP Policy (see <http://documents.manchester.ac.uk/DocuInfo.aspx?DocID=487>), in any relevant Thesis restriction declarations deposited in the University Library, The University Library’s regulations (see <http://www.manchester.ac.uk/library/aboutus/regulations>) and in The University’s policy on Presentation of Theses

## Acknowledgements

Firstly I would like to thank my supervisor Professor Ray Burgess for the endless support, advice and encouragement throughout this PhD. Ray's unwavering optimism has allowed me to persevere through the more difficult moments and grow as a scientist. I must also thank my other supervisors Dr Simon Brocklehurst and Dr Dave McGarvie for their guidance throughout field work in Iceland and helping me understand the fundamentals of the geological processes used throughout this PhD. Dr McGarvie is hands down the best Iceland geological tour guide. I pass my thanks on to the National Environmental Research Council (NERC) for providing the funding to conduct this research.

Next my thanks goes to the entire Isotope Research Group at Manchester. Without Dr John Cowpe's endless optimism and technical support in the lab I probably would have gone mad. Along with Dr Cath Davies and Dr Jon Fellowes whose advice and encouragement have helped me to move forward in trialling times. Thanks must go to Dr Katie Joy for the endless advice, support and beers, as well as Sarah, Torsten and Trish for all the fun times at the pub, Outreach events and conferences. I would not have been able to complete my PhD without the optimism and laughter of my office mates Nat Curran (C'mon you reds!), Mark Nottingham, Fran McDonald, Alex Clarke and Dayl Martin. Also the speedy finishers Rich McAllister, Lin Ma and Tracey Vaitekaitis. Michael Broadley, thank you for putting up with my incessant questions and teaching me how to use noble gas mass spectrometers. I'd be so much more confused without your help.

Beth and Emma thank you so much for your words of confidence and all the good times we've had throughout these past four years. Thanks must go to all of my extended family for all of their kind words and support.

Finally I cannot finish without thanking my parents, Claudia and Les, and my fiancée Alex. Dad you deserve a special shout out for getting me into science in the first place by taking me numerous times to the science and natural history museums and your open days at MSD. Mum, thank you for always being there to talk to, no matter the time of day, providing encouragement and hugs when I needed them most AND for proof-reading my thesis. Alex without your endless love, motivation, reassurance and faith in me I would have found the past four years unbearable. You guys are the best and have enabled me to become the scientist I am today.

# Chapter One Introduction

## 1.1 Introduction

Iceland possesses numerous subglacial volcanoes that act as land-based records of thick ice sheets that once spanned across the country. Flat topped summits are exhibited on the edifices that were able to penetrate through the ice (also known by their Icelandic name: tuya) and provide evidence on the ice sheet's minimum thickness when the eruption was in its final eruptive stage. It is unknown exactly when these edifices formed, due to the lack of accurate and reliable eruption ages. Exposure ages of the summits of certain subglacial volcanoes in Iceland have been determined using the cosmogenic nuclide  $^3\text{He}$  (Licciardi 2007; Eason et al., 2015). These exposure ages are considered to be minimum eruption ages because summits have been covered in snow and (on higher elevated summits) ice for the majority of every year. This shielding by snow and ice stops the cosmogenic nuclide  $^3\text{He}$  from building up in the surficial lava surfaces and so creates a discrepancy between the exposure age determined and the actual time at which the edifice first pierced through the ice. The true eruption age could be considerably older and this thesis represents the first attempt to tackle this problem.

Iceland not only provides a large number of potential subglacial edifices (rhyolitic and basaltic) to sample but is geologically interesting as it sits above a hotspot and spreading ridge (Fig 1.1). Whether the Icelandic hotspot is truly a mantle plume has been a matter of debate for the past few decades (Allegre et al., 1993; Allegre et al., 1994; Stuart, 1994; Anderson, 1998; van Keken and Ballentine, 1998; Porcelli and Ballentine, 2003; Ballentine and Holland, 2008). This has made Iceland a centre of attention for noble gas studies (specifically He isotopes), as their isotopes can be used to probe the origin of the mantle beneath Iceland. Helium isotopes are comprised of a mixture of magmatic helium trapped whilst in the mantle, cosmogenic helium built up by interaction with cosmic rays during surface exposure and radiogenic helium produced from the *in situ* decay of U and Th. Each of these components yield invaluable information on the mantle, time of eruption and length of exposure.

The majority of the subglacial volcanoes in Iceland exhibit various degrees of surface erosion. It is unknown whether these edifices erupted into the most recent period of ice cover or whether the eruptions span a range of glacial-deglacial cycles.

Was the erosive power of the ice sufficient to remove the entire previous glacial period of subglacial volcanism? Does subglacial volcanism occur during periods of ice retreat or from a pulse of the mantle plume? Are the subglacial volcanoes sourced from the spreading ridge or the mantle plume? Are the subglacial volcanoes mono- or polygenetic? Determining accurate eruption ages of the subglacial volcanoes can help us understand the temporal nature of glacial-deglacial volcanic processes and links with decompressional melting of the mantle during glacial unloading.

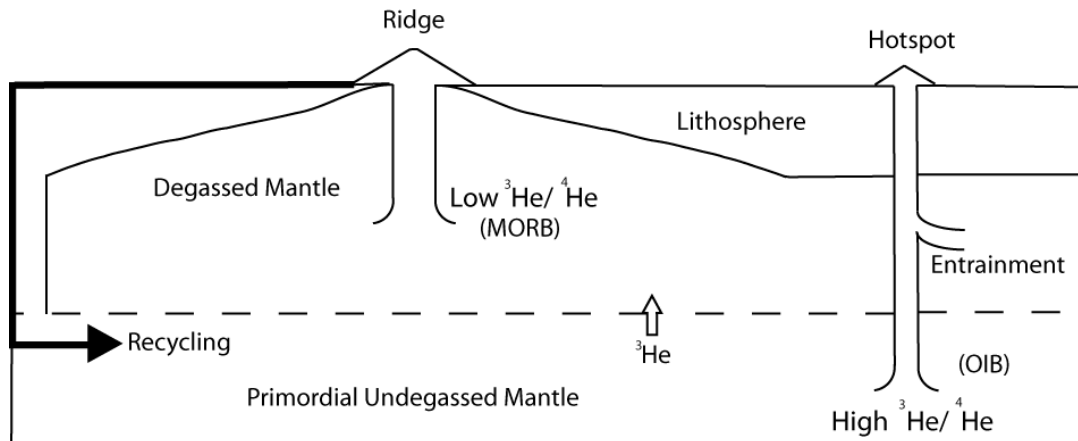


**Figure 1.1:** Suggested mantle model adapted from Anderson (1998) explaining the different  ${}^3\text{He}/{}^4\text{He}$  ratios seen between MORBs and OIBs.

## 1.2 Aims of the Study

The principal aim is to determine whether reliable and accurate eruption ages of basaltic subglacial volcanoes in Iceland are possible, by applying a relatively new geochronological tool: U-Th/He dating. This technique allows for the dating of relatively young volcanic rocks, particularly basalt that contains olivines, which are acquired from the base of the volcanic edifices. Previous attempts to determine accurate eruption ages has been hindered by commonly used dating techniques (radiocarbon, Ar-Ar, tephrochronology) not being feasible on olivine phenocryst samples. These new ages will help confirm precisely the time in which glacial cycle the edifices were formed and further address whether volcanism increases with glacial unloading (MacLennan et al., 2002).

Combining the eruption ages of the tuyas with cosmogenic exposure ages, using cosmogenic  ${}^3\text{He}$ , may help to establish changes in the ice surface elevation and thickness over time. Therefore, a secondary aim is to determine the exposure ages of the sampled subglacial volcanoes through  ${}^3\text{He}$  cosmogenic nuclide surface exposure dating. The minimum ice surface elevation can be determined from the height of the flat-topped summits, which is caused by the depression of the melting ice directly above the active vent. Determining whether each successive period of ice cover removes any evidence of subglacial volcanism from the previous period of ice can be resolved by comparing exposure and eruption ages.

Combining the eruption and exposure ages with glacial geomorphological evidence, enables reconstruction of the thickness and elevation of the ice sheet at the time and location of each subglacial volcanic eruption. This research therefore enables a link to be established between local ice thickness and broader palaeoclimatic change.

### 1.3 Outline of Thesis

A literature review outlining the geological background of Iceland is provided in Chapter two, including how subglacial volcanoes are formed and outlining the history of glacial activity on Iceland. Chapter three focuses on the methodology behind the He dating techniques used throughout this study: cosmogenic  ${}^3\text{He}$  surface exposure dating and U-Th/He eruption age dating. Chapter four presents the locations of subglacial edifices sampled and outlines the field work to collect samples. The experimental methods of noble gas mass spectrometry are described in Chapter five. Chapter six presents and discusses the data determined from crushing the samples to release helium and argon trapped within inclusions in the samples. Cosmogenic (Chapter 7) and radiogenic (Chapter 8) helium data are presented and are discussed in terms of the extent to which the techniques were successful for dating Icelandic basalts. Chapter nine contains the main conclusions and suggestions for further work.

# Chapter Two: Literature Review

## 2.1 Geological Setting of Iceland

### 2.1.1 Geological History and Tectonics



**Figure 2.1:** Aerial map of Iceland. Taken using Google Maps

Iceland is located in the North Atlantic Ocean, east of Greenland and west of Norway (latitude  $63^{\circ}23'N$  to  $66^{\circ}30'N$ ; Fig. 2.1), and sits across two tectonic plates: the Eurasian and the North American.

Iceland's existence is owed to two processes. The first process is the spreading of the Eurasian and North American tectonic plates, at the Mid-Atlantic spreading Ridge (MAR). The MAR diverges at a rate of 18.3 mm per year in the direction of  $105^{\circ}$  and  $285^{\circ}$  (DeMets et al., 1994), generating new oceanic lithosphere.

The second process is enhanced volcanism initiated by the Iceland Hotspot (Wolfe et al., 1997). The Icelandic Hotspot is commonly accepted as a mantle plume but this suggestion is still under scientific debate, (Foulger, 2002). This hotspot or mantle plume provides hotter, less dense material from the Earth's mantle, which is more buoyant than its surroundings, causing the material to rise to the surface.

The MAR aligned with the hotspot in the Miocene at approximately 27 Ma (Oskarsson et al., 1985), and has continued to realign itself with the hotspot by migrating in a series of “rift jumps” (Helgason, 1984, Hardarson et al., 1997). Evidence for which is provided by the existence of rift zones that are now extinct (Fig. 2.3).

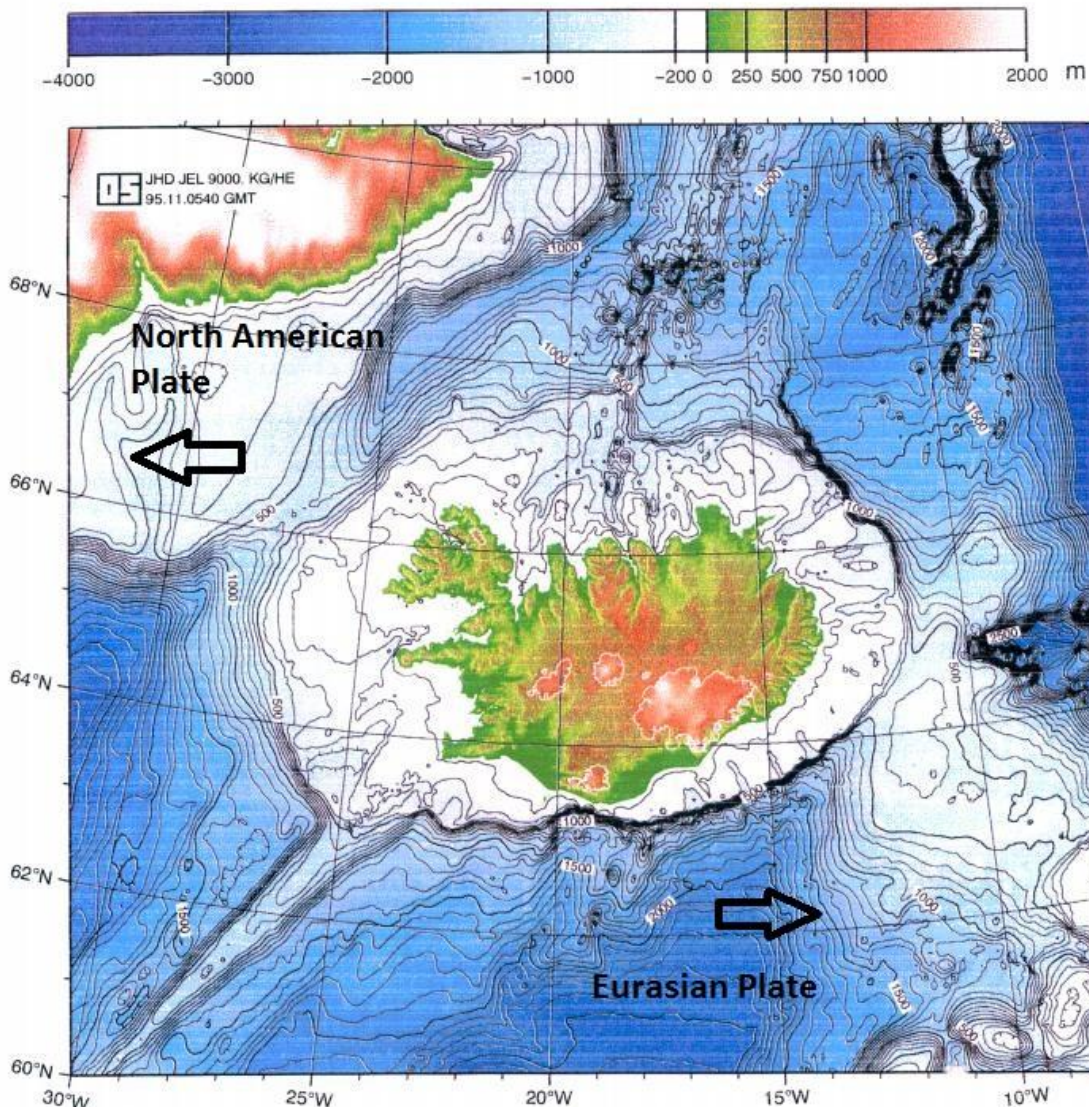


**Figure 2.2:** Bathymetry/topography of Iceland and the MAR running North and South of Iceland. Adapted from (Eysteinsson and Gunnarsson, 1995)

The production of basaltic and silicic volcanism created Iceland that started ~16 Ma (Saemundsson, 1979). The production rate of magma is extremely high due to the combination of the hotspot and the two spreading plates. The combination allows for a topographic high point on the MAR, eventually leading to the significant subaerial island found today. The Iceland Basalt Plateau covers ~350,000 km<sup>2</sup>, with only 30% of the Plateau above sea level (Fig. 2.2). The Plateau

rises over 3000 m, starting from the seafloor, reaching the top of Iceland's highest point of 2110 m, situated at Hvannadalshnúkur in the southeast (Thordarsson and Hoskuldsson, 2002).

In the centre of Iceland the rocks are largely younger (from the Holocene period), compared to the rocks found furthest from the active rift zones, in the east and west (from the Tertiary period). In the east, the oldest rocks have been dated at  $\sim$ 13 Ma and in the west  $\sim$ 16 Ma (Foulger, 2006 and references therein; section 2.1.3).

### 2.1.2 Rift zones of Iceland

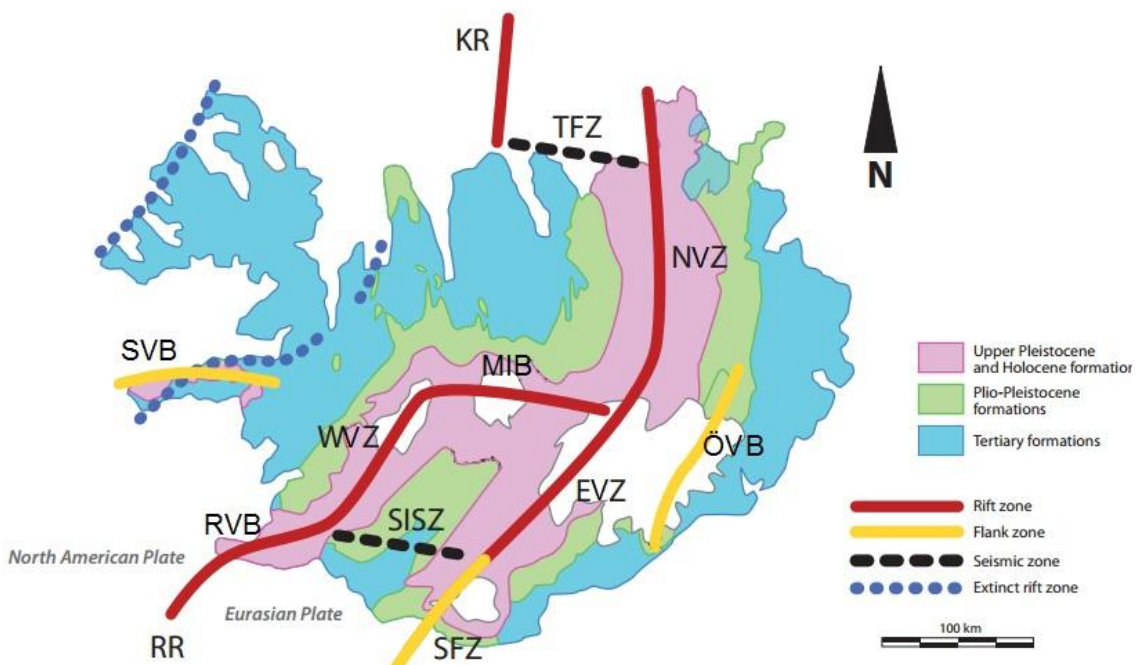


**Figure 2.3A:** A map of Iceland indicating the different regions of rift and volcanic activity. RR, Reykjanes Ridge; RVB, Reykjanes Volcanic Belt; WVZ, West Volcanic Zone; EVZ, East Volcanic Zone; SFZ, Southern Flank Zone; NVZ, North Volcanic Zone; KB, Kolbeinsey Ridge; SVB, Snæfellsnes Volcanic Belt; MIB, Mid-Iceland Belt; SISZ, South Iceland Seismic Zone; ÖVB, Öræfi Volcanic Belt; TFZ, Tjörnes Fracture Zone; KR, Kolbeinsey Ridge. Map adapted from Walker (2011), using terminology from Thordarsson and Hoskuldsson (2002). Central volcanoes seen on Fig. 2.10.

Volcanic activity in Iceland occurs on the active rift zones (Fig. 2.3A), which are defined as the subaerial expression of the active spreading ridge at the axial rift zones. Transform faults link the axial rift zones to each other and to the broader MAR. The rift zones produce largely NNE-trending fissure swarm eruptions, most of which originate from central volcanoes that run parallel to the rifting (Fig. 2.3B; Sigmundsson et al., 2015). Magma erupted from rift zones are generally of tholeiitic

composition. The tholeiitic magma series is one of the most common volcanic rocks produced, with a basaltic composition rich in Fe compared to Mg, a low K content and little variation in Si (Best, 2009). Also present are flank zones that develop active volcanism occurring away from the axial rift zones (Fig. 2.1, SVB, ÖVB and SFZ). Flank zones produce volcanic rocks with a more alkaline composition (Jakobsson, 1979). These zones represent the unzipping of new rifts and volcanic activity in the flank zones (such as the Southern Flank Zone) includes recent eruptions including the 2010 eruption of Eyjafjallajökull (Gudmundsson et al., 2010; Sigmundsson et al., 2010).

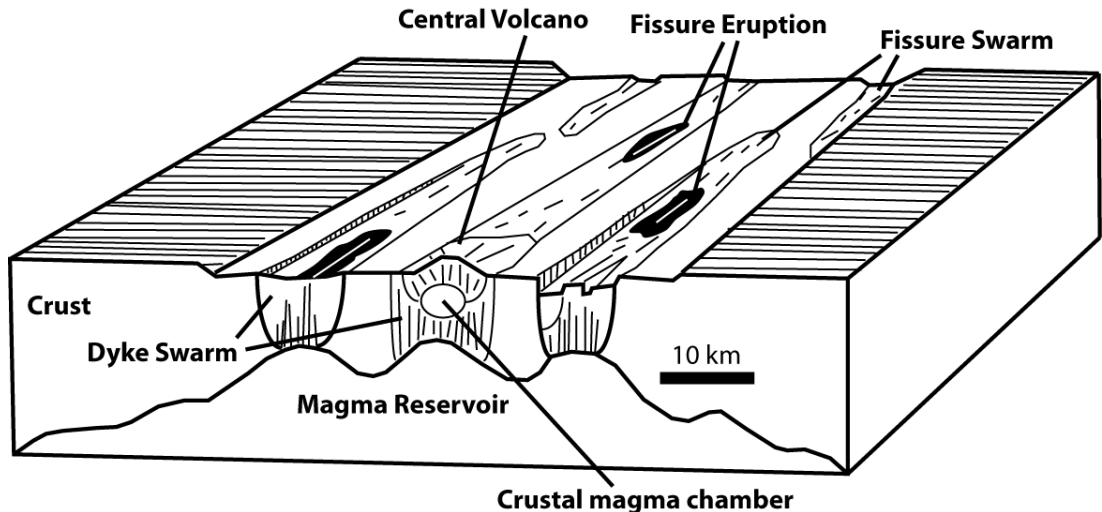


**Figure 2.3B:** Illustration of central volcanoes and fissure swarms (adapted from Thordarson and Larsen, 2006).

There are a variety of names for each rift system and/or volcanic zone that are used in the literature, which have not been standardised. The terminology used here, as shown in Fig 2.3A, is taken from Thordarsson and Hoskuldsson (2002) and discussed briefly below.

Iceland is on the MAR between the Reykjanes Ridge (RR) in the south and the Kolbeinsey Ridge (KR) in the north, which represent submarine segments of the MAR. The surface expression of the plate boundary across Iceland is seen in narrow belts of active faulting and volcanism that extend from the RR, zig-zagging across Iceland's surface to the north where it plunges back down into the Arctic Ocean. Iceland provides the only subaerial section of the MAR. The Reykjanes Volcanic Belt (RVB) is an example of the submarine RR emerging to become subaerial (Guðmundsson and Jakobsson, 2008).

Fractures and faults appear in the brittle crust from the spreading of the plates. These fractures can provide pathways for magma to rise to the surface as dykes. The

RVB is connected to the southern end of the East Volcanic Zone (EVZ) by way of the South Iceland Seismic Zone (SISZ), which is a transform fault (Fig. 2.3A). The RVB then bends northwards to join with the West Volcanic Zone (WVZ), which is connected to the Mid-Iceland Belt (MIB). The WVZ has been active since 7 Ma and its activity has dwindled throughout postglacial history (when compared to the EVZ). This drop in activity is suggested to have progressed from lowered tectonic activity and a reduced spreading rate as rifting transferring to the east, on EVZ and new rift to the east (Jakobsson and Johnson, 2012). The WVZ contains abundant evidence of volcano-ice interactions, including 258 basaltic subglacial formations (e.g. Hlöðufell; Skilling, 2009) in this area alone which encompasses 1350 km<sup>2</sup> (Jakobsson and Johnson, 2012). Subglacial volcanic processes and morphological features are described in detail in section 2.3.

Magmatism in the MIB has been limited to the Holocene and has geochemical similarity to the WVZ. The MIB is usually defined as a separate zone, which has previously been labelled as a leaky transform fault system (Oskarsson et al., 1985) that connects the WVZ to the North Volcanic Zone (NVZ) and EVZ.

The NVZ and EVZ can be defined as one system, but have been subdivided into two separate systems for geographical clarification. The NVZ extends from central Iceland to the north coast and sits slightly oblique to the direction of spreading, creating en-échelon (arranged in a step-like manner) fissure swarms. There are numerous subglacial volcanic edifices present in the NVZ such as Herðubreið, Bláfjall and Búrfell (Chapter 2.3). The NVZ does not adjoin directly with the submarine MAR and instead is connected to the MAR by a non-magmatic transform zone called the Tjörnes Fracture Zone (TFZ).

Directly south of the NVZ is the EVZ. The EVZ is aligned in a south-westerly direction; starting from the base of the NVZ. The EVZ is currently the most active rift zone in Iceland, with the south section of the EVZ sitting underneath the Vatnajökull ice cap (Fig. 2.3A). Central volcanoes produced from the EVZ have experienced frequent volcanic activity (Björnsson and Einarsson, 1990), including the relatively recent subglacial eruption of Gjálp in 1996 (Gudmundsson et al., 1997).

### 2.1.3 Geological History

Iceland's volcanic activity, expressed from the active rift zones, can be divided into four different chronological periods (Jóhannesson and Sæmundsson, 1998; Fig. 2.4):

1. The Tertiary: composed of basic and intermediate extrusive rocks with intercalated sediments, with ages older than 3.1 Ma.
2. Upper Pliocene and Lower Pleistocene (Plio-Pleistocene): composed of basic and intermediate extrusive rocks with intercalated sediments, with ages 0.7-3.1 Ma.
3. Upper Pleistocene: composed of basic and intermediate hyaloclastite, pillow lava and associated sediments (inter- and supra- glacial lavas), with ages younger than 0.7 Ma.
4. Holocene: composed of postglacial basic and intermediate lavas, with ages older than 1100 years.

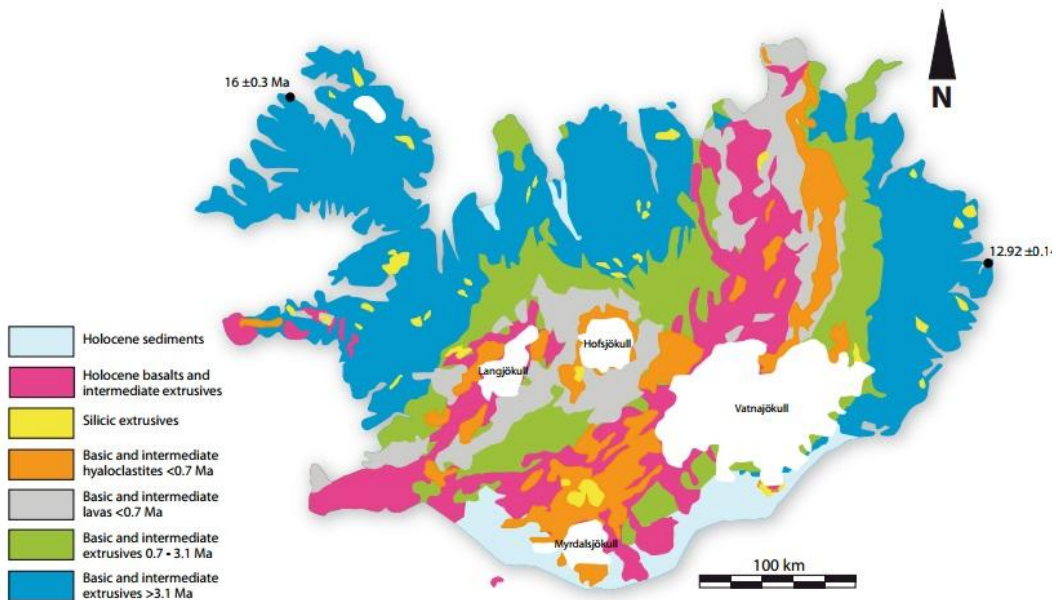


**Figure 2.4:** A geological map of Iceland. Adapted from Walker (2011), adapted from Jóhannesson and Sæmundsson (1998) and Thordarsson and Hoskuldsson (2002)

The distribution of these lavas, with their ages, corresponds to the rift zones. The remote flank zones contribute outliers of active volcanism while being surrounded by much older rock, such as the SVB (Fig 2.3A).

The majority of rocks that outcrop Iceland are basaltic, but approximately 8-12% of the outcrops are composed of silicic (rhyolite and granite) intrusions (Walker, 1966; McGarvie, 2009; Jónasson, 2007; Flude et al., 2010).

This research is mainly focused on the basaltic tuyas formed beneath former ice sheets (subglacial table-mountains; Chapter 2.3) found abundantly in the WVZ and NVZ. The remainder of this chapter therefore considers the records of climatic evolution and glacio-volcanic processes in Iceland.

## 2.2 Glacial History of Iceland

Reconstructing the nature of paleo-ice sheets in the northern and southern hemispheres, to better understand the palaeoclimate of Earth, can be achieved by mapping glaciovolcanic landforms. Glaciovolcanic landforms can be used partially in lieu of ice core data and they act as a land-based record of the localised Icelandic paleoclimate. Completing a reconstruction of paleo-ice from subglacial volcanic edifices helps to constrain Icelandic ice sheet behaviour and its relationship with global climatic change.

The extent of the ice cover over Iceland has deviated greatly since its first glaciation at around 2.6 Ma BP, with ~50 glacial cycles since (Einarsson and Albertsson, 1988; Gemsoorm and Eiriksson, 1994; Gibbard and Cohen, 2008). However, knowledge is poor of the glacial cycles that occurred before the last glacial maximum (LGM; ~21 ka, Ingolfsson, 1991; Norðahl, 1991; Hubbard et al., 2006). Evidence of previous glacial cycles, including moraines and tills, is readily erased by advancing glaciers from the most recent glacial period. This prevents any potential preservation of past glacial cycles. Helguson and Duncan, 2001, looks back into previous glaciations.

One way to better understand the cycles of glacial and interglacial periods is with ice cores. These cores allow the measurement of oxygen isotopes present in the layers of ice to reconstruct a climatic record. Fig. 2.5 shows the glacial and interglacial (warming) periods throughout the past 700 ka for the northern hemisphere. There are minor temperature fluctuations between the glacial and interglacial cycles. Short periods of warming within a glacial period are named interstadials, whereas short periods of cooling within an interglacial period are named stadials. Gibbard and Cohen (2008) have constructed a table displaying

extensive global chronostratigraphy of the past 2.7 Ma. Their table also includes oxygen isotope data from marine and ice cores.

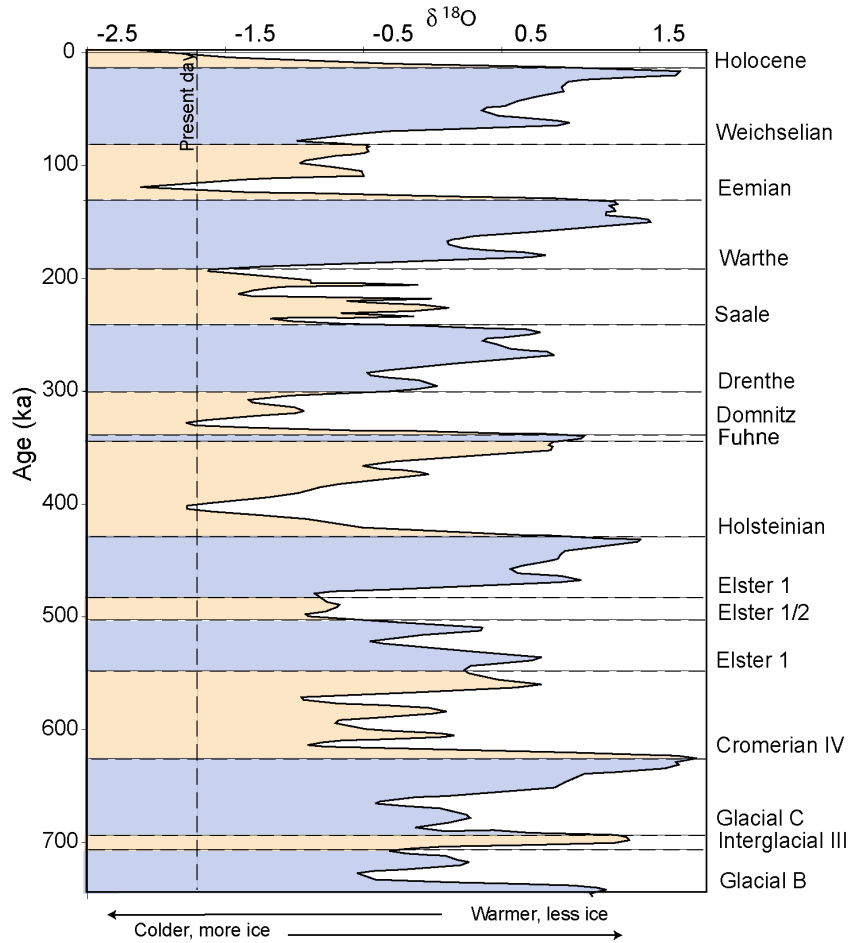


**Figure 2.5:** Oxygen isotope curve (Imbrie et al., 1984) showing the last 700 ka of glacial and interglacial periods, names taken from Lowe and Walker (1997). The higher the  $\delta^{18}\text{O}$  value indicates colder conditions enabling more ice, whereas low values indicate the opposite. Correspondingly, the blue sections indicate glacial periods and the pink sections are interglacial (warm) periods.

Looking at the oxygen ice core records, it can be seen that the onset of a glacial period is gradual, whereas deglaciation occurs rapidly. For example, the cold conditions for the glacial period of the Warthe increased gradually over ~60 ka. By comparison, the Eemian interglacial reaches the lowest  $\delta^{18}\text{O}$  in ~10 ka, indicating that deglaciation is a rapid process (Fig 2.5). This rapid retreat of a glacial period creates a large mass-balance shift of the Earth's crust (see 2.2.3 Decompression Mantle Melting).

## 2.2.1 Weichselian Timeline

Table 2.1 displays a timeline of significant events during the last glacial period in Iceland, the Weichselian, based on Norðdahl et al., (2008). Geomorphological evidence, including: the height of subglacial volcanic formations (tuyas), the lip-elevation of cirques, the orientation of glacial striae and the presence of frost shattering on mountain tops, has been used to deduce the history of ice sheet thickness and flow direction.

The Weichselian glacial period started  $\sim$ 100 ka BP, reaching the LGM  $\sim$ 21 ka BP and finishing  $\sim$ 10 ka BP (Einarsson and Albertsson, 1988; Ingolfsson, 1991; Norðdahl, 1991; Hubbard et al., 2006). Combining geomorphological data and 3D thermomechanical modelling has shown that the maximum thickness of the LGM ice sheet was  $1500\pm500$  m in central Iceland (Fig. 2.5), with an area of  $\sim$ 300,000 km<sup>2</sup> and volume up to 500,000 km<sup>3</sup> (Norðdahl, 1991; Norðdahl and Pétursson, 2005; Hubbard et al., 2006).

Central Iceland was continuously covered by a single, thick ice cap from which outlet glaciers flowed radially (Norðdahl, 1991). The glaciers extended far off shore at the LGM (Fig. 2.6), with glacial striae and till-like deposits demonstrating that the ice sheet reached and overrode the island of Grímsey, 40 km off the north coast of Iceland (Hoppe, 1968; Norðdahl, 1991). Warming in the early stage of the Bølling interstadial (between 15.5 and 13.6 ka; Table 2.1), allowed warm seawater to reach the north coast of Iceland. By this time the continental ice sheets, across the rest of the northern hemisphere, had already been melting for a few thousand years (Norðdahl et al., 2008). The subsequent dramatic rise in eustatic sea level forced the marine parts of the Iceland ice sheet to float, initiating extreme ice calving (Ingólfsson and Norddahl, 2001). The sea level rose at a faster rate than the isostatic rebound, causing the formation of high shorelines, between 50 and 60 m a.s.l. at  $\sim$ 12.6 ka BP (Norðdahl and Pétursson, 2005).

Era	Period	Epoch	Age	Stage	Substage	Events
Cenozoic	Quaternary	Holocene	0	Sub-Atlantic	Little Ice Age	
			500			5-6 ka: Neoglaciation
			1 000			6-7 ka, Mid-Holocene max: glaciers reduced or absent
			2 500			
			5 000			
			7 200			
		Upper Pleistocene	9 300	Sub-Boreal		<b>8 ka: Glaciers at similar extent to present day</b>
			10 000	Atlantic		
				Boreal		9.8 ka: Glaciers advance again close to Y. Dryas extent
				Pre-Boreal		
	Tertiary	Pliocene	11 000	Weichselian	Younger Dryas	10.3 ka: Y.Dryas ice regrowth maximum
			12 000		Allerød	Fast rising sea-level Earliest vegetation record
			15 000		Older Dryas	
			20 000		Bølling	
			70 000			<b>18 ka: Weichselian glaciers start to melt</b>
			120 000			<b>~21 ka: Glacial maximum</b>
		Lower Pleistocene	130 000	Eemian		<b>Last glacial stage</b>
			170 000	Saale		Interglacial warming
			352 000			Penultimate glacial stage
			700 000			
			2.5 Ma			Full scale glaciation
			3.3 Ma			
			7 Ma			First sign of cooling climate
			12 Ma			Warm temperate climate

**Table 2.1:** Geological timeline of Iceland (note that not all glacial/interglacials are stated). See text for description of terminology. Table based on Thordarsson and Hoskuldsson (2002) and adapted using events described from Norðdahl et al., (2008). Blue font indicating a stadial and red font indicating an interstadial (see **Fig. 2.5**).

Extreme and rapid deglaciation coupled with Iceland's hot buoyant mantle (how viscosity controls lithosphere in Iceland) caused an extensive isostatic rebound to occur on Iceland's lithosphere (see section 2.2.3 Decompression Mantle Melting). The rate at which Iceland rose from glacial isostacy was greater than the rise in eustatic sea level, causing the relative sea level (RSL) to revert to the slightly less

than current sea level between 12.2 and 11.5 ka BP (Ingólfsson and Norddahl, 2001; Norðdahl and Pétursson, 2005).

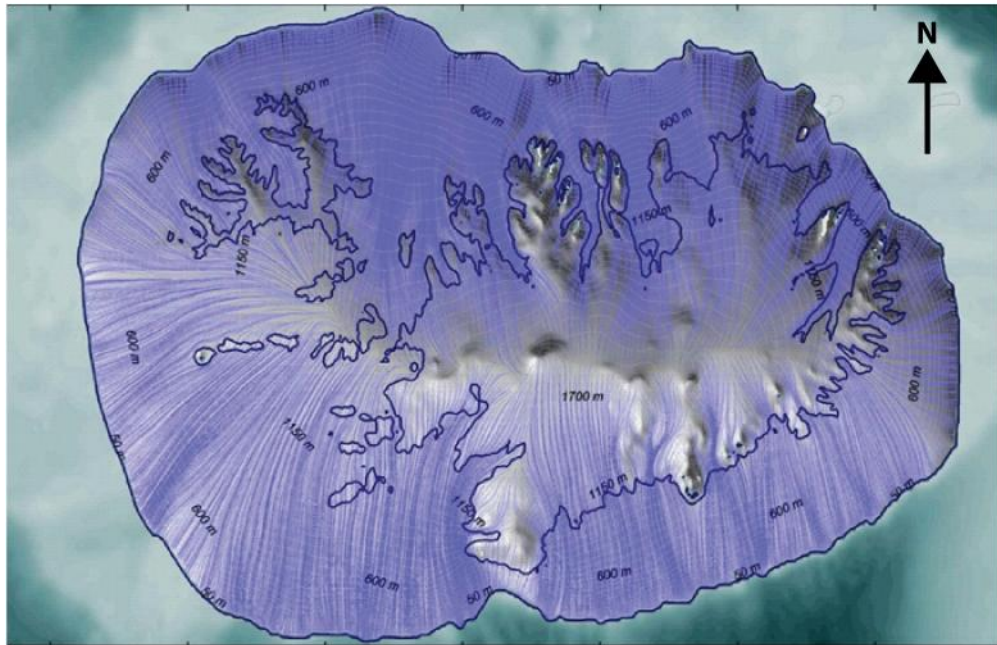


**Figure 2.6:** An adapted 3D thermomechanical model by Hubbard et al., (2006) showing the extent of the glaciers at LGM and its greatest thickness to be close to 2000 m

In the late Bølling, ~12.0 ka, the extent of the Icelandic ice sheet was 25% that of the LGM (Hubbard et al., 2006). Subsequently, the later stages of the Allerød interstadial (Table 2.1) saw an onset of cooling moving into the Younger Dryas and allowed re-growth of the ice sheet. The re-growth of ice, to a maximum at 10.3 ka, instigated an isostatic depression of Iceland's crust. The depression allowed for transgression of the RSL with shorelines as high as 60 m a.s.l. in the south west of Iceland (Norðdahl et al., 2008). At the maximum of the Younger Dryas, the margins of the re-grown ice sheet were situated close to the coastline, with only a few areas of dry land protruding beyond the ice sheet margins (Fig. 2.7; Norðdahl et al., 2008). A short period of glacial retreat followed after the Younger Dryas maximum, resulting in a drop in RSL close to 40 m.

Icelandic glaciers advanced again in the Pre-Boreal stage, with the extent of ice being slightly less than it was in the later stages of the Younger Dryas. The advancing glaciers climaxed at 9.8 ka, pushing Iceland's crust down into the sea, triggering the RSL to climb 20 m (Norðdahl et al., 2008). At ~9.4 ka, the RSL fell towards present sea level height, which was brought on by the retreat of the previously advancing ice sheet. The minimum RSL was reached at 8.9 ka BP when the RSL was 40 m below present sea level (Ingólfsson et al., 1995; Norðdahl et al.,

2008). The Younger Dryas and early Pre-Boreal ice sheets were fairly similar, apart from the region in north Iceland which saw the retreat of major outlet glaciers to the extent of 30-50 km (Norðdahl et al., 2008). By this point, the changes in RSL were triggered only by eustatic sea level changes, with uplift from glacio-isostacy coming to a supposed end (Tushingham and Peltier, 1991; Norðdahl and Pétursson, 2005).

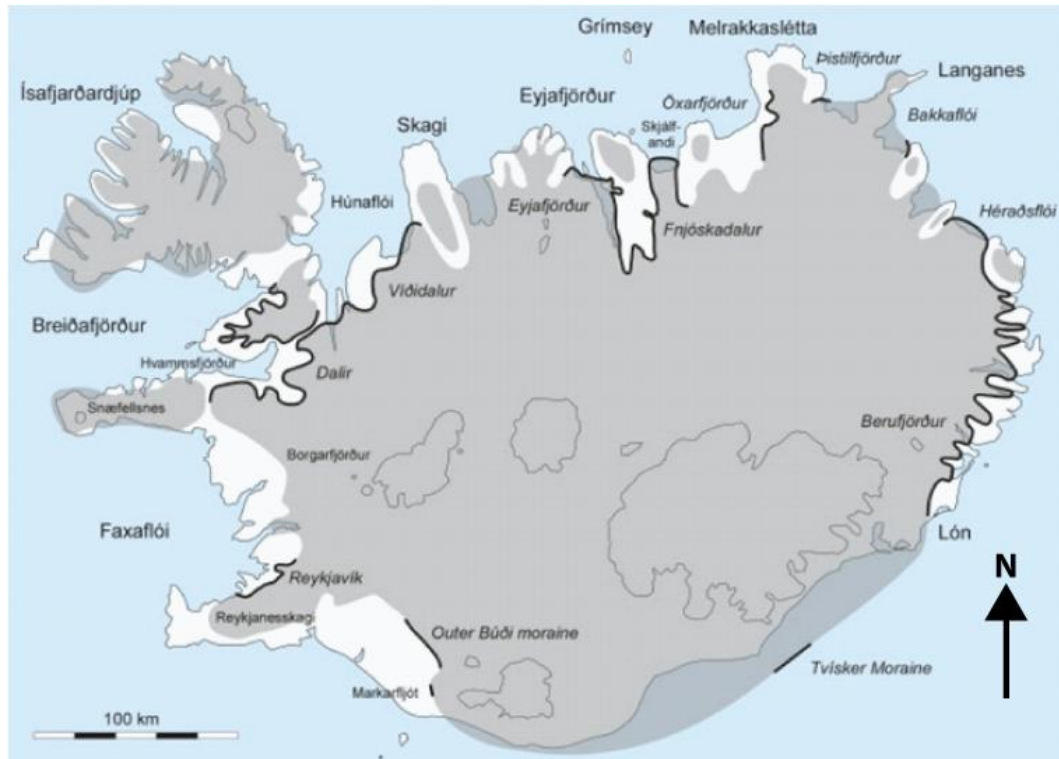


**Figure 2.7:** Extent of the Icelandic ice sheet at the maximum of the ice regrowth in the Younger Dryas; 10.3 ka BP. Adapted from (Norðdahl and Pétursson, 2005)

The Icelandic ice sheet had disintegrated by 7.8 ka (Norðdahl and Pétursson, 2005). The complete removal of ice was confirmed by the Thjórsárhraun lava flow (the largest Holocene lava flow on Earth), which took place in an ice-free region ~140 km inland from the coast of southern Iceland (Hjartarson, 1988). The glaciers present now started to form throughout the Neoglaciation ~5 ka and numerical ice-sheet modelling done by Flowers et al. (2008) implies that the Langjökull ice cap grew to cover the neighbouring peaks (Eiríksjökull, Ðórisjökull, Hrútfell and Geitlandsjökull). These peaks may have been covered by permanent snow cover for the majority of the past 2000 years (Flowers et al., 2008).

## 2.2.2 Ice Dynamics during the Weichselian

The patterns of ice flow of the Weichselian ice sheet has been reconstructed (Fig. 2.9) by Bourgeois et al., (1998, 2000) using glacial directional features (Fig. 2.7) obtained from field data and satellite, (SPOT and Landsat) images (Bourgeois et al., 2000; and references therein). The reconstruction has shown the dynamics of the ice sheet are controlled by various parameters. Precipitation is one parameter, which is more abundant in the south compared to the north of Iceland due to the oceanic and atmospheric circulation in the North Atlantic (Einarsson, 1988). This distribution of precipitation has contributed to producing the thickest part of the ice sheet in the southern regions of Iceland. Another parameter controlling ice sheet dynamics is the flux of geothermal heat. Areas with a high geothermal heat flux generated major ice routes at the surface, with ice streams draining melt-water from the central region of the ice sheet. These ice streams benefited from the high geothermal activity below and Bourgeois et al., (2000) has suggested that subglacial eruptions generated enough available soft material to be deformed into subglacial till layers. Bourgeois et al., (2000) and Bell (2008) state, “that the geothermal heat flux is a first-order parameter of the dynamics of ice sheets” in Iceland.

Preserved glacial striae (Fig. 2.8) have been used to determine the direction of past ice flows. The striae and preserved volcanic edifices can roughly indicate the location of ice divides (ID1-6; Fig. 2.9), as suggested by Einarsson and Albertsson (1988) and Bourgeois et al., (1998). Ice divides pinpoint the origin of ice flow, which flows outward toward the coastlines (Fig. 2.9). The more stable interior of the ice sheet most likely moved at a slower speed than the outer margins, or if it was cold enough, the basal ice may have frozen to the bedrock underneath, in such cases as glaciers in the polar regions (Goodfellow, 2007).

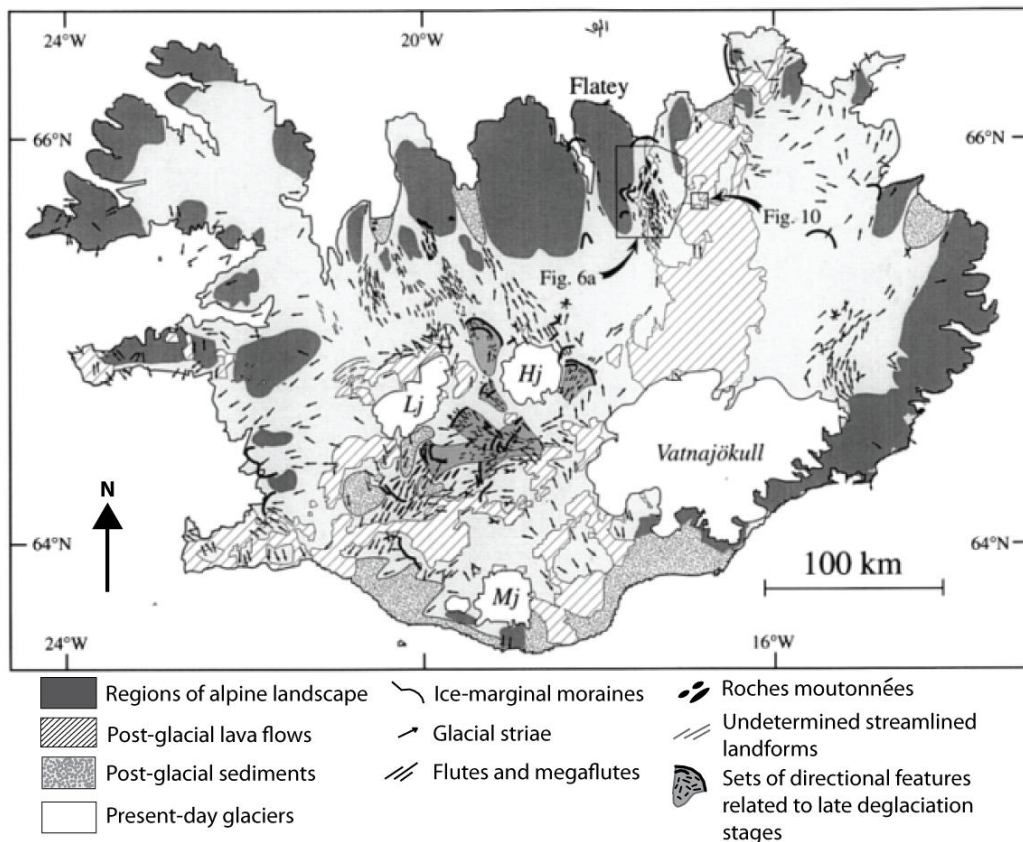


**Figure 2.8:** Glacial directional features used to reconstruct ice flows (Fig. 1.8) from field, SPOT and Landsat data. Adapted from Bourgeois et al., (2000) and references therein.

Subglacial volcanic products are commonly removed by the flow of ice (Helgason and Duncan, 2001). However, due to the presence of well-preserved subglacial edifices, it has been suggested these were emplaced below the ice divides, owing to the slow motion of ice in these locations (Nye, 1951). The opposite of this is where ice streams are present. Evidence of this is seen where particular subglacial volcanic edifices (specifically tindars – see Chapter 2.3) are noticeably eroded. Volcanic debris that has been dislocated is then incorporated into the moving ice until reaching the calving line, where it is deposited into the sea, creating coastal wedges (Bourgeois et al., 1998).

One process resulting in fast transportation of volcanic matter is jökulhlaups (massive subglacial water and debris flows; Björnsson, 2003), which are triggered from subglacial eruptions or geothermal heat rapidly melting the overlying ice. These flows are capable of carrying huge amounts ( $10^7$ - $10^8$  tons) of solid material, most usually contributed from the volcanic eruption, and either deposited as outwash plains or carried into the sea (Bourgeois et al., 1998; Björnsson, 2003).

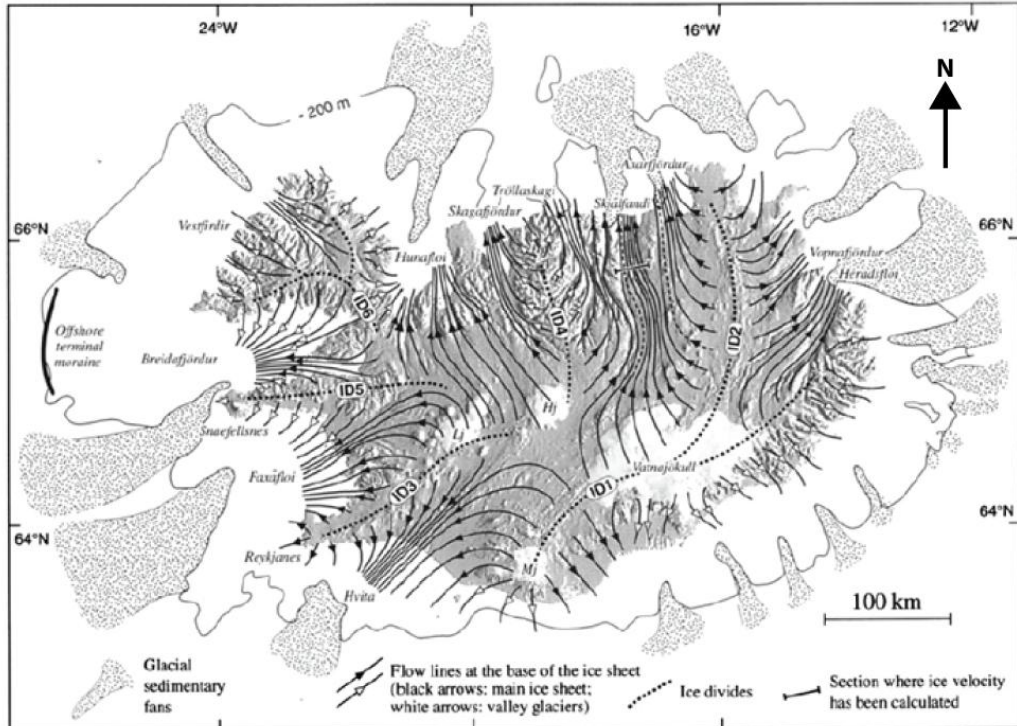


**Figure 2.9:** Ice sheet flow patterns and ice divides (ID1, ID2 etc) at LGM reconstructed using glacial directional features from Fig. 2.7 and large-scale glacial features observed using DEM data from USGS at 30 arcsec resolution. Adapted from Bourgeois et al., (2000) and references therein.

In the coastal alpine regions, nunataks (land protruding through the top of the ice) have been identified where the ice was proposed to flow around, hence acting as obstacles. However, nunataks did not act as obstacles in the north (Flatey Peninsula; Fig. 2.8). Instead the nunataks acted as their own glacial system instigating glacial dynamics to work independently of the rest of the ice sheet (Norðdahl, 1991; Bourgeois et al., 2000). The movement of these valley glaciers (Fig 2.9, white arrows) are distinguished from the main ice flow (black arrows) in the ice flow reconstruction map.

This reconstruction of ice flow and ice divides (Fig 2.9) suggests that subglacial volcanic edifices, which exhibit geomorphology diagnostic of preserved magma-ice interactions, were generated at some point in the Weichselian glacial period.

### 2.2.3 Decompression Mantle Melting

Iceland sits on large amounts of hot buoyant magma due to mantle upwelling from the plume/hotspot and so isostatic rebound of the Icelandic crust after the unloading of heavy ice can cause an increase in mantle melting and basaltic

volcanism (Hall, 1982; Maclennan et al., 2002; Carrivick et al., 2009). With a 30 time increase of basaltic volcanism suggested, near the end of the LGM (Maclennan et al., 2002; Sinton et al., 2005). Two models have been put forward to understand the relationship between increased eruption rates and ice unloading. The first is proposed by Gudmundsson (1986), which states the variation in crustal stress due to the unloading of ice allows for the tapping of magma chambers to be increased and so increases the eruption rates. The second is proposed by Jull and McKenzie (1996), which modelled the result of mantle melting created by ice removal. Jull and McKenzie (1996) found that a large increase in mantle melting rates can occur when the mantle is decompressed throughout deglaciation. This relationship then creates an increase in eruption rates. The arguments they present indicate that it is very difficult to stop an increase in melt production rates during deglaciation. This increase in mantle melting is only controlled by plate separation and so is only applicable to the rifting zones of Iceland, such as WVZ and NVZ, and not areas sourced by the mantle plume, such as EVZ (Maclennan et al., 2001). The models for mantle decompression set out by Jull and McKenzie (1996) show that melts produced from the unloading of ice will have varying rare earth element (REE) concentrations to times when decompression mantle melting is not occurring. Their models can be matched to changes in geochemistry between glacial and postglacial eruptions in the Theistareykir system (Slater et al., 1998). It has also been proposed that these geochemical variations occur in the magma chambers e.g. crystallization, mixing and assimilation of crust (Gee et al., 1998). However, models of these processes cannot provide evidence of the variation in REE geochemistry between eruptions in subglacial and early postglacial environments (Maclennan et al., 2002).

A temporal variation is seen in the compositions of major and trace elements presented for 80 basaltic and picritic samples from the Theistareykir and Krafla regions in the NVZ (Maclennan et al., 2002). The MgO content is similar in both subglacial and early postglacial eruptions, but the subglacial MgO content has a more narrow range, compared to the early postglacial, which can be >15 wt%. The content of MgO has been noted to decrease with the evolution of subglacial eruptions, i.e. as you increase up the tuya's height, the MgO content decreases (Moore and Calk, 1991). This is consistent with an increase in differentiation, which is connected to a decline in the supply of magma (Moore and Calk, 1991; Eason et al., 2015). This MgO differentiation through the height of subglacial units is also

correlated to the change in trace element ratios and can add difficulties in discerning the monogeneity of the subglacial edifice (Moore and Calk, 1991; Eason and Sinton, 2009; Eason et al., 2015). At a given MgO content the subglacial incompatible elements are much higher than those of early postglacial lavas. The most recent eruptions (within last 3000 years) in these regions have similar compositions to subglacial times. This composition variation is the same between subglacial, recent postglacial and early postglacial for REEs. Low REEs for decompression mantle melting is suggested by Jull and McKenzie (1996) as the depth at which the most melting occurs in the mantle is at 60km, where the mantle is depleted by ~15% melting. Certain subglacial lavas have close to 3 times more La content than early postglacial lavas and the Lu content being 1.3 times greater in subglacials (Nicholson et al., 1991; Nicholson and Latin, 1992; Slater et al., 1996; Slater et al., 1998; MacLennan et al., 2002). Eason et al. (2015) have analysed major elements in 19 subglacial edifices throughout the WVZ and has sub-categorized these 19 edifices into three separate chemical groups. The first group A obtains subglacial edifices with low amounts of REEs and major elements progressing to chemical group C with the largest concentrations of REEs and major elements sampled. Therefore the effects of initial deglaciation and decompression mantle melting can be seen in the geochemistry of certain subglacial edifices before the complete removal of ice (Eason et al., 2015). Water content can also increase the amount of melting in the mantle by up to 10% (depressing the mantle solidus) and is significant in the role of melt generation beneath Iceland, with evidence suggesting the mantle plume beneath Iceland is "wet" (Nichols et al., 2002).

These low REE concentrations and high rates of eruption are therefore explained by increased rates of generated melt occurring in the shallow mantle instigated by deglaciation of the ice sheet (Gee et al., 1998; MacLennan et al., 2002).

Olivine crystallises out very early on in basaltic magma chambers at high temperatures (~1400°C) and pressures, it is stable to up to a depth of 410km and makes up the majority of the basaltic mantle melt in shallower depths (Bowen's Reaction Series; Smyth et al., 2006). Therefore olivine is a great mafic mineral to use to trace basaltic mantle processes, especially decompression melting throughout glacial periods, as inclusions trapped in the phenocryst preserve the geochemistry of the mantle at the time of crystallisation.

### ***Short Timescale Compression***

Enough snow can produce a localised compression effect on central volcanoes located across Iceland. Triggering an eruption by decompression of the removal of snow is highly dependent on the load location and the shape of the magma chamber (Albino et al., 2010; Sigmundsson et al., 2010). This effect has been studied on Grímsvötn and Katla. In 2004 Grímsvötn erupted directly after a  $0.5 \text{ km}^3$  jökulhaup (outburst of glacial meltwater), which is suggested to have caused the eruption. A similar theory is put forward for Katla, which sits under the Mýrdalsjökull ice cap and sees an annual cycle of 6 metres of snow build up and melt. This is enough to create a pressure decrease on the magma chamber. A model has been made for central volcanoes with spherical or horizontal magma chambers that states eruptions are most likely when snow cover is minimal. This is consistent with the most recent eruptions of Katla having occurred throughout summer seasons (Albino et al., 2010; Sigmundsson et al., 2010).

## **2.3 Volcano-Ice Interactions**

A volcano-ice (or glaciovolcanic) interaction refers to any interaction between ice, snow and/or meltwater with a volcanic eruption. There are different terms used depending on the nature of the interaction. Subglacial is used for a volcanic eruption occurring beneath ice. Supraglacial is used for an eruption occurring above the ice (similar to subaerial eruptions which occur in the open air). Finally, englacial, ice-contact or ice-confined is used for an eruption occurring within the ice (perhaps part way through an ice sheet) and/or within close proximity to ice. Refer to Smellie and Edwards (2016) and/or Smellie (2000) encyclopaedia chapter.

Volcano-ice interactions are important when reconstructing local ice sheet response to global climate change. Investigation of mechanisms are of great interest, especially in Iceland. Subglacial edifices contain important information by acting as local proxies for paleoclimate reconstruction. These land-based proxies allow us to reconstruct the fluctuations in thickness and movement of ice sheets, including the effect this has on volcanism. Therefore, the information these subglacially erupted edifices hold has led to an increase in research into volcano-ice interactions. Also driven by the need to mitigate the hazards, especially in the past twenty years, initiated with pioneering research started in the 1940's (Kjartansson, 1943;

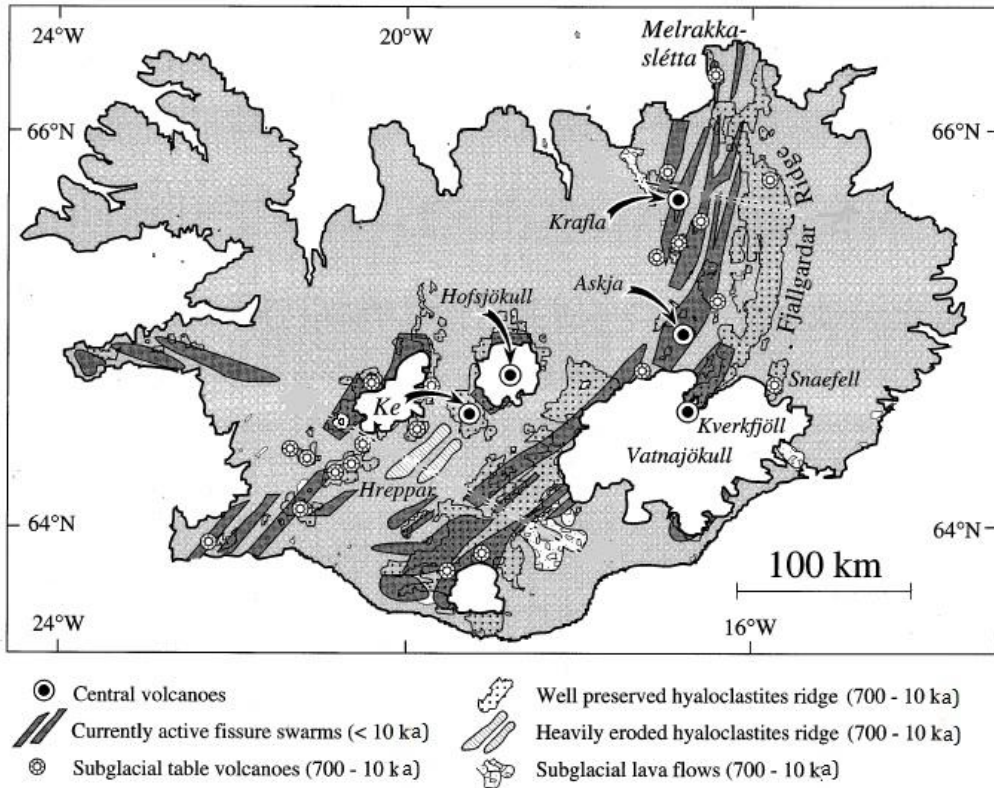


**Figure 2.10:** A map of Iceland illustrating the locations of volcanic subglacial formations including the fissures produced from active rifting. Adapted from Bourgeois et al., (1998)

Mathews, 1947), continuing to the present day. These include studies of facies (Jones, 1968a; Jones, 1968b; Grove, 1974; Allen, 1980; Smellie and Skilling, 1994; Smellie and Hole, 1997; Smellie, 2000; Chapman and Tanaka, 2001; Tuffen et al., 2001; Edwards and Russell, 2002; Tuffen et al., 2002; McGarvie et al., 2006; Chapman and Smellie, 2007; Jakobsson and Gudmundsson, 2008; Smellie et al., 2008; McGarvie, 2009; Skilling, 2009; Smellie, 2009; Flude et al., 2010; Tuffen et al., 2010; Jakobsson and Johnson, 2012), models of eruptions (Ghatan and Head, 2002; Gudmundsson et al., 2002; Tuffen, 2007; Sigmundsson et al., 2010), investigation of volcanic-climate links (Tuffen and Betts, 2010), observations of eruptions (Gudmundsson et al., 1997) and patterns of volcanism and relation to glacial cycles (Huybers and Langmuir, 2009; Tuffen, 2010).

Glaciovolcanic edifices appear in numerous regions on the Earth's surface with evidence of interactions between magma and ice in the Antarctic Peninsula (Smellie and Skilling, 1994), Alaska, USA (Clarke et al., 1989; Wood and Kienle, 1992), British Columbia in Canada (Hickson et al., 1995; Moore et al., 1995; Dixon et al., 2002; Edwards et al., 2011), New Zealand (Spörli and Rowland, 2015), Chile (Mee et al., 2006) and Mexico (Capra et al., 2015). However, subglacially formed

volcanoes are found especially across Iceland, specifically in the WVZ and NVZ (Fig 2.3A). Glaciovolcanic deposits from the Late Pleistocene cover 11,200 km<sup>2</sup>, with the glaciovolcanic formations numbering in the thousands (Jakobsson and Gudmundsson, 2008).

### 2.3.1 Subglacial Volcanic Edifices

There are two main types of subglacial formations: table-mountains and hyaloclastite ridges, these are known as tuyas and tindars respectively.

#### *Tuyas*



**Figure 2.11** Herðubreið (summit 1682m) is a large tuya in the NVZ. Photo credit Dr D. McGarvie

Tuyas (Mathews, 1947; Jones, 1968a; Smellie and Skilling, 1994) are the subglacial equivalent to a shield volcano (Werner et al., 1996), and form from focussed magma emission from a point source (Fig 2.10). Tuyas are commonly equi-dimensional and appear roughly circular to elliptical when viewed from above, with a length to width ratio close to <2 (Mathews, 1947; Jakobsson and Gudmundsson, 2008). Characteristic to tuyas are their steep sides and flat caps (Fig 2.11). The flat caps are a result of the transition from subaqueous to subaerial. Their steep sides are a result of being emplaced directly within the ice. Instead of forming a gently sloped shield volcano (typical of equivalent Holocene eruptions), the confinement created by the ice creates a tall steep sided edifice, up to 1400 m in height in the WVZ (Eiríksjökull; Jakobsson and Johnson, 2012 and 1682 m in the NVZ, Herðubreið; Licciardi et al., 2007).

Tuyas commonly originate from a single vent along an active rift zone (Section 2.1.2), produced from magma released by central volcanoes (Rossi et al., 1996; Thordarsson and Hoskuldsson, 2002). Central volcanoes can be short lived (few weeks) to long lived (several decades) and can vary in eruptive volume from 0.01 km<sup>3</sup> to 15 km<sup>3</sup>, with the majority being close to 1 km<sup>3</sup> (Rossi et al., 1996). The diameter of a central volcano can be directly proportional to its volume. Most all central volcanoes start as fissure eruptions (see *Basaltic Tindar Formation*). Tuyas can be defined as “central vents or short-fissure fed, ice-confined, eruptive centres with prominent development of subaerial lava-fed deltas” Skilling (2009). The largest monogenetic tuya recorded to date in Iceland is Eiríksjökull, situated north west of the Langjökull ice cap (Fig 2.10) and has a basal area of 77 km<sup>2</sup> (~48 km<sup>3</sup>) (Jakobsson and Johnson, 2012). Edifices such as Eiríksjökull, that have long lived eruptions with low effusion rates, are suggested to be continuously recharged with magma from the mantle, such as postglacial shield volcanoes (Rosi et al., 1996; Sinton et al., 2005). Shield and tuya producing eruptions can involve several periods of eruptive activity, hiatae, and can last from months to decades, consisting of lava from one chemically coherent source of magma (Eason et al., 2015). Rhyolitic tuyas are considered to be monogenetic (McGarvie et al., 2006; McGarvie et al., 2007; Stevenson et al., 2009; Stevenson et al., 2001; Owen et al., 2012). However, a monogenetic formation for all tuyas should not always be assumed, even though examples of polygenetic tuyas are rare. To date, Kjartansson (1943), Jones (1968a) and Skilling (2009) state that tuyas are formed monogenetically, whereas Werner et al., (1996; 1999) argue that others, including Hlöðufell and Herðubreið, have been generated through multiple sources in multiple pulses of chemically distinct magma.

### ***Basaltic Tuya Formation***

Basaltic tuyas are commonly produced in three or four stages. The following sequence is based on Jakobsson et al., (2008) and Skilling (2009), which should be referred to for a more detailed analysis on tuya formation, including lithofacies description:

1. The first stage (subglacial) involves magma melting the ice directly above to form a meltwater-filled cavity at the ice sheet base (Fig 2.12 A). The melting of the ice may cause a lateral escape of the meltwater at the base of the ice sheet to create an equivalent depression on the ice surface directly above (Thordarsson and Hoskuldsson, 2002). High ice pressures and

modest mass eruption rates during the initial stages of an eruption encourage the effusive eruption of pillow lava (Fig 2.12 A2), which forms the basal unit of the tuya (Jones, 1968a; Jakobsson and Gudmundsson, 2008; Skilling, 2009). Ice confinement features are found within this basal unit of the tuya (see *Ice Confinement Features*).

- 2 The second stage (subaqueous) occurs when the roof of ice melts completely or collapses to form an intraglacial lake (Fig 2.12 B; Jones, 1968a). As the subglacial edifice grows, the overlying water depth decreases and lower pressures trigger a transition from an effusive to an explosive eruption (Fig 2.12 B2: Image of the 1996 Gjálp eruption beneath the Vatnajökull ice cap). This explosive eruption produces a hyaloclastite tuff cone (Fisher and Schmincke, 1985), which is fragmented basalt that is created during explosive basalt-water interactions. Transition depth  $\approx 200\text{m}$  for onset of explosivity. This type of explosive reaction between water and magma is also known as a phreatomagmatic eruption. The vesicularity increases as the pressure drops. The hyaloclastite tuff covers the now subaqueous pillow basal unit and spreads out to the surrounding ice walls (Jones, 1968a; Thordarsson and Hoskuldsson, 2002; Skilling, 2009).
3. With further upwards growth of the volcano, water from the intraglacial lake is denied access to the vent and the eruption becomes subaerial and effusive, initiating the third stage of tuya formation. The flow of lava reaches the lake, fragmenting to form lava-fed deltas (also called flow-foot breccias; Jones, 1968a; Jakobsson et al., 2008; Skilling, 2009), comprised of pillow fragments and coarse grained hyaloclastites (Fig 2.12C and Fig 2.12C2). The transition from subaerial to subaqueous facies marks a fossilised water level that is called the “passage zone” (Fig 2.12DE2; Jones, 1968a; Skilling, 2002).
4. A final stage, noted occurring as an advanced phase of the third stage, is the formation of a subaerial lava cap (Fig 2.12D). The lava cap is composed of pahoehoe lava, which is formed purely in subaerial conditions and overlies the previous formations (Jones, 1968a). Pahoehoe lava is the subaerial equivalent of subaqueous pillow lava. The lava cap can reach thicknesses up to 350 m, which is found at Eiríksjökull (Jakobsson and Johnson, 2012). Intrusions can appear at this later stage and become a minor part of the

tuya. The intrusions can form buttresses throughout the hyaloclastite layer (Skilling, 2009), but the intrusions largely consist of dykes <1 m thick (Jones, 1968b).

After the withdrawal of the ice sheet from deglaciation, the full volcanic edifice is revealed (Fig 2.12E and Fig 2.12DE2). It is possible that the eruptive phase can pause long enough to allow ice to re-cover the tuya's summit. This can cause the subsequent eruptions to create benches in the tuya giving it a more irregular shape (Jones, 1968a).

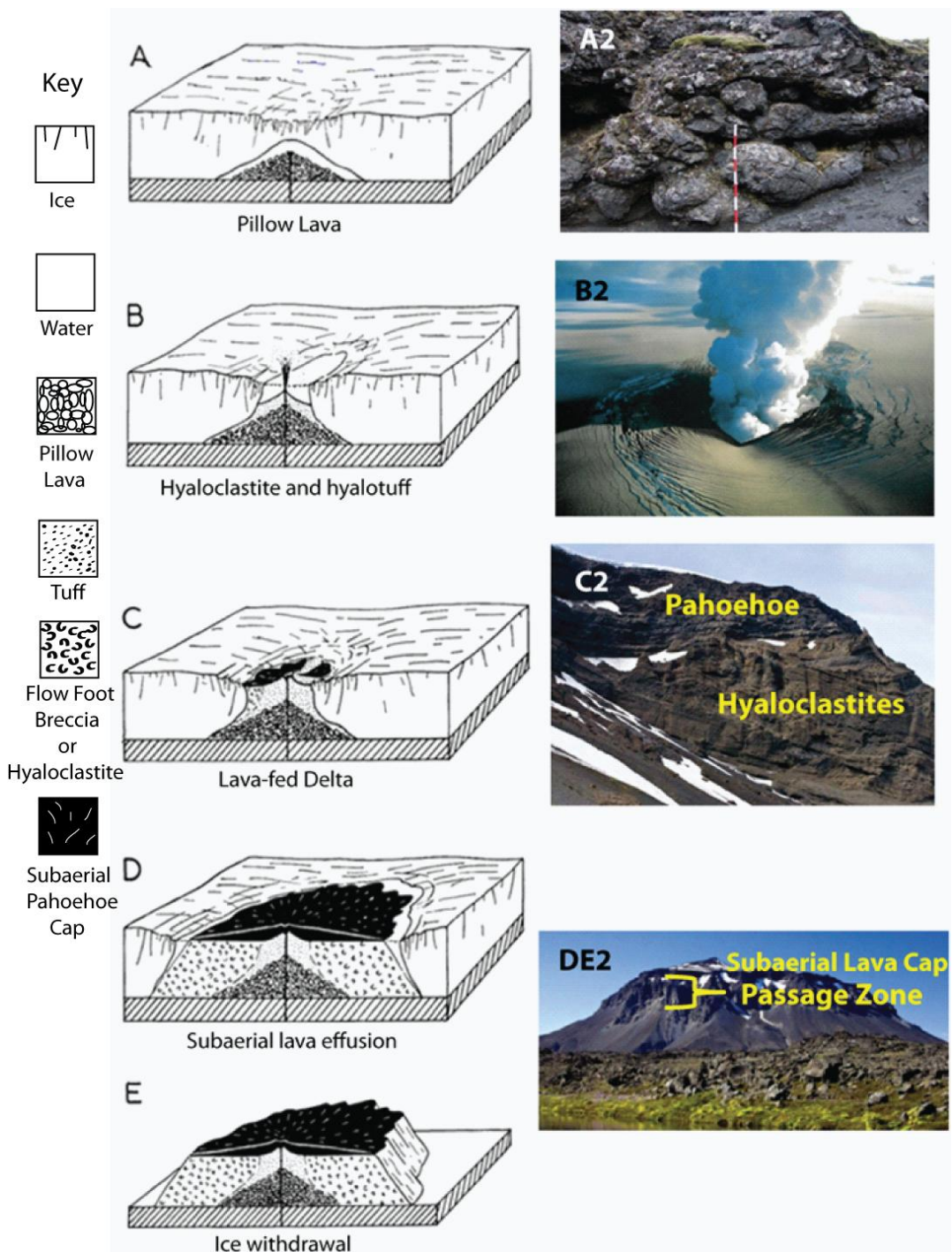


**Figure 2.12:** Illustrations adapted from Jones (1968a) on the production of a subglacial basaltic tuya compared with photographic evidence of these features taken by Dr. D. McGarvie. See text for explanation.

### ***Ice Confinement Features***

Characteristic metre-sized open cavities have been found in the basal unit of pillow lavas in certain tuyas (e.g. Hlöðufell), along with glassy, steep, and flat-sided to well-rounded lava bodies. The glassy flat-edged pillows are understood to be formed from the direct contact between the ice and lava, described as “ice-contact lava confinement surfaces” (Skilling, 2009). The metre-sized cavities, termed as “ice-block melt out cavities” commonly occur in the upper few metres of the basal unit of the tuya. Hyaloclastites have been found to fill the cavities via intrusions through the basal pillow lava. The cavities are thought to have been created by large blocks of ice becoming trapped between the ice sheet and the continuously expelled lava, which eventually engulfs the ice block during tuya formation.

These ice-contact features have a distinctive pillow shape with one flat side. Therefore, it has been suggested that these ice confined features were crafted by small tendrils of lava breaking out from the chilled magma surface. The lava tendrils would then flow into a water vault (kept between the ice and chilled lava), until contacting the ice itself to generate the glassy, steep and flat-sided pillows that have been recorded at Hlöðufell (Skilling, 2009).

### ***Basaltic Tindars***



**Figure 2.13** A tindar/hyaloclastite ridge located south of Askja

Tindars (hyaloclastite ridges; Fig 2.13) are the subglacial equivalent of fissure eruptions with lengths up to 35 km long, widths ranging between 2 to 4 km and heights reaching a few hundred metres. Fissure eruptions are related to tectonic activity such as, spreading or rifting and can be short-lived (days to weeks) or long-

lived (several years to decades). Tindars, usually aligned with the trend of the rift zones, are composed of pillow lavas and hyaloclastites broadly comparable to the lower units of tuyas. Tindars generally tend to have a length to width ratio greater than 2:1 (Thordarson and Larsen, 2007; Jakobsson and Gudmundsson, 2008; Russell and Edwards, 2014).

### ***Basaltic Tindar Formation***

Most large tindars e.g. Kálfstindar, SW Iceland (Jones, 1968b) exhibit pillow lavas as the basal unit, whereas in many smaller tindars this basal unit is missing (e.g. Helgafell, SW Iceland; Schopka et al., 2006). In areas where tindars are solely composed of pillow lavas, it is suggested that the eruption finished before fragmentation could occur to produce hyaloclastites (Jakobsson and Gudmundsson, 2008). This is observed at Undirhlíðar in SW Iceland, in some tindars north of Kverkfjöll in Central Iceland and is attributed to thick ice and high confining pressure (Höskuldsson et al., 2006).

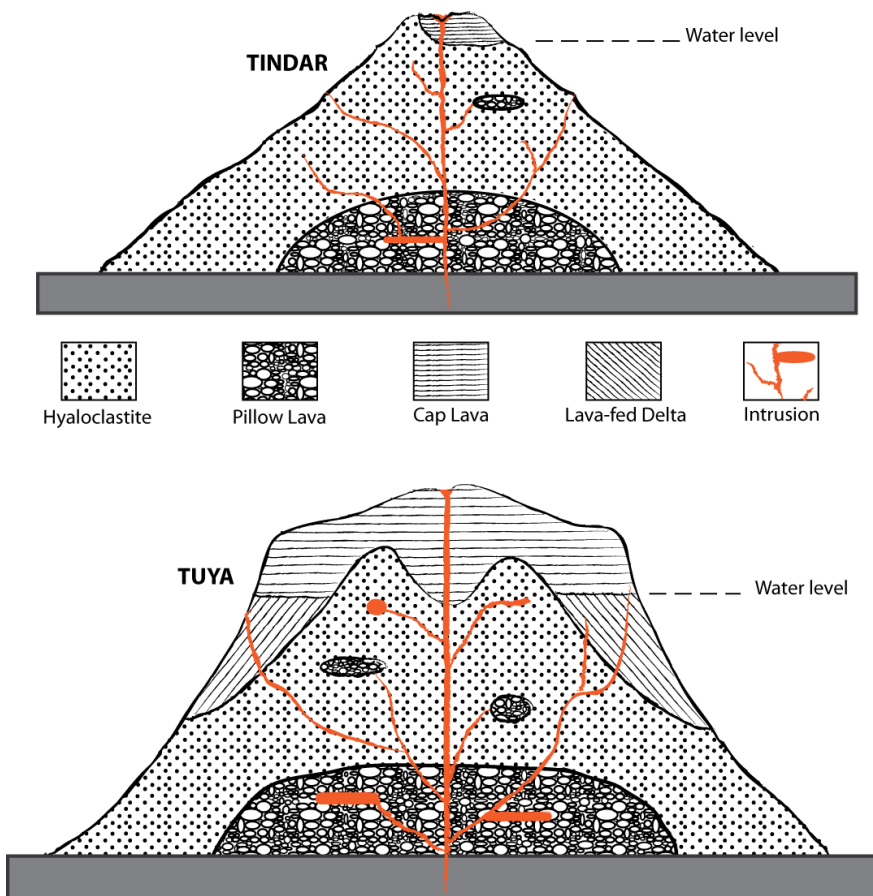


**Figure 2.14** Structures and lithofacies annotations of a typical tuya and tindar, illustrating tindars being less likely to bear a lava cap. Adapted from Jakobsson and Gudmundsson (2008).

A less intense flux of lava (or high brief flux) in the case of tindar formation, commonly results in lava not reaching the surface of the ice sheet to create a cap (Fig 2.14; Allen, 1979). It is uncommon for a tindar to have a subaerial lava cap, which suggests that the tindar forming eruption occurs over a relatively shorter time period compared to tuyas. This observation is consistent when low amounts of lava are released from fissure eruptions (Saemundsson, 1978; Gudmundsson, 1986; Bourgeois et al., 1998). Certain fissure eruptions can create some of the largest volcanic episodes seen on Earth, such as the Laki eruption in 1783 - 1784 A.D., which has a volume of  $20.5 \text{ km}^3$  (Thordarson and Larsen, 2007). Least eroded tindars are comprised of rows of peaks at semi-regular intervals (Fig 2.13). These peaks are a consequence of magma effusion becoming localised on the fissure and concentrated in a row of craters (Jakobsson and Gudmundsson, 2008).

The lack of a lava cap is observed mostly in the EVZ, even on subglacial formations reaching heights of 1000 m. This is interpreted as evidence that the ice sheet was thicker in this region compared to the WVZ (Bourgeois et al., 1998).

### ***Passage Zone and Lava Cap Height***

The height at which the “passage zone” is situated on a subglacial volcanic edifice (Fig 2.12 DE2 and Fig 2.14) signifies the minimum ice thickness at the time of eruption and is used as a fossilised water level of the intraglacial lake that was once present (Jones and Nelson, 1970; Werner and Schmincke, 1999). Passage zones are an important marker that enables subglacial deposits to be utilized as a palaeo-environmental indicator (Skilling, 2009; Smellie, 2000, 2001, 2006, 2007; Edwards et al., 2011, 2009b; Russell et al., 2013). The level of the melt-water lake was suggested by Smellie (2000) to be 10-15% lower than the height of the ice sheet for subglacial eruptions. However, more recent observations of the Gjálp eruption in 1996, showed lake levels to be 20-25% lower than the ice surface elevation (Jakobsson and Gudmundsson, 2008) and so the lakes are generally thought to be between 10-25% lower than the ice sheet surface for all subglacial eruptions. A change in the level of the intraglacial lake throughout tuya formation can cause variations in the elevation of the passage zone (Jones and Nelson, 1970; Skilling, 2002). The variation in passage zone heights can be attributed to an inflow or outflow of melt-water, either from jökulhlaups or basal discharge of the melt-water beneath the ice sheet (Smellie, 2006), causing the passage zone to become a dynamic feature. The extent of drainage is an important control on the melt-water lake level.

A good example of this is seen at Hlöðufell (Skilling, 2009) where a 150 m increase in passage zone height indicates that the water level rose at one point throughout the generation of the tuya. Another cause of a varied passage zone height could be from a collapse of the lava cap during and/or after its formation as suggested by Skilling (2002). Sloped passage zones can indicate the tuya erupted into a thinning ice sheet that was unable to contain the intraglacial lake for the length of eruption. Usually, passage zones are seen to dip towards the coastal regions or dip away from the interior of Iceland. This is most likely due to the effects of glacial isostacy and the crustal rebound after deglaciation with the increasing uplift seen towards the centre of Iceland (Eason et al., 2015). Conversely, the highest passage zones are seen in the north part of WVZ, which coincides with the ice sheet being thickest at higher elevations in central Iceland and becoming thinner as they progress towards the coast (Walker, 1965; Hubbard et al., 2006). This corresponds with higher dissolved H<sub>2</sub>O concentrations in pillow basalts (Nichols et al., 2002). The type of eruption that occurs depends on the water:magma ratio and how open or closed the surrounding ice is on the eruption. These can have an impact on the style of magma emplacement, changing it from effusive to explosive (or vice versa) and effect the consequent lithofacies, changing from subaqueous to subaerial (Russell et al., 2014). Both the pressure differences in water volume and surrounding ice can affect how explosive the eruption will be, the type of lava and how much of it is emplaced (pillow/hyaloclastites/pahoehoe). These variations and open or closed systems effect the type of edifice that is emplaced and can create very differently shaped volcanoes. This information is highly useful when attempting to reconstruct former ice sheet thicknesses over glacial cycles. If reliable eruption/closure ages of the tuyas are established, and combined with the elevations of the passage zones, a temporal reconstruction of ice sheet thickness is possible. An uncertainty in passage zone height can create an error in this reconstruction.

The presence of a lava cap has two main benefits for glacial reconstructions. Firstly the cap is indicative of the minimum ice surface elevation at the time of eruption (Walker, 1965; Bourgeois et al., 1998), which is a more robust indicator than volatile degassing alone (Tuffen et al., 2010). Secondly, samples of the cap can be used to determine an exposure age of the subaerial lava unit (Gosse and Phillips, 2001). Once the eruption has penetrated through to the surface of the ice sheet, the edifice is exposed to cosmic rays, which generate cosmogenic nuclides in minerals

found in the basalt (see section 3.1). Cosmogenic nuclide abundances can be quantified to calculate how long the cap of the tuya has been exposed to the atmosphere. A comparison of eruption (see section 3.3) and exposure ages may provide an estimate of deglaciation or erosion rate. Linking exposure age information with passage zone heights for multiple tuyas and tindars could enable reconstruction of the ice sheet thickness over time. While the record is discontinuous it opens up the possibility of extending the glacial record back through one or more glacial cycles.

One question that this study aims to test, is whether each glacial advance completely erases all subglacial edifices from the previous glaciation. Previous research assessing the preservation record of Icelandic tuyas is discussed below.

### ***Rhyolitic Edifices***

There are a number of rhyolitic tuyas present throughout Iceland (Tuffen et al., 2001; Tuffen et al., 2002; McGarvie et al., 2006; McGarvie, 2009; Stevenson, 2005; Stevenson et al., 2011). Rhyolitic tuyas comprise of poorly-consolidated fragmented material overlain by a lava cap and fragmented lithologies are poorly-exposed, being covered in large amounts of scree. One important difference from basaltic tuyas, is their lack of passage zone. Rhyolitic edifices are fewer in number and comprise only 10% of Icelandic crust (Saemundsson, 1979; Jo  asson, 2007). They appear to be monogenetic and palaeo-ice sheet thickness reconstruction in rhyolites have used the elevation of subaerial lava facies in tuyas and ridges (Tuffen et al, 2002; Tuffen and Castro, 2009), plus rhyolite concentrations in glasses (Owen et al., 2012). However, this research is focused specifically on basaltic tuyas, due to them exhibiting passage zones as preserved ice sheet tide marks.

### **2.3.2 Past Dating of Subglacial Formations**

Common dating techniques, such as radiocarbon dating and  $^{40}\text{Ar}$ - $^{39}\text{Ar}$  dating are not possible for dating basaltic tuyas and tindars. A lack of preserved organic material in tuyas (Dugmore et al., 2006) limits the possibility of using this method. However, ages can be constrained by using radiocarbon-dated lava flows that overlap or flow near to tuyas (Sinton et al., 2005). These tuyas are relatively young, low-K bearing, basaltic edifices.  $^{40}\text{Ar}$ - $^{39}\text{Ar}$  dating is more commonly used for rocks

older than 100 ka (Duncan and Hogan, 1994), and dating younger rocks via this method is usually not possible due analytical difficulties of measuring the low volumes of radiogenic  $^{40}\text{Ar}$  built up over the short time since formation. This is proved more difficult by the contamination of  $^{40}\text{Ar}$ , which is abundant in the atmosphere, and the affect of excess mantle-sourced  $^{40}\text{Ar}$ , which is trapped throughout quenched magma (Duncan and Hogan, 1994).

Tephrochronology (Kirkbride and Dugmore, 2001) provides useful age limits on glacial and volcanic stratigraphies but most of the ages based on tephra are restrained to the Holocene. This is mainly due to the biogenic record extending back only as far as the early Holocene. Also, there is not usually a tephra layer associated with tuya and tindar eruption. Therefore the history in Late Weichselian environment is held within the record of minerals in tuyas (Thorarinsson, 1981; Haflidason et al., 2000; Larsen and Eiriksson, 2008 ).

Lichenometry has become a more recently popular method of dating surfaces produced within the last 100-200 years or two and especially popular in dating recently deglaciated terrains (Matthews, 1994; Geirsdóttir et al., 2000; Bradwell, 2004). This method is only deemed appropriate on surfaces less than 600 years old and so is unsuitable for dating subglacial edifices predicted to be at least 20ka (Bradwell 2004).

U-Th/He dating (Farley, 2002; Section 3.2) is a relatively new technique used to ascertain the ages of young basaltic eruptions. This is the technique used in this research to assess whether determining eruption ages of tuyas and tindars will be helpful in reducing uncertainties in the exposure ages found.

Licciardi et al., (2007) has attempted to date a number of tuyas in Iceland using  $^{3}\text{He}$  cosmogenic exposure ages, arguing that these should be interpreted as eruption ages. As Iceland is covered in snow for a number of months every year (higher altitudes being covered the majority of the year) this affects the flux of cosmic rays. It is therefore suggested that these exposure ages have been underestimated and so should not be taken as definitive eruption ages, but more of a minimum age to when they were formed. Licciardi's exposure age data suggests that most of the tuyas are from the most recent glacial cycle, exhibiting exposure ages between 8.2 and 20.3k. This could provide evidence that subglacial edifices are removed with each glacial advance. However, Licciardi (2007) specifically sampled tuyas with little to no

erosion on the surface, to be expected for relatively young exposure ages. The main point of contention here is that Licciardi argues the point that the exposure ages can be taken as eruption ages. Clearly the exposure/"eruption" age of 8.2ka, which refers to Hlöðufell, cannot be correct. Hlöðufell could not have erupted at 8.2ka, as Iceland was relatively ice free and definitely did not have the required thickness of ice needed to produce a subglacial tuya such as Hlöðufell. More recently Eason et al., (2015) have published more  ${}^3\text{He}$  cosmogenic ages on subglacial edifices in the WVZ of Iceland. Eason notes that on discussion with Licciardi that the exposure/"eruption" age of Hlöðufell was in fact incorrect and has now determined an exposure age of 10.7ka. This updated exposure age for Hlöðufell has yet to be published by Licciardi.

This demonstrates the importance in determining the subglacial edifices true eruption ages by using a dating technique not affected by erosion and help to confirm whether each glacial cycle removes past evidence of subglacial volcanism.

The production of  ${}^3\text{He}$  in exposed basalt is not dependent on the chemistry of the impacted rock by cosmic rays. Instead its production and spatial distribution uniform throughout the rock's surface (Lal, 1987). For further detail on the production mechanisms of  ${}^3\text{He}$  in surficial rocks see section 3.2.6. The sampling method takes the uppermost part of the surface rocks where the production of  ${}^3\text{He}$  is most abundant (see section 3.2.4. Interactions with the Earth's Surface). High points of the surface were targeted such as the tops of tumuli and ropy pahoehoe textures, as this limited the amount of shielding from snow, ice and ash cover (see section 3.2.10 Temporal Variations and 3.2.11 for more detail on these factors).

# Chapter Three: Helium Dating Techniques

## 3.1 Introduction

Small amounts of  $^3\text{He}$  are produced at the atmosphere-surface boundary by cosmic ray spallation, whereas there are no significant processes that produce  $^3\text{He}$  in the mantle. Nevertheless,  $^3\text{He}/^4\text{He}$  ratios in the mantle are considerably higher than the atmosphere. The atmospheric ratio ( $R_A$ ) is  $1.399 \times 10^{-6}$  whereas  $^3\text{He}/^4\text{He}$  ratios in the mantle are 4 to 50 times greater (Graham, 2002; Stuart et al., 2003; Matsumoto et al., 2008; Graham et al., 2014). The high mantle helium isotope ratios are explained by the presence of primordial  $^3\text{He}$  retained in the mantle since the Earth formed 4.6 billion years ago. Helium is not recycled into the mantle and is constantly degassed into the atmosphere where it resides for between 1 to 10 million years before being lost to space (Mamyrin et al., 1969; Lupton and Craig, 1975; Tolstikhin, 1975; Craig and Lupton, 1976).  $^3\text{He}$  is an ideal tracer of the mantle source, as the major source of  $^3\text{He}$  is from mantle degassing. However, the origin of this trapped  $^3\text{He}$  still remains controversial and up for debate. The "helium paradox" indicates that the lower mantle is less degassed than the depleted upper mantle. This gives rise to high  $^3\text{He}/^4\text{He}$  ratios in basalts, but contradicts the concentrations of helium observed, which are higher in MORB than OIB (Allegre et al., 1993; Allegre et al., 1994; Stuart, 1994; Anderson, 1998; van Keken and Ballentine, 1998; Porcelli and Ballentine, 2003; Ballentine and Holland, 2008).

Argon ratios ( $^{40}\text{Ar}/^{36}\text{Ar}$ ) in the mantle are high compared to the atmospheric ratio of 298.6 (Lee et al., 2006). This is due to the early degassing of  $^{36}\text{Ar}$  from the mantle whilst  $^{40}\text{Ar}$  is produced from  $^{40}\text{K}$  throughout the mantle over time (Jambon et al., 1985).  $^{40}\text{Ar}/^{36}\text{Ar}$  values up to 40,000 are observed from mid-ocean ridge basalt (MORB; Burnard et al., 1997).

Helium isotopes have been used as a key tool in distinguishing between different reservoirs in the mantle and in helping to define models of mantle evolution. The majority of MORB samples originate from the upper mantle whereas samples from ocean island basalts (OIBs) have a more complex range of components and noble gas composition and are thought to sample a deeper, or less degassed source (Graham, 2002; Mourão et al., 2012; Graham et al., 2014).  $^3\text{He}/^4\text{He}$  ratios are normalized using the atmospheric ratio ( $1.399 \times 10^{-6}$ ). MORBs have  $^3\text{He}/^4\text{He}$  ratios that average  $\sim 8R_A$ .

OIBs  ${}^3\text{He}/{}^4\text{He}$  ratios are more varied, having ratios between 5.5 R<sub>A</sub> (Canary Islands) to 50R<sub>A</sub> (Baffin Island; Kurz et al., 1982; Graham, 2002; Stuart et al., 2003). The general trend is that most OIBs have higher  ${}^3\text{He}/{}^4\text{He}$  ratios than MORBs (Allegre et al., 1983; Macpherson et al., 1998).

On the other hand,  ${}^{40}\text{Ar}/{}^{36}\text{Ar}$  ratios are usually higher in MORBs than OIBs (Allegre et al., 1983). The maximum MORB  ${}^{40}\text{Ar}/{}^{36}\text{Ar}$  ratio is 40,000 (Burnard et al, 1997), but only 7000 for OIBs (Harrison et al., 1999; Mukhopadhyay, 2012).

## 3.2 Cosmogenic ${}^3\text{He}$ Exposure Age Dating

### 3.2.1 The Nature of Cosmic Rays and their Origin

In 1912 Victor Hess proved the existence of a source of radiation generated from space. The experiment he performed consisted of a gold-foil electroscope that has two leaves of gold-foil suspended from an electrode. The charge produced from radiation in the atmosphere cause the gold-foil leaves to separate. Hess took the gold-foil electroscope to an altitude of 5300m, demonstrating that an increase in altitude also increased the ionization. Therefore the higher an object is positioned in the atmosphere, the more radiation bombards the object. This radiation was coined “cosmic rays” by Robert Andrews Millikan in 1925. In 1936, after further observations confirmed cosmic rays, Hess was awarded a Nobel Prize for his discovery.

Due to their interaction with the Earth’s magnetic field, cosmic rays are composed of electrically charged particles. This discovery allowed analysis of high-energy physics and subatomic particles before the production of high energy particle accelerators, all deriving from the “rain of charged particles” (Powell et al., 1959). This pioneering research in high-energy physics laid the foundations of our understanding of cosmic rays.

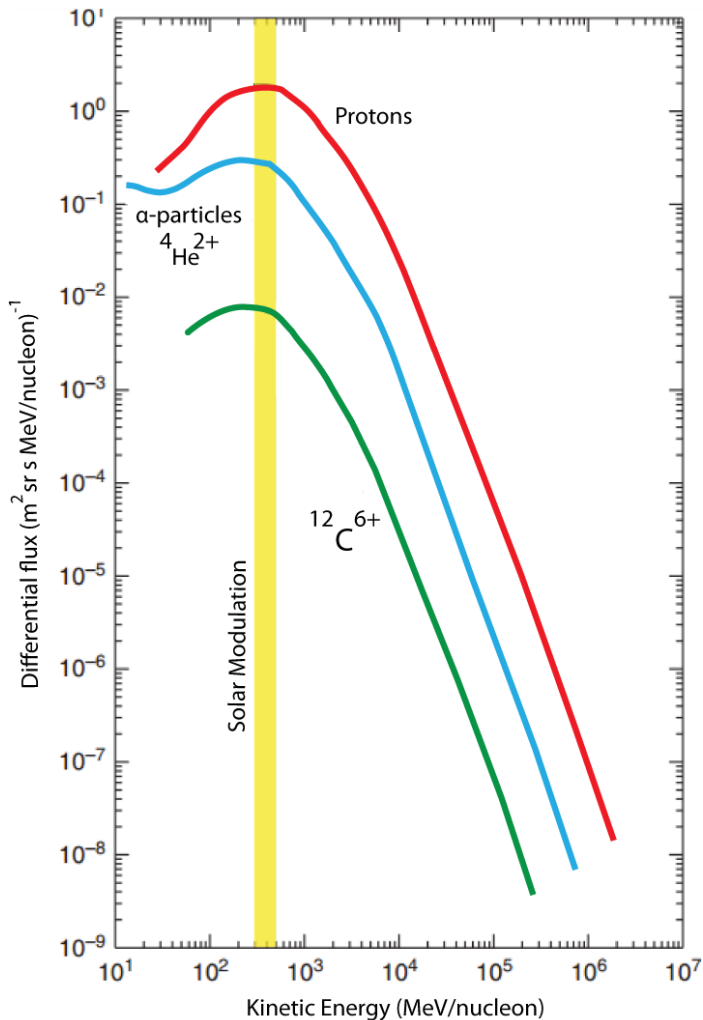


**Figure 3.1** The three main components of the primary cosmic ray flux are protons,  $\alpha$ -particles and heavy (carbon) nuclei. Carbon nuclei make only 1% of the flux. Data taken from Simpson (1983) and figure adapted from Dunai (2010)

### *The Source of Cosmic Rays*

Cosmic rays are comprised of atomic and subatomic particles that impact the Earth from every direction at a wide range of energies. The majority of primary cosmic rays reaching Earth have a maximum energy of a few hundred MeV, Fig 3.1 ( $1\text{eV} = 1.602 \times 10^{-19} \text{J}$ ). These “primary cosmic rays” are composed of ~98% nuclei and ~2% electrons and positrons. Of the 98% nuclei, ~87% are protons (hydrogen nuclei), ~12% are  $\alpha$ -particles (helium nuclei) and ~1% are nuclei of heavier elements (Fig.3.1; Simpson, 1983; Masarik and Reedy, 1995).

## ***Galactic Cosmic Rays***

Galactic cosmic rays (GCR) are high-energy primary cosmic rays (~100-5000 MeV; Reedy et al., 1983) that originate from outside the solar system. The source of galactic cosmic rays is uncertain, but is currently thought to be supernova explosions. A recent study by Ackermann et al. (2013), using decayed pions from the Fermi telescope, has shown that protons in primary cosmic rays are accelerated to their very high energies by supernova remnants, in the shockwave created from the explosion. The highest energy galactic cosmic rays ( $\sim 10^{20}$ eV) originate from supernovae outside our galaxy (Gosse and Phillips, 2001), which occur only once every fifty years (Friedlander, 1989), whereas cosmic rays originating within our galaxy produce radiation in the energy of at least  $10^{15}$ eV (Eidelman et al., 2004). There have been no significant fluctuations in GCR over the last  $10^7$  years and the time averaged flux has been considered to vary by less than  $\pm 10\text{-}15\%$  (Jokipii and Marti, 1986; Reedy et al., 1983). This minor variation over such a long period of time is negligible when applied to cosmic ray exposure dating on Earth.

## ***Solar Cosmic Rays***

About 98% of the particles emitted from the sun are protons, which have a much lower energy than galactic cosmic rays (~5-100 MeV) (Reedy et al., 1983, Masarik and Reedy, 1995). The flux of solar cosmic rays is increased during a solar flare event that is directed at Earth. A flare event produces solar cosmic rays that arrive at the Earth's atmosphere up to a few days after the flare has subsided. The flux of cosmic rays produced from solar flares reveal the scattering of cosmic rays by the heterogeneities of the Earth's magnetic field in the interplanetary medium (Lal and Peters, 1967).

Solar protons can reach the atmosphere only at high latitudes ( $>60^\circ$ ) due to their lower energy and a low cut-off rigidity near the poles (See section 3.2.2 *Cut-Off Rigidity*). Cosmic ray particles ( $<10$  GeV) are modulated by solar wind and the 11-year cycle of solar activity (Lal and Peters, 1967; Eidelman et al., 2004; See section 3.2.2 *Solar Modulation*). Solar cosmic rays can produce nuclides at the top of the atmosphere, but their contribution to cosmogenic nuclide production at the Earth's surface is negligible (Masarik and Reedy, 1995) and so will not be considered further.

### 3.2.2. Interactions with Earth's Magnetic Field

Primary cosmic rays are composed of positively charged particles (protons and  $\alpha$ -particles). This positive charge makes it difficult for the particles to enter the Earth's magnetosphere due to an imposing Lorentz force,  $F_L$ . The Lorentz force causes the charged particles to be deflected radially. This triggers the particle to move away from their initial vector of movement,  $v$ , and the dominating magnetic field,  $B$ , in a perpendicular fashion. The deflecting force will be stronger as the angle between the magnetic field and vector of movement increases. In other words, a particle with a high energy travelling at a faster speed will not be deflected as much as a slower moving, less energetic particle. The more easily a particle is affected by this deflection means the path it creates will become more complex. Primary cosmic rays are also accelerated or decelerated by electric fields depending on the field's direction (Smart et al., 2000).

#### *Rigidity*

The elaborate path a primary cosmic ray creates is dependent on its mass, velocity, charge and incidence angle. For a cosmic ray to interact with the Earth's atmosphere, it needs to overcome a certain rigidity:  $R$  (particle momentum,  $p$ ; per particle charge,  $e$ ; the velocity of light,  $c$ ; units of  $R$  are in giga-volts, GV; Equation 1) to penetrate the Earth's magnetic field first (Elsasser and Winckler, 1956).

$$R = \frac{pc}{e} \text{ [GV]} \quad \text{Equation 1}$$

For the charged particle to reach a certain point on the Earth's surface, the particle's trajectory and magnetic latitude at which it enters is critical.

#### *Cut-off Rigidity*

In 1955, Störmer summarized his work on the forbidden momentum of charged particles in a dipole field. Störmer's research highlighted the importance of understanding cut-off rigidities, which are a consequence of the fundamental motions of cosmic rays in the centred dipole field (Störmer, 1955). The geomagnetic cut-off rigidity,  $R_c$ , is the minimum rigidity required to penetrate the Earth's magnetic field and enter the atmosphere. A particle with vertical incidence cannot penetrate the magnetosphere if its magnetic rigidity is lower than the cut-off rigidity (Smart et al., 2000).

The magnetic cut-off rigidity is dependent on latitude as the orientation of the magnetic flux lines impacts the flux of cosmic rays. At low latitudes, such as the equator, (geomagnetic latitude  $0^\circ$ ), the Earth's magnetic field is perpendicular to any vertically incident cosmic rays. At high latitudes, such as the poles (geomagnetic latitude  $90^\circ$ ), incoming primary cosmic rays move parallel to the Earth's magnetic field. Therefore, practically all rigidities are allowed at the Earth's poles but only primary cosmic rays with rigidities well over 10GV ( $\sim 15\text{GV}$ , Fig 3.2; Masarik and Reedy, 1995; Lifton et al., 2005) have the potential to penetrate the Earth's magnetic field at the equator as shown by Fig 3.2 and 3.3.

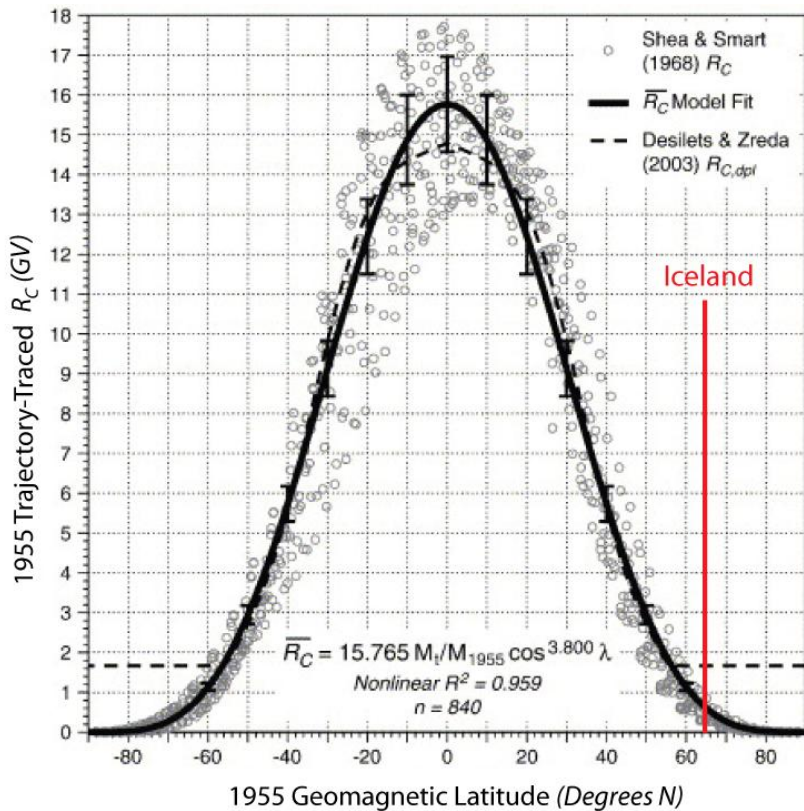


**Figure 3.2:** Different cut-off rigidity values with varying geomagnetic latitude, illustrating only cosmic ray particles with rigidities well over 10 GV can penetrate the Earth's magnetic field at low latitudes, such as the equator. Adapted from Lifton et al., 2005.

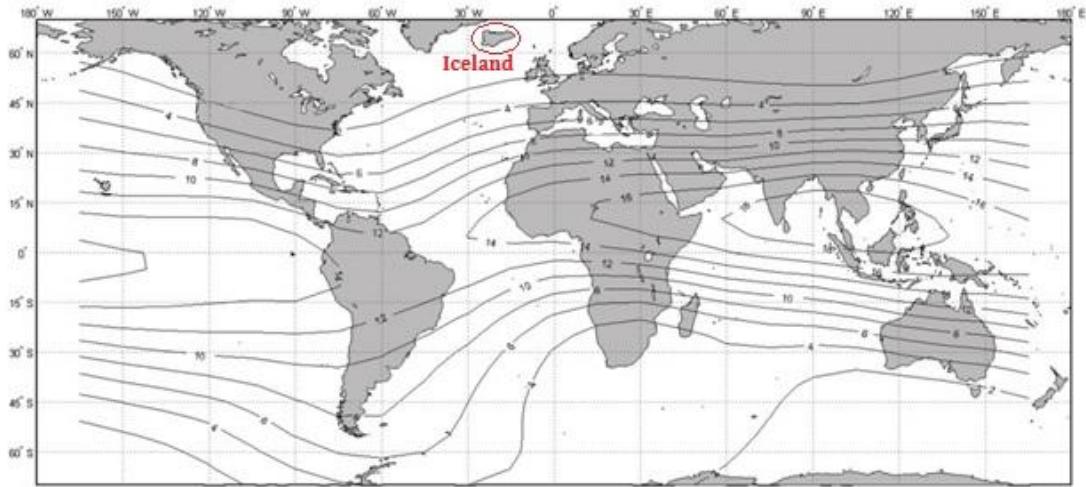


**Figure 3.3:** Global magnetic cut-off rigidities from Shea and Smart (2001), Smart and Shea (2005) and map adapted from Goehring et al. (2010)

### *Fluctuations in the Earth's Magnetic Field*

The centred dipole equation Størmer (1955) used for evaluating magnetic cut-off rigidities are limited due to his use of simplistic evaluations on magnetic latitude, distance from the Earth's actual magnetic centre, and failure to consider the effects of geomagnetic field evolution (Smart and Shea, 2005). The evolution of the geomagnetic field and its fluctuations over time can affect the cut-off rigidity values and distributions at high altitudes and low latitudes, where cut-off rigidities are at their highest (Lal, 1991; Smart and Shea, 1994; Lal and Peters, 1967). When the Earth's magnetic field is at a higher intensity, relatively less cosmic rays are able to penetrate the geomagnetic field, lowering the amount of nuclear interactions in the atmosphere and at the Earth's surface. Fig 3.4 illustrates the variations seen in nuclear disintegration rates when there is a change in magnetic field intensity.

Variation in dipole axis position may affect the production rate of cosmogenic nuclides at certain geomagnetic latitudes (Gosse and Phillips, 2001). The average position of the geomagnetic pole is 88.2°N, 84.6°E ( $\pm 1^\circ$ ; Ohno and Hamano, 1992), over the past 10000 years. When averaged over the past 5 Myr it lies approximately 87°N, 144° E (Merrill et al., 1996). Nevertheless, cosmogenic nuclide production rates pre-Holocene ( $> 7$  ka) will not be affected and the dipole axis position is seen as dependently geocentric (Gosse and Phillips, 2001; Dunai, 2001a). The greatest effect is seen on the late Holocene, where production rates can vary by  $>15\%$  (Dunai, 2001a).

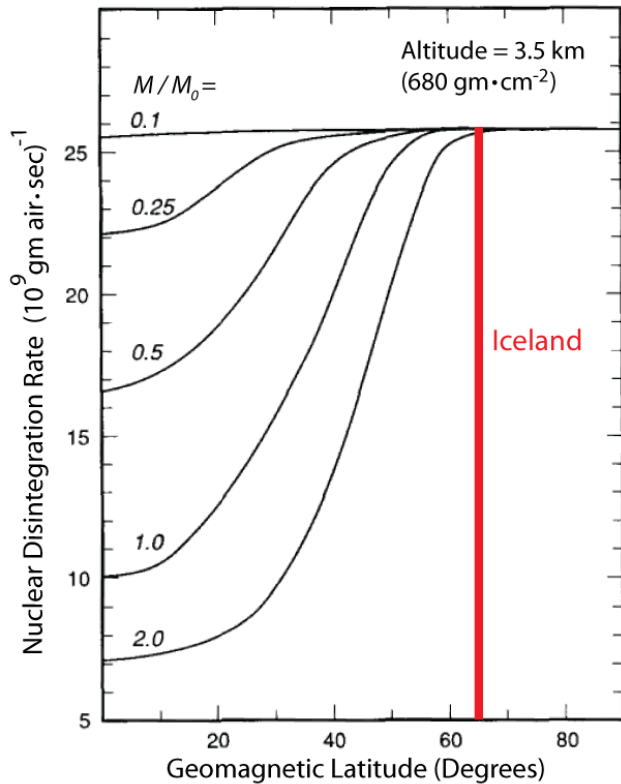


**Figure 3.4:** Nuclear disintegration rates as a function of geomagnetic latitude at an altitude of 3500m for fluctuating intensities of Earth's dipole field,  $M$ , compared to the present dipole field,  $M_0$ . Adapted from Lal (1991) using data from Lal and Peters (1967)

### Solar Modulation

Solar wind emitted from the sun can act as a barrier to certain low energy cosmic rays. There is a transition in the solar wind that changes the wind's speeds from supersonic to subsonic. This zone is called the termination shock. The barrier to cosmic rays is the area between the termination shock and the heliopause. As practically all rigidities are able to penetrate the magnetic field at the poles, this modulation by the solar wind prevents primary cosmic rays with rigidities lower than 0.6GV to enter the Earth's magnetic field (Michel et al., 1996). The cosmic ray flux plateaus near to the poles instead of continuing to increase; this caps the cosmic ray rigidities at values close to the solar modulation. Primary particles with similar solar modulation energies are not energetic enough to produce a cascade of secondary particles to reach the Earth's surface. This 'cap' is known as the 'latitude knee', coined by Compton and Turner (1937). Compton and Turner (1937) found the latitude at which the increase in cosmic ray flux becomes less rapid to be  $\sim 38^\circ$  and more recently Dunai (2000) has found the flux to stop increasing altogether above

$60^\circ$ . The decrease of cosmic rays with decreasing latitude below the latitude knee is known as the “latitude effect” (Dunai, 2000).

### 3.2.3 Interactions with the Earth’s Atmosphere

Primary cosmic rays that are able to penetrate the Earth’s magnetic field can enter the atmosphere and undergo nuclear collisions (spallation reactions) with atmospheric atoms to create a nuclear cascade of secondary cosmic rays. The secondary cosmic rays generated by spallation reactions are composed of a variety of nuclear and subatomic particles (Fig 3.5).

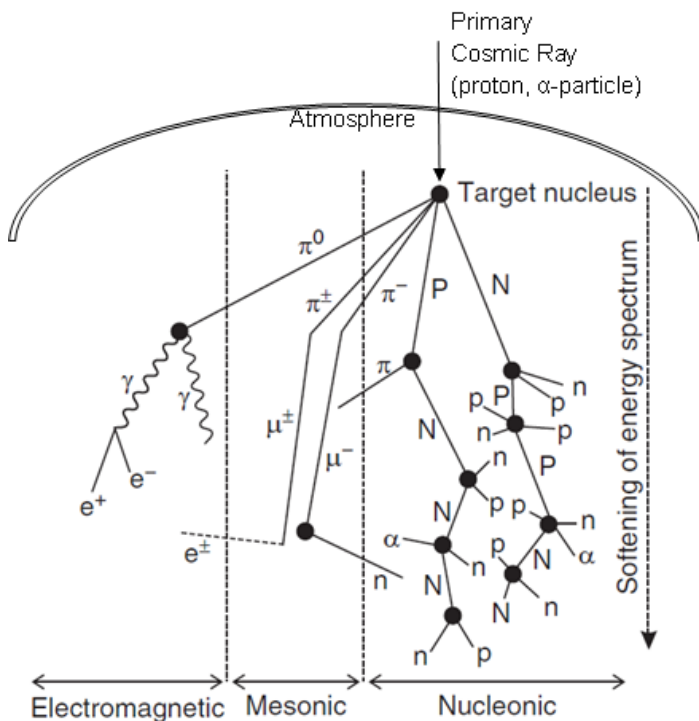


**Figure 3.5:** A nuclear cascade diagram showing the different components created from spallation of atmospheric nuclei with a primary cosmic ray; n, neutron; p, proton; (capital letters are for particles carrying the nuclear cascade),  $\alpha$ , alpha-particle;  $e^\pm$ , electron or positron;  $\gamma$ , gamma-ray photon;  $\pi$ , pion;  $\mu$ , muon. Adapted from Simpson and Fagot (1953) and Dunai (2010)

#### Nucleonic Component

Spallation occurs when atoms collide with primary cosmic rays, as the energy obtained from this collision is much higher than the typical binding energy of atomic nuclei ( $\sim 7\text{-}9\text{ MeV}$ ). Spallation causes nucleons (protons,  $p$ ; neutrons,  $n$ ;  $\alpha$ -particles,  $\alpha$ ; Fig 3.5) to spall off from the atmospheric atom and these secondary particles fragment further nuclei, creating a cascade. The large majority of cosmic rays that

enter the atmosphere are positively charged protons and alpha particles. Neutrons that are produced as secondary cosmic rays do not experience an ionization loss, unlike protons. Hence the primary composition that is dominated by high energy protons, at the top of the atmosphere develops to being dominated by lower energy neutrons near the Earth's surface (Lal and Peters, 1967; Masarik and Reedy, 1995).

### ***Mesonic Component***

Mesons are also produced from the spallation of atomic nuclei with primary cosmic rays. These mesons are mostly pions,  $\pi$  (the lightest meson), which decay into muons,  $\mu^- \mu^+$  (essentially an electron but  $\sim 200$  times heavier), after only a few metres of their trajectory (Fig 3.5) (Eidelman et al., 2004). Muons can reach the Earth's surface before they decay and their mean energy at sea level is  $\sim 4\text{GeV}$  (Eidelman et al., 2004). The most abundant secondary cosmic rays or particles at sea level are muons as their interaction with other matter is weak. The weak interaction of muons enable them to travel further than nucleons and thus dominate below the Earth's surface (Lal, 1988).

### ***Electromagnetic Component***

There is a final electromagnetic component to the nuclear cascade which is made up of electrons,  $e^-$ ; positrons,  $e^+$ ; and photons,  $\gamma$  (Fig 3.5). These are produced from the decay of the mesons (Eidelman et al., 2004). These electromagnetic particles do not have a significant effect on the production of cosmogenic nuclides at the Earth's surface and so will not be discussed further.

### ***Atmospheric Depth and Attenuation Length***

With an increase in atmospheric depth there is also a decrease in the abundance,  $N$ , of neutrons (Lal and Peters, 1967; Lal, 1991; Masarik and Reedy, 1995).

$$N(d) = N_0 e^{-\frac{d}{\Lambda}} \quad \text{Equation 2}$$

Beer's Law, equation 2, calculates the abundance of the nucleon which is dependent on atmospheric depth,  $d$  ( $\text{g cm}^{-2}$ ) and attenuation length,  $\Lambda$  ( $\text{g cm}^{-2}$ ) where  $N_0$  is the number of nucleons at the top of the atmosphere.

Attenuation length,  $\Lambda$ , is the distance a particle can travel into matter (atmosphere, Earth's surface) until its energy falls to  $1/e$  of its original energy. The volume of matter encountered affects the particle's attenuation length rather than the distance the particle has travelled. The attenuation length is not constant as it is a function of altitude and a function of cut-off rigidity,  $R_c$  (or geomagnetic latitude,  $\lambda$ ). These functions will affect changes in the energy spectrum of the nucleons produced. The attenuation path length is the actual distance the cosmic ray particle can travel before stopping in a specific density of matter/rock.(Lal, 1991; Dunai, 2001b; Desilets and Zreda, 2003; Gosse and Phillips, 2001).

As shown in Fig. 3.6, the effect of the geomagnetic latitude on attenuation length is demonstrated by a decrease in length from  $>145 \text{ g cm}^{-2}$  near the equator to  $130 \text{ g cm}^{-2}$  at the poles at altitudes below 5 km (Dunai, 2000; 2001a). The maximum flux of neutrons is at altitudes corresponding to an atmospheric depth range of  $75\text{-}125 \text{ g cm}^{-2}$ . This is correct for all latitudes and is due to the leakage of neutrons from the atmosphere at high altitudes (Masarik and Reedy, 1995).

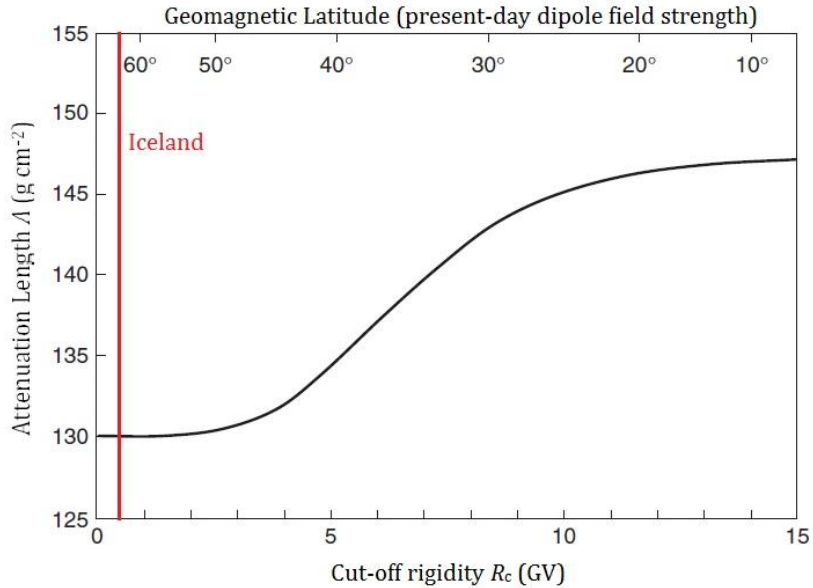


**Figure 3.6:** Variation in attenuation length shown as a function of cut-off rigidity  $R_c$ . Iceland is shown in red, displaying a very low  $R_c$  and hence a low attenuation length compared when with lower latitudes. Adapted from Dunai (2001a).

Consequently, spallation reactions between high energy neutrons ( $>40\text{MeV}$ ) and atmospheric nuclei are more abundant at the poles relative to the equator (Lal and Peters, 1967). The angle of trajectory of a cosmic ray particle will affect its attenuation length, as the smaller the incidence angle the greater the volume of atmosphere the particle has to travel to reach the Earth's surface. Therefore the

cosmic ray flux will be highest at the point of zenith and will decrease towards the horizon. Vertical incidence on a horizontal surface is termed the “true attenuation length” whereas any incidence which is non-vertical is termed the “apparent/effective attenuation length” (Gosse and Phillips, 2001). The apparent attenuation length is what is commonly used in Earth surface process calculations.

The attenuation length of muons [ $247 \text{ g cm}^{-2}$  (Lal, 1988)] is considerably greater than the attenuation length of neutrons due to their weak interaction with matter.

### 3.2.4. Interactions with the Earth’s Surface

The interactions of cosmic rays with the Earth’s surface are similar to those in the atmosphere except there is a much shorter mean free path (distance travelled before cosmic ray particle collides with nuclei) due to a much higher density of atoms in the surface of the Earth compared to the atmosphere. Protons are not involved in cosmic ray spallation at the Earth’s surface due to suffering ionisation losses throughout the atmosphere, causing spallation to be dominated by neutrons at the Earth’s surface (see section 3.2.3 *Nucleonic Component*).

#### ***High energy Neutrons***

The flux of cosmogenic high energy neutrons ( $10^{-1} - 10^3 \text{ MeV}$ ; energies  $>10 \text{ GeV}$  are absent at Earth’s surface) decreases exponentially once the neutrons encounter the air-surface interface (Masarik and Reedy, 1995). Different compositions of surface rocks (including varying water content) and a range in neutron energies can cause variations in the neutron’s attenuation length. Rock densities are typically in the range of  $2\text{-}4 \text{ g cm}^{-3}$ , therefore rock density variations are insignificant on attenuation length (Phillips et al., 2001). For example, attenuation path length in basalts (typical density  $\sim 3 \text{ g cm}^{-3}$ ) is approximately 50-60 cm whereas granite (typical density  $\sim 2.65 \text{ g cm}^{-3}$ ) is 57-68 cm (Brown et al., 1992). At a depth of five times the attenuation path length (2.5-3 m in most rocks) there is less than 1% of the original surface neutron flux seen (Phillips et al., 2001).

At the Earth’s surface the attenuation length ranges from  $150\text{-}180 \text{ g cm}^{-2}$  for high energy neutrons (Kurz, 1986; Gosse and Phillips, 2001). At high latitudes these values are lower compared to mid and low latitudes due to the decrease in cut-off rigidity with increasing latitude (similar to atmospheric depth: Fig 3.6; Brown et al.,

1992). In other words, neutrons with a higher energy will penetrate deeper than neutrons with lower energy, just like cosmic ray interactions with the Earth's atmosphere.

### ***Thermal-Neutrons***

Cosmogenic thermal-neutrons ( $10^{-8} - 10^{-6}$  MeV) originate as high energy neutrons that have lost energy during interactions with nuclei in the atmosphere or Earth's surface. Thermal-neutrons are readily absorbed by nitrogen in the atmosphere, which creates an abundance of thermal-neutrons in the sub-surface rocks of the Earth. The flux of cosmogenic thermal neutrons in rocks is larger by roughly one order of magnitude compared to the atmosphere (Phillips et al., 2001). Although the thermal-neutron flux fluctuates with altitude and latitude like high energy neutrons, thermal-neutrons move randomly, whereas high energy neutrons follow a downward flux with increasing depth (Phillips et al., 2001).

The maximum flux of thermal-neutrons is seen at ~20 cm depth below the surface, (Fig 3.7A) where it is roughly double the surface-atmosphere boundary flux (Phillips et al., 2001). The difference in thermal neutron flux at the surface and the maximum at a depth of 20 cm is the result of neutrons leaking from the surface–atmosphere interface (Fig 3.7). These leaked thermal neutrons are then readily absorbed by atmospheric nitrogen (Phillips et al., 2001).

Increasing water content in surficial rocks affects the flux of thermal-neutrons. An increase of up to ~5% water causes the thermal-neutron flux to increase by ~25% (Fig 3.7B). This increase is caused by a minimized effect of the elastic scattering in the rock due to the time neutrons spent in the high-energy range. The most effective moderator of neutron energy is hydrogen and so increasing the water content by more than 5% causes the thermal-neutron flux to decrease (Phillips et al., 2001). Ponded water or snow on the surface will have an effect on the thermal-neutron flux but this has yet to be investigated (Phillips et al., 2001).

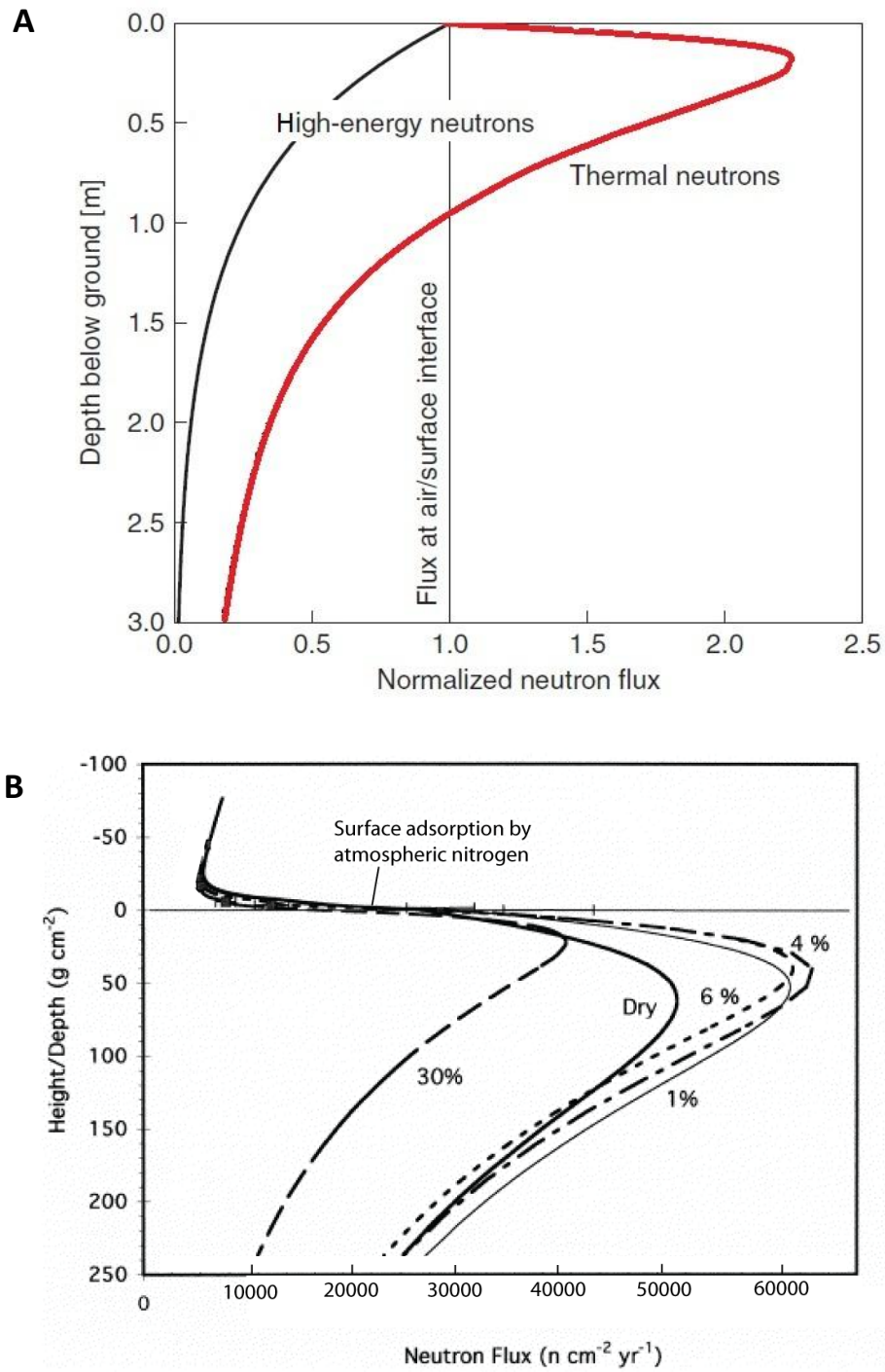


**Figure 3.7:** **A:** Neutron flux below the Earth's surface. The high energy neutron flux decreases exponentially with depth whereas thermal-neutrons can leak back into the atmosphere. This causes a humped profile. The hump location depends on the rock's composition and water content (Phillips et al., 2001). Flux profile calculated by Phillips and Plummer (1996) with fluxes being normalized to the corresponding air-surface flux. **B:** A neutron flux below Earth's surface in basalt dependent on the amount of water present in the ground. Sharp decrease in neutron flux at the surface interface due to leaking into the atmosphere and being absorbed by atmospheric nitrogen (Phillips et al., 2001).

## **Muons**

Compared to neutrons, muons interact weakly with matter. Muon's weak interaction enables them to travel deeper below the surface until they have lost energy through ionization to decelerate to a rest. Muons with a mean energy of 4 GeV at the Earth's surface (Eidelman et al., 2004) are decelerated 99.75% from ionization (Groom et al., 2001). The more energy a muon has, the longer its attenuation length will be (Groom et al., 2001). Furthermore, a muon's stopping distance is highly affected by the chemical composition of the matter it is penetrating (Groom et al., 2001). This dependence on chemical composition gives a mean muon attenuation length of roughly  $1000 \text{ g cm}^{-2}$  at the Earth's subsurface (Kurz, 1986) compared to  $247 \text{ g cm}^{-2}$  (Lal, 1988) in the atmosphere (Section 3.2.3). Muons become important and contribute significantly to cosmogenic nuclide production underneath  $\sim 3 \text{ m}$  of rock, corresponding to  $900 \text{ g cm}^{-2}$  (Lal, 1987) in a basalt with an assumed density of  $3 \text{ g cm}^{-3}$  (Lal, 1988).

### **3.2.5. Principles of Cosmogenic Nuclide Surface Exposure Dating**

At a certain depth, the production of cosmogenic nuclides occurs at a constant rate. The rate of production is affected by latitude, altitude, shielding (snow cover for example), postglacial isostatic rebound (uplift) and erosion (Section 3.2.8 Temporal Variations). There are multiple scaling methods and models for calculating nuclide production rates and exposure ages which take these factors into consideration. Cosmogenic nuclides generated in the surficial rock act as a geological clock that record how long the surface has been exposed to cosmic rays. These nuclides enable the calculation of exposure ages for geological features that have been previously unattainable through other geochronological methods. A simplified equation (Equation 3) for an exposure age,  $t$ , is calculated using the production rate,  $P$ , and the abundance of the stable cosmogenic nuclide,  $N$ .

$$t = \frac{N}{P} \quad \text{Equation 3}$$

Radioactive cosmogenic nuclides such as  $^{10}\text{Be}$ ,  $^{14}\text{C}$ ,  $^{26}\text{Al}$ ,  $^{36}\text{Cl}$ ,  $^{41}\text{Ca}$  and  $^{53}\text{Mn}$  decay over time, whereas  $^3\text{He}$  does not decay and is stable. The decay of these radionuclides affects and ultimately limits their use for exposure age dating.

## **What makes ${}^3\text{He}$ a good cosmogenic nuclide?**

### ***Cosmogenic Nuclide Abundance***

A good cosmogenic nuclide is naturally rare in its surrounding geological matter, providing a low background level of the specified nuclide and is produced at a sufficient rate to be detectable using modern analytical methods. High energy spallation reactions involve the direct interaction of incoming particles with the nucleons of the target nucleus, the isobaric yield is a function of the mass difference between target and product nucleus. Thus, production rates show a flat mass spectrum and cosmogenic contributions are most prominent on low abundance isotopes.

### ***Stability and Retentivity***

Stability is an important aspect when using cosmogenic nuclides as geochronological tools. The nuclide's half-life should ideally be of the same order if not greater than the exposure age being calculated to allow the measurement of long term processes. Cosmogenic  ${}^3\text{He}$  ( ${}^3\text{He}_c$ ) is stable, which means it is not limited in dating applications by half-life constraints which affect radioactive cosmogenic nuclides.

Cosmogenic noble gases are not retained by all minerals (e.g. quartz) and so an appropriate mineral should be used for analysis to acquire exposure ages. Of all the elements, He exhibits weak intermolecular attractions owing to its very small Van der Waals radius (140 pm). These weak interactions explain its inability to bond with the other matter surrounding it and allows He to diffuse out of minerals at relatively low temperature. The basaltic mineral olivine, however, is able to retain  ${}^3\text{He}$  at environmental temperatures (Trull et al., 1991).

### **3.2.6 Production Mechanisms of ${}^3\text{He}$ in Surface Rocks**

#### ***Spallation***

At the immediate surface of the Earth the predominant production of  ${}^3\text{He}$  is generated through spallation reactions. The interactions are induced by collisions of secondary cosmic ray neutrons with any major rock forming target elements (Si, Al,

Mg, O, Fe, Na, Ca) to produce  ${}^3\text{He}_c$ . The production of  ${}^3\text{He}_c$  is therefore independent of the rock's chemical composition (Lal, 1987).

### **Nucleogenic Thermal-Neutron Capture ( $n,\alpha$ )**

Even though the dominant production of  ${}^3\text{He}_c$  is through spallation, there is a production mechanism that only becomes important when considering minerals high in Li (>5ppm). This production mechanism is explained briefly here; for a more detailed explanation see Morrison and Pine (1955) and Lal (1987).

As a result of the low abundance of Li in mafic rocks, the generation of  ${}^3\text{He}_c$  from nucleogenic thermal-neutron capture contributes only 1.5-6% (Dunai et al., 2007). Li-rich minerals undergo thermal-neutron capture reactions. Thermal-neutrons (See section 3.2.4 *Thermal Neutrons*) are produced in rocks through ( $\alpha,n$ ) reactions (the  $\alpha$ -particles are generated from the decay of U and Th; See section 3.2.6 *Radiogenic Thermal-Neutron Capture*, see also Chapter 3.2). These thermal-neutrons are predominantly captured by  ${}^6\text{Li}$  and  ${}^{10}\text{Be}$ :



Tritium ( ${}^3\text{H}$ ) is generated on a greater scale than  ${}^3\text{He}$  due to  ${}^3\text{H}$  having a lower binding energy per nucleon (Lal, 1987), as in less energy is needed to generate  ${}^3\text{H}$ .  ${}^3\text{H}$  then decays ( $t_{1/2} = 12.5$  years) to  ${}^3\text{He}$  via beta decay (Equation 4 and 5).

### **Radiogenic Thermal-Neutron Capture ( $\alpha,n$ )**

Most  $\alpha$ -particles emitted from U and Th decay acquire two electrons (see Chapter 3.3) to become  ${}^4\text{He}$  atoms. A low proportion of  $\alpha$ -particles react with nuclei and produce neutrons by ( $\alpha,n$ ) reactions on rock-forming elements, such as *in-situ* Si, Al, Mg, Na, Ca. Out of every  $10^6$ - $10^8$   $\alpha$ -particles generated, only one produces a neutron (Martel et al., 1990) in which there is a  $\geq 0.8$  probability that it will be thermalised (Morrison and Pine, 1955; Ballentine and Burnard, 2002). Neutrons not reaching thermal energies, generated through ( $\alpha,n$ ) reactions, do not have sufficient energy to induce spallation and instead lose their energy by elastic scattering in the rock.  ${}^3\text{He}$

production through ( $\alpha$ ,n) reactions is dependent on the chemical composition of rock and is not influenced by cosmic rays for production.

Thermal-neutrons are also produced through the spontaneous fission of  $^{238}\text{U}$  and  $^{232}\text{Th}$ .  $^{238}\text{U}$  has a fission rate of  $7 \times 10^{-3}$  fissions  $\text{g}^{-1} \text{s}^{-1}$ , whereas the rate of  $^{232}\text{Th}$  fission is much slower at  $4 \times 10^{-5}$  fissions  $\text{g}^{-1} \text{s}^{-1}$ . The neutrons are produced at a rate of  $2.2 \pm 0.3$  neutrons per fission event (Morrison and Pine, 1955).

The production of  $^3\text{He}$  in this manner is negligible when compared to  $^3\text{He}_c$  produced through spallation, but can become important when considering ancient rocks (1-10Ma) that have had sufficient time to build up significant amounts of low energy neutrons.

Neutrons and  $\alpha$ -particles have a large difference in range, from centimetres to microns respectively. Thus, different minerals can have variable nucleogenic and radiogenic  $^3\text{He}/^4\text{He}$  ratios within the same rock. Therefore helium ratios produced are affected by the concentration of Li, U and Th in a mineral (Dunai et al., 2007).

### 3.2.7 Spallation Generated $^3\text{He}_c$ Production Rates

#### *Physical Principles*

Numerical simulations of the interaction of cosmic rays with the Earth's surface have been attempted using cosmic-ray flux rates combined with cross-sections of nuclear reactions (Masarik and Reedy, 1994, 1995; Masarik and Beer, 1999). However, the incomplete or relatively large uncertainties in cross-section data reduces accuracy (Masarik and Reedy, 1995), which preclude these approaches being applied to calculate *in situ* production rates.

The first estimation of the production rates of  $^3\text{He}_c$  and  $^3\text{H}$  generated in the atmosphere were achieved by Lal and Peters (1967). The data were presented using cosmic ray flux measurements and nuclear reaction probabilities for all atmospheric latitudes and altitudes. The atmospheric production rate of  $^3\text{He}$  estimated by Lal and Peters (1967) was 148 atoms  $\text{g}^{-1} \text{a}^{-1}$  at sea level and high latitude (SLHL)  $>50^\circ$ . This value was considered to be similar to the  $^3\text{He}_c$  production rate in surficial rocks as  $^3\text{He}_c$  production is independent of the rock's chemical composition (See section 3.2.5 *Production Mechanisms*).

An alternative theoretical method was first used by Lal (1991) to predict production rates by modelling cosmic ray neutron energies with proton excitations.  ${}^3\text{He}_c$  production through spallation, being independent of rock chemistry (See section 3.2.5 *Production Mechanisms*), causes a variation in production by only  $<\pm 20\%$  on different lithologies. Spallation-produced  ${}^3\text{He}_c$  (and  ${}^3\text{H}$ ) was calculated by Lal (1991) on common rock elements such as O, Mg, Al, Si, Ca and Fe at sea level and high latitude, which can be further scaled to any latitude and altitude using a polynomial equation (Table 3.1) to calculate the nuclear disintegration. These calculations have relatively high uncertainties of 25-30% (Lal, 1991). Altitude scaling methods are discussed further in Section 3.2.8.

Geomagnetic Latitude ( $^{\circ}$ )	Polynomial Coefficients			
	<b>a</b>	<b>b</b>	<b>c</b>	<b>d</b>
<b>0</b>	330.7	255.9	98.43	20.50
<b>10</b>	337.9	252.1	111.0	20.43
<b>20</b>	382.1	272.1	132.5	24.83
<b>30</b>	469.3	394.6	97.76	47.20
<b>40</b>	525.6	505.4	142.0	58.87
<b>50</b>	571.1	588.1	170.9	76.12
<b>60-90</b>	563.4	621.8	177.3	78.91

**Table 3.1:** Nuclear disintegration rates in the atmosphere fitted to a third order polynomial using the coefficients above. Disintegration rate,  $s = a + by + cy^2 + dy^3$ , where  $y$  is the altitude (km). From (Lal, 1991)

### *Irradiation Experiments*

Experimental irradiation of a sample with a beam of protons (Leya et al., 1998), muons (Heisinger et al., 2002b, 2002a) or neutrons (Nishiizumi et al., 2009) followed by analysis has been used to determine production rates of specific nuclides. These experiments also provide essential cross-section data for numerical simulations.

An alternative method for production rate calculation involves exposing a sample to ambient cosmic rays for a quantified time. These experiments enable cosmogenic nuclide production rates at varying altitudes and latitudes. For example, production rates of radionuclides,  ${}^{22}\text{Na}$  and  ${}^{24}\text{Na}$ , were determined experimentally by Yokoyama et al., (1977). They analysed fragments of aluminium and magnesium-bearing materials, exposed at different high altitudes for a number of years. The fragments having a known exposure age enabled a more reliable production rate measurement. The metal fragments were obtained from: an 8 year exposed television tower at 3840m, a  $>10$  year exposed pot cover from a chimney at 2070m, and an estimated 20

year exposed aeroplane wreckage near Mont Blanc's summit at 4600m. The respective production rates were estimated for various rock types due to Al and Mg being a similar atomic mass to the major rock forming element, Si.

### ***Geological Calibration***

The most frequently used method of obtaining cosmogenic nuclide production rates, is by sampling exposed, stable geological surfaces and measuring the abundance of the cosmogenic nuclide. Amounts of erosion, periodic burial, and prior exposure needs to be at a minimum to obtain accurate production rate determinations (See section 3.2.5 *Production Rate*). For stable cosmogenic isotopes, the measured abundance of cosmogenic nuclide of a geological sample is divided by the sample's age, which is determined with another reliable method (e.g. K-Ar dating when there is sufficient K for analyses). For analysis using radionuclides, the decay of the nuclide must also be considered.

Research Paper	Location	Latitude	Range of Altitude (m)	Cut-off Rigidity (GV)	Production Rate at SLHL (atoms g <sup>-1</sup> a <sup>-1</sup> )	Scaling Method Used
Kurz et al. (1990)	Hawaii, USA	19.4	18-2339	11	125-127	Lal (1991)
Cerling (1990), Poreda and Cerling (1992), Cerling and Craig (1994)	Western USA and France	41.8	860-1455	3-4	115 ± 4	Lal (1991)
Licciardi et al. (1999)	Oregon, USA	44.2	925-1622	3	116 ± 3	Lal (1991)
Dunai and Wijbrans (2000)	Canary Islands	28.9	30-197	10	118 ± 11	Dunai (2000)
Ackert Jr et al. (2003)	Argentina	-46.8	380-905	8	129-139	Lal (1991)/Stone (2000)
Licciardi et al. (2006)	Iceland	64.1	22-459	<2	132 ± 5	Lal (1991)/(Stone, 2000)
Blard et al. (2006)	Hawaii, USA and Mt Etna, Italy	19.4 and 37.7	40-3950	11 and 7	128 ± 5 136 ± 6	Lal (1991)/Stone (2000) Dunai (2000)

**Table 3.2:** A summary of production rates in the literature obtained by measuring cosmogenic  ${}^3\text{He}$  abundances in surface samples basalt lava flows independently dated using isotopic dating methods. Cut-off rigidity values taken from Lifton et al., (2005). Table adapted from Goehring et al. (2010).

Table 3.2 shows literature  ${}^3\text{He}_c$  production rates, for a wide range of latitudes and altitudes, of well-preserved basaltic lava flows with age controls from an independent source.

### 3.2.8 Production Rate Scaling Methods

There are five scaling methods used commonly (summarised in Table 3.3), each producing their own production rates for a specified cosmogenic nuclide.

Abbrev. method	Scaling Method	Description
<b>St</b>	Lal (1991)/Stone (2000)	Method is based on Lal (1991) scheme which is a function of latitude and altitude but adjusted by Stone (2000) to be a function of latitude and atmospheric pressure. Method does not consider magnetic field fluctuations; therefore production rates are constant over time.
<b>De</b>	Desilets et al. (2006)	Method is a function of atmospheric pressure and cut-off rigidity. Method considers magnetic field fluctuations; therefore production rates differ over time.
<b>Du</b>	Dunai (2001a)	Method is a function of atmospheric pressure and cut-off rigidity. Method considers magnetic field fluctuations; therefore production rates differ over time.
<b>Lif</b>	Lifton et al. (2005)	Method is a function of atmospheric pressure, cut-off rigidity and solar modulation. Method considers magnetic field and solar output fluctuations; therefore production rates differ over time.
<b>Lal-t</b>	Lal (1991)/Stone (2000) /Nishiizumi et al. (1989)	Method is <b>St</b> but with the addition of palaeomagnetic corrections from Nishiizumi et al. (1989). Method considers corrections in magnetic field; therefore production rates vary over time.

**Table 3.3:** Scaling methods used most often for production through spallation. “Abbrev method” gives a short-hand version of the scaling methods provided which are referred to in the text.

Production rates attained through geological calibration are typically normalized to SLHL. The scaling method used for the normalization of a reference production rate should be used consistently throughout the entirety of analysis. For example, if a reference production rate is used for a site of cosmogenic nuclide measurements, then the same scaling scheme used for that reference value should be used to normalize the calibration measurements. This will prevent incorrect results (Balco et al., 2008).

Balco et al. (2008) have provided detailed information on what is expected of a scaling method, what needs to be taken into account when calculating production rates and the effects of the differences in these methods when calculating exposure ages.

When calculating production rates at a sample site a reference production rate is needed for a certain time and location which is usually at SLHL and at present day. A reference production rate taken at SLHL is not an unconditional constant. Instead, it represents a production rate for a specific set of measurements using a specific scaling method. Systematic differences between cosmic ray exposure ages using the different scaling methods can occur. Future developments on these scaling methods are enabled by comparing the exposure ages and production rates determined via the scaling methods by identifying certain locations where the data produced by each scaling method appreciably deviate.

The scaling method St (Table 3.3) is the simplest, most commonly used method and gives results as a function of latitude and atmospheric pressure. This method does not consider the change in the Earth's magnetic field over time, however. The lack of consideration regarding changes in the Earth's magnetic field prompted others to develop new schemes (De, Du, Lif) which take this into consideration, with Lif also considering solar modulation and the sun's eleven-year cycle. These methods are not a function of changing magnetic field rather they are related to the magnetic cut-off rigidity which is calculated in each method in different ways (Balco et al., 2008).

### ***CRONUS-Earth***

For the sake of comparison,  ${}^3\text{He}_c$  production rates are usually calculated using all scaling methods. This is often achieved using the online CRONUS-Earth (Cosmic-Ray Produced Nuclide Systematics) application (<http://hess.ess.washington.edu>) developed by Balco et al. (2008) using MATLAB software to calculate the production rates of  ${}^{10}\text{Be}$  and  ${}^{26}\text{Al}$  and hence their corresponding exposure ages and erosion rates. Goehring et al. (2010) has developed this application to allow for  ${}^3\text{He}_c$  calibrations of exposure ages and erosion rates ([www.cronuscalculators.nmt.edu](http://www.cronuscalculators.nmt.edu)). The results can be calculated for each scaling method summarised in Table 3.3.

The input parameters required for the online calculator are:

- Sample name
- Scaling method
- Latitude (decimal degrees)

- Longitude (decimal degrees)
- Elevation/Atmospheric Pressure (m/hPa)
- Sample thickness from surface (cm)
- Bulk density (g/cm<sup>3</sup>)
- Shielding factor (unitless)
- Erosion rate (mm/ka)
- Attenuation length (g/cm<sup>2</sup>)
- Depth to top of sample (g/cm<sup>2</sup>)
- Year collected (Year A.D.)
- Concentration <sup>3</sup>He (Atoms of <sup>3</sup>He/g of sample)
- Uncertainties for each of these

Not all of these input parameters are needed for calculating the exposure age or erosion rate but the more that are provided, the more accurate the result. Further details on the implementation (inputs, outputs, coding, etc.) of CRONUS-Earth are discussed by Balco et al. (2008), Goehring et al. (2010), Phillips et al., (2016) and the CRONUS website. For further information on how the errors for each measurement and overall result are calculated, please refer to these papers.

Goehring et al. (2010) have taken data from the literature to evaluate <sup>3</sup>He production rates acquired from basaltic lava flows (Table 3.2; Section 3.2.7 *Geological Calibrations*), and data obtained from a study of Tabernacle Hill, Utah. The calibration data was combined to obtain global <sup>3</sup>He<sub>c</sub> production rates. These global <sup>3</sup>He<sub>c</sub> production rates were applied to CRONUS-Earth. Each sampled location (Table 3.2) was combined with an independently determined age, found using either: Ar-Ar, K-Ar or <sup>14</sup>C –dating for comparison.

Reference production rates modified for SLHL are presented for olivine and pyroxene (Table 3.4; Goehring et al., 2010). Pyroxene data show more scatter compared to olivine, however variations in the production rates for each mineral using different scaling methods were found to be minimal (Table 3.4; Goehring et al., 2010).

Scaling Method	${}^3\text{He}$ Production Rate (at $\text{g}^{-1} \text{yr}^{-1}$ )
<i>Olivine</i>	
St	$121 \pm 11$
De	$127 \pm 13$
Du	$126 \pm 14$
Li	$137 \pm 16$
Lal-t	$118 \pm 14$
<i>Pyroxene</i>	
St	$124 \pm 9.2$
De	$128 \pm 6.4$
Du	$129 \pm 7.8$
Li	$137 \pm 5.7$
Lal-t	$119 \pm 9.9$

**Table 3.4:** Reference SLHL  ${}^3\text{He}$  production rates evaluated for pyroxene and olivine data from production rates taken from past literature (Table 3.2) calculated by Goehring et al. (2010) using the arithmetic mean and standard deviations of the reference regional production rates (uncertainties reported at  $1\sigma$ ).

The major difference found in using different scaling methods (ignoring the differences due to considering/not considering Earth's magnetic field fluctuations) are that the nuclide production rates strongly depend on elevation in the methods of De, Du and Lif compared to St and Lal-t (Balco et al., 2008).

### 3.2.9 Factors Affecting Production Rates

#### *Altitude and Depth Dependence*

The deeper an exposed surface is in the atmosphere, the more atmospheric matter the secondary cosmic ray must interact with before reaching the exposed surface. Hence, exposed samples at different altitudes will have varying production rates of  ${}^3\text{He}_c$ , see Section 3.2.3 *Atmospheric Depth and Attenuation Length*.

#### *Latitude and Magnetic Field*

Varying latitudes can affect the production rates of  ${}^3\text{He}_c$  as explained in Section 3.2.2 *Cut-Off Rigidity*. Essentially all cosmic rays regardless of their rigidity can penetrate the Earth's magnetic field at high latitudes, which correlates to a relatively high production rate of  ${}^3\text{He}_c$  when compared to lower latitudes.

### 3.2.10 Temporal Variations

#### *Shielding*

When calibrating exposure ages in areas of high relief, it is important to take into account large solid obstructions to the incoming cosmic rays. Shielding affects the number of cosmogenic nuclides generated in the rock surface. For example, nearby trees or mountains provide shielding, as well as self-shielding from dipping surfaces, snow, ash and ice. Unreliable exposure ages can be obtained if shielding is not accounted for when calculating the exposure age of a surface rock.

Section 3.2.3 *Atmospheric Depth and Attenuation Length* explained that the cosmic ray flux is biased to vertically incident cosmic rays and so shielding corrections are usually relatively small. This correction is integrated into the CRONUS-Earth calculator (Section 3.2.8 *CRONUS-Earth*) enabling the input of shielding as a measurement of inclination. The topographic shielding at the specified sampling site is found by measuring the inclination,  $\theta$ , of the visible horizon using an inclinometer. Horizon obstruction by trees requires an estimation of the horizon location by interpolation.

Sampling from a sloping surface will reduce the amount of cosmic radiation received on that surface due to a vertical incidence of cosmic radiation being preferred for interaction. In cases of sampling sloped surfaces, a normal topographic shielding correction is adequate, especially when inclined by less than 30° (Balco et al., 2008).

Self-shielding can occur on samples taken to be analysed depending on the sample's thickness. The bottom of the sample will be shielded by the mass of the rest of the sample above. This is dependent on the density of the sample and the attenuation coefficient for spallation reactions. Sampling thickness is an input parameter in CRONUS-Earth and is therefore considered. For more information on topographic- and self-shielding see Gosse and Phillips (2001) as these factors are discussed at great length.

#### *Erosion*

The exposure age could be highly underestimated if the surface is continually eroded. The erosion removes exposed rock that includes cosmogenic nuclides formed over time. If erosion is not considered, the exposure age of the surface will

be erroneously low (Fig. 3.8). Sampling sites should be targeted that appear to have minimal erosion to minimize this effect. Even so, zero erosion is not a realistic assumption.

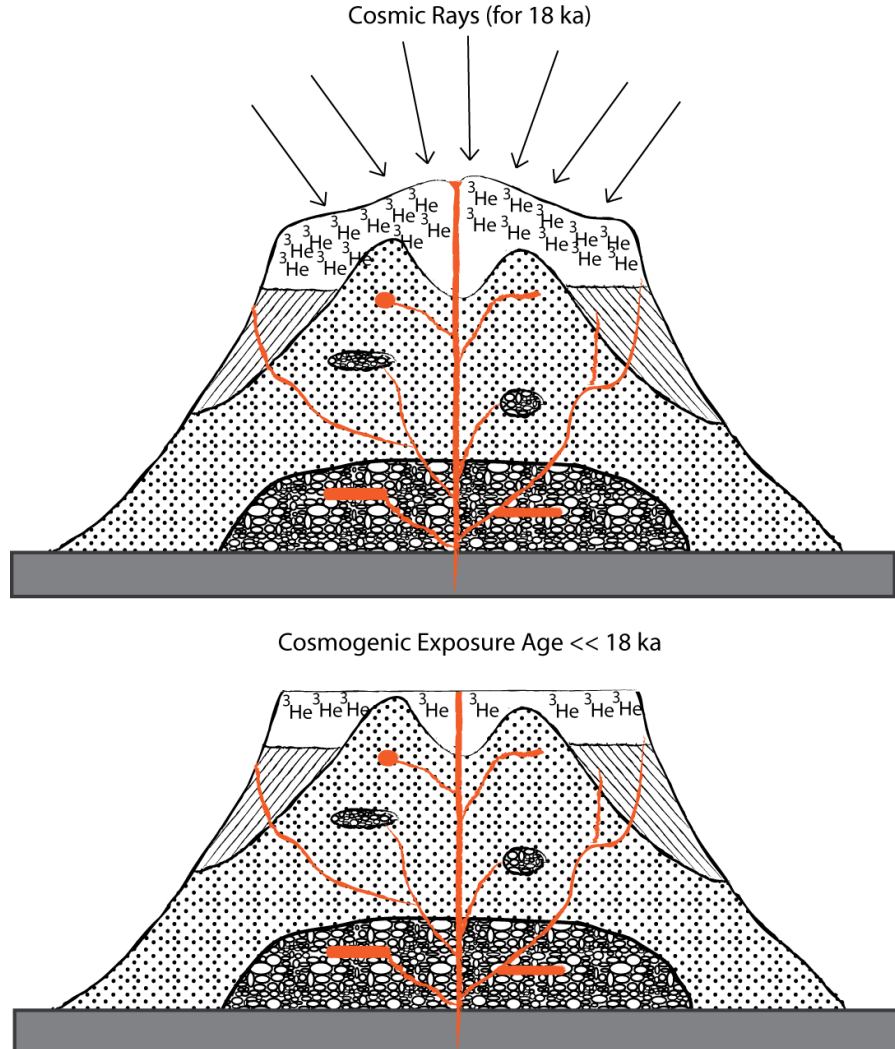


**Figure 3.8:** Illustration of the effect of erosion on cosmogenic exposure ages. The build up of cosmogenic  ${}^3\text{He}$  is significantly less after the summit has been eroded, leading to a miscalculation of exposure ages when erosion is not taken into consideration

See section 3.2.11 Factors Affecting  ${}^3\text{He}$  Exposure Age Dating Specific to Iceland and this Study *Erosion* for more information on erosion.

### ***Post-glacial Isostatic Uplift***

Exposure ages can be affected by the amount of isostatic rebound that occurs after a glacial event. Analysed surficial rock could initially have started at a lower altitude, giving rise to fewer cosmogenic nuclides produced in that rock. This reduction of produced cosmogenic nuclides is brought upon by the increase in atmospheric shielding with increasing atmospheric depth (See sections 3.2.3

*Atmospheric Depth and Attenuation Length* and 3.2.9 *Altitude and Depth Dependence*). If the rock surface is uplifted from rebound, the production rate of  ${}^3\text{He}_c$  will be increased as the atmospheric shielding decreases. Scaling a cosmogenic nuclide production rate based on the specific altitude will be higher than the actual production rate at a site that has undergone isostatic rebound. Taking this rebound effect into consideration will lower an effective production rate. The differences found in exposure ages, when taking rebound into effect, will increase when there is a higher amount of total rebound and when the rate of recovery from this rebound is slow.

Calculating this effect on the exposure ages necessitates knowing the rate of rebound through the duration of exposure of the sample site, which is not straightforward (Licciardi et al., 2007). However, the variation in atmospheric depth which is associated with isostatic rebound has been calculated to be <1% over long exposure periods (Gosse and Phillips, 2001).

### **3.2.11 Factors Affecting ${}^3\text{He}$ Exposure Age Dating Specific to Iceland and this Study**

#### ➤ **Interactions with Earth's Magnetic Field**

##### *Cut-Off Rigidity*

In Iceland (geomagnetic latitude 63°-66°N, geographic east longitude 15-24°) the vertical cut-off rigidity has been found to be between 0.68 and 0.74 GV (Smart and Shea, 2008). This means virtually all cosmic rays with an allowed trajectory will be able to penetrate the Earth's magnetic field at the specific latitude and longitude of Iceland.

##### *Fluctuations in Earth's magnetic Field*

The temporal variation of the Earth's geomagnetic field does not significantly affect cut-off rigidity values at the relatively high geomagnetic latitude of Iceland. Therefore the effect of magnetic field fluctuation will not be considered further.

## ➤ Production Mechanisms of ${}^3\text{He}$ in Surface Rocks

### *Spallation*

Considering the attenuation length of high energy neutrons and the density of basalt, their corresponding stopping distance is 50-60cm in basalt. Therefore spallation produces  ${}^3\text{He}$  in only the top metre of basalt with a newly calibrated Icelandic  ${}^3\text{He}$  production rate of  $132 \pm 5 \text{ atoms g}^{-1} \text{ a}^{-1}$  at SLHL (Licciardi et al., 2006). This production rate is relatively high due to the enhanced production of  ${}^3\text{He}$  in Iceland brought on by the influence of the low atmospheric pressure above Iceland throughout the Holocene (Licciardi et al., 2006).

### *Nucleogenic Thermal-Neutron Capture ( $n,\alpha$ )*

Detailed chemical compositions of the Icelandic tuyas in the Western Volcanic Zone are given by Jakobsson and Johnson (2012). The data reveals that Li is not significantly present in these subglacial volcanoes. Using data compiled in geochemical database, GEOROC (Geochemistry of Rocks of the Oceans and Continents), Li concentrations in Icelandic basalts are reported to be up to 78ppm. These high Li concentrations are found in the coastal areas (such as Reyðarfjöldur in the east), acidic extrusives, postglacial lava flows and Holocene sediments (on the south coast). These areas are not sampled in this study.

The production of cosmogenic nuclides is greatest on the direct rock surface and surface samples are usually collected for this reason. Using surface samples also means muon induced  ${}^3\text{He}$  is at a minimum and does not need to be considered.

### *Nuclide Abundance*

Noble gases commonly have low backgrounds due to their incompatibility with other elements, thus eliminating their incorporation into minerals (Porcelli and Ballentine, 2002). This enables a simpler analytical procedure for determining  ${}^3\text{He}$  abundances.

### *Overview of ${}^3\text{He}$ Surface Production*

Spallation generates 100% of  ${}^3\text{He}$ , muon production is negligible and thermal neutrons produce  ${}^3\text{He}$  on Li concentrated rocks (Dunai, 2010).

## ➤ Factors Affecting Production Rates

### *Altitude and Depth Dependence*

The highest point in Iceland is at Hvannadalshnúkur in the south-east which is 2110 m ( $\sim 800 \text{ g cm}^{-2}$  atmospheric depth or 75 kPa atmospheric pressure), therefore any exposed basalt used for analysis will be below this elevation. Icelandic tuyas have a range of heights, the highest being 1400 m of Eiríksjökull in the WVZ and 1682 m of Herðubreið in the NVZ.

### *Olivine Composition*

Lal (1991) has suggested that different olivine composition may give rise to varying  ${}^3\text{He}$  production rates. This is unlikely to be a factor due to the small variation in composition throughout these basaltic edifices (Licciardi et al., 2007).

## ➤ Temporal Variations

### *Shielding*

When considering Icelandic tuyas, temporary ash, water, snow and ice-cover could affect these calculated ages by shielding the surface from cosmic rays. Areas in the NVZ have minimal snow fall due to lying in the "rain shadow" of the ice cap Vatnajökull and highlands of the interior. However, the mean annual temperature is colder in the NVZ and so snow fall in the winter months may be deeper and last longer than in the WVZ. Nevertheless, snow cover is an important factor to consider in both the WVZ and NVZ when considering samples acquired for cosmogenic dating taken from the summits. There is a distinct lack of well-constrained information on snowpack at the sites sampled, which prevents an accurate quantification of the effect of snow cover on cosmogenic exposure ages (Licciardi et al., 2007). The effect of snow cover can be estimated by assuming there is snow cover between the months of October and May. For example, a minimum of 10 cm with  $0.2 \text{ g cm}^{-3}$  density and a maximum of 100 cm with  $0.5 \text{ g cm}^{-3}$  would increase the exposure ages by 0.8% and  $\sim 17.9\%$  respectively (Licciardi et al., 2007). Unlike water content in surficial rocks (see 3.2.4 *Thermal Neutrons*; Fig. 3.7), currently, there is no suitable model calibration to account for snow cover (Phillips et al., 2001).

To negate the effect of shielding (from snow cover and/or ash) surfaces chosen for sampling should still preserve the ropey appearance of pahoehoe lava and be taken from the topographic high of the tumuli (domes created from fracturing of lava crust), where possible.

### ***Erosion***

When considering Iceland's basaltic tuyas (Section 2.3), the erosion rates could vary from the base of the volcanic edifice to its peak, due to the contrasting harshness of environment between these two points (Licciardi et al., 2007). During glaciation the factors affecting the rate of erosion are dependent on ice thickness, the speed at which the glaciers and ice sheet move at the location of the edifice, such as their distance from the ice sheets ice divide (see 2.2.1 Weichselian Timeline) and the amount of meltwater drainage occurring at the base of the ice sheet. Erosion occurs greatly when thick ice travels down the slope of a tuya, carrying with it the lava surface underneath the ice (Eason et al., 2015). Thinner glaciers and thin ice sheets are less likely to flow and so it could be possible that some tuyas were buried in ice but do not exhibit any surface erosion. The action of freeze-thaw alone could cause widespread fracturing of the surface and produce blocky surfaces that were once continuous flows (Eason et al., 2015). Post-glaciation factors that affect erosion are the amount of precipitation, slope of surface, amount of vegetation such as lichens and moss and the wind speed (Hart, 1995). These localized temporal contributions to erosion occur at various rates and are difficult to quantify accurately. All of these factors can make it complicated to relate surficial erosion to the age of a surface. In general terms, the morphology of the edifice is used to determine the amount of erosion that has occurred. Well-preserved surfaces are most likely indicative of younger lava flows whereas any indication of glacial scouring would suggest significant ice cover in the past (Eason et al., 2015).

One aim of this research is to shed more light on the rates of erosion and shielding by comparing the differences in age of eruption and exposure length.

### ***Postglacial Isostatic Rebound (Uplift)***

Postglacial isostatic uplift affects Iceland significantly as Iceland sits on top of a buoyant hotspot. The removal of ice sheets creates a considerable uplift of the

Iceland's crust that can affect exposure ages (Licciardi et al., 2007). Evidence shows that the uplift and compression of the Icelandic crust less than  $\pm 100$  m throughout the onset and deglaciation of the Weichselian ice sheet (see 2.2.1 Weichselian Timeline). This means that the difference in exposure age will only be between 0.5 - 1% (Gosse and Phillips, 2001).

The exact rates of erosion and isostatic rebound are difficult to assess. Combining the exposure ages with eruption ages will help to provide some clarity and understanding on these rates and will show what effect they have on the exposure ages found.

### **3.3 (U-Th)/He Dating**

#### **3.3.1. Why use (U-Th)/He dating?**

One of the aims of this research is to determine reliable eruption ages of the basaltic subglacial volcanic formations (tuyas) in Iceland. Radiocarbon, Ar-Ar and tephrochronology are common dating techniques which are not suitable methods to apply to tuyas. This thesis assesses the application of (U-Th)/He dating to determine the age of basaltic eruptions in Iceland.

The ability to date minerals via the build-up of  ${}^4\text{He}$  from decay of U and Th has been known for around a century (Strutt, 1905), but since then has been relatively unsuccessful in its application. The technique was virtually abandoned due to unreliable low ages being obtained, suggested as a result from helium loss through diffusion in minerals (Farley, 2002). Improved understanding of the behaviour of He in minerals (Zeitler et al., 1987; Wolf et al., 1996), the development of analytical techniques (Farley, 2002), and the requirement for new chronological tools (House et al., 1998; Aciego et al., 2003) has seen a revival in the interest in dating minerals by means of  ${}^4\text{He}$  ingrowth over the last 50 years.

#### ***Minerals suitable for basaltic (U-Th)/He dating***

The ability to date relatively young volcanic rocks (<1Ma) is important for temporal understanding of tectonic, geomorphic and climatic processes. Basaltic eruptions can be difficult to date using (U-Th)/He dating due to a low amount or lack of basaltic minerals that contain high amounts of U and Th, such as zircon and apatite (Farley et al., 2002; Ehlers and Farley, 2003). For the dating of young lava flows to be viable, this dating technique needs to be applicable to common phenocrystal minerals present in basalts, such as olivine and clinopyroxene (Trull et al., 1991; Trull and Kurz, 1993).

### 3.3.2. U-series Radioactive Decay

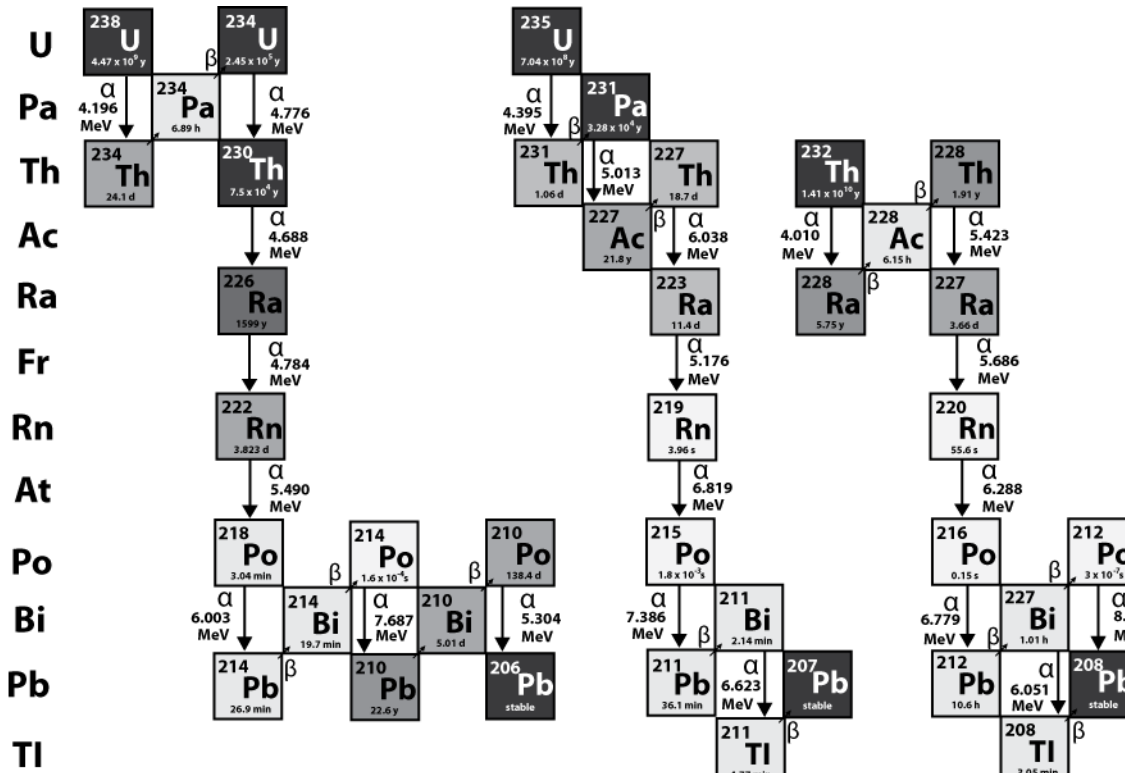


**Figure 3.9:** Schematic of the decay chains of  $^{238}\text{U}$ ,  $^{235}\text{U}$  and  $^{232}\text{Th}$ . Grey-scale shows half-lives, the darker tones denote longer the half-lives. From Bourdon et al. (2003)

During the decay of naturally occurring actinides  $^{238}\text{U}$ ,  $^{235}\text{U}$ ,  $^{232}\text{Th}$ , multiple  $\alpha$ -particles (essentially nuclei of  $^4\text{He}$ ) are formed (Fig. 3.9). A series of intermediate nuclides are produced with varying half-lives from microseconds to hundreds of thousands of years before ending at a stable isotope of lead. The term "disequilibrium" is used to indicate when insufficient time has elapsed to establish an equilibrium between parent and the stable isotope at the end of the chain (Bourdon et al., 2003). A non-steady state decay (Fig 3.10) produces differing amounts of various daughter particles throughout time, whereas a steady state decay has equilibrated to produce consistent amounts of each daughter particle, monotonous throughout time. When the decay is at a steady state, the condition is under secular equilibrium.

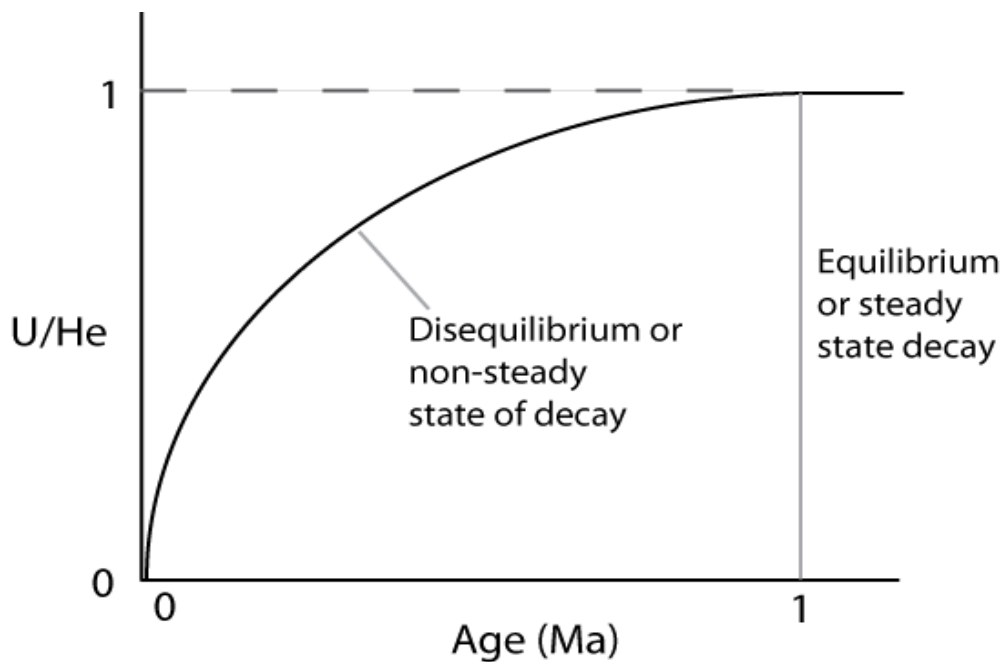


**Figure 3.10:** A plot of U/He ratio vs. age illustrating the non-steady state of U decay to produce He atoms over time and reaching equilibrium where the decay occurs at a steady state.

The secular equilibrium equation is:

$${}^4\text{He}_{\text{eq}} = 8 {}^{238}\text{U} (e^{\lambda_{238}t} - 1) + 7 ({}^{238}\text{U} / 137.88) (e^{\lambda_{235}t} - 1) + 6 {}^{232}\text{Th} (e^{\lambda_{232}t} - 1) \quad \text{Equation 6}$$

$$\text{or} \quad {}^4\text{He}_{\text{eq}} = (8 {}^{238}\text{U}\lambda_{238} + 7 {}^{235}\text{U}\lambda_{235} + 6 {}^{232}\text{Th}\lambda_{232})t = Pt \quad \text{Equation 7}$$

where  ${}^4\text{He}$ , U and Th are their respective concentrations,  $t$  is the accumulation time, and  $\lambda$  are the relevant decay constants (Table 3.5). The coefficients before the concentrations of U and Th refer to the number of  $\alpha$ -particles which are produced in each decay series (Fig. 3.9), and 1/137.88 is the present day ratio of  ${}^{235}\text{U}/{}^{238}\text{U}$ .  $P$  in equation 7 refers to the production rate of He (Farley, 2002; Farley et al., 2002). Secular equilibrium is reached after  $\sim 5$  half-lives (Fig 3.9) of the longest lived intermediate nuclide undergoing fractionation (Farley et al., 2002).

Parent	Half-life (10 <sup>9</sup> yr)	Decay constant <sup>a</sup> , $\lambda$ (x10 <sup>-10</sup> yr <sup>-1</sup> )	Daughter	Yield	Atomic weight of parent	Percent abundance (atomic)	Noble Gas Production (cm <sup>3</sup> STP/g)	Rate (yr <sup>-1</sup> )	Accumulation <sup>b</sup>
<sup>238</sup> U	4.468	1.551	<sup>4</sup> He	8	238.029	99.280	11.602 x 10 <sup>-8</sup>	7.479 x 10 <sup>2</sup>	
<sup>235</sup> U	0.7038	9.849	<sup>4</sup> He	7	235.044	0.720	0.467 x 10 <sup>-8</sup>	4.746	
<sup>232</sup> Th	14.010	0.495	<sup>4</sup> He	6	232.038	100	2.868 x 10 <sup>-8</sup>	5.796 x 10 <sup>2</sup>	

**Table 3.5:** Radionuclides with their noble gas daughters and atomic production. Adapted from Ozima and Podosek (1983) and references therein. <sup>a</sup> Decay constants taken from Farley (2002) <sup>b</sup> Accumulation = rate x (1/λ)

When dating relatively young samples ( $t \ll 1/\lambda_{235}$ ), there is a more straightforward, linear approximation given by Meesters and Dunai (2005) and Vermeesch (2008). Both methods determine the age by calculating the production rate of <sup>4</sup>He (α-particles) from the decay of determined U and Th concentrations and their corresponding decay constants. Meesters and Dunai (2005) used a weighted-mean decay rate ( $\lambda_{wm}$ ) whereas Vermeesch (2008) did not, however both approaches are very similar and the ages calculated vary by 1%. Vermeesch (2008) gives the calculation for the ingrowth of helium over time as:

$$[He] = \left( 8 \frac{137.88}{138.88} (e^{\lambda_{238}t} - 1) + \frac{7}{138.88} (e^{\lambda_{235}t} - 1) \right) [U] + 6(e^{\lambda_{232}t} - 1) [Th].$$

*Equation 8*

Equation 8 can be solved iteratively, but a more accurate linear approach is given by:

$$t = \frac{[He]}{P} \quad \text{Equation 9}$$

Where t is the accumulation time (age) and [He] is the given radiogenic helium concentration and P is the modern day production rate of He given by:

$$P = \left( 8 \frac{137.88}{138.88} \lambda_{238} + \frac{7}{138.88} \lambda_{235} \right) [U] + 6\lambda_{232} [Th] \quad \text{Equation 10}$$

This method by Vermeesch (2008) is accurate to better than 1% for ages up to 100Ma.

When dating volcanic rocks less than ~1 Ma, secular equilibrium is unlikely to be reached. In this case, using the equations above (6 and 7) will provide incorrect (U-Th)/He ages by as much as 50% (Farley et al., 2002; Aciego et al., 2007; Aciego et al., 2003; Blard and Farley, 2008).

During the decay of the  $^{238}\text{U}$  series (Fig 3.8), the longest lived intermediate nuclide is  $^{234}\text{U}$  ( $t_{1/2} = 248$  ka), but the fractionation of the  $^{234}\text{U}/^{238}\text{U}$  ratio in magmatic conditions is negligible (Farley et al., 2002). The most important fractionation in the  $^{238}\text{U}$  series is that of  $^{230}\text{Th}$  ( $t_{1/2} = 75$  ka). Volcanic crystals, in particular, tend to form with high  $^{230}\text{Th}/^{238}\text{U}$  ratios (Farley et al., 2002; Farley, 2002; Wood et al., 1999; Aciego et al., 2007). Consequently, the decay of each  $^{238}\text{U}$  produces less than 8  $\alpha$ -particles until reaching secular equilibrium. An intermediate nuclide that can undergo fractionation produced from the decay of  $^{230}\text{Th}$  is  $^{226}\text{Ra}$  ( $t_{1/2} = 1.6$  ka). The disequilibrium from this nuclide has a small effect on He ages, unless the age is less than ~10  $^{226}\text{Ra}$  half-lives. Therefore, this only needs to be considered when dealing with ages close to or less than 16 ka (Farley et al., 2002). It is unknown how large the effect is on the determined ages by ignoring this  $^{226}\text{Ra}$  disequilibrium, but is most likely accounted for in the discrepancy (up to 50%) found between ages in equilibrium and disequilibrium.

In the decay of the  $^{235}\text{U}$  series, there is minimal He produced from  $^{235}\text{U}$  (per cent abundance; Table 3.5) allowing for no significant degree of secular disequilibrium (for example from  $^{231}\text{Pa}$ ) so does not affect the overall production of He (Farley et al., 2002). In the  $^{232}\text{Th}$  series, there is a lack of intermediate nuclide with a half-life over 7 years and so secular disequilibrium is not a factor in this case (Farley et al., 2002).

The correction for  $^{230}\text{Th}/^{238}\text{U}$  radioactive equilibrium is calculated using the Aciego et al. (2003) equations adapted from Farley et al. (2002b):

$${}^4\text{He} = P_{se}(U, Th)(1 + F_{dis}) \quad \text{Equation 11}$$

where:

$$P_{se}(U, Th) = 7({}^{235}\text{U})(e^{\lambda_{235}t} - 1) + 6({}^{232}\text{Th})(e^{\lambda_{232}t} - 1) + 2({}^{238}\text{U})(e^{\lambda_{238}t} - 1) \quad \text{Equation 12}$$

is the rate of  ${}^4\text{He}$  production expected for a system in equilibrium, and ignoring the effect of  ${}^{226}\text{Ra}$  secular disequilibrium, the correction used for any divergence from equilibrium is given by  $F_{\text{dis}}$ :

$$F_{\text{dis}} = \frac{1}{P_{\text{se}}(U, Th)} \left\{ 6D_{230} \left( \frac{\lambda_{238}}{\lambda_{230}} \right) ({}^{238}\text{U}) e^{\lambda_{238}t} (1 - e^{-\lambda_{230}t}) + 6({}^{238}\text{U}) \lambda_{238} e^{\lambda_{238}t} \left[ \left( \frac{1}{\lambda_{238}} \right) (1 - e^{-\lambda_{238}t}) + \left( \frac{1}{\lambda_{230}} \right) (e^{-\lambda_{238}t} - 1) \right] \right\}$$

*Equation 13*

${}^4\text{He}$ ,  ${}^{235}\text{U}$ ,  ${}^{232}\text{U}$  and  ${}^{238}\text{U}$  are their corresponding concentrations,  $\lambda$ 's are the decay constants and  $D_{230}$  is the initial  $[{}^{230}\text{Th}/{}^{238}\text{U}]$  activity ratio at the time of helium closure. This can be determined experimentally by  $({}^{232}\text{Th}/{}^{238}\text{U})_{\text{crystal}}/({}^{232}\text{Th}/{}^{238}\text{U})_{\text{magma}}$  (Farley et al., 2002b). Values of  $D_{230} < 1$  correspond to  ${}^4\text{He}_{\text{diseq}}/{}^4\text{He}_{\text{eq}} < 1$  as  ${}^{230}\text{Th}$  is lacking initially, whereas when  $D_{230} > 1$ , they indicate that  ${}^{230}\text{Th}$  was initially present in excess amounts and so produces an excess of He (Farley et al., 2002).

The age when considering samples in disequilibrium is determined using:

$$\text{Age} = \frac{{}^4\text{He}(1-F_{\text{diff}})F_T}{P_{\text{se}}(U, Th)(1+F_{\text{dis}})}$$

*Equation 14*

where  ${}^4\text{He}$  and  $P_{\text{se}}(\text{U}, \text{Th})$  are determined from their measured concentrations. The remaining factors are  $F_{\text{diff}}$  and  $F_T$ , which are the corrections for the diffusive loss of helium and the ejection of alpha particles ( ${}^4\text{He}$ ) respectively.

A large error in U-Th/He eruption ages can be attributed to U-Th rich inclusions within the comparatively low U-Th olivine matrix. The U-Th rich inclusions (e.g. zircon, monazite) eject  ${}^4\text{He}$  or alpha particles into the surrounding olivine matrix, creating "parentless" helium, which is analysed as radiogenic helium produced by U-Th in the olivine matrix (Lippolt et al., 1994; House et al., 1997; Farley and Stockli, 2002; Fitzgerald et al., 2006; Min et al., 2006). This problem is resolved by dissolving the olivine phenocrysts as a whole (including inclusions) in a strong acid such as HF. This method then includes any U-Th rich inclusions as if they are part of the mineral lattice as they were trapped at the time of crystallisation of the olivine (Min et al., 2006; Vermeesch et al., 2007; Vermeesch, 2008).

The factor that must be considered, when considering melt inclusions, is the possibility of U-Th rich inclusions being held by the edge of the phenocryst and

ejecting  ${}^4\text{He}$  out of the olivine phenocryst. The recoil distance an alpha particle can travel through olivine ( $F_{0.50}$ ), when ejected by the decay of U and Th, is close to 20  $\mu\text{m}$  (Ziegler, 1977). He loss during recoil is sufficient to reduce the calculated age by up to 1% (Aciego et al., 2003). The correction factor for recoil loss is calculated by:

$$F_T = 1 - \frac{3S}{4R} + \frac{S^3}{16R^3} \quad \text{Equation 15}$$

where  $S$  is the stopping distance (20  $\mu\text{m}$ ) and  $R$  is the spherical crystal radius (Farley et al., 1996), ~292  $\mu\text{m}$  on average in samples presented here.  ${}^4\text{He}$  implantation into adjacent olivine grains is possible, however the spacing between the parent-rich olivine crystals is  $>>20\mu\text{m}$  in most rocks, so the implantation of alpha particles from nearby crystals can be ignored. However, implantation from the surrounding basaltic matrix needs to be considered (Blard and Farley, 2008). To alleviate the effects of implantation (and ejection), mineral separates are air abraded or chemically etched to remove the outer 20  $\mu\text{m}$  (Min et al., 2006; Aciego et al., 2007; Blackburn et al., 2007; Gayer et al., 2008).

The distribution of the inclusions can have a large effect on the U and Th concentration in the olivine grain. Min et al (2006) performed Monte Carlo simulations assuming a random dispersal of inclusions. It was noted that  $F_T$  is more variable for samples with few large inclusions ( $F_T = 0.78 - 0.85$ ) compared to samples containing many small inclusions ( $F_T = 0.85$ ). The model was run with typical amounts of inclusions and generated values of  $F_T$  that were identical to correction factors for alpha ejection calculated with a homogeneous dispersal of U and Th.

Vermeesch (2008) noted that correcting an age for alpha ejection after determining the age can result in a loss of accuracy by 30%. The alpha ejection correction should be applied directly to the radiogenic  ${}^4\text{He}$  concentration before the age is determined.

### **3.3.3 Factors Affecting (U-Th)/He Dating Specific to Iceland**

#### **➤ Minerals Suitable for (U-Th)/He Dating**

Clinopyroxene has the advantage of a high U and Th concentration, but its ability to retain helium is highly composition dependent (Trull and Kurz, 1993). Pyroxene minerals obtain cleavage, which are a built in weak point that can allow He to diffuse out more easily, whereas olivine does not. Olivine has a high retention for helium irrespective of its composition. Due to olivine's extensive use for cosmogenic  ${}^3\text{He}$  studies its diffusion properties have been well-studied on numerous occasions (Hart, 1984; Trull et al., 1991; Niedermann, 2002). Olivine is the most abundant porphyritic mineral in Icelandic subglacial basalt (clinopyroxene phenocryst are absent or rare) and thus was selected for use in this research.

#### **➤ Helium Diffusion**

Olivine retains helium throughout the cooling of extrusive basalts. However, it is possible that diffusive loss of He from the olivines could occur if they were heated during a later eruptive episode (e.g. by an overlying lava flow or intrusion). This is unlikely, as olivine samples were collected from a half metre to a metre depth from the surface and far from any recent lava (postglacial) flows.

#### **➤ Alpha-Particle Ejection/Implantation**

Abrasion of the olivine phenocrysts can help to remove grain boundaries affected by alpha-particle implantation (Min et al, 2006; Aciego et al, 2007). Min (et al 2006) studied the difference in eruption age on mineral grains that were abraded and those that were not. The eruption ages of non-abraded fayalite olivine (found in rhyolite but not basalt) were 1% larger than the non-abraded minerals. The largest difference seen was that the alpha-ejection correction ( $F_T$ ) varied from 0.90 and 0.96 for the non-abraded samples whereas the abraded samples showed no variation. Therefore the samples in this study did not undergo abrasion as it was considered not to produce an appreciable effect in age.

In this study the spherical solution (radius of  $\sim 292 \mu\text{m}$  on average in this study) for alpha-particle ejection from Farley et al (1996) is used giving an  $F_T$  alpha ejection correction value of 0.95.

## 3.4 Separating multiple sources of He

### 3.4.1 Sources of $^4\text{He}$ in (U-Th)/He Dating

Olivine has one disadvantage in having relatively low U and Th abundances. This means olivine has a low concentration in radiogenic  $^4\text{He}$ , and this must be distinguished from magmatic  $^4\text{He}$  trapped in fluid/melt inclusions and from any  $^4\text{He}$  implanted from the surrounding basalt (Aciego et al., 2007; Blard and Farley, 2008).

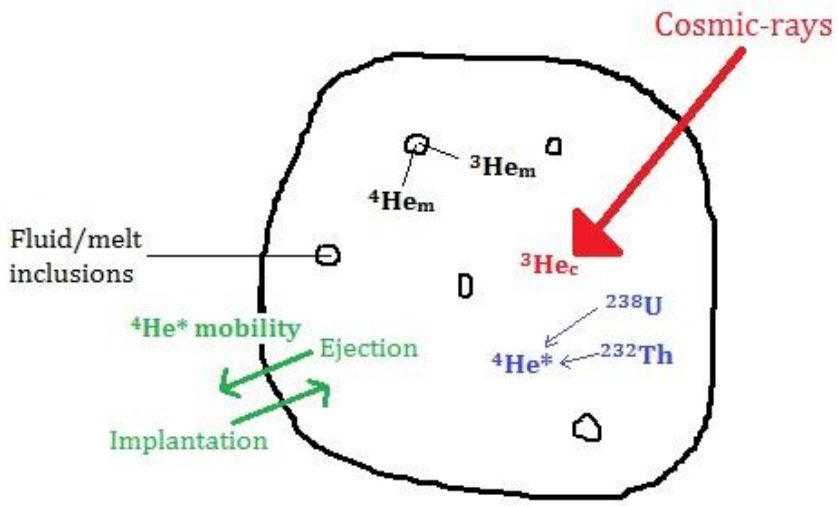


**Figure 3.11:** Olivine mafic phenocryst illustrating the potentially different sources of helium. Nucleogenic sources of helium not shown because it has negligible abundance in low-Li, low age samples (see Chapter 3.3). Adapted from Blard and Farley (2008)

$${}^4\text{He}^* = {}^4\text{He}_{\text{melt}} - {}^4\text{He}_{\text{trap}} - {}^4\text{He}_c \quad \text{Equation 16}$$

Equations 6 and 7 (chapter 3.3.2) give the general equation used to calculate the amount of radiogenic  $^4\text{He}$  produced solely from the decay of U and Th ( ${}^4\text{He}^*$ ). The subscripts in equation 16 denote the  ${}^4\text{He}$  released after melting the phenocrysts (*melt*), cosmogenic  ${}^4\text{He}$  (*c*), and the initial (magmatic)  ${}^4\text{He}$  released not from crushing (*trap*) (Aciego et al., 2007; Blard and Farley, 2008).

#### **Magmatic (Trapped) ${}^4\text{He}$**

The magmatic  ${}^3\text{He}/{}^4\text{He}$  ratio is established by releasing helium trapped in fluid and melt inclusions in the olivine phenocrysts. This helium is released by crushing aliquots of olivine phenocrysts used for both (U-Th)/He age dating and cosmogenic  ${}^3\text{He}$  exposure dating (Fig. 3.11). Not all of the trapped component is released during crushing because excessive crushing can lead to loss of radiogenic and cosmogenic He from the crystal matrix (Blard et al., 2006; Blard et al., 2008). Samples are

relatively lightly crushed whilst the sample is kept at room temperature (Blard et al., 2008). The total helium extracted by fusion of the crushed residue can then be corrected for the magmatic component using the crushing data (Blard et al., 2008; Aciego et al., 2007) using equation 17.

$${}^4\text{He}^* = {}^4\text{He}_{\text{melt}} - ({}^3\text{He}_{\text{melt}})({}^4\text{He}/{}^3\text{He})_{\text{crush}} - {}^4\text{He}_c \quad \text{Equation 17}$$

### ***Implanted and Ejected ${}^4\text{He}$***

Implantation of  ${}^4\text{He}$  from the surrounding basalt (Fig 3.11) can lead to ~5% underestimation of production rates, such as Ackert Jr. et al. (2003) and Blard and Farley (2008). Blard and Farley (2008) discuss the separation of implanted  ${}^4\text{He}$  from inherited/magmatic  ${}^4\text{He}$  and radiogenic  ${}^4\text{He}$ , providing equations taken from Farley et al. (1996) and Dunai and Wijbrans (2000) on  $\alpha$ -implantation into and out of a sphere. If this approach was taken, the concentrations of U and Th present in the surrounding basalt of the olivine phenocrysts must be known and taken into consideration as well as the specific geometry of each olivine grain.

#### **3.4.2. Sources of ${}^3\text{He}$ for cosmogenic exposure dating**

Samples collected from surfaces were used for exposure age dating (Chapter 3.3). These helium data are corrected for magmatic  ${}^3\text{He}$  using analogous approach to radiogenic  ${}^4\text{He}$ .

$${}^3\text{He}_c = {}^3\text{He}_{\text{melt}} - ({}^3\text{He}/{}^4\text{He})_{\text{crush}}({}^4\text{He}_{\text{melt}}) \quad \text{Equation 18}$$

Implantation and ejection of cosmogenic  ${}^3\text{He}$  can occur similarly to radiogenic  ${}^4\text{He}$ , but the net change in the concentration of  ${}^3\text{He}$  depends on the differences in  ${}^3\text{He}$  production rates between the groundmass and olivine phenocryst. Production rate differences calculated from Masarik and Reedy (1996) show that when olivine and basalt are considered, the difference is minor and the implantation/ejection effect of  ${}^3\text{He}_c$  becomes negligible (Aciego et al., 2007).

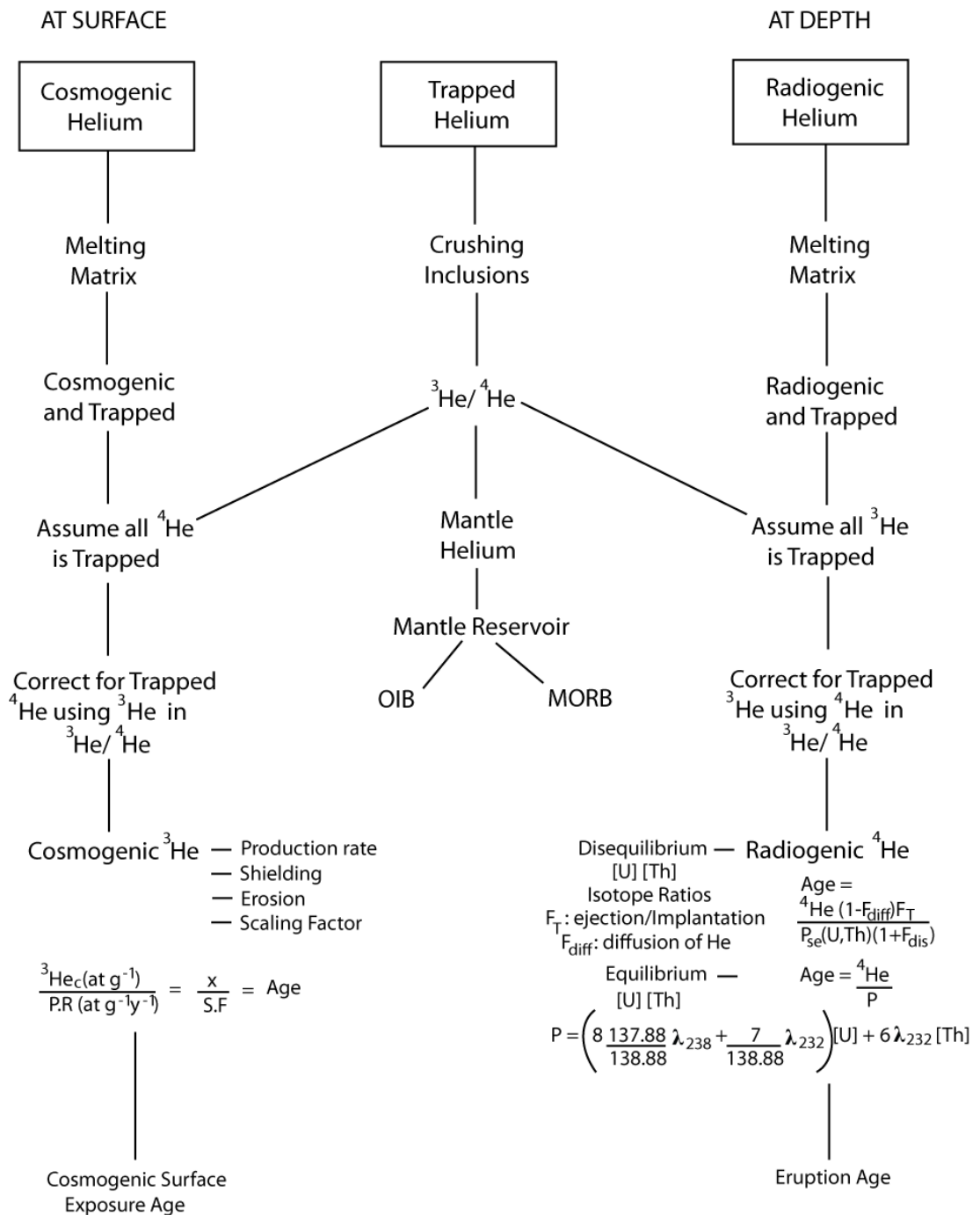


**Figure 3.12:** Flow chart showing the different sources of Helium in an olivine phenocryst and what is needed to determine both eruption and exposure ages

### 3.4.3 Sample Heterogeneity

The distribution of U and Th is heterogeneous, not only within the individual olivine grains, but also between grains and aliquots of olivine phenocrysts from one rock sample. To overcome this it is usual practice to use the same sample aliquot for He, U and Th analyses (Aciego et al., 2007).

# **Chapter Four: Fieldwork and Sample Preparation**

## **4.1 Introduction**

The aim of this research is to use helium (He) as a geochronological tool to pinpoint the eruption ages of Icelandic subglacial volcanoes. Isotopic dating methods usually used for basaltic rocks are not suitable. Icelandic basalts are too young for Ar-Ar dating (or have too low K abundances) and contain insufficient organic material for  $^{14}\text{C}$ -dating. Helium has two stable isotopes ( $^3\text{He}$  and  $^4\text{He}$ ), which have very low atmospheric abundances.  $^4\text{He}$  is formed by the decay of U and Th isotopes and can be used for eruption ages, and surface exposure to cosmic rays produces  $^3\text{He}$ , which can be used to date exposure of the surface e.g. following ice retreat.

This chapter provides a summary of the field work carried out to obtain samples used for analysis and gives a detailed account of the preparation and mass spectrometric techniques used to analyse the samples acquired.

## **4.2 Sample Collection and Field Protocol**

Basalt samples containing visible olivine phenocrysts were collected along the active rift zones of Iceland. Along the Western and Northern Volcanic Zones of Iceland, the samples were collected from the summit of three tuyas and the base of 14 tuyas, four tindars and one shield volcano (Fig 4.1 and see 2.3 Volcano-Ice Interactions). The samples acquired from the summits of tuyas were collected for the purpose of cosmogenic  $^3\text{He}$  dating (exposure age), whereas samples collected from the base of the subglacial volcanoes were for U-Th/He dating (eruption age). Altitude and latitudes were recorded at each sample location using a Garmin eTrex<sup>®</sup> GPS. The GPS location was accurate to  $\pm 12$  ft (3.66 m).

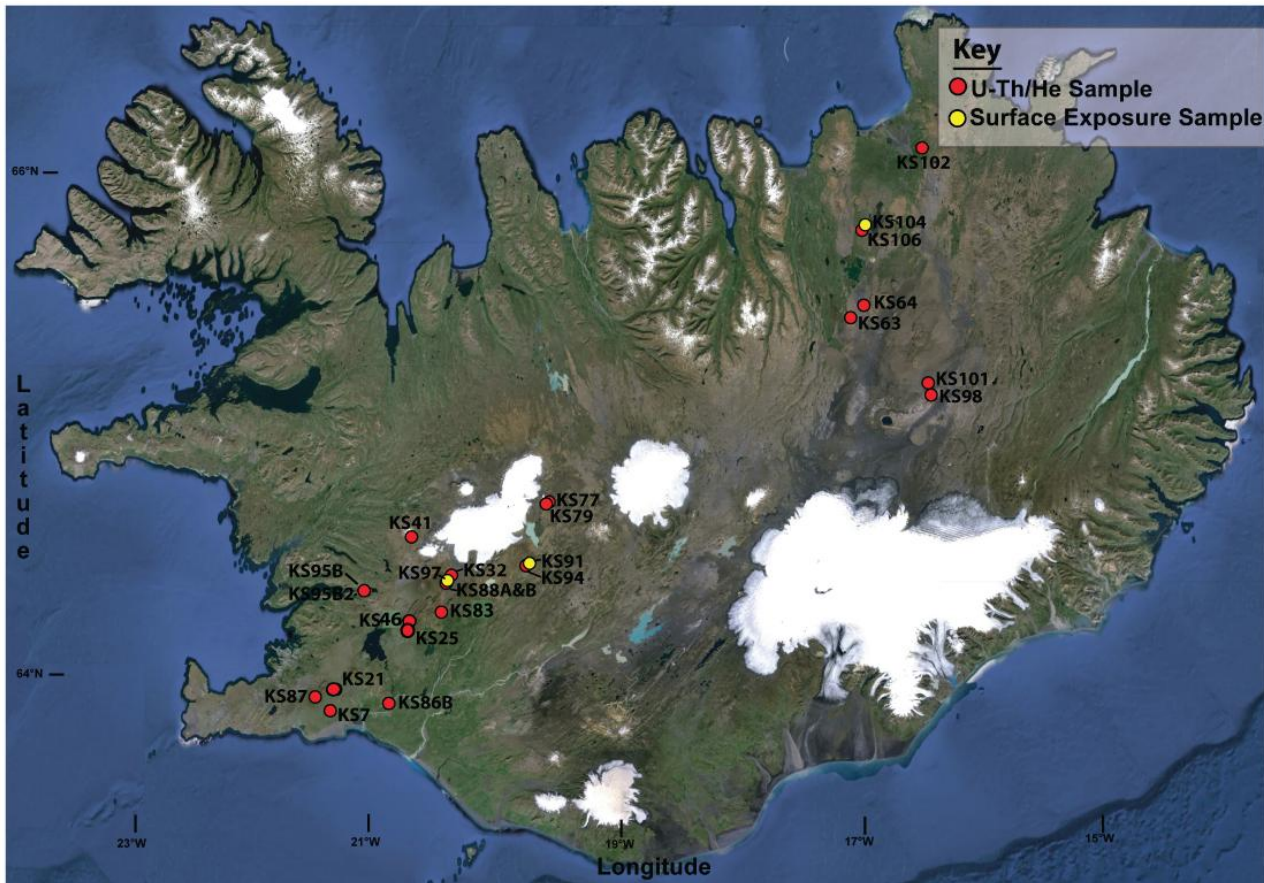


**Figure 4.1:** Localities of samples. Red dots show samples collected for eruption ages (U-Th/He dating). Yellow dots show sample localities for surface exposure ages (cosmogenic  ${}^3\text{He}$  dating). KS7: Geitafell, KS21: Lambafell, KS25: Kalfstindar, KS32: Þorolfsfell, KS41: Ok, KS46: Kálfstindar, KS63: Sellandafjall, KS64: Bláfjall, KS77 and KS79: Hrútfell, KS83: Raudafell, KS86B: Ingolfsfjall, KS88A and KS88B: Hlöðufell, KS87: Bláfjöll, KS91 and KS94: Bláfell, KS95B and KS95B2: Hvalfell, KS97: Hlöðufell, KS98: Herðubreiðatögl, KS101: Herðubreið, KS102: Hafrafell, KS104 and KS106: Gæsafjöll. See **Table 4.1** for more details on location and edifices sampled.

#### **4.2.1 Basal Pillow Samples for Eruption Ages**

Basalt pillow lobes from the base of a subglacial volcano are produced during the tuya's initial eruptive stage (see 2.3 Volcano-Ice Interactions). Sampling the basalt pillow lobes for U-Th/He dating involved manually excavating the pillow lavas at the base of the tuya to a minimum sampling depth of 50 cm below the surface (the stopping distance of high energy neutrons in basalt is 50 - 60 cm in basalt; see 3.2.4 High Energy Neutrons and 3.2.11 Production Mechanisms of  ${}^3\text{He}$  in Surface Rocks: Spallation). The samples collected from this depth, containing visible olivine phenocrysts, were considered to be sufficiently shielded from cosmic rays for the samples to contain negligible levels of cosmogenic He isotopes.

Some initial sampling of near-surface samples proven to be problematic and required re-sampling of certain earlier acquired samples. Particularly, any initial eruption age samples taken from a scree slope or taken in proximity of surficial lava layers needed to be re-sampled. These initial samples, when analysed, showed a high cosmogenic  ${}^3\text{He}$  contribution (see Table 4.1). The high cosmogenic contribution seen in these initially acquired near-surface samples could not be from over crushing, as care was taken to prevent this (see Sample Crushing).

The  ${}^3\text{He}/{}^4\text{He}$  of 533 and 115  $\text{R}_\text{a}$  found after crushing (indicating the initial  ${}^3\text{He}/{}^4\text{He}$  at the time of the olivine closure) are considerably higher than values typical for the trapped mantle component of Icelandic basalts, which is between 4 and 24  $\text{R}_\text{A}$  (Condomines et al., 1983; Kurz et al., 1985; Hilton et al., 1990; Burnard et al., 1994; Dixon et al., 2000; Dixon et al., 2003; Licciardi et al., 2007; Füri et al., 2010; Weston, 2013). Further samples were collected from a greater depth from *in-situ* outcrops and did not show the same high cosmogenic He contribution.

Table Mountain	Sample Location	Coordinates (dd°mm.mmm')		${}^3\text{He}$ (cc $\times 10^{-13}$ )	${}^4\text{He}$ (cc $\times 10^{-9}$ )	R/R <sub>a</sub>
		Lat	Long			
Ingolfsfjall	Scree slope surface	63°59.108'	20°59.257'	4.94	1.97	533
Blafjöll	Scree slope surface (ski slope)	63°58.578'	21°38.607'	4.49	8.25	115
Raudafell	20 cm below surface of meltwater channel	64°19.841'	20°35.596'	0.098	2.23	9.3
Kalfstindar	Meltwater channel excavated very deep into basal side	64°13.107'	20°53.196'	0.509	5.50	19.6

**Table 4.1:** Helium concentrations and isotope ratios demonstrating the importance of collecting well-shielded samples for U-Th/He dating.  ${}^3\text{He}/{}^4\text{He}$  ratios (R) were normalized to the atmospheric ratio ( $1.39 \times 10^{-6}$ ; R<sub>a</sub>) and blank corrected. Typically these values range from 2-40 (Weston et al 2012) in Icelandic basalts and so the values calculated for Ingolfsfjall and Blafjöll are considerably high. These are assumed to have a cosmogenic contribution and were re-sampled. The samples were all crushed in the same manner, *in vacuo* for 300 beats in 5 minutes.

In order to reduce the risk of a cosmogenic contribution, the remainder of the samples were collected at an ideal depth of 1 m. In some cases this depth was not possible to achieve and so a depth of 50 cm from the surface was considered to be a reasonable minimum.

The high energy neutrons that produce  ${}^3\text{He}$  through spallation have an attenuation length of 150-180 g cm<sup>-2</sup> (Kurz, 1986; Gosse and Phillips, 2001), which corresponds to a stopping distance of 51-62 cm when assuming a basalt density of 2.9 g cm<sup>-3</sup> (Lal, 1988). Or 2 - 19% of the equivalent surface cosmogenic  ${}^3\text{He}$  production depending on the attenuation length at that sample's location.

To reach these depths, a sledgehammer and pry bar were used to excavate the surficial layers of lava. Relatively young meltwater gullies (see Fig 4.2) and scars (created by erosion from melting ice, snow and jökulhlaups) in the flanks of the tuyas presented opportunities to sample pillow lobes already deep below the initial surface (e.g. Gaesafjöll, Ðórólfssfell; Fig 4.2). The meltwater gullies provided extra shielding from cosmic rays as the samples were taken from 50 cm depth below the gully surface and was shielded further by itself from the sides of the gully and so were assumed to be highly shielded from cosmic rays. Care was taken to sample lava lobes that were *in-situ* with bedrock and were ensured to be highly shielded from cosmic rays in all directions.

Hyaloclastites were sampled at several volcanic edifices to compare the olivines found in these rocks with those found in the pillow lobes (see 2.3 Volcano-Ice Interactions). Hyaloclastite is relatively unconsolidated and therefore has the

potential advantage of readily providing olivine phenocrysts with reduced sample preparation time. It was found however, that the olivines in the hyaloclastite were hydrothermally altered and heavily fragmented and therefore not suitable for He isotope analysis.

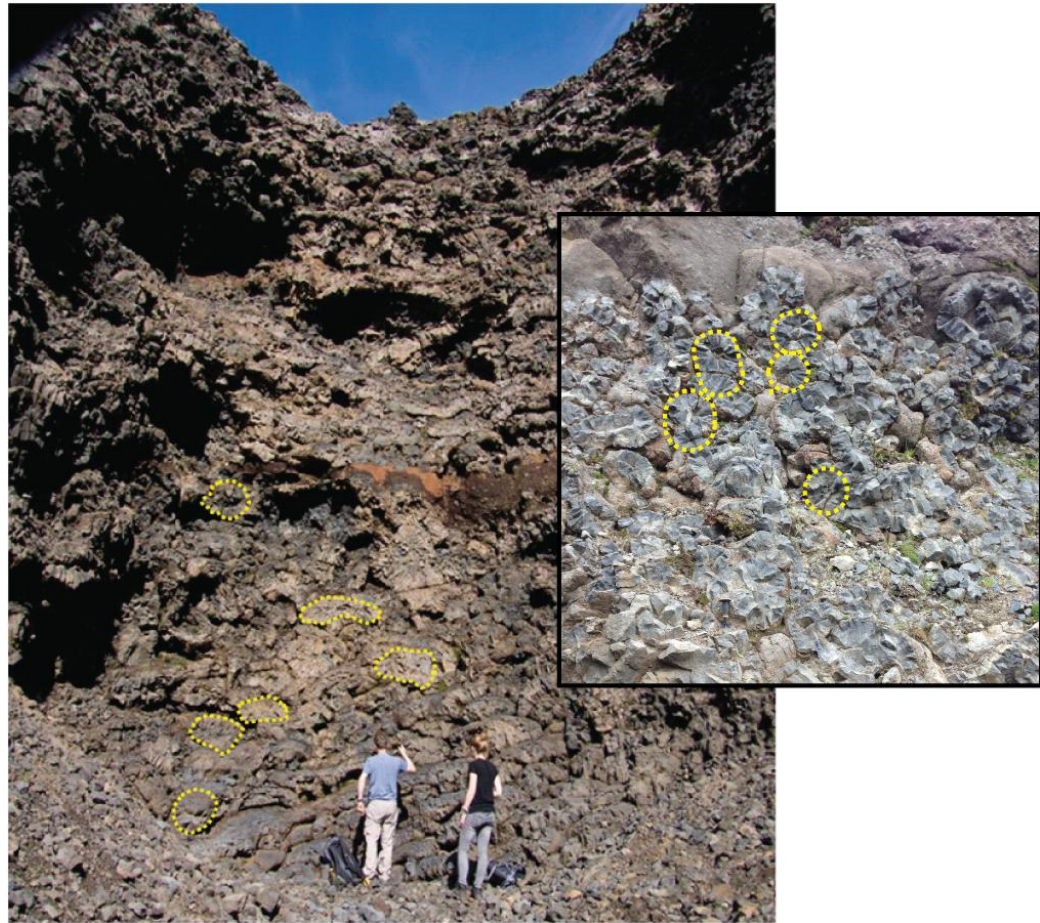


**Figure 4.2:** In a meltwater channel at Dórlófsfell collecting a well-shielded olivine rich sample. Dashed yellow lines illustrate examples of basaltic pillows found at the base of the subglacial volcanoes. The inset picture shows a closer image of basaltic pillows.

#### 4.2.2 *Capping Lava Samples for Cosmic-Ray Exposure Dating*

The samples taken from the summit were comprised of basalt capping lavas. These capping lavas have received the most exposure to cosmic rays. The presence of subaerial lavas indicate the eruption broke through an overlying ice sheet. The duration of subaerial exposure can be determined from the volume of cosmogenic  $^{3}\text{He}$  trapped in the matrix of olivine phenocrysts.

Relatively unmodified pahoehoe surfaces with ropy features were sampled. Where possible, olivine-rich lavas were targeted from high-standing areas to minimize any effects from burial by snow. Summits that showed the least amount of

shielding by their surrounding environment were sampled (see 3.2.10 and 3.2.11 shielding factors). Once a sample was collected, any shielding was noted using an inclinometer, but generally was deemed to be negligible. Sample localities that were shielded by edges, bluffs and cliffs were avoided to ensure  $2\pi$  ( $180^\circ$ ) exposure. The capping lavas were sampled at the highest stratigraphic level possible, at an altitude higher than the tuya's observed passage zone (where the subaerial capping lavas have flown into a interglacial melt-water lake surrounding the edifice (see 2.3 Volcano-Ice interactions). This ensured that the final eruptive stage was sampled.

The latitude, longitude and altitude of each sample locale were also recorded to determine  $^3\text{He}$  production rates at each location.

Of the tuyas visited, only one was deemed suitable for surface exposure analysis in the NVZ, on the summit of Gaesafjoll (NNE of Lake Myvatn). Intact and preserved pahoehoe ropes were found on the south side and close to the central crater, which contained small visible olivines (See Appendix B for images).

Other table mountains in the NVZ were not suitable to acquire an ideal surface exposure sample, or it was not possible to sample at the time of field-work. For the latter, a contributing factor was low cloud cover, which restricted the visibility to find suitable sample locations at the summits. The low clouds also created a hazardous field-work environment as most pathways to the summits were steep.

Sampling points were targeted with minimal erosion and evidence of remaining primary flow features, or surface category 2 (see section 7.2.3) as set out by Eason et al. (2015) to reduce problems with the burial of past snow and ice (Licciardi et al 2007). Therefore, samples were collected in areas where snow and ash cover were least likely to accumulate and only on well-preserved pahoehoe ropes, which indicated the original flow morphology. In the WVZ, where multiple tuya summits were sampled, a specific tuya (Bláfell) with visible erosion was targeted to compare with the tuyas that exhibited minimal erosion (see table 4.2).

An additional problem whilst acquiring summit samples proved to be moss cover on a majority of the lower lying summits. Moss cover made it difficult to determine the presence of olivine and find a completely exposed section suitable for cosmogenic dating. Thus the majority of samples collected were basal pillow lobes for U-Th/He dating, as the nature of exposures were optimal for this type of sampling.

Sample # (KS)	Volcanic Edifice	Exposure Sample	Eruption Sample <sup>a</sup>	Coordinates (dd°mm.mmm'')		Base Elev. (m)	Summit Elev. (m)	Sample Altitude (m)	Notes and Facies/Outcrop type
				Latitude	Longitude				
<b>WVZ</b>									
7	Geitafell		✓	63°56.886'	21°30.788'	180	500	274	Isolated tuya in the middle of a postglacial lava field. Pillow lava
21	Lambafell		✓	64°00.586'	21°27.775'	263	532	279	Tuya with fairly eroded summit and quarry at the base.
25	Kalfstindar		✓	64°13.107'	20°53.196'	195	615	228	Tindar amongst postglacial lava field with melt-water channel
32	Ðorolfsfell		✓	64°26.910'	20°31.005'	521	711	533	Small eroded tuya NE of Hlöðufell
41	Ok		✓	64°33.446'	20°51.382'	637	1181	669	Interglacial shield volcano, W of Langjökull. Shielded meltwater channel sampled
46	Kalfstindar		✓	64°15.228'	20°53.978'	718	522	539	A tindar different to Kalfstindar of KS25, E of Hrafnabjörg
77	Hrutfell		✓	64°44.718'	19°41.051'	1361	614	710	Large tuya E of Langjökull with small ice cap.
79	Hrutfell		✓	64°44.655'	19°40.554'	1631	614	635	79 is a xenolith found with the debris flow fan of scree
83	Rauðafell		✓	64°19.841'	20°35.596'	466	906	545	Tuya in N Laugarvatn region with meltwater gullie
86B	Ingolfsfjall		✓	63°57.680'	21°03.230'	43	540	44	Largest tuya in this region (Selfoss) with large quarry
87	Blafjöll		✓	63°58.565'	21°38.625'	510	604	573	Ski slope cut into the tuya
88A	Hlöðufell		✓	64°24.074'	20°32.895'	465	1157	515	Large tuya in N Laugarvatn region with large SSW meltwater
88B	Hlöðufell		✓	64°24.074'	20°32.895'	465	1157	515	channel. 88B taken from a greater depth than 88A on same outcrop
97	Hlöðufell	✓		64°25.078'	20°32.051'	465	1157	1163	Tuya summit sample obtained original pahoehoe flow
91	Bláfell	✓		64°29.186'	19°51.715'	584	1165	1163	Large tuya estimated from an earlier glacial cycle
94	Bláfell		✓	64°29.569'	19°54.618'	584	1165	573	Summit is covered in huge cracks and boulders indicating past ice cover and erosion. 91: Top of in-situ boulder lacking pahoehoe.
95B	Hvalfell		✓	64°22.976'	21°15.870'	89	815	91	94: meltwater stream gullie excised fresh pillows near base Tuya furthest W from rift zone, close to W coast, excised behind waterfall

NVZ								
63	Sellandafjall	✓	65°25.836'	17°01.965'	425	943	562	Moss covered eroded tuya with large meltwater channel on NE
64	Blafjall	✓	65°28.351'	16°53.943'	439	1197	419	Large tuya, sample taken from massive boulder recently fallen with <i>in situ</i> basalt
98	Herðubreiðartögl	✓	65°06.974'	16°19.884'	562	957	575	Small tindar S of Herðubreið
101	Herðubreið	✓	65°10.477'	16°23.135'	523	1660	783	Large iconic tuya. 101A taken from a greater depth than 101B
102	Hrafnafell	✓	66°03.266'	16°20.749'	165	521	471	Furthest north sampled tuya, fairly moss covered with shielded overhang of <i>in situ</i> basalt.
104B	Gaesafjöll	✓	65°45.935'	16°53.755'	411	869	803	Large tuya close to Myvatn with large meltwater gullie on SW
106	Gaesafjöll	✓	65°45.330'	16°55.226'	411	869	523	Summit retained pahoehoe flow.

**Table 4.2:** Details of sampling locations, where samples were taken, at what altitude and further information on edifice.

<sup>a</sup> All eruption samples collected were pillow basalts

See Appendix B for further images on sampling locations on tuyas where both exposure age samples and eruption age samples were taken. These images provide a better sense of the locales of samples taken for eruption ages. Only three samples were taken for cosmogenic exposure dating and these are shown in images in Appendix B.

### 4.3 Sample Preparation

The olivine phenocrysts within the basalt were separated from the surrounding matrix of basalt. The surrounding matrix may have a different helium concentration compared to the olivine phenocryst and would therefore impact the isotope measurements. Any adhered groundmass analysed with the olivines would produce an incorrectly high He age as the contiguous basalt usually has a higher concentration of U and Th than the olivine phenocryst (Aciego et al, 2007).

Samples taken for surface exposure dating were cut to contain only basalt from the uppermost 3 cm ofropy pahoehoe subaerial lava.

For olivine extraction, the bulk sample was initially cut into ~ 3 cm sized blocks, enabling the pieces to fit into a disc mill crusher and crushed into mm-sized fragments. This was then sieved into three fractions using 710 and 420  $\mu\text{m}$  sieves to remove dust and larger, uncrushed pieces of lava, which required further slight crushing to liberate the whole olivine phenocrysts. The mid-sized fraction was handpicked under a binocular microscope to ensure whole olivine phenocrysts were chosen for analysis. The use of whole phenocrysts allows an equilibrium of alpha-ejection and implantation between the phenocryst and the surrounding basalt to be more probable (Farley 1996).

A gram of handpicked olivines, per sample, was required for analysis. The abundances of trapped  $^3\text{He}$  (magmatic helium trapped in inclusions) and U and Th concentrations, which decay to produce the daughter nuclide  $^4\text{He}$  (alpha particle), are very low and so a gram, or as close to as possible, is required for analysis. Each gram of sample was cleaned in an ultrasonic bath, first in deionised water for twenty minutes and then in acetone for five minutes. This was done to remove any adhering fine basalt material from the surfaces of the olivine grains. The olivine phenocrysts

were checked a final time under the microscope to confirm that all traces of adhering basalt matrix had been removed.

The olivines were dried under a heat lamp, before being loaded into the crushing system. The loaded samples were baked at 190°C ( $\pm 10^\circ\text{C}$ ) for 24 hours and allowed to cool, before being analysed. This baking procedure helped to liberate any adsorbed air contamination from sample surfaces and the crusher walls to be released and pumped away. Whilst being baked and allowed to cool, the samples loaded in the crushers and extraction line were pumped down, until an ultra high vacuum (UHV) was reached ( $1 \times 10^{-9}$  mbar).

See Appendix B for images of the various stages of sample preparation and picked olivines ready for noble gas analyses.

# Chapter Five: Experimental Methods

This research used three mass spectrometers: an Isotopx VG5400, Thermo Fischer Helix-MC, both used to analyse helium and argon isotopes, and a Thermo Fischer Neptune Multi Collector - Inductively Coupled Plasma - Mass Spectrometer, used to analyse the isotopes of uranium and thorium. This section focuses on their design and their methods of analysis.

## 5.1 Theoretical Basis of Mass Spectrometry

Noble gas mass spectrometers ionise and then magnetically separate different isotopes, as a function of their mass prior to detection. Noble gases are ionised in an electron impact ion source, where they are electrically accelerated and mass separated using an electromagnet, prior to detection of the ion current intensities using detectors.

The ability to receive these ionised isotopes is relative to the magnetic field and depends on the mass of each ion. This mass difference allows the separation of the individual isotopes. This relationship can be expressed as:

$$E = eV = \frac{1}{2}mv^2 \quad \text{Equation 19}$$

Where E is the ion's kinetic energy, eV is the charge of the particle (e) at a voltage potential (V), m is the ion's mass and v its velocity. Therefore ions with the equivalent charge (e) will have identical kinetic energies (E) during acceleration by a potential voltage (V). This is the main premise behind all mass spectrometers.

### 5.1.1 Ionisation

The initial step during noble gas analysis is to ionise the gas. The electron impact source is composed of a thermionic emission metal filament that emits an electron beam during the application of a current. The electron beam crosses paths with the inlet gas by utilizing a potential voltage difference on the trap electrode.

The electrons impact the noble gas atoms with sufficient energy to eject an electron, producing positive ions. To increase the chances of ionisation certain ion sources increase the path length that the electrons must travel across from the source. The ionising path length of the electron beam is increased using a weak magnetic field produced by two, externally mounted permanent magnets. Any electrons emitted from atoms are forced to travel in a spiral pattern, which greatly increases

the likelihood of electron-atom interaction to produce positively charged ions. The ions produced are "pushed" away from the source area by a repeller plate that possesses a small positive charge. The positive ions are given the same kinetic energy by accelerating them with a potential difference of several kV.

### 5.1.2 Mass Analyzer

Once the sample gas has been ionised, the following step separates the positive ions according to their mass to charge ratio ( $m/e$ ), which is accomplished by using a magnetic sector on a noble gas mass spectrometer.

Mass spectrometers, with magnetic sectors, consist of an arc flight tube that is surrounded by a magnetic field. The accelerated ions travel through the flight tube and the radius ( $r$ ) of the ion's path is dependent on the strength of the magnetic field ( $B$ ):

$$r = \frac{mv}{eB} \quad \text{Equation 20}$$

The positive ion's velocity can also change the radius of its path. It is possible to express the radius in relation to magnet field, mass and velocity by substituting the term of velocity (from equation 20) into equation 21.

$$r = \frac{m}{eB} \left( \frac{2eV}{m} \right)^{\frac{1}{2}} \quad \text{Equation 21}$$

This shows that holding the voltage and magnetic field at constant values indicates the radius of the ion path will be proportional to the square root of the charge to mass ratio ( $eV/m$ ). The radius of the flight tube itself and the accelerating voltages are kept constant. Therefore it is possible to change the radius of the ion flight path by only altering the magnetic field. This variation in magnetic field allows the ions of a specific mass (specifically charge/mass ratios) to be directed through the flight tube and into a detector.

### 5.1.3 Detectors

The detectors on a noble gas mass spectrometer need to be able to measure the intensity of the positive ion beam directed into them from the flight tube. The most common detector, which is used for high abundance ion beams, is the Faraday Cup. The Faraday Cup is comprised of a metal cup designed to measure the intensity of a beam of ions. The incident ion beam generates a current across a high gain resistor

(usually  $10^{11} \Omega$ ), which determines the current of the ion beam by measuring the voltage drop across the resistor.

Low abundance isotopes such as  ${}^3\text{He}$  will produce less intense ion beams,. In these cases, an electron multiplier is used. The electron multiplier (Fig 5.1) is comprised of a series of metal plates called dynodes, and when hit by an ion produces an emission of secondary electrons from atoms in the surface of the dynode. The dynodes are held at a negative potential (Fig 5.1), with each metal plate increasing in negativity towards the collector end. Once an ion hits the first dynode releasing secondary electrons, these secondary electrons are pulled into the next plate where the process repeats. Each electron that collides with a metal plate emits, on average, another two electrons. Therefore a very small beam of ions can create, via a cascade effect, enough electrons to be detected (Fig 5.1). Electron multipliers are usually operated in two modes: pulse or analogue. Pulsed mode operates at a higher gain, which enables a measurable pulse to be produced for each ion that arrives. The ion pulses are measured for a fixed period of time. This technique is mostly used for isotopes that are less abundant, especially for those with a one mass unit separation from a more abundant isotope ( ${}^3\text{He}$  from  ${}^4\text{He}$ ). The analogue mode is useful for higher count rates. The multiplier voltage is reduced and each ion arrival is not directly counted. Instead the electron multiplier uses an analogue amplifier. Multipliers typically have gains of  $10^6$ .

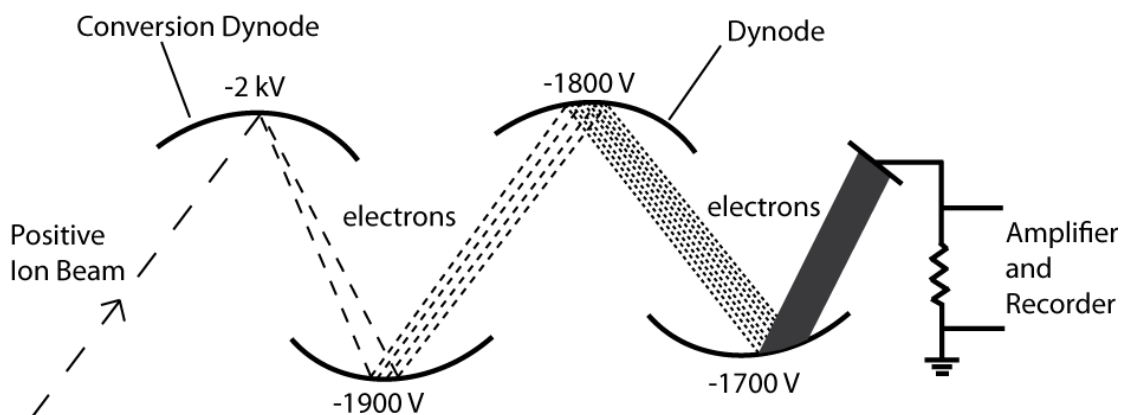


**Figure 5.1:** Illustration showing how an electron multiplier works with dynode plates.

## Noble Gas Analysis

Mass Spectrometer	Magnetic Sector	Radius	Ion Source	Filament	Detectors	Resolution
VG5400	90°	57 cm	Nier type electron impact	1 mm 4 turn Tungsten coil	Faraday cup and Burle Channeltron electron multiplier	~500
Helix-MC	120°	35 cm	Electron impact with octopole and flatapole	1 mm 4 turn Tungsten coil	5 Faraday and electron multiplier cups	1500

**Table 5.1:** Different components that make up both noble gas mass spectrometers used in this study

### 5.2 VG5400 Noble Gas Mass Spectrometer

Isotopic analyses of He and Ar were carried out using an upgraded VG5400 noble gas mass spectrometer. The VG5400 has a 90° magnetic sector with a 57 cm radius. The spectrometer was run in static mode (not pumped dynamically during measurements). The VG5400 is attached to an extraction line and is kept under UHV via two Varian® ion pumps that sit at the ion source and collector ends of the spectrometer. These pumps maintain an UHV of  $<1 \times 10^{-9}$  torr, within the spectrometer and extraction line. The ion source is a Nier-type electron impact source constructed of a 1 mm diameter, four-turn tungsten coil filament. There were two detectors on the spectrometer; a Faraday cup and a Burle Channeltron electron multiplier. A Daly knob is set at a negative voltage to steer the beam of ions into the electron multiplier.

GV ISOWORKS software allows the source and detector parameters to be tuned to achieve maximum sensitivity and optimum peak shape. The parameters tuned were the ion detector, trap and y-axis (a half-plate voltage used to steer the ion beam in the y-dimension) for both helium and argon and on both detectors. These parameters varied from one noble gas to the other and were optimised using an aliquot (0.2 cc shot of laboratory air and/or laboratory air with He spike) from the calibration bottle. Isobaric interferences, such as HD from  $^3\text{He}$ , could be resolved due to the spectrometer exhibiting a mass resolution of ~500 (Fig 5.2). The mass resolution is the higher mass required to be separated (HD: 3.022 amu) divided by the delta mass or difference in both masses separated (HD -  $^3\text{He}$  = 0.006), which

gives a mass resolution of 503.67. The mass values were taken from the centre of each peak. A blank spectrum (residual gas remaining in the line after pumping) was examined regularly to assess any significant increase in interference peaks. An SAES® NP10 getter was located on the spectrometer's source, which reduced active gases (water, hydrogen, carbon dioxide etc) in the spectrometer volume. Data collection was carried out by the ISOWORKS software (see 5.2.4 Isotopic Analysis).

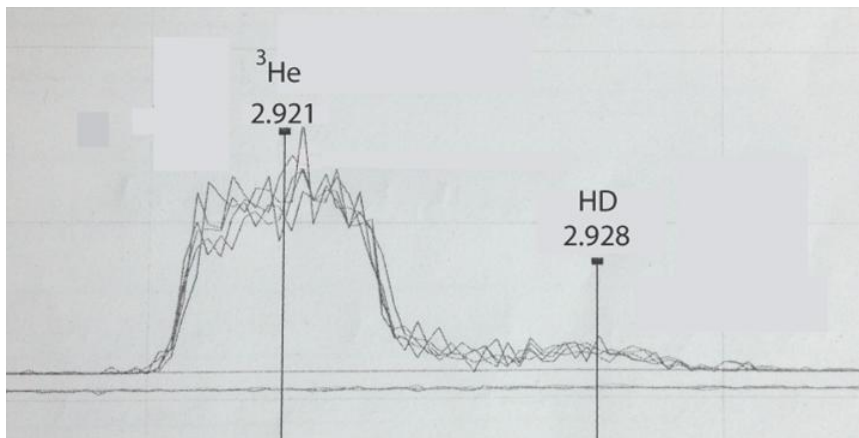


**Figure 5.2:** Mass scan showing the degree of resolution between HD and  ${}^3\text{He}$  on the VG5400,  ${}^3\text{H}$  cannot be resolved.

### 5.2.1 Trapped Helium Analysis (Sample Crushing)

The olivine samples were crushed to release gases contained within inclusions to obtain the magmatic (or trapped)  ${}^3\text{He}/{}^4\text{He}$ . If over-crushed and/or over-heated during crushing, matrix-sited gas such as cosmogenic  ${}^3\text{He}$  and radiogenic  ${}^4\text{He}$  can also be released (Hilton et al 1993, Hilton et al 1999, Blard et al 2006). Originally the samples were crushed 300 times/beats in 5 minutes (Moreira and Madureira 2005, Aciego et al 2007), but this was decreased to 50 times in 5 minutes, after further discussion with Prof. Burgess and others with olivine crushing experience, to ensure no matrix gases were liberated from the olivines (Graham et al 1998, Hilton et al 1993 and Stuart et al 1994).

Noble gases released by crushing of olivine separates were analysed by both the VG5400 and the Helix MC Plus noble gas mass spectrometers. The same crushing procedure was used for both spectrometers.

	300 Crushes			50 Crushes	
Sample Name	>100µm	<100 µm	Sample Name	>100µm	<100 µm
KS25	93.11%	6.89%	KS94	92.30%	7.70%
KS55	93.35%	6.65%	KS95B	87.33%	12.67%
KS64	93.72%	6.28%	KS88A	83.23%	16.77%
KS82	91.34%	8.66%	KS88B	94.10%	5.90%
KS83	94.10%	5.90%	KS86B	92.44%	7.56%

**Table 5.2:** Percentages of fractions over and below 100 µm for various samples with different amounts of crushes

### *Crushing System*

Cylindrical steel tubes, designed for the purpose of crushing (Sumino et al 2001) are attached to the extraction line (Fig 5.3). The cleaned olivine phenocrysts are loaded into separate steel tubes, with a nickel piston inside, carefully resting on top of the sample. Once the steel tube is attached, the tubes are pumped and then baked for 24 hours to remove adhered atmospheric gases. Crushing is not commenced until the crushing tubes are at a pressure of  $\sim 10^{-9}$  mbar and a stable blank is achieved (see 5.4 Line Blanks and Air Calibrations). In order to crush samples, the nickel piston is lifted and released down onto the sample by an electromagnetic field generated by a solenoid, whilst isolated from the ion pumps.

Following crushing the gases released through crushing were purified and separated as described in section 5.2.3.

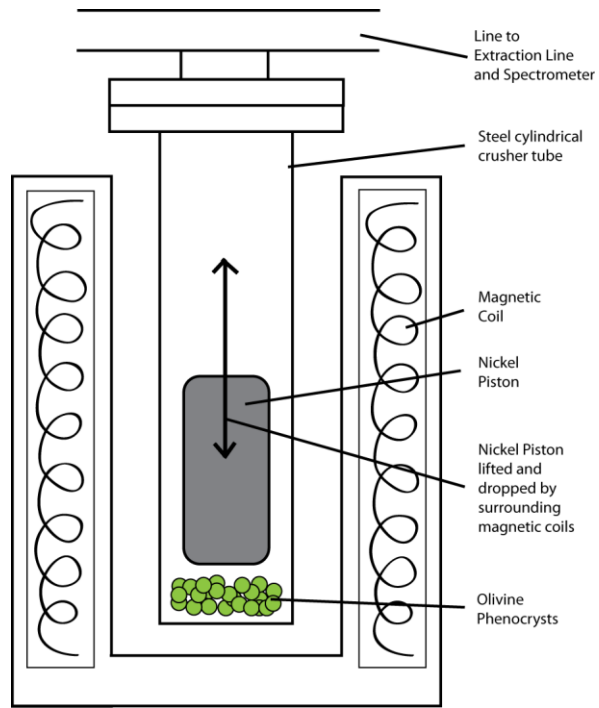


**Figure 5.3:** Schematic of solenoid crushers containing an olivine sample connected to VG5400 extraction line (not to scale)

### 5.2.2 VG5400 Extraction Line

To analyse the helium, a noble gas extraction and purification line is attached to the VG5400. The extraction line (Fig 5.4) is constructed from stainless steel tubing connected by Nupro® 0.5 inch bellow-sealed valves. This line is maintained at UHV ( $<1 \times 10^{-9}$  mbar) via a Varian® 40 litre ion pump. To achieve UHV, a turbomolecular pump and two-stage rotary pump are connected to the extraction line to evacuate atmosphere after loading samples or following maintenance. The extraction line is used to purify and separate each noble gas after crushing, prior to analysis. First any active gases are removed using two Zr-Al alloy getters: one hot SAES® NP10 getter at  $\sim 200^\circ\text{C}$  and a SAES® NP10 getter at room temperature. The room temperature getter is more efficient at removing hydrogen. To separate the noble gases, a charcoal finger is cooled with liquid nitrogen for 10 minutes, which traps the heavy noble gases (Ar, Kr, Xe), but not the light noble gases (He and Ne). A liquid He cryogenic trap is also attached to the extraction line. The cryogenic trap separates He from Ne at 57K ( $-216^\circ\text{C}$ ) but as Ne was not analysed, this was not used. See Sample Analysis for the full method on noble gas purification and separation.

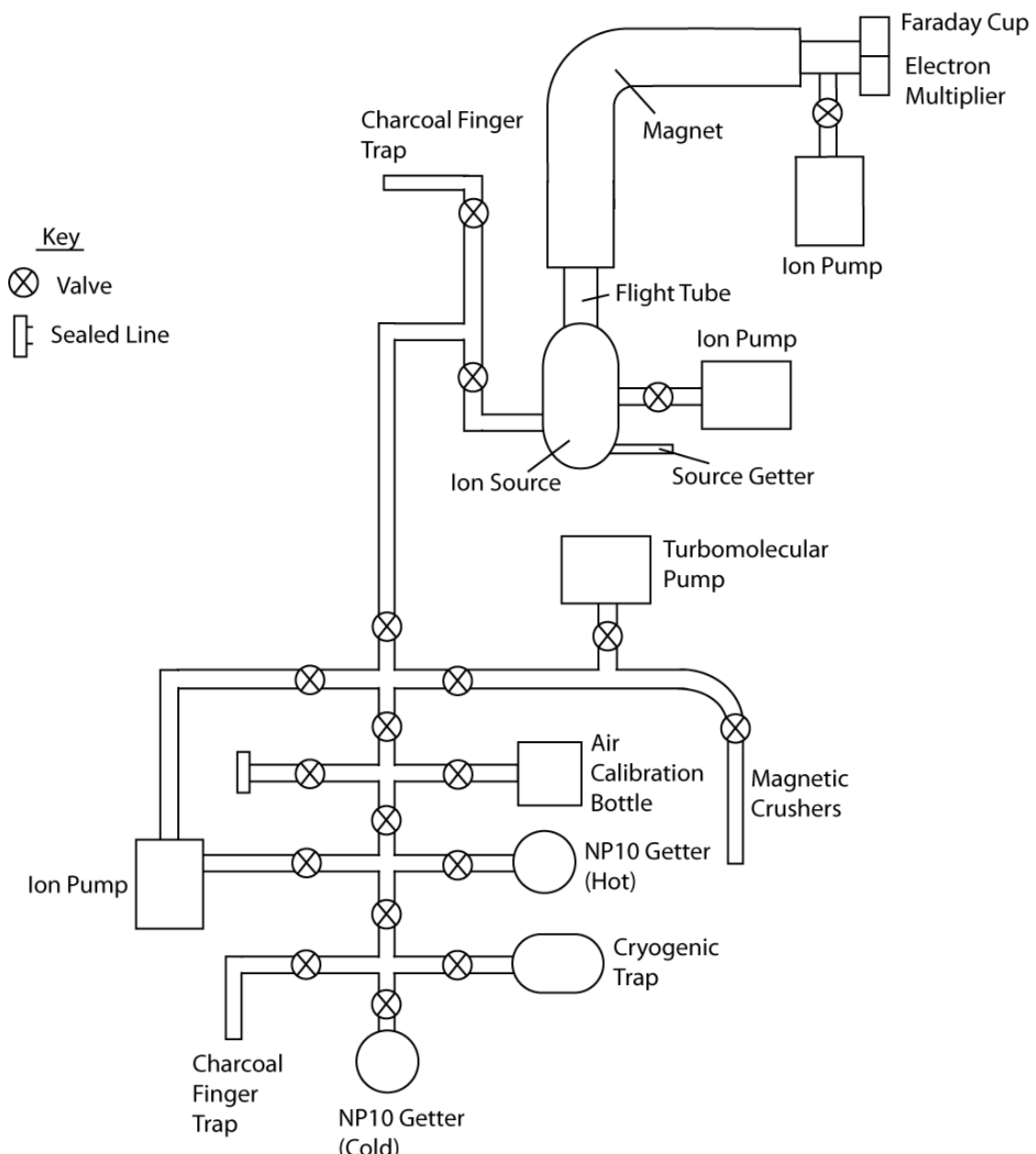


**Figure 5.4:** Schematic of extraction line attached to the VG5400 mass spectrometer (not to scale)

Two calibration bottles are attached to the line that enables the mass spectrometer's sensitivity and mass discrimination to be monitored. One bottle is filled and sealed with laboratory air at low pressure, and the other is also filled and sealed with laboratory air with the addition of a spike of He. The He spiked bottle has a known volume of  $1000 \text{ cm}^3$  and was filled at 0.17 torr with a  ${}^3\text{He}/{}^4\text{He}$  ratio of  $448R_A$ . The  ${}^3\text{He}/{}^4\text{He}$  ratios and concentrations have been calibrated to the atmospheric  ${}^3\text{He}/{}^4\text{He}$  ratio ( $1.399 \times 10^{-6}$ ) using a 0.2cc aliquot of laboratory air (see 5.4 Line Blanks and Air Calibrations). The concentration and isotopic ratios of Ar

were calibrated using the bottle of laboratory air (known volume of 869.37 cm<sup>3</sup>) filled at 0.01106 torr.

### 5.2.3 Purification and Separation of Noble Gases

The gases released during crushing of olivine grains were purified on two SAES® NP10 getters: one at ~200°C and another at room temperature for 15 minutes, which reduced the presence of active gases. The gases were then exposed to a charcoal finger, cooled with liquid nitrogen, to trap the heavy noble gases (Ar, Kr and Xe). The heavy noble gases were exposed to the cold finger for 10 minutes and then isolated from the rest of the extraction line. The lighter noble gases were then expanded into the VG5400 mass spectrometer, with only He being analysed. The content of <sup>20</sup>Ne was analysed alongside <sup>3</sup>He and <sup>4</sup>He, as analysing <sup>20</sup>Ne allows for an air correction to be carried out on the He measurements. Also, high levels of both <sup>20</sup>Ne and <sup>4</sup>He could indicate that a leak had developed throughout the crushing process. A second liquid-nitrogen cooled charcoal finger was located close to the mass spectrometer source to maintain a low background of Ar during helium isotope determinations. <sup>3</sup>He was measured using a Burle Channeltron electron multiplier, and <sup>4</sup>He was measured using the Faraday cup. During He analysis in the spectrometer, the extraction line was isolated and pumped to high vacuum for 10 minutes to remove any remaining background gases.

Following He analysis, the liquid-nitrogen was removed from the charcoal finger and it was heated to ~150°C to liberate the gases from the charcoal. All of the heavy noble gases were expanded into the spectrometer, however only Ar was analysed. The most abundant Ar isotopes, <sup>40</sup>Ar and <sup>36</sup>Ar were measured using the Faraday cup; whereas less abundant <sup>38</sup>Ar was measured on both the Burle Channeltron electron multiplier and the Faraday cup. Analysing <sup>38</sup>Ar on both detectors allowed the electron multiplier's sensitivity to be monitored.

The getters were degassed each week to release adsorbed gases throughout analyses. The NP10 getters were heated to ~750°C, for 15 minutes into the turbomolecular pump, and finally the ion pump overnight.

### 5.2.4 Isotopic Analysis

Isotopic measurements of the noble gases released into the VG5400 mass spectrometer were carried out using the GV ISOWORKs software. The software enabled multiple method files to be written in advance; one file for each noble gas. The method file determined which isotopes to measure, baseline offsets, detector settings and number of cycles/counting time required for each analysis. The tuning settings had to be adjusted and saved for each noble gas to ensure the highest measurement of sensitivity was achieved.

When the isotopic analysis procedure was started, the software recorded the time as *t-zero* and if enabled, peak-centring would start. When peak-centring was enabled, the software scans the magnetic field to determine the centre position of each peak. Peak-centring was initiated only for the Ar isotopes and not the He isotopes because of the low abundance of  ${}^3\text{He}$  found in olivines. HD having a mass (2.938 atomic mass units) so close to  ${}^3\text{He}$  (2.931 amu) would mean the peak-centring would have focused on HD, not  ${}^3\text{He}$ , as in most cases HD was more abundant. Consequently the HD peak was centred and the  ${}^3\text{He}$  was analysed at a fixed mass jump of -0.007 amu from HD. The  ${}^3\text{He}$  would be analysed at this mass regardless of peak shape. Throughout air calibrations, the mass of  ${}^3\text{He}$  would be monitored regularly to ensure the correct mass value was being detected and had not drifted significantly. Following the peak-centring, the background noise would be measured at an offset before and after (usually 0.3 mass units) each isotopic mass. These baselines would then be automatically subtracted from the peak heights measured by the software.

The software analyses of each noble gas were run in cycles, which were repeated seven times. Scans started from the lowest mass and peak jumped until finishing at the highest mass. When a large mass jump would occur, from the end of one cycle to the beginning of the next, the magnet would be allowed to settle for 20 seconds before the lowest mass was analysed again. The most abundant isotopes ( ${}^4\text{He}$  and  ${}^{40}\text{Ar}$ ) were measured for 20 seconds, whereas those with a low abundance ( ${}^3\text{He}$ ) were analysed for longer, generally 60 seconds.

After each cycle, the peak intensity would be recorded by the software (in counts per second) and results for seven cycles would be regressed to *t-zero*. This was necessary as the volume of gas to analyse would decrease with each cycle as the

gases were ionised by the source and implanted in the detectors. Regressing the data would then give a consistent set of values for all the peaks at a common point in time, *t-zero* (Fig 5.5). The values at *t-zero* formed the raw data that was then corrected for the collector sensitivity using the air calibrations to calculate the abundances of each isotope.

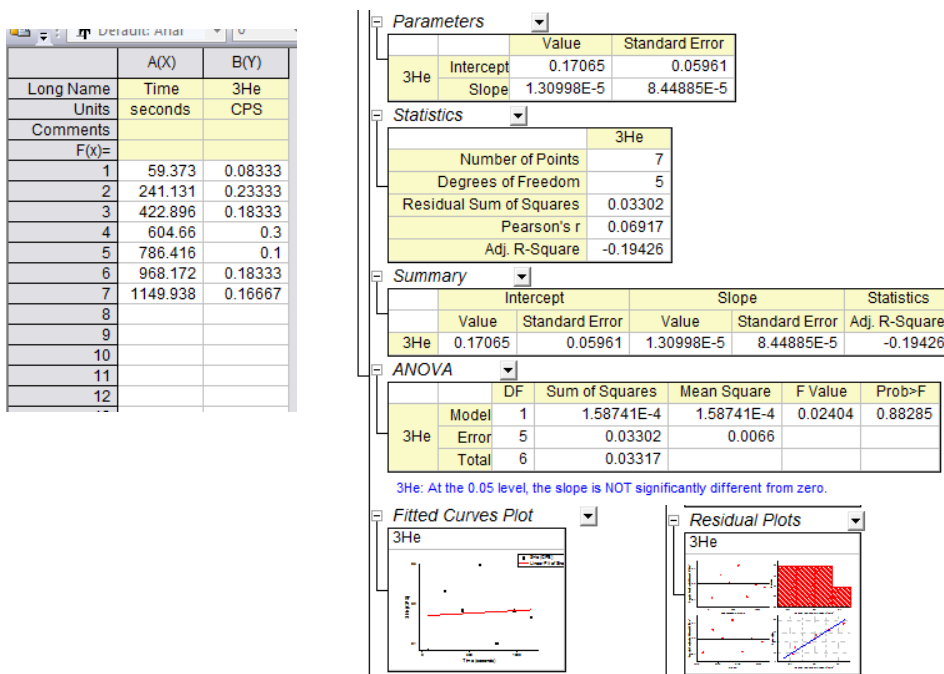


**Figure 5.5:** Regression analysis tool used in Origin to regress  ${}^3\text{He}$  data taken from VG5400. This shows the average CPS of  ${}^3\text{He}$  taken from the 60 points taken for each 5 consecutive runs

The ISOWORKs software uses basic linear regression to calculate the amount of gas at *t-zero*. To ensure the correct values were used, the regression was checked using the software ORIGIN. Both software packages produced consistent values for *t-zero*, and for the standard error at the y-intercept (*t-zero*) .

See Appendix A for error quantification process.

### 5.3 Helix MC Plus Noble Gas Mass Spectrometer

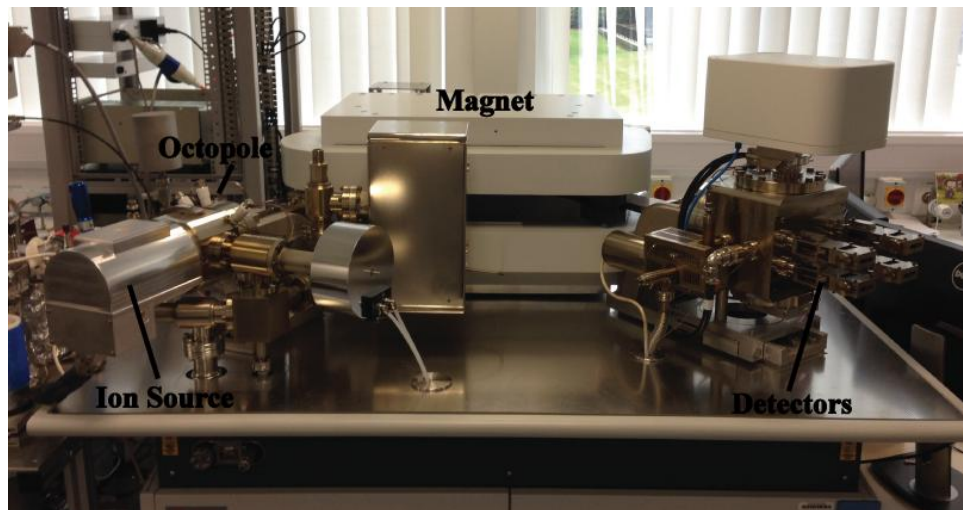


**Figure 5.6:** Annotated photo of Helix-MC Plus noble gas mass spectrometer showing the main components.

The Thermo Fischer Helix MC Plus (Fig 5.6) is a static mass spectrometer that uses an electron impact ion source, a sector field electromagnet and multiple Faraday cup and ion counters as detectors. Sample gas enters the ion source and the ions formed accelerated into the flight tube, which is surrounded by the magnet. The ions are detected using an array of spatially adjustable collectors.

The Helix mass spectrometer is kept under UHV via an Agilent VacIon Plus 40 litre StarCell™ ion pump. The ion pump is positioned close to the ion source and is controlled through by an automatic pneumatic VAT valve controlled through Thermo Qtegra software. These pumps maintain an UHV of  $<5 \times 10^{-9}$  mbar within the spectrometer. The Qtegra software allows the source and detector parameters to be tuned to achieve maximum sensitivity and optimum peak shape. These parameters varied between helium and argon and each was optimised using an aliquot from an air calibration bottle. An internal pyroxene He standard was used with a known  $R_A$  of 10 (Marty et al, 1998). The 35 cm magnetic sector has 120 degree extended geometry ion optics with a mass resolution of 1500. Such a high mass resolution enables isobaric interferences of HD from  $^3\text{He}$  to be fully resolved, including  $^3\text{H}$  (Fig. 5.7).

Data collection was carried out by the Qtegra software. See Appendix A1 for error quantification process.

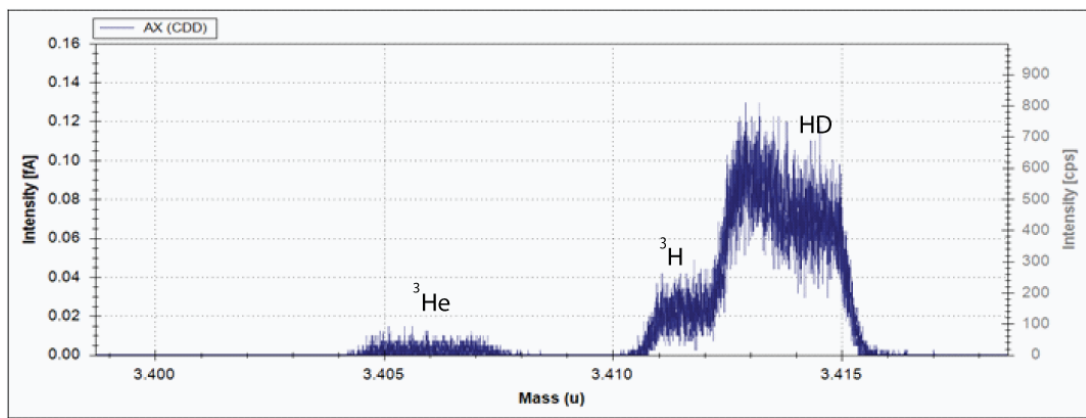


**Figure 5.7:** Mass scan illustrating the fully resolved  ${}^3\text{H}$  and HD peaks from  ${}^3\text{He}$

### ***Ion Source***

The ion source (10 kV) uses electron impact ionization and has a Zr-Al alloy getter, at room temperature, to remove any reactive gases (mainly hydrogen) and impurities from the sample gas, not purified in the extraction line, before they enter the ion source. Next to the ion source is an automatic, pneumatic valve that allows pumping of sample gas introduced into the spectrometer. An ion gauge is attached for monitoring of the pressure.

There is a lens system that sits directly behind the ion source. This consists of an octopole and a flatapole, which focus the ion beam and enhance its alignment. The octopole has eight rods that can be supplied with positive or negative potentials. This is located directly behind a variable entrance slit, the aperture of which can be changed depending on whether high sensitivity or high resolution is preferred. Three different slits are available of 0.25 mm, 0.1 mm or 0.05 mm. Extraction plates in the ion source focus the ion beam onto a deflection slit, which then is focused by another lens onto the variable entrance slit. The flatapole consists of flat plates and inside has two hollow plates that can be supplied with identical positive or negative potential. Other plates that are arranged above and below them are at ground potential. The flatapole affects the focal length of the ion beam.

The focussed ion beam is accelerated from the source at 10kV into the flight tube and magnetic field.

## Multicollector

The multicollector detects the ions by using either Faraday cups and/or multipliers (Charged Couple Device - CDD - multipliers). There are up to five combined Faraday multiplier packages, contained in five cup holders (Fig 5.8). Four of the cup holders, two either side of the central axial holder (H2, H1 and L2, L1), can be manually moved. The axial (central) cup is fixed. The cup position can be changed manually by using "wobble sticks" and the cup's position is dependent on which masses are to be analyzed. The "wobble sticks" are on the right side for the cup holders on the right of the axial (H1 and H2) and on the left side for the cup holders to the left of the axial (L1 and L2). The position of the cups can be monitored through readouts by the software Qtegra.

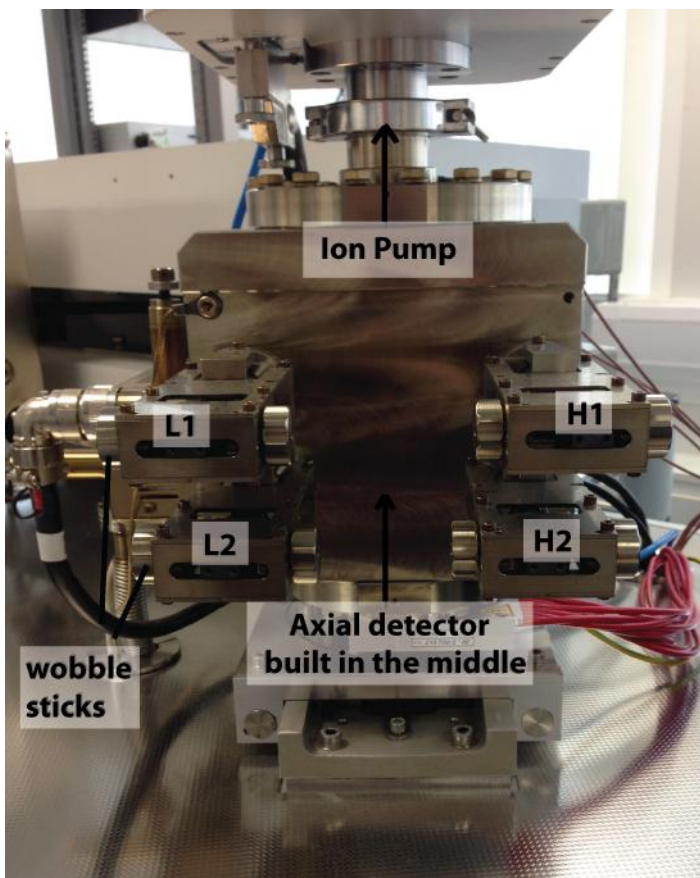


**Figure 5.8:** Annotated photo of the Helix MC Plus collector block. The five cups (L1, L2, axial, H2 and H1), wobble sticks to move the detector slits and ion pump are shown.

### 5.3.1 Radiogenic and Cosmogenic Helium Analysis (Sample Fusion)

A resistance furnace and loading system (designed and custom built by Mr D. Blagburn and Dr. P Harrop) permits *in vacuo* loading of up to ten crucibles containing crushed samples. The furnace is used to release radiogenic  ${}^4\text{He}$  and cosmogenic  ${}^3\text{He}$ . The resistance furnace was attached to the Helix MC Plus mass spectrometer for analysis of the extracted sample gases (see Purification and Separation of Noble Gases).

#### *Crucible Loading System*

The sieved, crushed olivine samples were loaded into molybdenum crucibles (Fig 5.9) that had specially designed screw-thread lids. These lids allow for the gases released from melting to escape from the crucible, whilst containing the sample inside. The lids are prevented from rotating off by special lid locks sitting on top of the crucible lid (Fig 5.9). Once loaded, the crucibles were lowered into the furnace using a hook-and-rod system. Up to ten crucibles can be loaded into a holding tray, with one remaining slot empty to enable a  $45^\circ$  angled mirror, which allows viewing down into the furnace tube itself. This sight line enables crucible extraction to be carried out with greater ease, as the hook needs to be rotated under the catch of the crucible lid for furnace insertion and extraction. This is carried out more easily when knowing the alignment of the crucible and hook, thanks to the mirror on the holding tray (Fig 5.10 and Fig 5.11).



**Figure 5.9:** Annotated pictures of molybdenum crucibles with screw top lid and platinum foil used to wrap crushed olivine sample

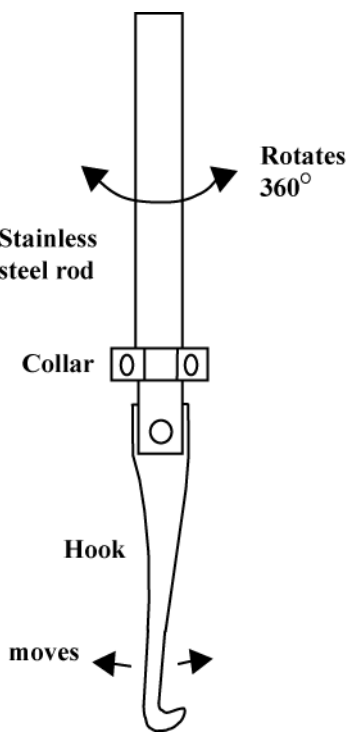


**Figure 5.10:** Hook system used to lower and retrieve crucibles from the furnace. The  $45^\circ$  angled mirror allows sight down into the furnace to see alignment of crucible lid so can move hook down alongside and under the lid. Not to scale.

The holding tray sits on two horizontal stainless steel rods that allows the tray to move back and forth laterally. This is necessary to permit the crucibles to be lowered into the furnace through a larger hole in the centre of the tray. The lateral movement is executed via a wobble stick, *in vacuo*, at the back of the loading system (Fig 5.11).

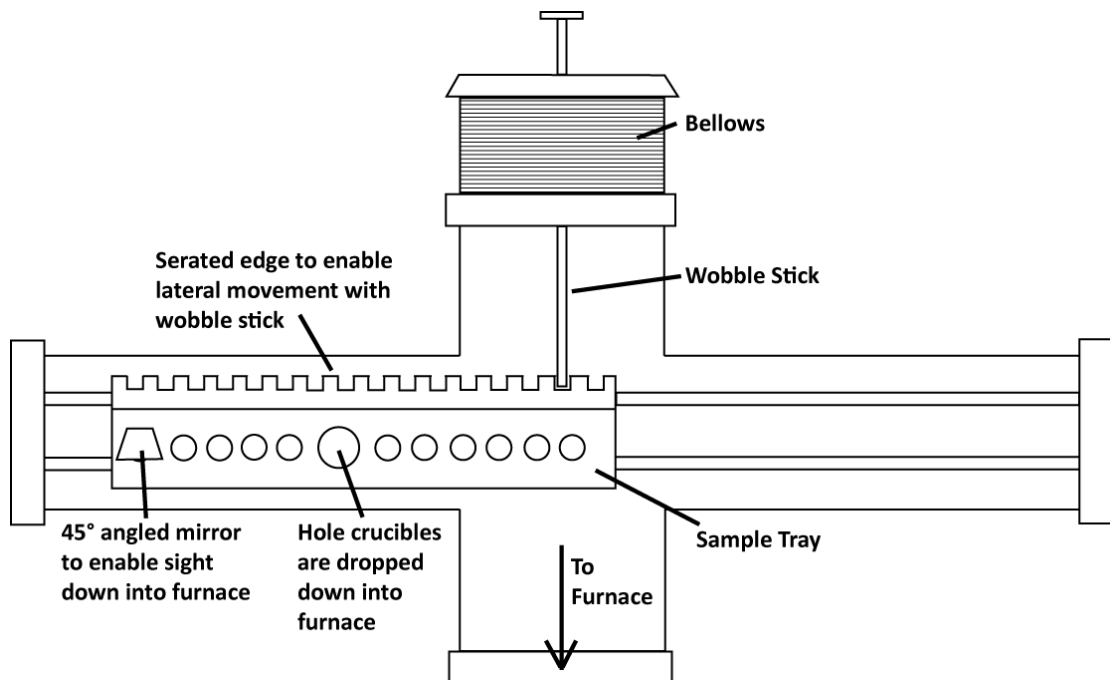


**Figure 5.11:** Furnace crucible and sample holder tray

The system used for loading the sample tray into the furnace is illustrated in Fig 5.11. The furnace itself is isolated from the loading bay via a gate valve, which prevents the furnace from being contaminated with air during sample loading (Fig 5.12). In addition, the gate valve ensures that any large volumes of gas or evaporates released from the samples during melting do not reach and contaminate the other samples in the loading bay. Below the gate valve and above the furnace, a moveable shutter prevents any evaporates from coating and compromising the gate valve's copper seal.

To lower the crucibles into the furnace, a stainless steel rod with a hook attached to the end extends vertically out of the vacuum system. The hooked rod (Fig 5.10) can move in and out of the furnace system and also rotate 360°. The rod meets the furnace loading bay through a pumped chamber. This 'O' ring-sealed, rotary-pumped chamber allows the hook system inside the loading system and furnace to be separate from the remaining, externally manipulated section of the rod. As the pumped chamber is sealed via an 'O' ring, a high vacuum is maintained throughout the furnace and loading bay whilst the hooked rod is repositioned. As the gate valve and shutter are opened, the hooked rod can pick up a crucible and then drop it down into the furnace through the larger central hole on the loading tray.

Following loading of samples into the tray, the furnace was gradually de-gassed in 30 minute manually controlled cycles running up to 1500°C. Controlled heating was not possible with the installed controller due to rapidly over shooting the set temperature. Therefore all heating and cooling was controlled manually and a temperature vs. time path is not available. The sample tray and holder were degassed to evacuate air adsorbed onto the surfaces of the tray, crucibles and samples at 200°C for 24 hours before analysis.

The furnace temperature was calibrated using an optical pyrometer. A thermal gradient existed between the furnace exterior and the external thermocouple. This was assessed by comparing measurements from the thermocouple and pyrometer. The difference in temperature between the pyrometer and thermocouple was found to be negligible. Temperatures referred to from henceforth will be the actual interior temperature.

### ***Loading Furnace with Samples***

The crucibles were loaded with ~0.2 - 0.3 grams of the crushed sample. To prevent samples boiling over their crucibles and into the furnace interior, fusing the crucible into the furnace, a tantalum liner was used that protected the interior and did not overload the crucibles. To further prevent over-boiling, each crushed sample was wrapped inside platinum foil (25mm x 25mm). Being wrapped in platinum foil was essential as otherwise the olivines would be able to fuse to the molybdenum crucibles creating difficulty for further use. Wrapping the samples in Pt foil also allowed the fused sample to be retrieved from the crucibles for further isotope analysis if required.

The crucible lids have a screwed design that allows gas to be released whilst containing the sample itself. This screw-thread design lengthens the path a molten sample would have to travel before reaching the furnace interior. To increase the length further, several molybdenum and tantalum disks were placed on top of the sample inside the crucibles, which stopped the samples from reaching the lids themselves.

To lower the crucibles into the furnace, the hooked rod was rotated over a selected crucible until the hook could catch the crucible's lid. The crucible was then lifted to allow the loading tray to be moved across and aligned with the larger central hole in the tray. Once the crucible was lowered into the furnace, the hook could be rotated 180° and retracted back up to the loading bay. Following the rod retraction, the shutter was emplaced and the gate valve closed.

### ***Crucible Degassing***

The crucibles are manufactured from machine rolled molybdenum rods drilled with 8 mm inner holes (outer is 10 mm in diameter). They were degassed at 800°C for a few hours, off-line under UHV conditions using a resistance furnace to remove adhered atmospheric gases on the metal. The release of atmospheric gases, such as CO<sub>2</sub>, were monitored on a quadrupole mass spectrometer.

To allow re-use of each crucible after sample analysis, the crucibles were placed in 85% hydrofluoric acid (HF) overnight. Placing the crucibles in strong acid ensured any fused sample still stuck to the crucible was dissolved. Following this, the crucibles were washed with Decon 90 solution, deionised water and acetone.

Finally the washed crucibles were degassed again in an offline UHV resistance furnace at 900°C for 6 hours, to remove contaminants adhered throughout the cleaning process, particularly fluorine from the HF wash. The degassing was monitored on a quadrupole mass spectrometer. Blank levels of fluorine were found to be below the detection limit during on-line heating to 1400°C verifying the crucibles were clean and could be re-used.

### **Resistance Furnace**

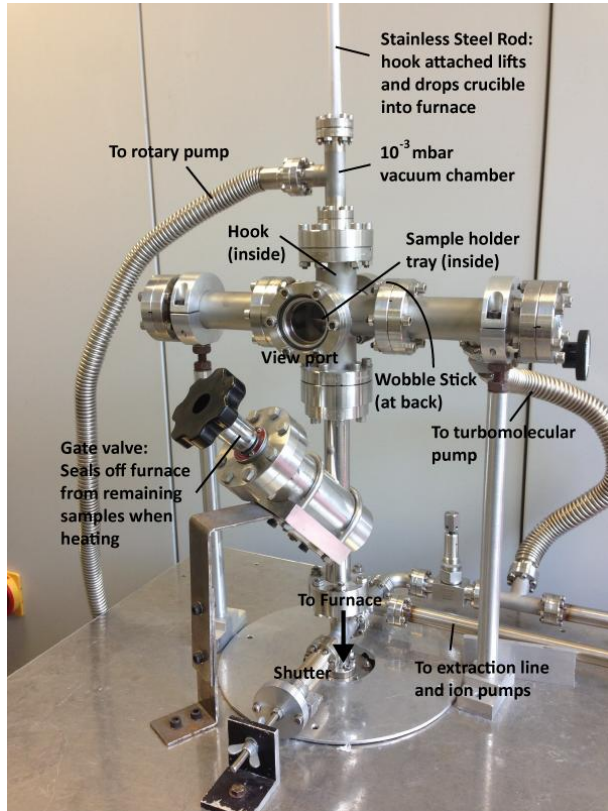


**Figure. 5.12:** Annotated picture of the sample introduction system into the furnace (furnace itself not seen here) To control the heating of the furnace, a Eurotherm 881 temperature controller was used.

The gas release was measured in two steps: a 300°C step to release any adsorbed noble gases and a step at 1500°C to release cosmogenic  ${}^3\text{He}$  or radiogenic  ${}^4\text{He}$ , depending on the experiment. The desired temperatures were reached during a period of 15 minutes (increasing at 250°C per minute), held at that temperature for 30 minutes and then after the final heating step, cooled for another 15 minutes (decreasing at 500°C per minute). Gradual heating prevented forceful boiling and spillage of sample from the crucible. An additional 15 minute step of 1500°C was measured after the 30 minutes at 1500°C to ensure all gases had been fully released in the earlier steps. Platinum has a melting temperature of ~1800°C and so it was established 1500°C was the highest temperature that could be used.

The gas produced throughout heating and melting the olivines was released into the extraction line to be purified and separated. See 5.4 Line Blanks and Air Calibrations for information on blank procedures and typical concentrations determined.

### ***Sample Gas Extraction***

The helium extracted during melting the olivines will be a mixture of: (1) trapped helium not released from the melt inclusions during crushing, which is inherited helium from the mantle ( $\text{He}_i$ ), (2) cosmogenic helium-3 ( ${}^3\text{He}_c$ ) from the olivine lattice, (3) radiogenic helium-4 ( ${}^4\text{He}^*$ ) produced from the decay of U and Th and (4) adsorbed helium from the air. A part of the  $\text{He}_i$  will have been extracted from the crushing done previously. The cosmogenic helium will be extracted from the few samples taken for cosmogenic helium dating. The majority of samples were used to extract radiogenic helium to be used with the U and Th determination in an attempt to estimate a minimum eruption age. An aliquot of the crushed olivines were heated to a fusion point of 1500°C to release the cosmogenic and radiogenic gases.

See Appendix B for images of fused olivines after analyses.

### 5.3.2. Helix Extraction Line

Before the sample gas is analysed in the spectrometer it is first purified and separated in the extraction line (Fig. 5.13)

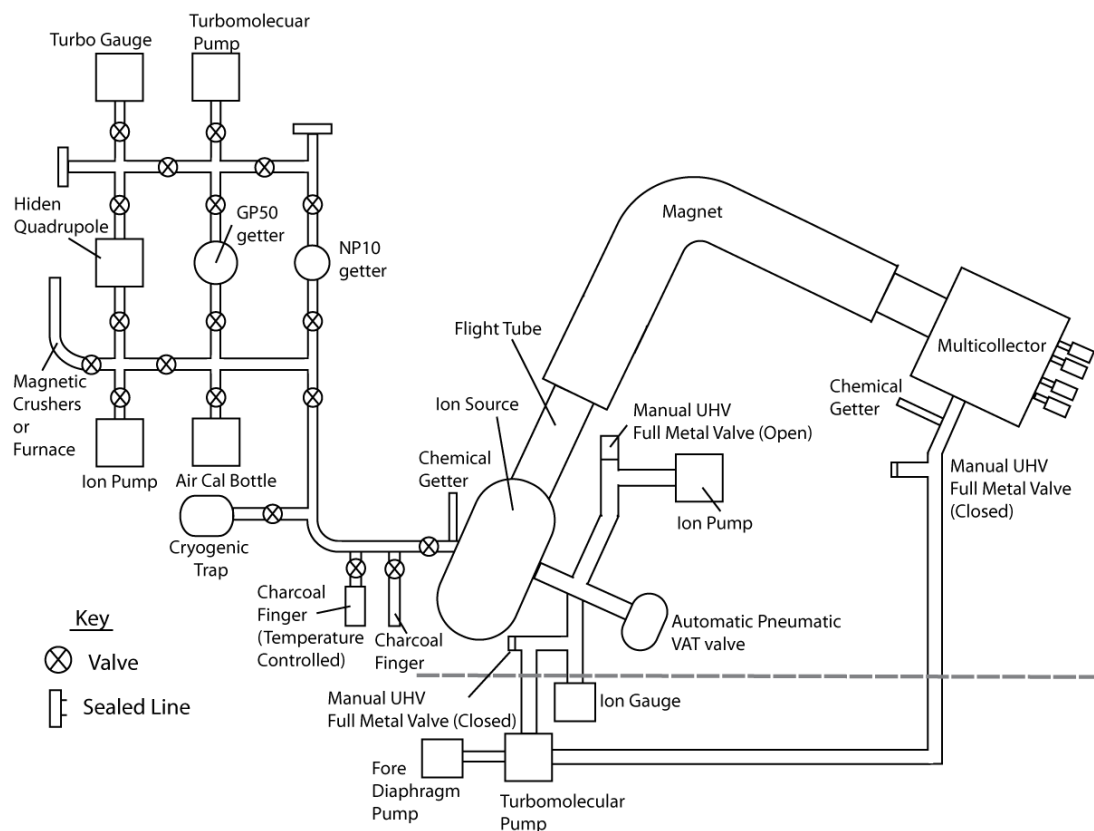


**Figure 5.13:** Schematic of extraction line attached to the HELIX-MC mass spectrometer (not to scale)

The extraction line is constructed from stainless steel tubing connected by Nupro® 0.5" bellow-sealed valves. This line is maintained at UHV ( $1 \times 10^{-9}$  torr or lower) through a Varian® 40 litre ion pump. To evacuate from air, a turbomolecular pump backed by a diaphragm pump are connected to the extraction line and is used to evacuate from air following loading samples or maintenance. Sample gas is introduced to the extraction line after the crushing and melting of olivine separates. The sample noble gases are purified using two Zr-Al alloy getters to remove active gases present. One getter is hot: SAES® NP10 getter 200°C and a SAES® GP50 getter at room temperature. To separate the noble gases a temperature controlled charcoal finger is cooled with liquid nitrogen for 5 minutes, which traps the heavy noble gases (Ar, Kr, Xe) but not the light noble gases (He and Ne). A liquid He cryogenic trap is also attached, to enable separation of Ne from He, however this was not utilised in this study.

An air calibration bottle is attached to the line that enables the sensitivity of the spectrometer to be monitored and is filled with laboratory air at a known pressure. To enable the calibration of  ${}^3\text{He}$  sensitivity and to cross-calibrate the ion gain between the axial multiplier and axial Faraday cups a standard was used with a known concentration of helium. The concentration and isotopic ratio of Ar were calibrated using only the bottle of air. The bottle has a known volume of  $842.3 \text{ cm}^3$  and filled at 0.0159 torr.

A Hiden quadrupole (HAL201) is attached to the extraction line, which allows for leak detection and background levels to be monitored after samples have been loaded and attached and before any samples are analysed.

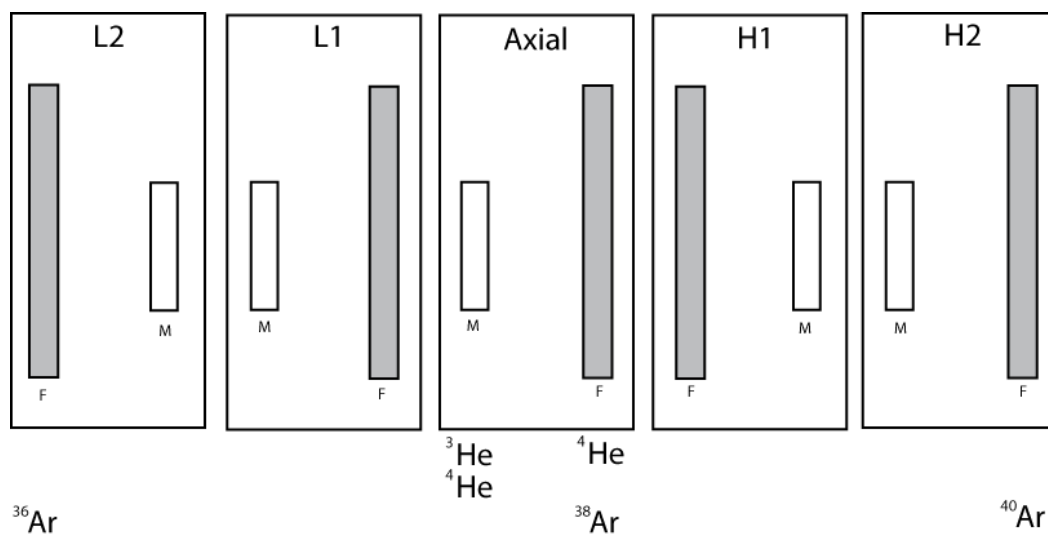


**Figure 5.14:** Multicollector cup holders with illustrated locations of multiplier and Faraday detectors and their corresponding analysed isotopes. (Illustrated interior of Fig 5.8)

For helium analyses, only the axial cup was used, in peak jumping mode. This allowed for both  ${}^3\text{He}$  and  ${}^4\text{He}$  to be analysed on the same cup on either the multiplier or Faraday detectors.  ${}^3\text{He}$  was analysed only on the multiplier, whereas  ${}^4\text{He}$  was analysed on both the multiplier and Faraday cups.

For argon analyses, the L2, axial and H2 cups were used for  ${}^{36}\text{Ar}$ ,  ${}^{38}\text{Ar}$  and  ${}^{40}\text{Ar}$  respectively. In the case of argon, each isotope was detected simultaneously via the multi-collection system (Fig. 5.14 and Fig 5.15). Once the sample gas was introduced into the spectrometer peak centring of m/z 40 was carried out on the H2 cup.

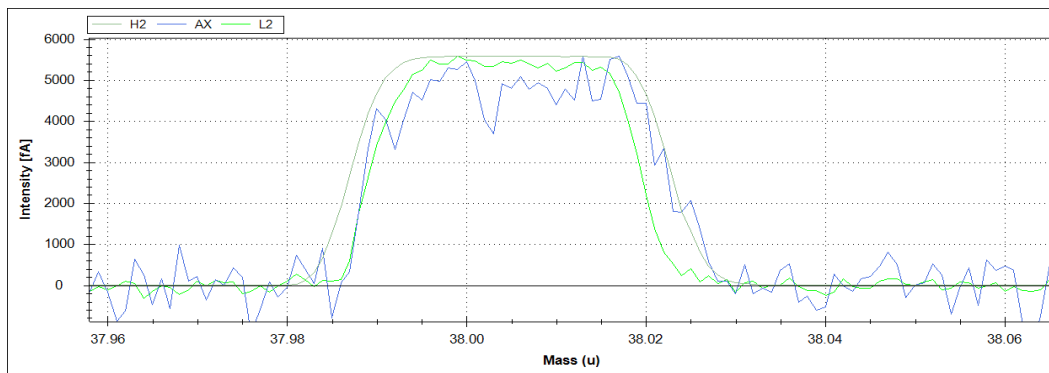


**Figure 5.15:** Mass spectrum showing the multi-collection of  $^{36}\text{Ar}$ ,  $^{38}\text{Ar}$  and  $^{40}\text{Ar}$  on H2, Axial and L2 cups respectively

The compact discrete dynodes (CDD) have a built in deflection system to protect them from damage from intense ion beams. If the ion beam intensity is too high for detection on a multiplier, a small voltage applied to an entrance plate will deflect the ion beam away. They are also positioned so that ion beams cannot be inadvertently focussed into the multipliers. If the deflection plates were not used, the life span of the multipliers would degrade at a much faster rate.

As well as a Zr-Al alloy getter being located by the ion source, there is another getter close to the collector block, which can be degassed without contaminating the mass analyzer. Both getters are operated at room temperature.

### 5.3.3 Purification and Separation of Noble Gases

The purification and separation of the sample gas released from crushing and melting of the olivine separates executed on the Helix extraction line was very similar to that done on the VG5400 extraction line.

Minor differences included purification of crushed sample gas by one SAES® GP50 getter operated at 230°C and an SAES® NP10 getter at room temperature for 10 minutes. For both crushed and fusion gases; the heavy noble gases were trapped on a liquid nitrogen cooled charcoal finger for 5 minutes (10 minutes for fusion released gases) and then isolated from the line.  $^3\text{He}$  was measured on the axial multiplier (CDD) whereas  $^4\text{He}$  was analysed on both the axial multiplier and Faraday cups. A liquid nitrogen cooled charcoal finger was used to minimise the level of  $^{40}\text{Ar}$  in the mass spectrometer throughout the He isotope analysis.

Following helium analysis, the temperature controlled charcoal finger was heated to 57°C (330 K) to prepare the argon gas for analysis. Once the helium analysis was

completed, the spectrometer was evacuated with the ion pump and the cup settings were changed for argon and the source and focussing parameters adjusted using the Qtegra software. Once stabilised the argon gas was released into the spectrometer and the three isotopes were analysed via multi-collection (see Multicollector).

Each day following analysis, the NP10 getter was degassed to 200°C to release any adsorbed gases into the turbomolecular pump and finally the ion pump overnight. The GP50 getter was degassed to release adsorbed gases once a week.

### 5.3.4 Isotopic Analysis

Isotopic measurements of helium and argon gases analysed by the Helix MC Plus controlled by Qtegra software. Template files were created for both helium and argon that included the appropriate source settings and cup configurations for each noble gas. Each template allowed adjustments for analysis of baseline offsets, detector settings, magnet settling times and the number of cycles for each measurement procedure. Peak centring was performed for each isotope analysed, which accounted for any mass drift. A slight drift in mass was common for helium isotopes due to hysteresis of the electromagnet. Due to the low abundance of  $^3\text{He}$  the HD peak was centred on and jumped down a mass of 0.0075 amu to analyse  $^3\text{He}$ . Initially before  $^3\text{He}$  analysis, the magnet was allowed to settle for 16.78 seconds (at mass 2.5) and then a baseline measurement was taken before the  $^3\text{He}$  mass on the multiplier. Each baseline was measured for 4.19 seconds before each corresponding mass. After each mass jump a magnet settling time of 10 seconds was implemented and then each isotope was analysed for 8.39 seconds. Each cycle was then repeated ten times.

For argon, peak centring occurred simultaneously on each isotope based on  $^{40}\text{Ar}$  centred on the L2 cup, as it is the most abundant argon isotope (see Multicollector). Following peak centring the baseline offset was measured for 4.19 seconds. Each cycle was repeated 20 times.

## 5.4 Line Blanks and Air Calibrations

Blanks and air calibrations were carried out using the same procedures used for sample analyses. Line blanks were run after samples were loaded into the crushers,

which enabled checking for leaks and monitoring the background level of gases throughout the line and spectrometer.

Two types of blanks were run: active blanks and static blanks. Active blanks were run by actively crushing an empty tube and static blanks were run with no active crushing. In a static blank a background would be left to build up throughout the line and then analysed. The analysis was run in the same way as a sample measurement and a successful static blank showed no contribution of  ${}^3\text{He}$ . On the VG5400 static blanks averaged  $1.849 \times 10^{-11} \text{ cm}^3$  Standard Temperature and Pressure (STP)  ${}^4\text{He}$  and  $3.224 \times 10^{-11} \text{ cm}^3$  STP  ${}^{40}\text{Ar}$  whereas active blanks averaged  $5.106 \times 10^{-12} \text{ cm}^3$  STP  ${}^4\text{He}$  and  $6.828 \times 10^{-10} \text{ cm}^3$  STP  ${}^{40}\text{Ar}$ . Samples were corrected using the static blank values which were run every day of analysis.

Static blanks on the Helix-MC averaged  $1.1 \times 10^{-7} \text{ cm}^3$  STP  ${}^4\text{He}$  and  $2.6 \times 10^{-7} \text{ cm}^3$  STP  ${}^{40}\text{Ar}$ . Furnace blanks were carried out at room temperature and hot ( $1500^\circ\text{C}$ ), including an empty crucible. The cold blanks averaged  $0.06 \times 10^{-6} \text{ cm}^3$  STP  ${}^4\text{He}$  and  $0.93 \times 10^{-6} \text{ cm}^3$  STP  ${}^{40}\text{Ar}$  and the hot blanks averaged  $2.34 \times 10^{-6} \text{ cm}^3$  STP  ${}^4\text{He}$  and  $205.2 \times 10^{-6} \text{ cm}^3$  STP  ${}^{40}\text{Ar}$ .

Routine weekly air calibrations enabled sampling of noble gas concentrations and any mass discrimination effects to be resolved. Each aliquot of air expanded into the extraction line had a known  ${}^3\text{He}/{}^4\text{He}$  ratio of  $448 \text{ R}_A$  (on the VG5400) and  $1\text{R}_A$  (laboratory air on the Helix-MC). The samples were calibrated from an average of the air calibrations analysed. The average sensitivities determined for the helium spiked bottle (on the VG5400) were  $2.37 \times 10^{-14} \text{ cc/cps}$  STP for  ${}^4\text{He}$  and  $0.03 \times 10^{-14} \text{ cc/cps}$  STP for  ${}^{40}\text{Ar}$ . The average sensitivities determined for the laboratory air filled air calibration bottle on the Helix-MC were  $2.1 \times 10^{-10} \text{ cc/fA}$  STP for  ${}^4\text{He}$  and  $0.04 \times 10^{-10} \text{ cc/fA}$  STP for  ${}^{40}\text{Ar}$ .

Figure 5.16 shows the reproducibility of He isotope ratios in the VG5400 spiked bottle. Fig 5.17 and Fig 5.18 show  ${}^{40}\text{Ar}/{}^{36}\text{Ar}$  isotopic ratios over multiple calibrations in the VG5400 non-spiked bottle. Figure 5.19 shows the  ${}^4\text{He}$  concentration and Fig 5.20  ${}^{40}\text{Ar}/{}^{36}\text{Ar}$  for the bottle of air attached to the Helix-MC.

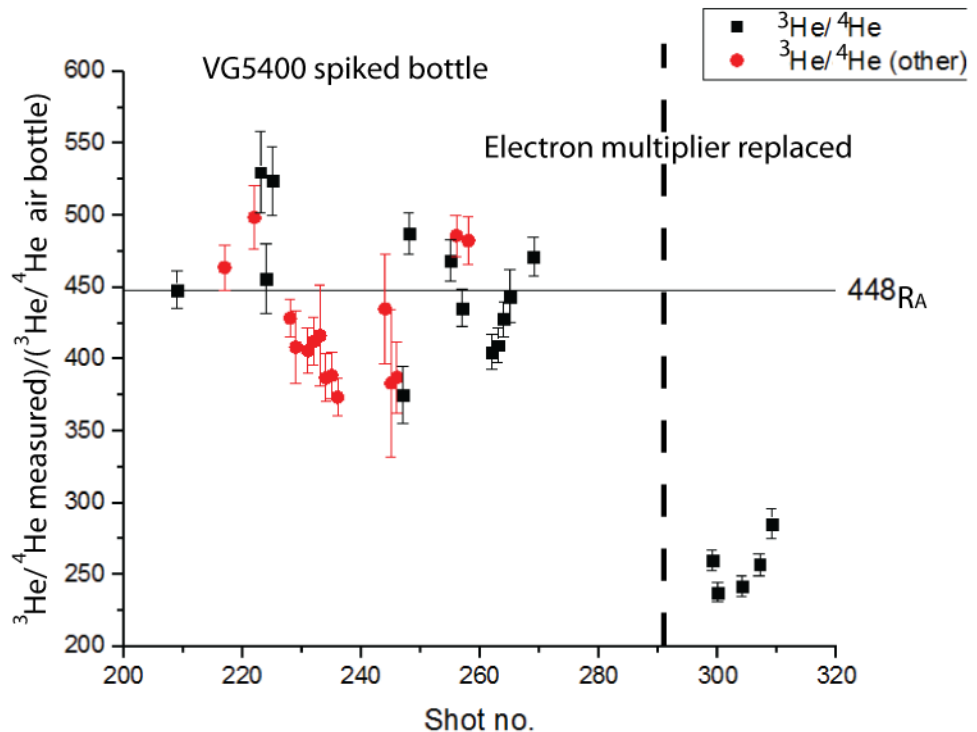


**Figure 5.16:** Measured  ${}^3\text{He}/{}^4\text{He}$  ratio within spiked air calibration bottle attached to VG5400, relative to its known ratio ( ${}^3\text{He}/{}^4\text{He}$  of 448). The air calibrations before the replacement of the electron multiplier shows an average deviation of 8.2% from the calculated  ${}^3\text{He}/{}^4\text{He}$  ratio of the spiked bottle. Errors are to 1 standard deviation. The decrease in  ${}^3\text{He}/{}^4\text{He}$  ratio from shot number 220 to 240 was due to a slight shift in masses causing the edge of the helium peak to be analysed. Shot numbers 220 to 240 were not analysed by myself but a colleague and not used towards sample calibrations and added here for a more complete spread. The helium analysis file was retuned after this. The air calibrations made after the replacement of the electron multiplier are less stable and hence further analyses were carried out on the Helix-MC. The data shown was analysed over a seven month period.

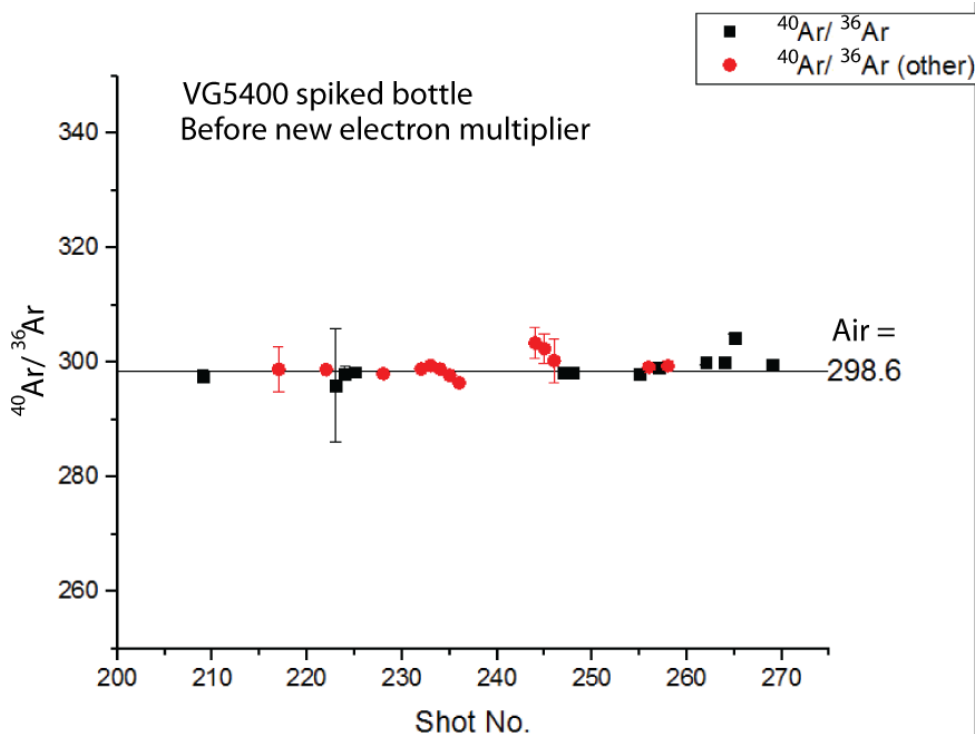


**Fig 5.17:**  ${}^{40}\text{Ar}/{}^{36}\text{Ar}$  of spiked air calibration bottle attached to the VG5400. During the period of average deviation of 0.72% from the atmospheric ratio of 298.6. Errors are to 1 standard deviation.

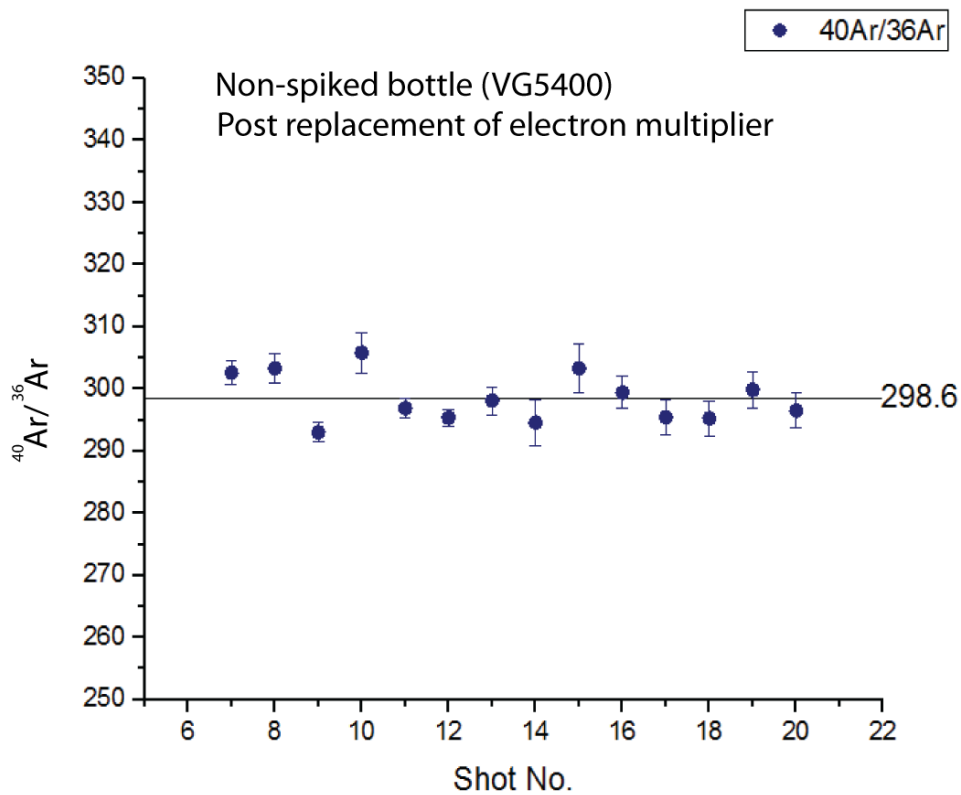


**Figure 5.18:**  ${}^{40}\text{Ar}/{}^{36}\text{Ar}$  of non-spiked air calibration bottle (on the VG5400) following the replacement of the electron multiplier and movement of the filament. The air calibrations show an average deviation of 1.1% from the atmospheric ratio of  ${}^{40}\text{Ar}/{}^{36}\text{Ar}$ , which is 298.6. Errors are to 1 standard deviation.

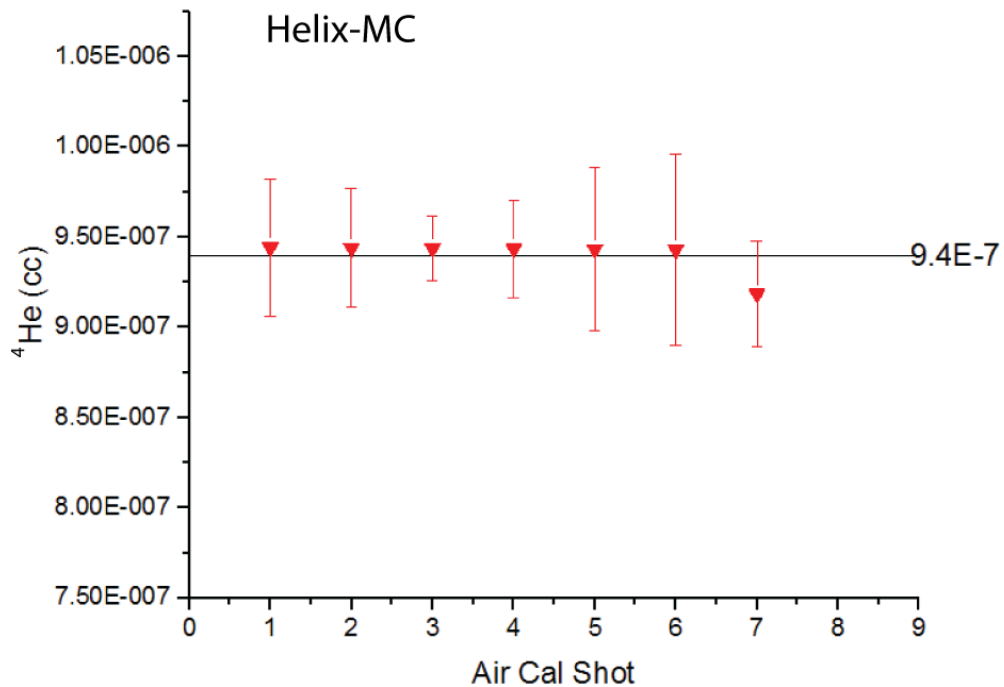


**Figure 5.19:**  ${}^4\text{He}$  concentration in a non-spiked air calibration bottle attached to the Helix-MC. An average deviation of 0.65% is shown in relation to the average  ${}^4\text{He}$  concentration analysed. Errors are to 1 standard deviation

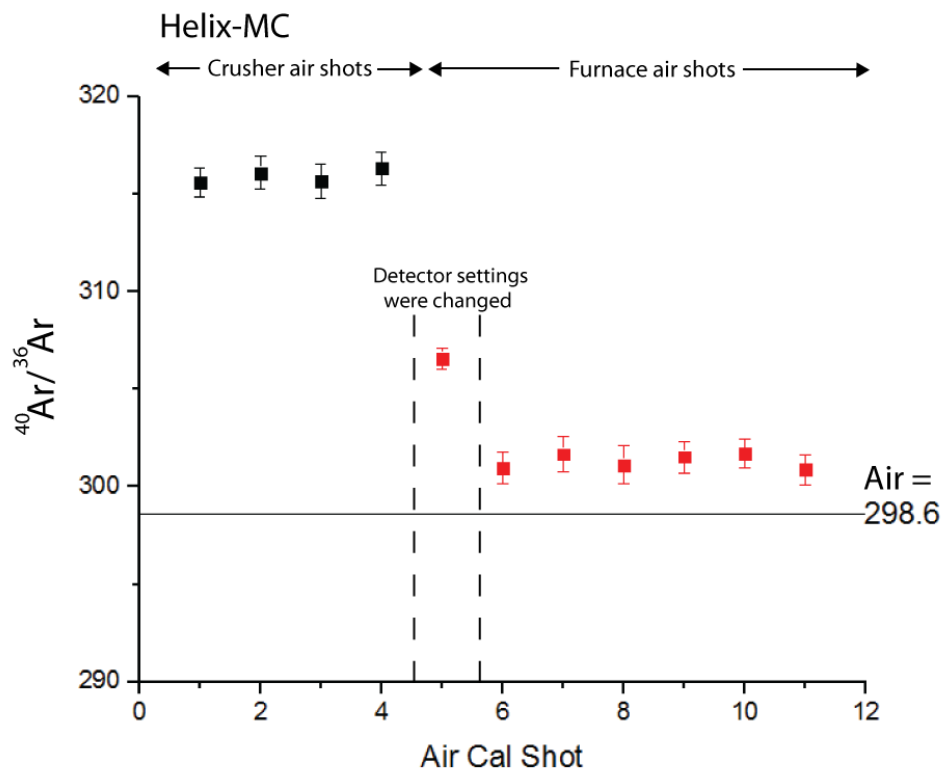


**Figure 5.20:**  ${}^{40}\text{Ar}/{}^{36}\text{Ar}$  of a non-spiked air calibration bottle used on the Helix-MC. The first four data points relate to air shots analysed with crushers attached. These show an average deviation of 0.08%. The last seven data points relate to air shots analysed with the resistance furnace attached. These show an average deviation of 0.42% in relation to the known atmospheric ratio of  ${}^{40}\text{Ar}/{}^{36}\text{Ar}$  of 298.6. Errors are to 1 standard deviation. The first air shot analysed with the furnace attached is higher compared to the following shots due to the detector settings being changed before and after analysed.

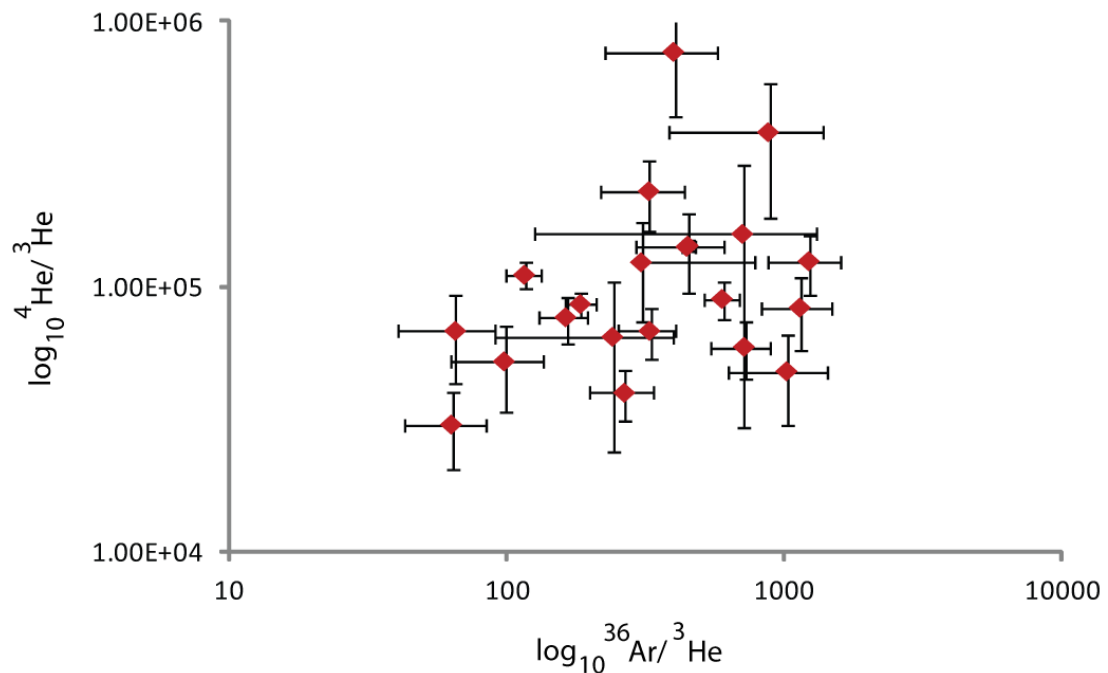


**Figure 5.21:** A logarithmic plot of  ${}^4\text{He}/{}^3\text{He}$  vs.  ${}^{36}\text{Ar}/{}^3\text{He}$ . There is no positive correlation shown, which shows that no correction for air needs to be made on the helium data.

No correction for air contamination on the helium data is required as shown in Fig 5.21. The lack of positive correlation between the logarithmic plots of  $^{4}\text{He}/^{3}\text{He}$  vs.  $^{36}\text{Ar}/^{3}\text{He}$  demonstrates no connection between air derived  $^{36}\text{Ar}$  and  $^{4}\text{He}$ .

## 5.5 Analysis of Uranium and Thorium Isotopes

To acquire accurate isotope ratios of U and Th their concentrations must exceed a few 10s of ng of U and Th. In this case, most of the samples being analysed were only a few ng in concentration, with the majority less than 1 ng. Therefore abundances in the olivine samples were too low to obtain accurate U and Th isotope ratios. Instead the samples were digested and analysed for U and Th concentrations with high accuracy. These analyses were carried out at the Open University by Dr. Bruce Charlier.

### 5.5.1 Sample Digestion

#### *Inductively Coupled Plasma Mass Spectrometer (ICPMS)*

Aliquots of olivine samples were sent to Dr Bruce Charlier at the Open University, who analysed the concentrations of U and Th using a Agilent 7500s ICPMS with a retarding potential quadrupole system.

Prior to analyses the olivines were placed in a HF-HNO<sub>3</sub> solution, inside a 60 ml wrench cap, at 160°C for a few days. Samples were then fluxed in a solution of HCl and HNO<sub>3</sub> to ensure the removal of any formation of fluorides. This acidic solution was evaporated and the samples re-dissolved in 2% HNO<sub>3</sub> for analyses on the MC-ICPMS.

A standard of bismuth was used to check for any instrumental drift and was analysed between blocks of samples. Bismuth was used as this element is unlikely to be in olivine. The standard gave great external precision (between analyses) and internal precision (during analyses). As well as the in house made bismuth standard, a TML rock standard was used to confirm the accuracy of concentrations analysed. The resulting precision was 2.7% 2 standard deviation for Th and 5.2% 2 standard

deviation for U. Blanks analysed on U and Th between analyses were below detection (<0.5 ppt).

As a result the produced concentrations of U and Th, even though are very low, are accurate and can be used with confidence.

Due to the late determination of low U and Th concentrations, an aliquot of the olivine samples (separate to the aliquot used for He analyses) was used for U and Th analysis. This means the He, U and Th analyses were not carried out on the exact same aliquot of olivines. However, the concentrations of each element were so low that any discrepancies between aliquots were very small (see chapter 8, Table 8.2).

# Chapter Six: Mantle Helium Isotope Ratios

## 6.1 Introduction

Iceland is unusual in that it represents both MORB and OIB (hotspot) contributions (Wolfe et al, 1997; Helmberger et al, 1998; Shen et al, 1998). This combination of mantle reservoirs is reflected in the noble gas ratios analysed from Icelandic volcanic samples. Comprehensive studies on  ${}^3\text{He}/{}^4\text{He}$  ratios have been conducted on basaltic glass and minerals (Fig 6.1) across Iceland (Condomines et al, 1983; Kurz et al. 1985; Hilton et al, 1990; Burnard et al, 1994; Dixon et al, 2000; Dixon et al, 2003; Licciardi et al, 2007; Füri et al, 2010; Weston 2013). Geochemical influence from a mantle hotspot with high  ${}^3\text{He}/{}^4\text{He}$  is construed by the wide range of  ${}^3\text{He}/{}^4\text{He}$  ratios observed across Iceland. These ratios range from MORB-like ( $8\text{R}_A$ ) in the Reykjanes ridge to over  $30\text{R}_A$  in central Iceland (Fig 6.1). However, a handful of the highest  ${}^3\text{He}/{}^4\text{He}$  ratios observed are in the NW fjords of Iceland (Hilton et al, 1999). The NW fjords are ~250km from the proposed mantle plume centre, which is beneath the NW corner of the Vatnajökull ice cap (Sigmarsson and Steinthorsson 2007). These high ratios are thought to be an indication that there is a complex relationship between content of helium in erupted samples and the parent melts (Hofmann et al, 2011). Low  ${}^3\text{He}/{}^4\text{He}$  ratios found in the north of the NVZ and Oræfajökull-Snæfells system are interpreted as addition of radiogenic  ${}^4\text{He}$  (Hilton et al, 1990).

Neon isotopes have also been well studied on both basaltic samples and geothermal fluids from Iceland (Dixon et al, 2000; Dixon 2003; Füri et al, 2010). High  ${}^{20}\text{Ne}/{}^{22}\text{Ne}$  and low  ${}^3\text{He}/{}^{22}\text{Ne}$  ratios have been attributed to a solar-like signature attributed to the Icelandic plume (Harrison et al, 1999; Moreira et al, 2001). Mixing of MORB and OIB components has been suggested based on a model by Dixon (2003), which fits with the  ${}^3\text{He}/{}^{22}\text{Ne}$  representation across the Reykjanes peninsula. Füri et al, (2010) expand on this with further data.

The inherent "trapped" helium and argon isotopes have been analysed in crushed olivine samples taken from twenty tuyas and four tindars both from the WVZ and NVZ and an interglacial shield from the WVZ, in Iceland. On three of the subglacial edifices, surficial samples exposed to cosmic rays were also sampled, the rest were sampled from the base of the edifices. This chapter presents and discusses the sources of the helium isotopic ratios observed that are trapped from their mantle

sources. Differences in  ${}^3\text{He}/{}^4\text{He}$  ratios are observed in tuyas and tindars of the WVZ and NVZ.

## 6.2 Results

### 6.2.1 ${}^3\text{He}/{}^4\text{He}$

${}^3\text{He}/{}^4\text{He}$  ratios (Table 6.1) from the different edifices sampled (Fig 4.1) show a range in  ${}^3\text{He}/{}^4\text{He}$  between  $1.0 \pm 0.4 R_A$  for Geitafell (KS7) to  $23.8 \pm 7.6 R_A$  for Bláfell (KS94).  ${}^3\text{He}/{}^4\text{He}$  ratios are less than the average ratio of MORB ( $\sim 8 R_A$ ) in six of the tuyas, three of the tindars and the interglacial shield sampled in the WVZ. Only one tuya sampled from the NVZ show a  ${}^3\text{He}/{}^4\text{He}$  ratio less than  $8 R_A$ . The highest ratio observed,  $23.8 \pm 7.6 R_A$ , is from Bláfell in the NE of the WVZ. The widest range of  ${}^3\text{He}/{}^4\text{He}$  ratios are seen in the WVZ ( $1-24 R_A$ ); conversely the NVZ exhibits a narrower range ( $4-11 R_A$ ). The ranges of  ${}^3\text{He}/{}^4\text{He}$  ratios presented here in both WVZ and NVZ agree with  ${}^3\text{He}/{}^4\text{He}$  ratios already published in both zones (Fig 6.1). In the WVZ the lowest published  ${}^3\text{He}/{}^4\text{He}$  ratio is  $1.9 \pm 1.0 R_A$  for Þórisjökull (Eason et al, 2015) and the highest is observed for an area SW of Blagnipa at  $20.9 R_A$  (Kurz et al, 1985).

Dixon et al (2000) reported a  ${}^3\text{He}/{}^4\text{He}$  ratio for Lambafell of  $19 \pm 2 R_A$  compared to  $5.1 \pm 0.7 R_A$  reported here. Kurz et al (1985) report  ${}^3\text{He}/{}^4\text{He}$  ratios of  $14 R_A$  for Kalfstindar whereas values of  $6.6 \pm 0.4 R_A$  and  $11.1 \pm 7.0 R_A$  are reported here. Four samples presented here (Rauðafell/KS83, Ingolfsfjall/KS86B, Lambafell/KS21 and Kalfstindar/KS25) exhibit lower  ${}^3\text{He}/{}^4\text{He}$  ratios (between  $4-8 R_A$ ) when compared to published data in the same regions of the WVZ, which are somewhat higher between 12 and 20  $R_A$  (Fig 6.1; Condomines et al, 1983; Kurz et al, 1985; Burnard et al, 1994; Dixon 2000; Licciardi et al, 2007; Füri et al, 2010). This may be due to low contents of magmatic gas and/or contamination of samples by radiogenic helium, as suggested by Füri et al (2010). The remainder of the samples analysed in the WVZ compare well with published data in the surrounding areas (Kurz et al, 1985; Dixon 2003; Licciardi et al, 2007; Füri et al, 2010). Published  ${}^3\text{He}/{}^4\text{He}$  data compares especially well in the NVZ (Kurz et al, 1985; Licciard et al, 2007; Füri et al, 2010). These comparisons can be seen in Fig 6.1.

Sample Number and Tuya Name	Weight Crush (g)	Latitude dd°mm.mmmm'	Longitude dd°mm.mmmm'	${}^4\text{He} \times 10^{-9}$ cc/g	R/R <sub>A</sub>	${}^{36}\text{Ar} \times 10^{-11}$ cc/g	${}^{40}\text{Ar}/{}^{36}\text{Ar}$	${}^4\text{He}/{}^{40*}\text{Ar}$
<b>WVZ</b>								
KS7 Tuya <b>Geitafell</b>	0.473	63°56.886'	-21°30.788'	8.832±0.101	0.93±0.40	4.61±0.40	405.4±34.8	17.9±4.3
KS21 Tuya <b>Lambafell</b>	1.003	64°00.586'	-21°27.775'	0.594±0.019	5.09±1.70	1.88±0.23	361.0±43.9	5.1±2.9
KS25 Tindar <b>Kalfstindar</b>	1.047	64°13.107'	-20°53.196'	5.039±0.055	6.61±0.43	N/A <sup>a</sup>	N/A <sup>a</sup>	N/A <sup>a</sup>
KS32 Tindar <b>Dorolfsfell</b>	0.818	64°26.910'	-20°31.005'	4.697±0.078	6.49±0.77	4.94±0.45	1219.5±112.1	1.0±0.03
KS41 Shield Interglacial <b>Ok</b>	1.085	64°33.446'	-20°51.382'	0.611±0.045	1.88±0.98	1.41±0.33	488.2±116.1	2.3±0.9
KS46 Tindar <b>Kalfstindar</b>	1.111	64°15.228'	-20°53.978'	2.368±0.059	11.11±6.98	8.87±0.46	370.3±19.7	3.7±0.8
KS77 Tuya <b>Hrutfell</b>	1.025	64°44.718'	-19°41.051'	4.071±0.102	13.75±4.92	7.67±0.64	363.5±31.1	8.2±3.2
KS79 Tuya (xenolith) <b>Hrutfell</b>	0.799	64°44.655'	-19°40.554'	1.170±0.030	4.55±3.70	5.27±0.67	360.6±47.2	3.6±2.3
KS83 Tuya <b>Raudafell</b>	1.065	64°19.841'	-20°35.596'	2.030±0.028	3.13±0.93	2.90±0.49	1230.1±206.2	0.8±0.04
KS86B Tuya <b>Ingolfsfjall</b>	1.015	63°57.680'	-21°03.230'	0.210±0.007	5.76±1.50	2.07±0.27	347.1±47.0	2.1±1.7
KS87 Tuya <b>Blafjöll</b>	1.041	63°58.565'	-21°38.625'	0.466±0.017	18.08±3.96	3.13±0.44	196.5±27.7	-1.5±0.6
KS88A Tuya (basal pillows) <b>Hlöðufell</b>	1.019	64°24.074'	-20°32.895'	0.085±0.011	5.81±2.35	0.21±0.32	2219.6±3337.5	0.2±0.06
KS88B Tuya (basal pillows) <b>Hlöðufell</b>	1.022	64°24.074'	-20°32.895'	0.085±0.010	15.00±5.52	1.82±0.28	386.3±59.6	0.5±0.3
KS91 Tuya (lava cap) <b>Bláfell</b>	0.908	64°29.186'	-19°51.715'	0.366±0.011	2.82±1.01	19.11±0.37	333.5±14.1	1.3±0.5

KS94	Tuya (basal pillows)	1.044	64°29.569'	-19°54.618'	3.519±0.090	23.82±7.59	7.41±0.62	391.5±33.5	5.1±1.4
<b>Bláfell</b>									
KS97	Tuya (lava cap)	0.508	64°25.078'	-20°32.051'	0.641±0.010	12.05±9.99	8.01±0.29	403.2±9.2	0.3±0.02
<b>Hlöðufell</b>									
KS95B	Tuya	1.043	64°22.976'	-21°15.870'	0.177±0.024	8.63±2.64	2.43±0.19	409.8±32.2	0.7±0.2
<b>Hvalfell</b>									
KS95B2	Tuya	1.063	64°22.976'	-21°15.870'	0.213±0.011	12.13±2.88	2.60±0.19	475.0±37.5	0.5±0.1
<b>NVZ</b>									
KS63	Tuya	1.105	65°25.836'	-17°01.965'	0.424±0.036	8.00±1.24	2.83±0.22	352.9±26.9	2.8±1.2
<b>Sellandafjall</b>									
KS64	Tuya	0.962	65°28.351'	-16°53.943'	2.386±0.034	10.55±3.86	2.30±0.22	335.7±32.5	27.9±21.7
<b>Bláfjall</b>									
KS98	Tindar	1.040	65°06.974'	-16°19.884'	1.963±0.036	8.36±0.92	4.23±0.29	398.1±27.4	4.7±1.0
<b>Herdubreidatögl</b>									
KS101	Tuya	0.704	65°10.477'	-16°23.135'	7.509±0.187	9.38±1.83	16.07±0.75	371.9±17.9	6.4±1.3
<b>Herdubreid</b>									
KS102	Tuya	1.011	66°03.266'	-16°20.749'	0.399±0.008	10.56±2.32	1.93±0.16	383.0±32.2	2.5±0.7
<b>Hafrafell</b>									
KS104	Tuya (lava cap)	0.993	65°45.935'	-16°53.755'	3.850±0.100	3.93±3.72	7.06±0.68	384.9±37.7	6.3±2.1
<b>Gaesafjöll</b>									
KS106	Tuya (basal pillows)	1.067	65°45.330'	-16°55.226'	4.055±0.054	5.03±0.25	12.83±0.35	390.2±10.5	3.5±0.3
<b>Gaesafjöll</b>									

**Table 6.1:** Concentrations analysed of helium and argon isotopes released from melt/fluid inclusions held within the olivine phenocrysts taken from each sample. <sup>a</sup>KS25 has no argon data due to the gas being pumped before analysis. <sup>40\*</sup>Ar = [<sup>36</sup>Ar] \* <sup>40</sup>Ar/<sup>36</sup>Ar - 298.6. Raw data can be found on attached CD.

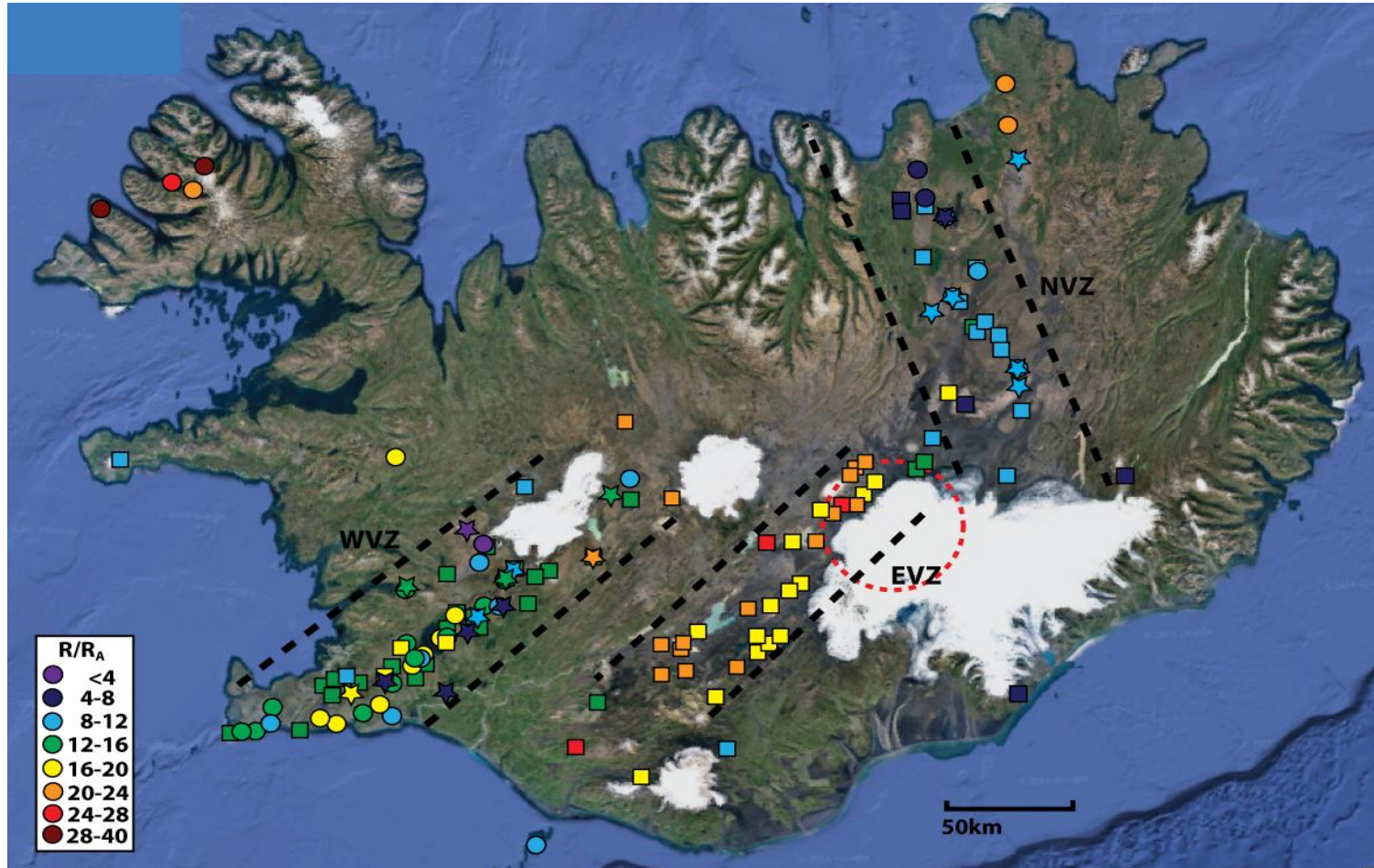


**Figure 6.1:**  ${}^3\text{He}/{}^4\text{He}$  ( $R/R_A$  where  $R$  is analysed  ${}^3\text{He}/{}^4\text{He}$  and  $R_A$  is the atmospheric  ${}^3\text{He}/{}^4\text{He}$  ratio:  $1.399 \times 10^{-6}$ ) ratios from published data across Iceland along and include  ${}^3\text{He}/{}^4\text{He}$  ratios analysed in this study. Published data comes from Condomines et al (1983), Kurz et al (1985), Burnard et al (1994), Hilton et al, (1999), Dixon et al (2000), Dixon et al (2003), Licciardi (2007), Füri et al (2010), Weston (2013), Eason et al, (2015). Stars: **unpublished olivine** data presented here, taken from pillow basalts. Circles: **published olivine** data. Squares: **published glass** data. Image taken from Google Earth. Red dashed circle shows the proposed mantle plume centre taken from Sigmarsdóttir and Steingrímsson (2007).

## 6.2.2 Mantle reservoir

High  $^{40}\text{Ar}/^{36}\text{Ar}$  and low  $^3\text{He}/^4\text{He}$  ratios are indicators of a degassed depleted mantle as  $^3\text{He}$  and  $^{36}\text{Ar}$  were depleted by mantle outgassing.  $^{40}\text{Ar}$  and  $^4\text{He}$  are produced from the decay of K and U-Th respectively and so the abundance of  $^{40}\text{Ar}$  and  $^4\text{He}$  are dependent on the concentration of the parent elements in the mantle and the time of residence of noble gases in the mantle (Matsuda and Marty 1995). Data indicating a MORB source is interpreted by the mixing of air and a depleted mantle component. An OIB source is indicated by the mixing of air, the depleted mantle and an end-member plume composition. Plotting data as  $^{40}\text{Ar}/^{36}\text{Ar}$  vs.  $^3\text{He}/^4\text{He}$  produces data plotted as a curve, which makes it difficult to determine the exact  $^{40}\text{Ar}/^{36}\text{Ar}$  ratios that are plume related, due to the apparent mixing of the depleted and un-depleted mantle component. Therefore, it is more ideal to plot MORB and OIB trendlines using MORB and OIB end-member values,  $1.1 \times 10^{-5}$  and  $4.2 \times 10^{-5}$ , respectively. These values are taken from averaged MORB and OIB values by Matsuda and Marty (1995; Hiyagon et al., 1992).

Plots of  $^3\text{He}/^{40*}\text{Ar}$  vs.  $^4\text{He}/^{40*}\text{Ar}$  have been created below (Fig 6.2 A and B). Using a common denominator ( $^{40*}\text{Ar}$ ) enables both OIB and MORB to be plotted on a straight line.  $^{40*}\text{Ar}$  refers to  $^{40}\text{Ar}$  that has been corrected for any air contribution, indicating the amount of excess  $^{40}\text{Ar}$  present:  $^{40*}\text{Ar} = (^{36}\text{Ar})_m(^{40}\text{Ar}/^{36}\text{Ar})_m - 298.6$ , where  $(^{36}\text{Ar})_m$  and  $(^{40}\text{Ar}/^{36}\text{Ar})_m$  refer to measured  $^{36}\text{Ar}$  concentration and ratios respectively and 298.6 is the atmospheric value of  $^{40}\text{Ar}/^{36}\text{Ar}$ . It effectively removes the air component from the data so that MORB and OIB sources can be distinguished based on their contrasting helium isotope ratios.

The  $^4\text{He}/^{40*}\text{Ar}$  values range from 0.2 to 27.9, but the majority of the  $^4\text{He}/^{40*}\text{Ar}$  values (21 out of 24 samples) are less than or close to 6, which coincides with previous low values for MORB (higher than 0.3 and usually between 2-6) seen for Iceland (Marty et al., 1993; Harrison et al., 1999; Füri et al., 2010).  $^4\text{He}/^{40*}\text{Ar}$  can be used to determine the degree of diffusive loss or fractionation in analysed samples. The ratios can also be used as a function of time due to the difference in decay constants of U and Th and  $^{40}\text{K}$  (Harrison et al., 1999; Füri et al., 2010).

The plots (Fig 6.2) show that the majority of the samples sit on the MORB component line, with there being notable exceptions exhibiting ratios closer to the OIB component line (Bláfell/KS94 and Hrútfell/KS77) and a couple of outliers

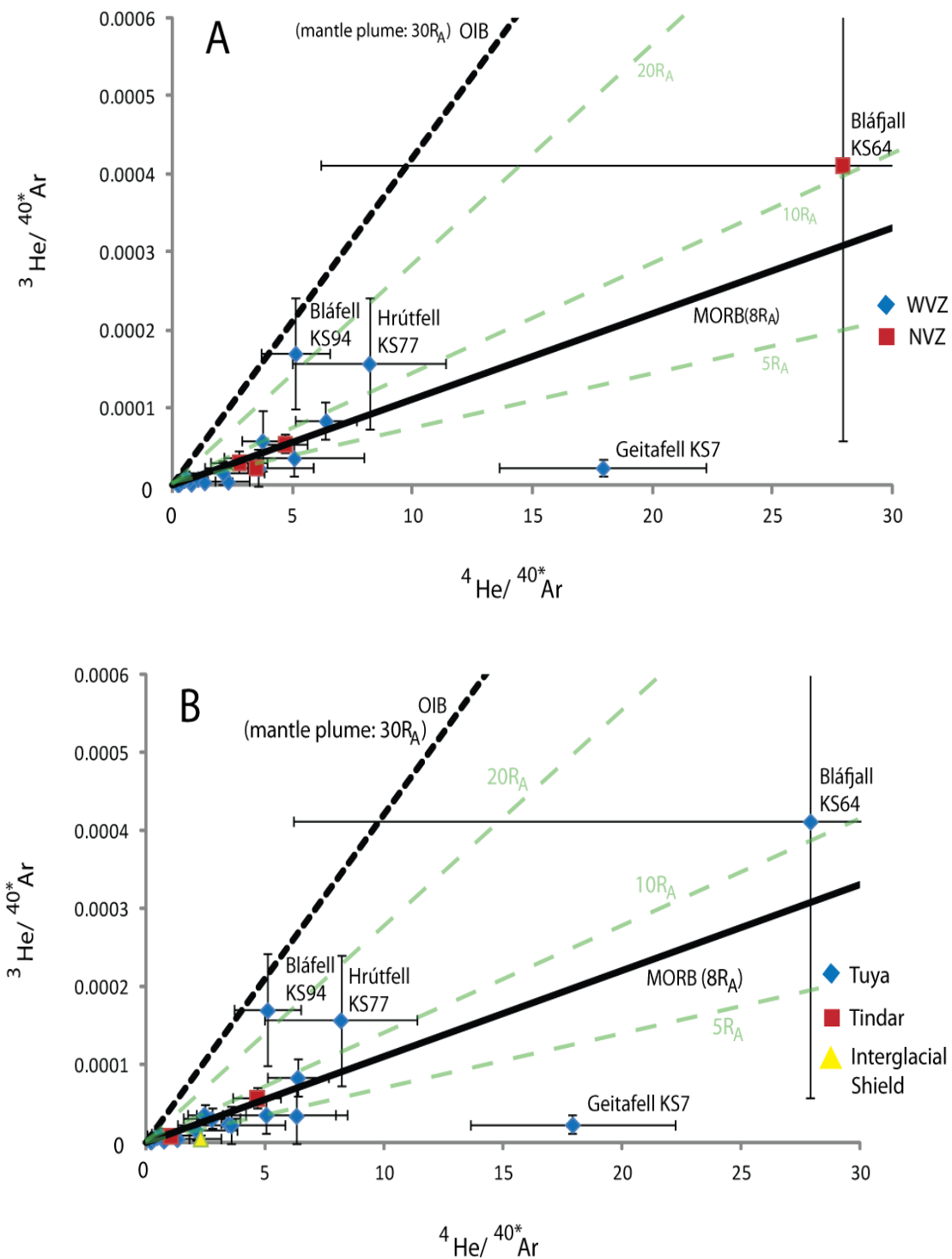


**Figure 6.2:** Plots of  ${}^3\text{He}/{}^{40*}\text{Ar}$  vs.  ${}^4\text{He}/{}^{40*}\text{Ar}$ . **A** samples grouped according to sample location in WVZ or NVZ and **B** by type of edifice: tuya, tindar and shield. The trend lines are taken from Matsuda and Marty (1995) and indicate end members of OIB ( $4.2 \times 10^{-5}$ ) and MORB ( $1.1 \times 10^{-5}$ ).  $5 R_A$ ,  $10 R_A$  and  $20 R_A$  trend lines have been added to help for comparison with Fig. 6.1.

(Geitafell/KS7 and Bláfjall/KS64). One outlier, Geitafell, exhibits a  ${}^4\text{He}/{}^{40}\text{Ar}$  ratio of  $17.9 \pm 4.3$  and  ${}^3\text{He}/{}^{40}\text{Ar}$  ratio of  $2.34 \times 10^{-5} \pm 1.15 \times 10^{-5}$ , which places it far to the right of the MORB component line. The other outlier Bláfjall sits between the MORB and OIB component lines and has the highest ratios in this plot. It is difficult to determine where Bláfjall sits as the errors obtained on both ratios are too large to conclude concisely. However, the spatial location and  ${}^3\text{He}/{}^4\text{He}$  ratio ( $10.6 \pm 3.9\text{R}_A$ ) of Bláfjall indicates that a MORB-like composition is the most likely.

Figure 6.2 shows that Bláfell plots higher than the MORB component line and within error of the OIB component line. This suggests Bláfell could have erupted from a source more comparable to OIB or a mantle plume than a MORB source. The OIB sourced here could also have been contaminated by a MORB-like component or both mantle reservoir sources could have been mixed. The highest  ${}^3\text{He}/{}^4\text{He}$  ratio seen at Bláfell fits well with previous noble gas studies (Kurz et al, 1985; Hilton et al, 1990; Wolfe et al, 1996; Dixon 2003; Sigmarsdóttir and Steinhóðsson 2007) showing that the effects of the proposed mantle plume are seen greatest towards the centre of Iceland. The highest  ${}^3\text{He}/{}^4\text{He}$  ratios are seen in central Iceland (Kurz et al, 1985; Hilton et al, 1990; Wolfe et al, 1997; Dixon, 2003), close to the location of the proposed mantle plume (Fig 6.4). Bláfell is estimated to be an older tuya (extensive evidence of glacial erosion at the summit and therefore, most likely erupted into a previous glacial cycle than the most recent) and is one of the most centrally located tuyas sampled in this study. The other most centrally located tuya sampled is Hrútfell (KS77). Hrútfell has a fairly high  ${}^3\text{He}/{}^4\text{He}$  ratio of  $13.8 \pm 4.9\text{R}_A$  like Bláfell and also fits between the MORB and OIB component lines in Fig 6.2, but is closer to MORB than OIB.

### **WVZ vs. NVZ and Tuya vs. Tindar**

Figure 6.2A shows that both the WVZ and NVZ source helium from a MORB-like source. However, in detail the two volcanic zones have different  ${}^3\text{He}/{}^4\text{He}$  ratios. The  ${}^3\text{He}/{}^4\text{He}$  ratios published for the NVZ (Condomines et al, 1983; Kurz et al, 1985; Burnard et al, 1994; Dixon et al, 2000; Dixon et al, 2003; Licciardi 2007; Füri et al 2010; Weston 2013) are generally lower ( $4\text{-}12\text{R}_A$ ) compared to those found in the WVZ ( $8\text{-}20\text{R}_A$ ) and data presented here concurs with this observation (Fig 6.1). These data indicate there is heterogeneity in the MORB component sampled by Icelandic volcanic systems.

Figure 6.2B shows a plot of  ${}^3\text{He}/{}^{40}\text{Ar}$  vs  ${}^4\text{He}/{}^{40}\text{Ar}$  comparing different types of volcanic edifices: tuyas, tindars and an interglacial shield. No significant differences can be seen between the three types of edifices. All sit along the MORB component line, with the only variations in sourced mantle seen amongst the tuyas. This difference in sourced mantle amongst the tuyas could be better understood if well established age constraints were known for each edifice. This would then enable a link to whether the tuyas sourcing MORB occurred during the onset of deglaciation due to decompression mantle melting (see section 2.2.3). Both Hrútfell and Bláfell (closest to OIB on Fig 6.2B) may have erupted in a period where the ice was at a steady state and so not linked to decompression mantle melting, but instead from a pulse in the plume.

The data presented here shows there is no change in the range of helium isotopes observed between the interglacial shield and tuyas and tindars.

### 6.2.3 ${}^{40}\text{Ar}/{}^{36}\text{Ar}$

The majority of  ${}^{40}\text{Ar}/{}^{36}\text{Ar}$  ratios (Fig 6.3) are close to the atmospheric value (298.6). A few samples exhibit higher values,  $1219.5 \pm 112.1$  and  $1230.1 \pm 206.2$ , at Þorolfsfell/KS32 and Rauðafell/KS83 respectively (Table 6.1). Blafjöll (KS87) in the WVZ was the only sample to give an unusually low  ${}^{40}\text{Ar}/{}^{36}\text{Ar}$  of  $196.5 \pm 27.7$ . It is unlikely that this could be explained by mass fractionation in the sample ( ${}^4\text{He}/{}^{40}\text{Ar}$ :  $-1.5 \pm 0.6$  or  ${}^4\text{He}/{}^{40}\text{Ar}$ : 0.75). Fusion of this sample released Ar (Chapter 8) with a  ${}^{40}\text{Ar}/{}^{36}\text{Ar}$  ratio of 325.8. Thus the crush value of Blafjöll/KS87 is considered to be anomalous and will not be considered further. All  ${}^{40}\text{Ar}/{}^{36}\text{Ar}$  ratios presented here are lower than the estimates for MORB (32000 - 40000; Burnard et al., 1997) and OIB (6500  $\pm$  1500; Trieloff and Kunz, 2005).

Fig 6.3 plots  ${}^{40}\text{Ar}/{}^{36}\text{Ar}$  vs.  ${}^3\text{He}/{}^{36}\text{Ar}$  and shows that the majority of the argon isotope ratios are close to atmospheric value ( ${}^{40}\text{Ar}/{}^{36}\text{Ar} = 298.6$ ). This implies that argon is derived from an atmospheric source and agrees with previously published argon data on Icelandic basalts being similar to the atmospheric value (Burnard et al., 1997; Harrison et al., 1999; Füri et al., 2010). The helium abundance in air is very low so air addition will not usually influence the He isotopic composition. The contribution of atmospheric gas may be derived from contamination or interaction with air in the mantle. The most likely scenario is atmospheric argon adsorbed at the

surface, however, the presence of ubiquitous argon makes it difficult to distinguish between atmospherically contaminated argon and argon trapped in the mantle (Burnard et al., 1997).

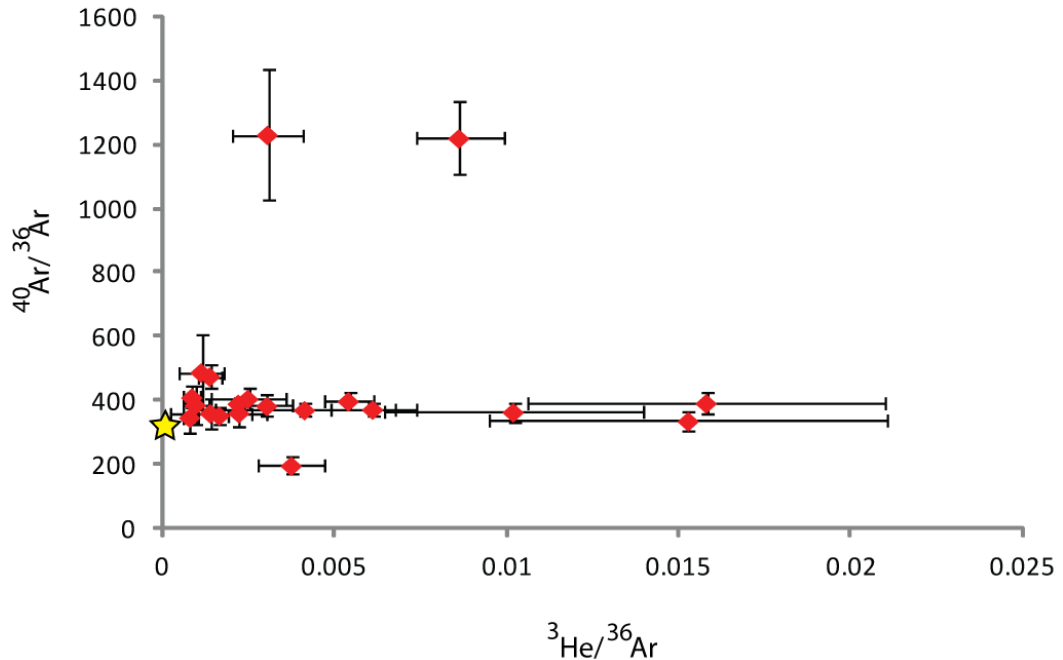


**Figure 6.3:**  ${}^{40}\text{Ar}/{}^{36}\text{Ar}$  vs.  ${}^3\text{He}/{}^{36}\text{Ar}$  for gas released by crushing olivine.  ${}^{36}\text{Ar}$  originates from the atmosphere. The star indicates the atmospheric ratio for both ( ${}^{40}\text{Ar}/{}^{36}\text{Ar}$ : 298.6 and  ${}^3\text{He}/{}^{36}\text{Ar}$ :  $2 \times 10^{-7}$ ). The majority of  ${}^{40}\text{Ar}/{}^{36}\text{Ar}$  ratios correspond to the atmospheric ratio.

## 6.3 Discussion

### 6.3.1 ${}^3\text{He}/{}^4\text{He}$ ratios

Licciardi's (2007)  ${}^3\text{He}/{}^4\text{He}$  trapped ratio in olivine for Geitafell was consistently analysed at  $\sim 17\text{R}_A$  but a much lower value of  $\sim 1\text{R}_A$  is obtained in this study. The  ${}^3\text{He}/{}^4\text{He}$  ratio of  $1\text{R}_A$  at first suggests that the sample was contaminated by air. Neon and argon abundances are low in the mantle and high in air so are often a good proxy for air contamination. The  ${}^{20}\text{Ne}/{}^4\text{He}$  and  ${}^{20}\text{Ne}/{}^{40}\text{Ar}$  ratios analysed for Geitafell were  $4.62 \times 10^{-3}$  and  $1.74 \times 10^{-4}$  respectively, where their corresponding ratios in air are  $3.15$  and  $1.77 \times 10^{-3}$ . Therefore, this suggests that air contamination is not the reason for the low  ${}^3\text{He}/{}^4\text{He}$  ratio observed here. This corresponds with the addition of air having a smaller effect on the He isotopes compared to Ar isotopes (Matsuda and Marty, 1995). The  ${}^4\text{He}$  concentration analysed for this sample is the highest out of

the samples presented here ( $8.8 \times 10^{-9} \pm 0.1$  cc g<sup>-1</sup>) and the  ${}^3\text{He}/{}^4\text{He}$  ratio of  $1\text{R}_A$  is significantly lower than other ratios published in this region of Iceland (8-20 R<sub>A</sub>; Fig 6.1).

A low  ${}^3\text{He}/{}^4\text{He}$  ratio is seen for the interglacial shield volcano Ok at  $1.9 \pm 1\text{R}_A$ . This low ratio could also be attributed to an atmospheric contamination or could be due to the eruption occurring at atmospheric pressures. The  ${}^{20}\text{Ne}/{}^4\text{He}$  and  ${}^{20}\text{Ne}/{}^{40}\text{Ar}$  ratios analysed for Ok were  $5.2 \times 10^{-5}$  and  $8.9 \times 10^{-8}$  respectively. These ratios are much lower than air (3.15 and  $1.77 \times 10^{-3}$ ) and suggest erupting at atmospheric pressure is more likely the cause than being contaminated with air. Subaerial eruptions consistently have lower MgO than their corresponding subglacial eruptions (Eason et al., 2015). This is linked with the internal chemical variation becoming more differentiated with increasing height, e.g. MgO content much lower at top of eruptive units compared to the base (Moore and Calk, 1991; Eason et al., 2015). The shield volcano Ok is in close proximity and sits NW to Þorisjökull. Eason et al. (2015) analysed a similarly low trapped  ${}^3\text{He}/{}^4\text{He}$  ratio of  $1.9 \pm 1.0\text{R}_A$  for Þorisjökull (Fig 6.1), and they noted that the lavas from this volcano show extreme depletion in incompatible trace elements. Low amounts of incompatible trace elements are usually consistent with low amounts of magmatic  ${}^3\text{He}$ ; producing low  ${}^3\text{He}/{}^4\text{He}$  ratios (Eason et al., 2015).

The samples having low  ${}^3\text{He}/{}^4\text{He}$  ratios (<4 R<sub>A</sub>) could be explained by atmospheric and/or crustal contamination or less likely by an analytical effect resulting from detecting low levels of  ${}^3\text{He}$ . Usually low  ${}^3\text{He}$  signal is manifested by high errors, such as two samples from Hlöðufell. Both samples have identical  ${}^4\text{He}$  concentrations (KS88A:  $0.085 \pm 0.011 \times 10^{-9}$  cc g<sup>-1</sup> and KS88B:  $0.085 \pm 0.010 \times 10^{-9}$  cc g<sup>-1</sup>), but show different R<sub>A</sub> values (KS88A:  $5.8 \pm 2.4$  and KS88B:  $15.0 \pm 5.5$ ) and have large errors due to  ${}^3\text{He}$  measurement. In this respect both samples are within 2sd and the variation reflects the high degree of inaccuracy of the measurement. However, most samples have readily detectable  ${}^3\text{He}$  so the lower helium ratios (4-7 R<sub>A</sub>) may relate to the heterogeneity amongst both MORB and OIB samples (Kurz et al, 1982, Graham, 2002, Stuart et al, 2003; Graham et al, 2014). This effect could have been determined to a greater degree had further samples been taken from the same edifice. Licciardi et al. (2007) analysed multiple samples from the same edifice and some edifices showed more variability than others. For example, Herðubreið  ${}^3\text{He}/{}^4\text{He}$  ranged from  $5.0 \pm 0.6$  to  $12.4 \pm 2.3$  R<sub>A</sub>, whereas Bláfjall ranged

from  $9.9 \pm 1.0$  to  $11.3 \pm 0.3$  (Licciardi et al., 2007). Previously  ${}^3\text{He}/{}^4\text{He}$  less than  $8R_A$  have been obtained in olivine samples from SE of Iceland at the Oraefajökull-Snæfells system (Peate et al, 2010). The majority of lower  ${}^3\text{He}/{}^4\text{He}$  ratios presented here are seen in the NVZ (Fig 6.3) and are consistent with previously published helium data in this region, as mentioned previously.

### 6.3.2 Mantle Source

The majority of samples in this suite indicate a MORB-like source. This suggests that volcanic activity in the WVZ and NVZ regions taps a more depleted mantle and favours rift opening plate separation over a mantle plume source. Volcanic activity in these regions could be further increased by the onset of deglaciation, which produces a large increase in mantle melting brought on by the decompression of the shallow mantle (Jull and McKenzie, 1996; Maclennan et al., 2002). A significant difference can be seen (Fig 6.1) in  ${}^3\text{He}/{}^4\text{He}$  ratios between the NVZ and WVZ. This indicates the MORB sourced in the NVZ is more depleted in  ${}^3\text{He}$  isotopes than that in the WVZ, indicating a regionally heterogeneous mantle beneath Iceland (Zindler et al, 1979; Kurz et al, 1985; Dixon et al, 2000; 2003; Füri et al, 2010).

The intermediate  ${}^3\text{He}/{}^4\text{He}$  ratios ( $>8R_A$ ) also suggest the possibility of a mixture of both MORB and plume sources. This agrees with previous studies based on Ne isotopes which show a mixture of MORB and OIB mantle sources (Harrison et al, 1999; Dixon et al, 2003; Füri et al, 2010; Weston et al, 2015). The EVZ, which is located in close proximity to the plume head, exhibits high  ${}^3\text{He}/{}^4\text{He}$  ratios (Fig 6.1) and has been argued as a plume source based on Sr-Nd-Pb isotopes (Furman et al., 1995).

Variable mixing between the MORB and OIB mantle reservoirs can provide an explanation to the pattern of  ${}^3\text{He}/{}^4\text{He}$  ratios seen across Iceland (Kurz et al, 1985; Dixon, 2003). The main MORB component of lower  ${}^3\text{He}/{}^4\text{He}$  ratios are associated with the main spreading rifts at the WVZ and NVZ and the higher  ${}^3\text{He}/{}^4\text{He}$  ratios caused by a mantle plume. This system can be explained with a heterogeneous mantle consisting of 1) a mantle component that is depleted in noble gas isotopes 2) an enriched plume with high  ${}^3\text{He}/{}^4\text{He}$  that is sourced from a less degassed mantle, either from the shallow or deep regions. Bláfell has the highest  ${}^3\text{He}/{}^4\text{He}$  ratio analysed at  $23.8R_A$ . Bláfell is thought to have erupted during a period of ice cover

before the most recent glacial period of the Weichselian, perhaps either the Warthe or Drenthe glacial cycle (see Chapter 2.2: "Glacial History of Iceland"). Therefore Bláfell may be over 100ka, possibly 300ka, and shows extensive evidence of glacial scouring, with its surface covered in blocky broken up sections of lava. No original ropey textures remained on the surface of the tuya. This can be seen even when comparing Bláfell with other tuyas, such as Hlöðufell, which retains a well-defined passage zone whilst Bláfell does not.

See Appendix B2 for images of Bláfell's surface. Fig. B2 photos B C and D all show the summit with no evidence of remaining ropey pahoehoe textures but instead, big blocky eroded features. In contrast see Appendix B1 for images on Hlöðufell that show remaining ropy pahoehoe features on the surface of Hlöðufell, evidence of less erosion and glaciation than Bláfell. On the overview photo of each tuya, it can be seen that there is a distinct lack of passage zone for Bláfell compared to Hlöðufell's, which remains intact (Fig B1A and B2A).

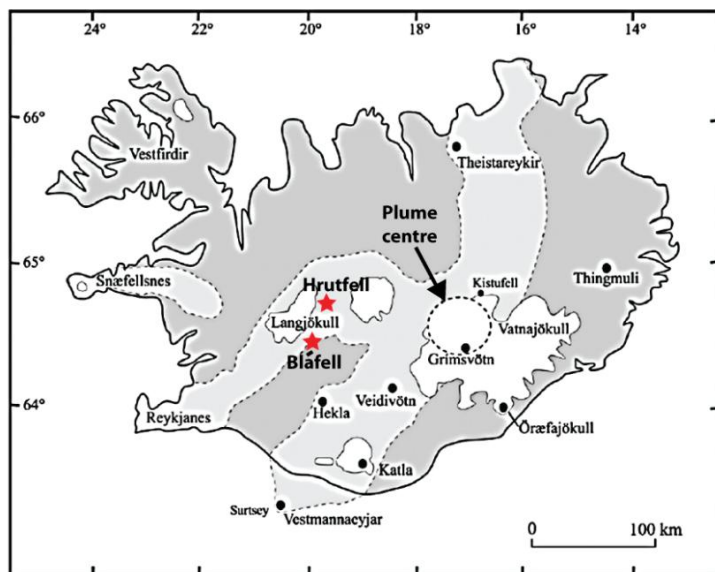


**Figure 6.4:** Proposed mantle plume centre adapted from Sigmarsdóttir and Steinhó尔sson (2007).

These erosional features are indicative that Bláfell has a relatively high age and could indicate that the plume source may have been further west than its current location under the NE corner of the Vatnajökull ice cap (Fig 6.4).

At the time of Bláfell's formation, it may have been closer to the plume centre, before the ridge was re-positioned west (Molnar and Stock, 1987). Seismic studies have also provided evidence of the mantle plume being sourced from the top part of

the lower mantle and being tilted caused from a shear of horizontal flows between high and low levels of the mantle. This is suggested to be driven by northward flow of the upper mantle or a southward flow of the lower mantle or both together (Morgan 1972; Shen et al, 1998; Steinberger 2000; Shen et al, 2002). Another reason could be that the plume spans a large enough area to reach both the EVZ and the WVZ simultaneously and differentially pulses between the two zones over time (Fig 6.5; Kurz et al, 1985).

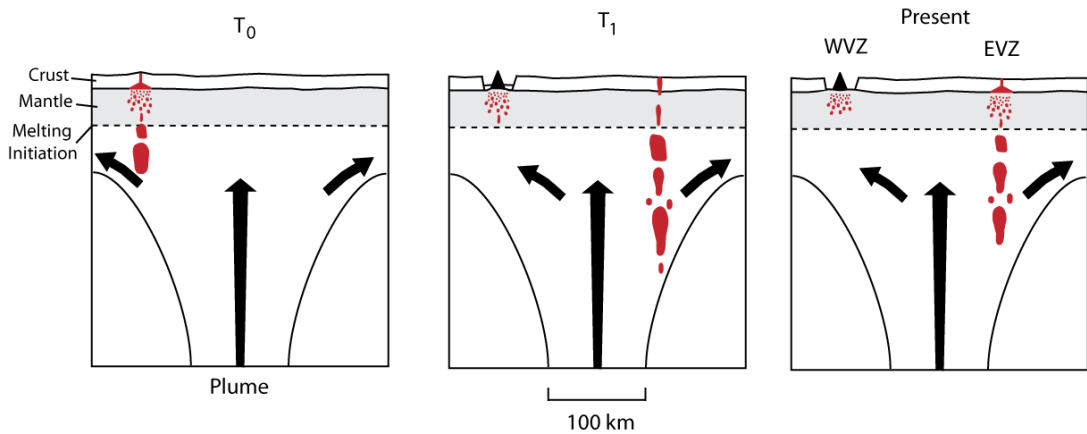


**Figure 6.5:** Model illustrating the preferential sourcing of mantle plume across both the WVZ and EVZ over time in relation to the MORB sourced mantle across Iceland. Adapted from Kurz et al (1985).

### 6.3.3 Basaltic Glass vs. Olivine

There are some differences between  $^3\text{He}/^4\text{He}$  ratios presented here and published data on specific edifices, for example, Bláfell 23.8R<sub>A</sub> (Füri et al 2010: 15.4R<sub>A</sub>), Kalfstindar 6.6R<sub>A</sub> (Kurz et al 1985: 14R<sub>A</sub>) and Lambafell 5.1R<sub>A</sub> (Dixon et al 2000: 19R<sub>A</sub>). These differences could perhaps be attributed to analyses being carried out on basaltic glass instead of olivine phenocrysts. Basaltic glass is magma that is essentially frozen magma or whole mantle melt, whereas olivine is a mineral that crystallizes first out of the magma at  $\sim 1400^\circ\text{C}$ , according to the Bowens reaction series. Therefore olivine is seen more as a true representative of the early, pre-fractionated sourced mantle. Whereas glass is used as a whole rock representative of the mantle frozen at the time of eruption.

The analysed olivine phenocrysts presented here contain preserved melt/fluid inclusions containing gas trapped in the mantle. The basaltic glass may not be as indicative of the deeper mantle component because glass may sample He closer to the surface and may rupture and partially degas upon quenching or even post-

quenching. Basaltic glass is unstable and will devitrify over time. The glass may contain crystallites and will hydrate or become hydrothermally altered during interaction with water in subglacial environments. The olivine phenocrysts have trapped earlier, deeper magmatic helium than the gas that is analysed from basaltic glass.

## 6.4 Conclusions

- Helium isotope data indicates that nearly all samples in this suite obtain a MORB-like mantle source, with the exception of one of the two most central tuyas sampled being closer to an OIB/plume source (Bláfell) and the other (Hrútfell) suggesting a mixture of both components or perhaps being sourced from an OIB/plume-like component contaminated with MORB.
- There are no significant differences in mantle reservoir source when comparing the different types of edifices sampled (tuyas, tindars and the interglacial shield). There is a noticeable difference in  ${}^3\text{He}/{}^4\text{He}$  ratio in the WVZ compared to NVZ, as clear from Fig 6.1. This difference implies the NVZ sources a more depleted MORB source than the WVZ. This provides further evidence to the mantle being heterogeneous beneath Iceland, producing a wide range of  ${}^3\text{He}/{}^4\text{He}$  MORB ratios.
- Large differences in  ${}^3\text{He}$  concentration can be seen from one sample aliquot to the next, greater than those in the  ${}^4\text{He}$  concentration. This can significantly affect the  $R_A$  values given between each analysed aliquot. This could be due to analytical difficulty in analysing such small volumes of  ${}^3\text{He}$  gas compared to  ${}^4\text{He}$  or due to the highly heterogenic mantle sourced.

# Chapter Seven: Cosmogenic Helium

## 7.1 Introduction

Lava caps of three tuyas were sampled, one from the NVZ and two from the WVZ. The aim was to target ropey pahoehoe lava surfaces bearing visible olivines and taken from the highest stratigraphic level accessible, which allowed the final subaerial eruptive stage to be dated.

The three tuyas sampled are Hlöðufell and Bláfell in the WVZ and Gaesafjöll in the NVZ. Hlöðufell (Fig 7.1) is a large tuya located in the north-eastern end of the WVZ and exhibits a bench in its passage zone, and has two plateau or lava caps (Fig 7.1) from the caldera. The same location as Licciardi et al (2007) was sampled to determine if comparable data could be obtained. Hlöðufell has an intact (non-eroded) passage zone indicating it erupted throughout the last period of ice cover and therefore is predicted to have a relatively young exposure age.

Bláfell (Fig 7.2) is a large, eroded tuya that sits at the south-eastern corner of the Langjökull ice cap in the WVZ. The topmost surface of a large in-situ boulder positioned at the highest point of Bláfell's summit was sampled. Bláfell shows evidence of extensive glacial scouring and no longer has a preserved passage zone. This level of erosion suggests that Bláfell may be much older than surrounding tuyas in the WVZ, which still retain fully intact passage zones. Bláfell is one of the larger tuyas in the WVZ and parts of the summit and slopes remain covered in snow throughout each year. One of the reasons for sampling Bláfell was to compare surface exposure and eruption ages on an eroded tuya. If a difference in age was obtained then it would be possible to establish an erosion rate.

Gaesafjöll (Fig 7.3 and Fig 7.4) is a large tuya located ~10km north of Mývatn and has a very large flat lava cap. The sample was taken from the topmost part of ropey pahoehoe found within the vicinity of the summit shield (Fig 7.4). There is evidence of some freeze-thaw erosion but no glacial scouring on the summit of Gaesafjöll.

None of the sites sampled required corrections for topographic shielding.



**Figure 7.1:** Tuya Hlöðufell (1188m) exhibiting a preserved passage zone. Photo was taken on NW side of Hlöðufell facing SE.



**Figure 7.2:** Photo was taken on top of the west side of Bláfell (1158m) facing NW towards Langjökull and Hvítárvatn. A distinct lack of passage zone, with snow still present in the summer month of August. Also observed is the blocky eroded texture on the summit.



**Figure 7.3:** Gaesafjöll (882m) image taken from Google Earth on Gaesafjöll's west side facing NE, with a passage zone still seen.



**Figure 7.4:** Pahoehoe surface texture observed sampled on the summit of Gaesafjöll. The presence of moss within cracks of pahoehoe ropes provides evidence of freeze-thaw erosion from annual snow cover.

For more images on each sampled tuya see Appendix B. Overview photos of each tuya, plus sample localities and images of samples acquired are shown in greater detail.

## 7.2 Results

Sample and <b>Tuya Name</b>	Olivine	Sample	Surface	Latitude	Longitude	${}^3\text{He}/{}^4\text{He}$ , R/R <sub>A</sub>	${}^3\text{He}/{}^4\text{He}$ , R/R <sub>A</sub>	${}^3\text{He}_c$ (x10 <sup>5</sup> ) at g <sup>-1</sup> )	Scaling Factor	Age (ka)	Published Cosmogenic Age
	Crush	altitude (km)	Category			(Crush)	(melt)				
				dd°mm.mmm'							
KS91	0.908	1.163	SC4	64°29.186'	-19°51.715'	2.82±	128.15±	257.5±	2.930 <sup>L</sup>	<b>66.6±0.7</b>	
<b>Bláfell</b>	<b>0.302</b>					1.0	9.8	2.5	3.020 <sup>C</sup>	<b>64.5±0.6</b>	
KS97	0.508	1.163	SC2	64°25.078'	-20°32.051'	12.05±	14.89±	1.9±	2.930 <sup>L</sup>	<b>0.50±7.4</b>	8.2±1.0 or
<b>Hlöðufell</b>	<b>0.341</b>					9.9	62.8	28.6	3.023 <sup>C</sup>	<b>0.48±7.2</b>	10.7*
KS104	0.993	0.803	SC2	65°45.935'	-16°53.755'	3.93±	913.77±	307.3±	2.162 <sup>L</sup>	<b>107.7±46.0</b>	14.4±1.0
<b>Gaesafjöll</b>	<b>0.215</b>					3.7	399.32	131.4	2.206 <sup>C</sup>	<b>105.5±45.1</b>	

**Table 7.1:** Helium data from samples collected for cosmogenic  ${}^3\text{He}$  determinations. Surface Category was taken from Eason et al (2015) and demonstrates the extent to which the surface is eroded, SC1 being the least eroded and SC4 being the most. This is explained further in the text (7.2.3). Published ages are from Licciardi et al (2007) \*The updated age of 10.7ka is taken from Eason et al (2015) via verbal communication with Licciardi. Scaling factors labelled with <sup>C</sup> were obtained using the CRONUS-Earth web calculator whereas those labelled with <sup>L</sup> were calculated using Table 2 in Lal (1991). The scaling factor is the ratio of production at the sample's location in relation to the production at sea level and high latitude. Raw data can be found on the attached CD.

### **7.2.1 Production Rates**

The  ${}^3\text{He}$  production rate used to calculate the exposure ages in Table 7.1 is identical to that calculated by Licciardi et al (2006), Licciardi et al (2007) and Eason et al (2015) on similar Icelandic samples. The production rate is  $132 \pm 5 \text{ atoms g}^{-1} \text{ yr}^{-1}$  and normalised to sea level at high latitudes. This production rate is relatively high due to the enhanced production of  ${}^3\text{He}$  in Iceland due to the influence of the low atmospheric pressure above Iceland throughout the Holocene (Licciardi et al, 2006).

### **7.2.2 Scaling Factor**

The scaling factors (see 3.2.8 Production Rate Scaling Methods) in Table 7.1 were produced using the CRONUS-Earth Web Calculator and calculated using the values provided in Table 2 in Lal (1991). The scaling factor corrects the production rate of  $132 \pm 5 \text{ atoms g}^{-1} \text{ yr}^{-1}$  as it determines the ratio of production at the sample's location altitude relative to the production at sea level at high latitudes.

The CRONUS-Earth Web Calculator takes into account the scaling method, latitude, longitude, altitude/atmospheric pressure, sample thickness, bulk density, shielding factors, erosion rates, attenuation length, the concentration of  ${}^3\text{He}$  and their equivalent uncertainties. The scaling method is from Lal (1991) and updated by Stone (2000) to include atmospheric pressure as well as altitude.

The exposure ages calculated employing the scaling factor proposed by Lal (1991) are used here.

### **7.2.3 Surface Categories**

Surface categories classification of Eason et al, (2015) have been used for each tuya studied. Surface category 2 represents edifices with mild to moderate amounts of modification to the surfaces, with primary flow features such as ropy pahoehoe morphologies still observed. Hlöðufell exhibits mild surficial erosion whilst Gaesafjöll exhibits moderate surficial erosion and so are both categorised as surface category 2. Surface category 4 represents a much more extensive modification to the surface, with evidence of glacial erosion, glacial striae and blocky textures. This is representative of Gaesafjöll.

For images representing what each category looks like, see Appendix B where images are shown of each edifice summit and sample location in greater detail.

## 7.2.4 $^3\text{He}$ Cosmogenic Ages

The  $^3\text{He}$  concentrations produced are low (Gaesafjöll:  $2.5 \times 10^{-13} \text{ cm}^3$ , Hlöðufell:  $8.6 \times 10^{-15} \text{ cm}^3$  and Bláfell:  $2.9 \times 10^{-13} \text{ cm}^3$ . These equate close to 1 count per second. The validity of the  $^3\text{He}$  cosmogenic exposure ages determined are discussed below.

### *Hlöðufell*

The surface exposure age produced for Hlöðufell ( $0.5 \pm 7.4 \text{ ka}$ ) is very low and has a high uncertainty compared to published data for Hlöðufell ( $8.2 \pm 1.0 \text{ ka}$ ; Licciardi et al., 2007) when including the large error of  $\pm 7.4 \text{ ka}$ . The  $^3\text{He}/^4\text{He}$  ratio produced from the melting of the olivine phenocrysts is  $14.9 \pm 63 \text{ R}_A$ . The error is too large to conclude whether it is indicative of a cosmogenic  $^3\text{He}/^4\text{He}$  ratio. Licciardi et al, (2007) published  $^3\text{He}/^4\text{He}$  cosmogenic ratios in the range of  $58 - 1321 \text{ R}_A$  for Hlöðufell. Licciardi et al. (2007) cosmogenic age for Hlöðufell has recently been updated in Eason et al. (2015) via personal communication to  $10.7 \text{ ka}$ , which coincides with surrounding tuya's exposure ages (Raudafell:  $12.2 \pm 0.2 \text{ ka}$  and Skriða:  $10.5 \pm 0.2 \text{ ka}$ , Licciardi et al 2007 and Dórisjökull:  $11.6 \pm 0.6$ , Eason et al., 2015) and relates with the corresponding ice sheet retreat around this time. Around  $8.2 \text{ ka}$  there was a lack of ice certainly insufficient to produce the observed lithofacies architecture at Hlöðufell (Skilling, 2009) with its passage zone at 300-500 m above its base. This discrepancy between helium ratios presented here for Hlöðufell and those published by Licciardi (2007) could indicate that the olivine phenocrysts did not melt (Fig 7.5) to release the cosmogenic helium held within the matrix (See 7.3 Discussion for more on this).

### *Bláfell*

The calculated exposure age for Bláfell here is  $67 \pm 0.7 \text{ ka}$ . This corresponds to a period of ice cover (Weichselian glacial period; Fig 2.5) and is not unreasonable considering an unpublished Ar-Ar age of Bláfell being anywhere between 100-300ka (personal communication with Dr McGarvie). The tuya's summit is covered with snow and ice for the majority of the year due to its high elevation and close proximity to the Langjökull ice cap. Modelling has suggested that the area around Langjökull has had a passive glacier or permanent snow cover for the majority of the last 2000 years (Flowers et al., 2008). The summit would be covered for at least half of every year since its formation, perhaps even more so, which would still make the

exposure age of 67ka a lower limit. This is the first subglacial surface exposure age determined to be >20 ka. Licciardi et al. (2007) found their highest published exposure age to be  $20.3 \pm 6.7$  ka for Sandfell in the NVZ. However, this exposure age is deemed uncertain as the three samples analysed gave a wide scatter of ages (13.5, 20.5 and 26.8 ka). The next highest exposure age determined by Licciardi et al (2007) is  $14.4 \pm 1.0$  ka for Gaesafjöll, which is also in the NVZ.

### *Gaesafjöll*

The exposure age of  $108 \pm 46$ ka for Gaesafjöll appears to be inconsistent with the well-preserved subglacial morphology. The morphology of Gaesafjöll indicates that it has erupted into a relatively recent period of ice cover (e.g. Weichselian) compared to Bláfell. This is due to it retaining a partial passage zone. Gaesafjöll's passage zone is not as well preserved as Hlöðufell's and so may indicate Gaesafjöll has a larger exposure age than Hlöðufell. This is consistent with Licciardi's (2007) exposure ages of 10.7ka and 14.4ka respectively.

## 7.3 Discussion

### 7.3.1 Olivine Fusion

The low concentration of  ${}^3\text{He}$  observed for Hlöðufell may be due to the olivines not reaching a sufficiently high temperature to melt and release all of the  ${}^3\text{He}$  (Fig 7.5). The furnace temperature was measured using a thermocouple to be  $1500^\circ\text{C}$  for 45 minutes in total (one step of 30 mins and a further step of 15 mins), but a step of  $1600^\circ\text{C}$  may have been required, such as the method carried out by Aciego et al. (2007), but not possible with the furnace used here. If olivine concentrations were known then a better idea of furnace temperature could be determined e.g. to melt at  $1500^\circ\text{C}$  the olivine would need to be  $>40\%$  F<sub>a</sub>.

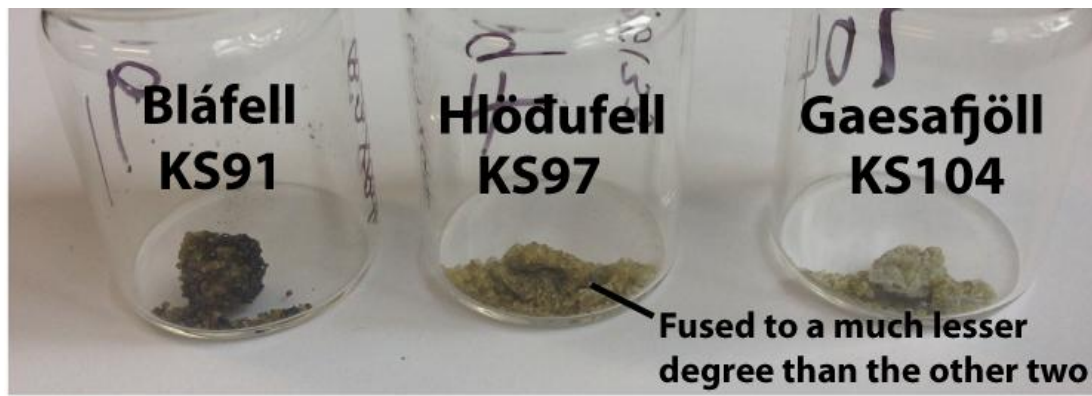


**Figure 7.5:** Olivine samples after furnace heating. Both Bláfell and Gaesafjöll samples have fused more than Hlöðufell, which could explain the low exposure age determined for Hlöðufell as less helium was released. See Appendix B for a better image of fused olivine samples.

### 7.3.2 Erosion

The calculation of these exposure ages could be improved (especially the most eroded tuya Bláfell) by knowing relevant erosion rates for each tuya sampled. As the surface layers are eroded the exposure age is reduced, becoming progressively lower than the eruption age. For example, the extensive erosion that has occurred on Bláfell's surface would mean that the exposure age is increased by ~2-3% if an erosion rate of 2 mm ka is used (Licciardi et al, 2007). Exposed surfaces exhibiting little to no erosion can be considered a minimum eruption age of that edifice. Bourgeois et al (2000) present ice flow dynamics for the most recent period of ice cover (Fig 2.9). The location of ice-divide 2 (Fig 2.9) indicates a possible reason why Gaesafjöll exhibits moderate erosion with a relatively young exposure age of 14.4ka as obtained by Licciardi et al (2007). An exposure age of 14.4ka implies Gaesafjöll erupted during the retreat of ice since the LGM. The ice cover then had another surge during the Younger Dryas and so Gaesafjöll formed during a period of increased ice thickness. Hlöðufell (exposure age of 10.7ka) erupted during the Younger Dryas and thereafter the ice retreated to present day extent. This fits well with Gaesafjöll being located to the west of ice-divide 2 whilst Hlöðufell, which shows little to mild erosion, sits under ice-divide 3 (Fig 2.9). Directly beneath the ice-divide is where little to no movement of basal ice occurs and therefore small amounts of glacial erosion occur on the lava's surface. On the other hand, flowing ice will generate more glacial erosion, which seems to be the case for Gaesafjöll. Since Gaesafjöll's formation the ice retreated, built back up again and retreated again, creating moderate surface erosion. Bláfell sits just to the south in close proximity of ice-divide 3 but displays significant erosion on its surface and so this

argument cannot be applied to Bláfell, which most likely erupted during a previous glacial period.

### 7.3.3. Geochemical Links

Eason et al., (2015) have discovered a link between the major element composition, incompatible element depletion, passage zone heights and lava surface preservation on tuyas in the WVZ. Evidence is presented that shows the least modified surfaces demonstrate geochemical signatures related to enhanced decompression melting and are related to edifices having the thinnest passage zones. This means that a thinner ice sheet brought on by the onset of deglaciation creates smaller subglacial edifices with a thinner transition between subaqueous to subaerial eruptions and a smaller melt-water lake. Therefore, tuyas with lower exposure ages will have the least evidence of surficial erosion, have thinner passage zones, which evidently correspond with geochemical compositions relating to enhanced decompression melting (Jull and McKenzie, 1996; Maclennan et al., 2002). This tells us that the effects of decompression triggered by deglaciation can be observed in the geochemistry (see 2.2.3 Decompression Mantle Melting) of the tuya before the ice has fully retreated (Eason et al., 2015). If Gaesafjöll's exposure age is 108ka, as determined here, it does not fit with this evaluation as its passage zone is relatively thin being 40-100m thick and it exhibits mild to moderate erosion. However, the assessments by Eason et al., (2015) relate to the WVZ specifically, and have not been verified for NVZ tuyas. Conversely, Gaesafjöll does fit this argument when using Licciardi's (2007) published age of 14.4ka. Gaesafjöll's thinner passage zone with moderate erosion could be attributed to enhanced decompression melting due to the thinner crust exhibited in the NVZ (Maclennan et al 2001). In other words, areas such as the NVZ comprising of a thinner crust will exhibit the effects of decompression from deglaciation to a greater degree. This suggests that tuyas in the NVZ will be older/erupted earlier than those in the WVZ due to feeling the effects of decompression sooner than the thicker crust in the WVZ and have a longer time to be eroded than those in the WVZ. A more depleted, shallow, MORB source underlying the NVZ would be consistent with the difference in He isotope ratios discussed earlier (Chapter 6; Fig 6.1). It has been argued that volcanism following deglaciation is from a relatively isotopically depleted mantle (Maclennan et al., 2002; Sims et al, 2013). This is consistent with an increase in mantle melting occurring in the shallow depleted parts of the mantle (Jull and McKenzie 1996;

Maclennan et al., 2002; Sims et al., 2013; Eason et al., 2015). Data presented by Maclennan et al., (2002) however shows that high amounts of REEs are present in Gaesafjöll (opposite of early postglacial decompression mantle melting) and so decompression melting may not be the case for a thinner passage zone and therefore, may just be due to ice being thinner at Gaesafjöll's location.

### 7.3.4 Passage Zones

Eason et al. (2015) also recognised that there was a more general link between passage zone and exposure age, in that the passage zone heights were found to be highest in the tuyas with older exposure ages, and as the exposure ages decrease so do passage zone heights. This corresponds with tuyas erupting into a thinning ice sheets; creating thinner and shorter passage zones. Consequently, the thinner passage zone and lower summit altitude of Gaesafjöll may suggest it erupted into a thinner ice sheet than other tuyas in the WVZ, e.g. Hlöðufell's passage zone is 200m thicker. Hlöðufell's thicker passage zone may have been due to eruption in a thick ice sheet, one that corresponds closer to the LGM, as estimates for the Younger Dryas ice sheet are much thinner (Geirsdóttir et al., 2007). The lack of surface erosion observed for Hlöðufell indicates that any burial by snow and ice after formation was insufficient to erode the surface extensively. This suggests the effects of deglaciation affected the NVZ before the WVZ, mainly due to the ice being thickest towards the centre of Iceland, at higher elevations and thinned out towards the coast (Walker, 1965; Hubbard et al., 2006). The thinner crust in the NVZ (Maclennan et al., 2001) may also have accentuated the effects of decompression further.

### 7.3.5 High ${}^3\text{He}$ exposure Ages

It is unclear why large exposure ages have been calculated for Bláfell and more specifically, Gaesafjöll. Bláfell's large exposure age can be argued to be realistic when considering the evidence given by its geomorphological features (erosion, lack of passage zone). However, Gaesafjöll's large exposure age cannot be argued similarly. Some possible reasons are considered here.

The scaling factor used for  ${}^3\text{He}$  production rate has a large effect in the exposure age determined. If the scaling factor is too low, then the production rate and exposure age are increased. The magnitude of this effect can be assessed by comparing scaling methods of Lal (1991) and the CRONUS-web calculator (Table

7.1). For example, an increase in Gaesafjöll's scaling factor from 2.16 (Lal) to 2.21 (CRONUS) produces a slight decrease in exposure age from 108ka to 106ka respectively.

$^4\text{He}$  released upon melting is used to correct for trapped mantle  $^3\text{He}$ . If not all of the  $^4\text{He}$  was released during heating then this would under-correct for mantle  $^3\text{He}$ , leading to erroneously high exposure ages as the determined cosmogenic  $^3\text{He}$  would be higher than correct. This was most likely due to the heating limitations on the resistance furnace used. A maximum temperature of 1500°C was reached, when ideally a higher temperature of 1700-1750°C (Kurz, 1986) would have enabled a full release of any matrix-held helium.

This problem was most likely brought on by using a large sample size. A large sample size was required to increase the amount of helium analysed, but could have caused incomplete crushing of the trapped melt inclusions due to the cushioning effect caused by the large sample size. This was also a large problem when determining accurate eruption ages in chapter 8.

## 7.4 Conclusions

- The exposure age of Hlöðufell presented here ( $0.5\pm7.4$  ka) is too imprecise to be useful.
- The exposure age of Bláfell presented here ( $66.6\pm0.7$  ka) is argued to be realistic when taking its geomorphological features (erosion and lack of preserved passage zone) into account. Due to the erosion it exhibits, this age must be taken as a minimum exposure age.
- The exposure age of Gaesafjöll ( $107.7\pm46.0$  ka) is determined to be too high to be an accurate exposure age for this edifice, especially when compared to published age  $14.4\pm1.0$  ka (Licciardi et al., 2007). It is unclear why a large exposure age was determined.
- Large samples were acquired for exposure age dating based on the sampling method of Licciardi et al, (2007) who was successful in determining exposure ages on subglacial edifice summits in Iceland. A large sample size was required due to the low concentration of  $^3\text{He}$  found within the olivine

phenocrysts, but made it difficult to effectively crush the entire sample effectively due to a self cushioning effect.

- The morphology exhibited on the sampled tuyas provide evidence and allow further assumptions to be made on the presented exposure ages. Such as the assessment made by Eason et al, (2015) that there is a link between the extent of surface erosion, geochemical composition and passage zone height that all relate to time.

# Chapter Eight: Radiogenic Helium

## 8.1 Introduction

Whole olivine phenocrysts were separated from samples of pillow basalts taken from the base of sixteen tuyas, five tindars and one interglacial shield volcano across the WVZ and NVZ.

The objective was to analyse the radiogenic  ${}^4\text{He}$  produced by the decay of U and Th residing within the olivine phenocrysts. This radiogenic  ${}^4\text{He}$  could then be used to calculate an eruption age using the U-Th/He determinations. Samples were taken from a 0.5-1m depth in the base of the pillow pile to ensure any cosmogenic contribution of helium in the olivines was negligible. The radiogenic  ${}^4\text{He}$  (Equation 22) is calculated by correcting for any the trapped helium component (see Chapter 6).

$${}^4\text{He}_{\text{rad}} = {}^4\text{He}_{\text{melt}} - ({}^3\text{He})_{\text{melt}} ({}^4\text{He} / {}^3\text{He}_{\text{crush}}) \quad \text{Equation 22}$$

The subscripts *rad*, *melt* and *crush* denote radiogenic helium, total helium produced from melting and crushing combined, and the helium produced from crushing the olivines prior to melting, respectively.

The  ${}^4\text{He}$  data presented in Table 8.1 refers to  ${}^4\text{He}_{\text{rad}}$  as calculated by equation 22 and not the total  ${}^4\text{He}$  released in the melt. The age is calculated using the secular equilibrium equation:

$$t = {}^4\text{He}_{\text{rad}} / P \quad \text{Equation 23}$$

Where  $P$  is the production rate of  ${}^4\text{He}$  or alpha particles, which is determined by the concentrations of U and Th in each olivine sample and their corresponding decay constant of each isotope (Chapter 3.2).

The eruption age of each sample was calculated using only the secular equilibrium age equation (equation 23) after it was discovered that the samples of olivine separates had very low concentrations of U and Th and isotopic analysis of these elements was not possible. Disequilibrium occurs in samples younger than  $\sim 1\text{Ma}$  and so is most likely the case in all samples presented here. However, due to the lack of U and Th isotope ratios analysed, minimum eruption ages can still be calculated using the secular equilibrium age equation (Equation 23). Eruption ages

in disequilibrium are determined to be 13-50% higher than ages determined in secular equilibrium when  $<1$  Ma (Farley et al, 2002; Aciego 2003; Aciego 2007). The concentration of  ${}^4\text{He}_{\text{rad}}$  was corrected for helium ejection ( $F_T$ ) before the eruption age was determined, as described by Farley et al (1999), Min et al (2006), Blard and Farley (2008) and Vermeesch (2008). This increased  ${}^4\text{He}_{\text{rad}}$  concentrations by ~5%. See chapter 3.2 for details.

## 8.2 Results

Table 8.1 presents the calculated eruption ages using the secular equilibrium age equation (Equation 23). The ages determined are anomalously high and range from 0.4 to 80.4 Ma, the latter being older than Iceland itself, which formed at 16-18 Ma (Saemundsson 1979).

The concentrations are in the range  $1.8 - 47.1 \times 10^{-5}$  nmol/g for radiogenic  ${}^4\text{He}$ , 0.002 - 0.04 nmol/g for U and 0.01 - 0.1 nmol/g for Th. There is a distinct lack of published data on U and Th concentrations on similar subglacial olivine samples acquired from Iceland to make a direct comparison with the concentrations presented here. However, Kokfelt et al, (2003) have published  ${}^{238}\text{U}$ - ${}^{230}\text{Th}$  disequilibria concentrations on whole rock samples taken from postglacial to historic lavas in Iceland. The concentrations range from 0.04 - 3.78 nmol/g for U and 0.17 - 16.4 nmol/g for Th. The maximum concentrations presented here for U and Th are similar to the minimum concentrations presented by Kokfelt et al, (2003) and some concentrations are three orders of magnitude smaller than those presented by Kokfelt et al, (2003). This reflects the difference in U and Th concentration between whole rock basaltic samples and olivine phenocrysts separated from the whole rock.

The U concentrations found here are one to two magnitudes of order lower when compared to published U concentrations on olivine samples (0.1 - 0.3 nmol/g U; Aciego et al, 2007) and the majority of samples are a magnitude of order lower when comparing published Th concentrations on olivine (0.3 - 0.7 nmol/g Th; Aciego et al, 2007). The concentrations of U and Th in the minerals mentioned previously range from 70 - 80 nmol/g U and 100 - 140 nmol/g Th for garnet (Aciego et al, 2003), 508 - 1235 nmol/g U and 288 - 995 nmol/g Th for zircon (Farley et al, 2002) and 21 - 32 nmol/g U and 93 - 142 nmol/g Th (Farley et al, 2002) and 23 - 139 nmol/g U and 12 - 99 nmol/g Th (Vermeesch 2008) for apatite.

Comparing the corresponding U and Th concentrations emphasises the very low abundances present in Icelandic olivine samples. The anomalously old ages presented are considered to be partly explained by olivine having very low concentrations of U and Th and partly because of the relatively high radiogenic  ${}^4\text{He}$  concentrations. The concentration of U and Th is proportional to the amount of radiogenic  ${}^4\text{He}$  released i.e. a low initial concentration of U and Th produces a low concentration of radiogenic  ${}^4\text{He}$ . Therefore, comparing published U-Th and He concentration data of well established U-Th/He ages, it is evident that the correction made for trapped  ${}^4\text{He}$  remaining in the fused sample was too low. The radiogenic  ${}^4\text{He}$  concentrations presented here are still very high compared to the very low concentrations of U and Th, creating anomalously old ages.

The concentration of U and Th are fixed as there are no other sources for U and Th than what has been analysed in the olivine matrix. The U-Th and  ${}^4\text{He}$  analyses were carried out on separate aliquots, but heterogeneity in U and Th concentrations between aliquotted samples was found to be minimal. For example, the U and Th concentrations in two aliquots of olivines picked from the same bulk lava sample of Hvalfell (KS95B and KS95B2) were 0.012 U and 0.022 Th nmol/g and 0.010 U and 0.025 Th nmol/g respectively. The concentrations of U and Th analysed are confident to be accurate due to the high precision of measurements made, 2.7% 2sd for Th and 5.2% 2sd for U. The U and Th concentrations were analysed along with a standard to ensure high precision was maintained at the low concentrations analysed.

The radiogenic  ${}^4\text{He}$  concentration, however, may vary as it depends on 1) all of the helium to be extracted during the melting of the phenocrysts, 2) the correction made on the total  ${}^4\text{He}$  analysed to compensate for any remaining trapped mantle  ${}^4\text{He}$ , and 3) the possibility of the presence of "parentless" helium, which increases the amount of  ${}^4\text{He}$  analysed. These factors could have contributed to the determination of the anomalously old ages determined and are discussed below.

The  ${}^{40}\text{Ar}/{}^{36}\text{Ar}$  ratios range from  $292.1 \pm 1.1$  to  $340.0 \pm 2.4$ , indicating that they are all similar to values corresponding to the air ratio of 298.6.

Sample and Tuya Name	Weight Crush <b>Melt</b> (g)	Latitude dd°mm.mmm'	Longitude dd°mm.mmm'	[U] nmol/g	[Th] nmol/g	[ <sup>4</sup> He]x10 <sup>-5</sup> nmol/g	<sup>40</sup> Ar/ <sup>36</sup> Ar	Equilibrium Age (ka)	Published Cosmogenic Age (ka)
WVZ									
KS7 Tuya	0.473 <b>0.196</b>	63°56.886'	-21°30.788'	0.0375	0.0620	20.7±1.5	325.3±1.5	3280.8±229.5	11.4±0.7
<b>Geitafell</b>									
KS21 Tuya	1.003	64°00.586'	-21°27.775'	0.0317	0.0981	2.7±0.06	331.4±83.1	414.2±9.6	
<b>Lambafell</b>	<b>0.248</b>								
KS25 Tindar	1.047	64°13.107'	-20°53.196'	0.0069	0.0102	19.8±0.4	338.1±60.4	17546.4±369.9	
<b>Kalfstindar</b>	<b>0.196</b>								
KS32 Tindar	0.818	64°26.910'	-20°31.005'	0.0158	0.0226	17.9±1.6	336.2±1.2	7019.5±636.9	
<b>Dorolfsfell</b>	<b>0.267</b>								
KS41 Interglacial shield	1.085	64°33.446'	-20°51.382'	0.0053	0.0126	21.0±1.8	292.1±1.1	20874.2±1840.5	
<b>Ok</b>	<b>0.262</b>								
KS46 Tindar	1.111	64°15.228'	-20°53.978'	0.0086	0.0280	4.9±0.1	327.1±86.3	2660.0±617.0	
<b>Kalfstindar</b>	<b>0.277</b>								
KS77 Tuya	1.025	64°44.718'	-19°41.051'	0.0036	0.0098	38.1±1.5	318.7±0.9	53296.6±2146.3	
<b>Hrutfell</b>	<b>0.260</b>								
KS79 Tuya - xenolith	0.799	64°44.655'	-19°40.554'	0.0077	0.0223	-12.6±0.4*	325.5±86.2	-8050.2±265.8*	
<b>Hrutfell</b>	<b>0.222</b>								
KS83 Tuya	1.065	64°19.841'	-20°35.596'	0.0110	0.0354	45.0±2.1	338.4±1.6	19268.0±908.8	12.2±0.3
<b>Raudafell</b>	<b>0.174</b>								
KS86B Tuya	1.015	63°57.680'	-21°03.230'	0.0226	0.0671	-12.2±0.4*	323.3±1.2	-2621.1±76.3*	
<b>Ingolfsfjall</b>	<b>0.283</b>								
KS87 Tindar	1.041	63°58.565'	-21°38.625'	0.0134	0.0421	-1.4±0.07*	325.8±1.1	-508.4±233.9*	
<b>Blafjöll</b>	<b>0.206</b>								

KS88A	Tuya	1.019	64°24.074'	-20°32.895'	0.0053	0.0169	18.1±1.5	340.0±2.4	16129.9±1306.0	8.2±1.0
<b>Hlöðufell</b>		<b>0.338</b>								or 10.7*
KS88B	Tuya	1.022	64°24.074'	-20°32.895'	0.0051	0.0161	2.6±0.3	327.5±3.5	2402.7±238.3	
<b>Hlöðufell</b>		<b>0.311</b>								
KS94	Tuya	1.044	64°29.569'	-19°54.618'	0.0131	0.0369	4.1±0.09	325.0±58.0	1539.4±36.0	
<b>Bláfell</b>		<b>0.250</b>								
KS95B	Tuya	1.043	64°22.976'	-21°15.870'	0.0117	0.0216	7.0±0.7	344.1±4.0	3454.5±367.7	
<b>Hvalfell</b>		<b>0.279</b>								
KS95B2	Tuya	1.063	64°22.976'	-21°15.870'	0.0097	0.0247	5.3±0.2	336.3±1.8	2804.3±122.5	12.6±0.4
<b>Hvalfell</b>		<b>0.238</b>								
NVZ										
KS63	Tuya	1.105	65°25.836'	-17°01.965'	0.0029	0.0100	18.7±0.9	328.4±1.2	29594.0±1431.6	
<b>Sellandafjall</b>		<b>0.216</b>								
KS64	Tuya	0.962	65°28.351'	-16°53.943'	0.0086	0.0227	32.2±1.5	328.9±1.4	19111.9±909.7	14.4±0.4
<b>Bláfjall</b>		<b>0.182</b>								
KS98	Tindar	1.040	65°06.974'	-16°19.884'	0.0021	0.0066	35.8±1.4	333.6±1.1	80420.0±3226.8	
<b>Herðubreiðatögl</b>		<b>0.202</b>								
KS101	Tuya	0.704	65°10.477'	-16°23.135'	0.0052	0.0171	1.8±0.09	325.1±2.4	1641.2±780.7	10.5±0.6
<b>Herðubreið</b>		<b>0.212</b>								
KS102	Tuya	1.011	66°03.266'	-16°20.749'	0.0139	0.0452	5.8±0.6	295.1±1.6	1973.6±200.8	11.1±2.2
<b>Hafrafell</b>		<b>0.199</b>								
KS106	Tuya	1.067	65°45.330'	-16°55.226'	0.0044	0.0125	47.1±4.6	307.5±1.0	53227.3±5186.2	14.4±1.0
<b>Gaesafjöll</b>		<b>0.215</b>								

**Table 8.1:** Uranium, thorium and helium data from olivine phenocryst separates taken from the basal pillow basalts of subglacial edifices and an interglacial shield volcano. Published cosmogenic ages are listed for comparison. The data marked with \* are negative as the  ${}^3\text{He}$  correction on the  ${}^4\text{He}$  released by the melt is larger than the total  ${}^4\text{He}$  released producing a negative value for the radiogenic  ${}^4\text{He}$  in the sample [ ${}^4\text{He}_{\text{melt}} - ({}^3\text{He}_{\text{melt}} \times {}^4\text{He} / {}^3\text{He}_{\text{crush}}) = {}^4\text{He}_{\text{rad}}$ ]. These samples will not be considered further in the discussion. Raw data on attached CD.

## 8.3 Discussion

### 8.3.1 Concentration Variation in Different Minerals

Data has been published on U, Th and He concentrations used to determine eruption ages employing olivine and other mineral separates elsewhere. The majority of radiogenic  ${}^4\text{He}$  concentrations presented here (between  $18 - 47.1 \times 10^{-5}$  nmol/g) are higher by an order of magnitude compared to published  ${}^4\text{He}$  concentrations determined on olivine ( $3 - 4 \times 10^{-5}$  nmol/g; Aciego et al., 2007). Garnet has similar radiogenic  ${}^4\text{He}$  concentrations ( $16 - 18 \times 10^{-5}$  nmol/g; Aciego et al., 2003), whereas other minerals, such as zircon ( $17600 - 48600 \times 10^{-5}$  nmol/g; Farley et al., 2002) and apatite ( $2190 - 2820 \times 10^{-5}$  nmol/g; Farley et al., 2002. 30900 -  $222600 \times 10^{-5}$  nmol/g; Vermeesch, 2008) have exhibited much higher radiogenic  ${}^4\text{He}$  concentrations. The Icelandic olivines are still lower in U and Th concentration than olivines acquired by Aciego et al. (2007) in Box Canyon, Idaho.

Concentrations are much higher when analysing whole rock samples of basalt, as is indicated by U and Th concentrations published by Kokfelt et al. (2003). It would be difficult to determine accurate eruption ages using whole rock basalt samples due to the heterogeneity of composition within the whole rock. For example, it would be difficult to establish the amount of helium implanted and ejected from the numerous minerals contained within the whole rock. The high U-Th concentrations published by Kokfelt et al. (2003) indicate that it may be possible to determine U-Th isotopic ratios on whole rock samples. However, accurate eruption ages are more easily determined on mineral separates instead of whole rock samples due to the heterogeneity and various fine-grained minerals with different helium diffusion properties present in whole rock samples. This possibly hinders the applicability of U-Th/He eruption age dating on subglacial Icelandic basalts as the most abundant mineral found in these basalts, with high helium retention, is olivine with low concentrations of U and Th.

### 8.3.2 Radiogenic ${}^4\text{He}$

The radiogenic  ${}^4\text{He}$  concentration determined from the fusion of the olivine phenocrysts appears to be quite high. For that reason, the amount of radiogenic  ${}^4\text{He}$  required to produce a range of eruption ages (10 - 160 ka) were calculated using

Vermeesch's (2008) production rate of  ${}^4\text{He}$  and the concentrations of U and Th analysed in each sample (Table 8.1):

$$P = \left( 8 \frac{137.88}{138.88} \lambda_{238} + \frac{7}{138.88} \lambda_{235} \right) [U] + 6\lambda_{232} [\text{Th}] \quad \text{Equation 24}$$

The production rates and various ages, as  $t$ , were then entered in equation 24 to determine the concentration of radiogenic helium that should be produced with analysed U and Th concentrations. These modelled concentrations have been plotted in Fig 8.1.

Figure 8.1A shows the radiogenic  ${}^4\text{He}$  produced for various ages for samples taken in the WVZ and Fig 8.1B for samples from the NVZ. Also shown for reference is the average concentration of  ${}^4\text{He}$  analysed by the Helix-MC mass spectrometer in each shot of air used as a calibration. Fig 8.1 shows that the amount of radiogenic  ${}^4\text{He}$  falls below the detection limit of the Helix-MC. The main issue is that the  ${}^4\text{He}$  analysed is not radiogenic  ${}^4\text{He}$  alone but both radiogenic  ${}^4\text{He}$  and trapped  ${}^4\text{He}$  combined. The overwhelming volume of trapped  ${}^4\text{He}$  analysed compounds the following correction made to determine the radiogenic  ${}^4\text{He}$ . This is illustrated in Fig 8.2 which shows Herdabreidatögl/KS98 from the NVZ. The total helium analysed from the melt is shown and the following line is the determined radiogenic  ${}^4\text{He}$  once the total  ${}^4\text{He}$  was "corrected" for any remaining trapped  ${}^4\text{He}$ . This shows that the correction made is not large enough to compensate for the low radiogenic  ${}^4\text{He}$  concentrations modelled.

Samples were not crushed intensely to avoid the release of radiogenic  ${}^4\text{He}$  held in the olivine lattice. Therefore a significant amount of remaining trapped  ${}^4\text{He}$  is not unexpected. The trapped helium remaining in the uncrushed inclusions would have been released when fusing at a high temperature and then analysed along with the radiogenic helium released from the olivine's matrix. A large sample size ( $\sim 1$  gram) was required to increase the amount of radiogenic  ${}^4\text{He}$  produced over a relatively young age with low U and Th concentrations. However, this meant the samples created a self-cushioning effect whilst being crushed and the olivine samples and held inclusions were incompletely crushed.

The correction, even if large, should work correctly if the  ${}^3\text{He}/{}^4\text{He}$  from crushing and the  ${}^3\text{He}$  released from melting are correctly determined. In this case, not enough

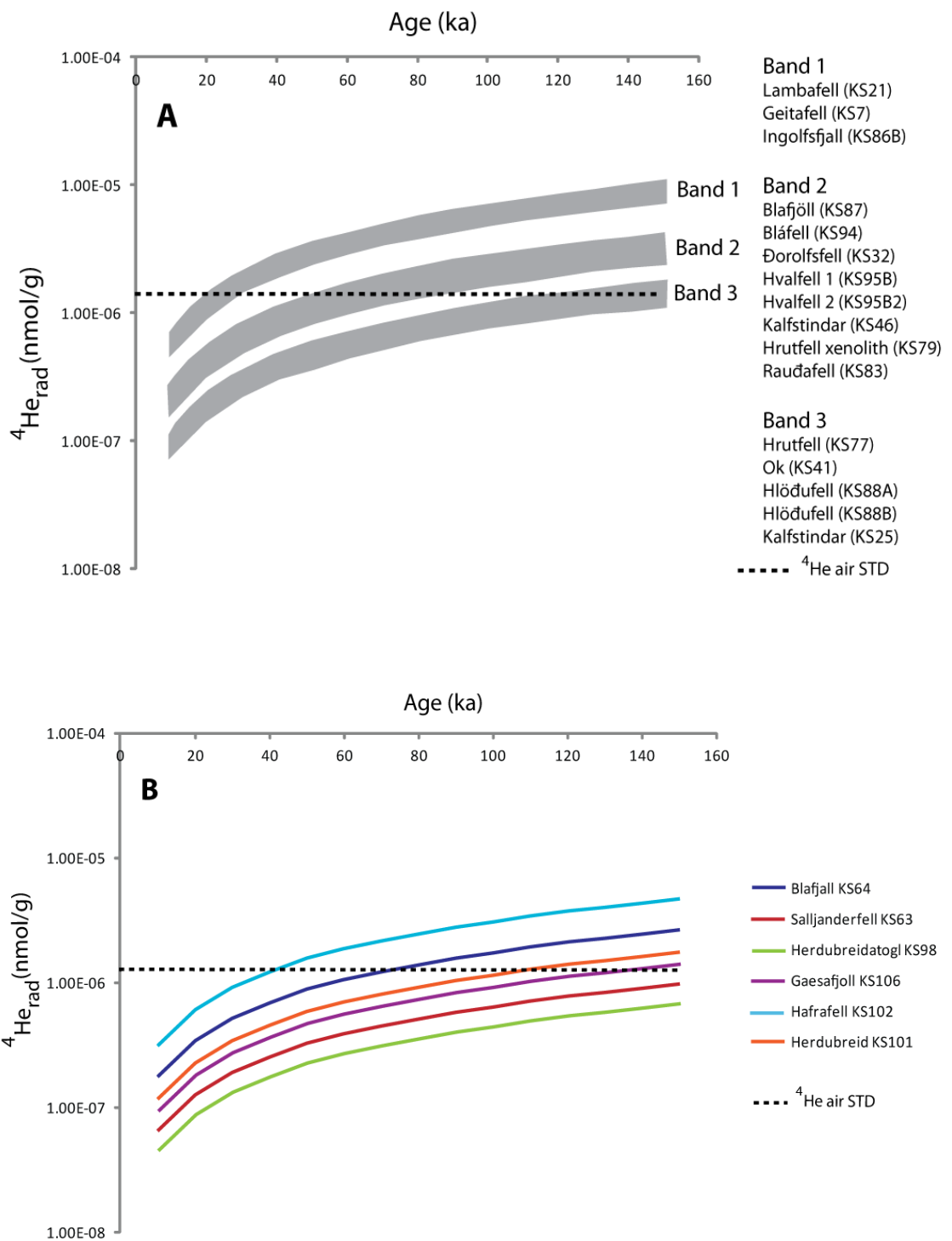


**Figure 8.1:** The concentration of radiogenic  ${}^4\text{He}$  expected as a function of age calculated using the measured U and Th concentrations in each sample of olivine phenocrysts from **A** the WVZ and **B** the NVZ. The concentration of  ${}^4\text{He}$  analysed in a typical shot of air used as a standard is shown as a horizontal line.

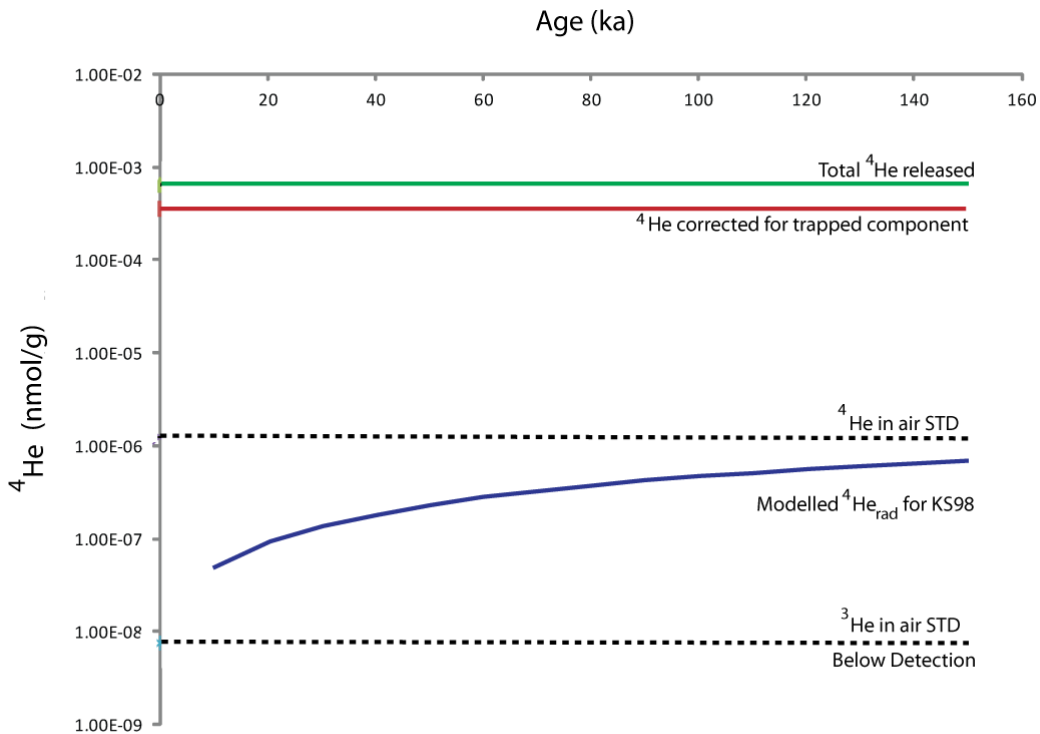


**Figure 8.2:** The concentration of radiogenic  ${}^4\text{He}$  as a function of age based on the U and Th concentration in olivines sample KS98 for Herðabréidatögl. The concentration of  ${}^4\text{He}$  and  ${}^3\text{He}$  analysed in a typical air calibration are shown. The plot shows the total release of  ${}^4\text{He}$  by melting and the magnitude of the correction for trapped  ${}^4\text{He}$  (equation 22). The amount of  ${}^4\text{He}$  remaining after trapped correction is  $\sim 1000$  times higher than the predicted concentrations of radiogenic  ${}^4\text{He}$ .

trapped  ${}^4\text{He}$  is being removed by the correction and so, there was either a problem from under detecting  ${}^3\text{He}$  released during melting or the  ${}^3\text{He}/{}^4\text{He}$  determined from crushing was too low. The minority of samples released detectable amounts of  ${}^3\text{He}$  (only 5 out of the 22 analysed olivine samples released detectable  ${}^3\text{He}$  when melted), which suggests that an under detection of  ${}^3\text{He}$  is the most probable scenario in this case. Equation 22 can be rearranged to calculate the amount of  ${}^3\text{He}$  required to be released during melting that corresponds to the radiogenic  ${}^4\text{He}$  modelled (Fig 8.1 and Fig 8.2):

$${}^3\text{He}_{\text{melt}} = ({}^4\text{He}_{\text{melt}} - {}^4\text{He}_{\text{rad}}) \div {}^4\text{He} / {}^3\text{He}_{\text{crush}} \quad \text{Equation 25}$$

For example, for Herðabréidatögl/KS98 the amount of radiogenic  ${}^4\text{He}$  determined to produce an eruption age of 20 ka (Fig 8.2) is  $9.37 \times 10^{-8}$  nmol/g ( ${}^4\text{He}_{\text{melt}} = 6.47 \times 10^{-4}$  nmol/g and  ${}^4\text{He} / {}^3\text{He}_{\text{crush}} = 85516$ ). This corresponds to  $7.57 \times 10^{-9}$  nmol/g  ${}^3\text{He}$  required to be released during melting, which is below detection on the Helix-MC and is similar to the concentration of  ${}^3\text{He}$  that would be analysed in a shot of air used

as a standard (Fig 8.2). Therefore this suggests that not detecting  ${}^3\text{He}$  released throughout melting can significantly affect the correction made on the crushed  ${}^3\text{He}/{}^4\text{He}$  ratio and contribute to determining an erroneously high eruption age.

### 8.3.3 Parentless ${}^4\text{He}$

A possible reason to explain the excess  ${}^4\text{He}$  is implantation of  ${}^4\text{He}$  into the olivine from the surrounding groundmass. This would create erroneously high eruption ages as the implanted  ${}^4\text{He}$  would be "parentless", meaning the U and Th that produced the analysed  ${}^4\text{He}$  originated outside the olivine grain (Spencer et al, 2004; Fitzgerald et al, 2006). This is made evident when comparing the U and Th concentrations of whole rock samples analysed by Kokfelt et al (2003) to olivine phenocrysts analysed here. Kokfelt et al (2003) whole rock samples are up to 1000 times higher in U and Th concentration than the olivine samples here. Similarly there could be different grains in close proximity to the olivine phenocrysts that prevented the  ${}^4\text{He}$  from being ejected from the phenocryst. This would cause an overestimate on the ejection correction ( $F_T$ ) and produce a larger than correct age (Belton et al 2004a; Fitzgerald et al, 2006). Further analyses into the presence of ejection preventing grains such as zircon, titanite and epidote would need to be carried out. As well as analysing the concentration of U and Th on the surrounding groundmass to determine how large the implantation of  ${}^4\text{He}$  effected this study.

## 8.4 Conclusions

- Olivine is ideal for helium studies due to the lack of helium diffusion that occurs within its lattice over time. However, as Icelandic olivine contains very low concentrations of U and Th, it is not possible to analyse the U and Th isotopic ratios, and thus the degree of disequilibrium of samples cannot be established. This prevents accurate eruption ages being determined using U-Th/He dating. Other minerals potentially amenable to U-Th/He dating (such as zircon, apatite and garnet) may contain higher concentrations of U and Th but are rare in Icelandic subglacial basalts.
- Incomplete crushing of the olivine phenocrysts caused remaining trapped mantle helium within non-crushed inclusions to be released at high

temperatures when fusing the sample to release radiogenic  ${}^4\text{He}$ . Also the amount of  ${}^3\text{He}$  released during melting was below detection, which caused the following correction made for the remaining trapped helium to be too small. Both of these problems contributed in the erroneously high eruption ages presented here, making it impossible to determine in which glacial cycles the subglacial edifices were erupted.

- Kokfelt et al, (2003) analysed U-Th concentrations on whole rock samples of Icelandic basalts that were up to 1000 times higher than the olivine separates themselves. Therefore further analyses is required on the surrounding groundmass that held the analysed olivine phenocrysts to determine how much of the helium analysed was implanted into the olivine samples, or whether grains preventing  ${}^4\text{He}$  ejection were in close proximity to the analysed olivine grains.
- Further studies into helium implantation from the groundmass and improving the method of crushing the olivine samples may enable more accurate equilibrium (minimum) eruption ages to be determined on Icelandic olivine samples. However, the isotopic ratios of U and Th are still required to establish maximum disequilibrium eruption ages. It is possible to analyse U and Th isotopic ratios on whole rock basalt samples (Kokfelt et al, 2003) but does not seem to be as easily determined on Icelandic olivine phenocrysts themselves.

# Chapter Nine

## 9.1 Conclusions

This overarching aim of this thesis has been to determine reliable and accurate eruption ages of basaltic subglacial volcanoes in Iceland, using the relatively new geochronological tool of U-Th/He dating. While of limited success, it has enabled the validity of using this dating method with U-Th poor olivine phenocrysts on relatively young volcanic samples be determined.

1. Nearly all samples presented here, sampled from the WVZ and NVZ, have a trapped  ${}^3\text{He}/{}^4\text{He}$  ratio indicative of MORB mantle, with no significant difference being found between the tuyas, tindars or interglacial shield volcano that were sampled. Samples taken from the NVZ are lower in  ${}^3\text{He}/{}^4\text{He}$  compared to the WVZ but still both obtain MORB-like ratios. The range of  ${}^3\text{He}/{}^4\text{He}$  confirms the previously inferred heterogeneity of the mantle beneath Iceland. A noticeable difference can be seen when comparing a sample taken from close to the centre of Iceland, Bláfell, which has a high  ${}^3\text{He}/{}^4\text{He}$  ratio more indicative of a mantle plume source. It is suggested that, due to the combination of high erosion and high  ${}^3\text{He}/{}^4\text{He}$  ratio, this tuya may have formed during an earlier glacial cycle than the most recent Weichselian, and therefore that the mantle plume was once located further west than it is currently. This coincides with the large  ${}^3\text{He}$  exposure age determined for Bláfell, which is  $66.6 \pm 0.7$  ka. Bláfell's true exposure age is most likely higher than this due to the extensive amount of erosion evident on the tuya's summit.
2. Links can be made to better understand estimates on the ages of the subglacial edifices in Iceland. Using geomorphological evidence, such as, surface erosion and the passage zone height, combined with the edifices geochemical composition, conclusions can be made on the edifices ages (Eason et al., 2015). As well as being able to deduce whether edifices in close proximity erupted from a single magma chamber or not. The geochemical composition of the subglacial edifices provide evidence that the effects of deglaciation could be seen before the ice was completely removed. This may provide further insight

into the  ${}^3\text{He}$  cosmogenic surface exposure ages already published and future work on eruption age dating on these edifices.

3. Great care must be taken when using U-Th/He as a dating tool for Icelandic samples. Many factors can create issues in determining eruption ages. The low U and Th abundances meant isotopic ratios of U-Th could not be analysed, thus the degree of disequilibrium in the decay of U-Th could not be established. The U-Th decay is most usually in disequilibrium on samples assumed to be less than 1Ma, which was the case here. Disequilibrium ages can be 13 - 50% larger than their equilibrium equivalent, depending on the age of the sample (Farley et al, 2002; Aciego et al, 2003; Aciego et al, 2007). Minimum eruption ages can be obtained by ignoring disequilibrium effects. However, the secular equilibrium age can become erroneously high for a number of reasons: not including and dissolving U-Th rich inclusions in U-Th analyses (Farley 2002; Lippolt et al, 1994), analysing broken grains that assumes the distribution of alpha-particle ejection incorrectly, non-crushed inclusions could contribute trapped mantle helium to the released radiogenic helium during fusion, alpha-particles can be injected into the analysed mineral grain from adjacent minerals or conversely the alpha-ejection from U-Th decay could be inhibited (Belton et al, 2004a; Spencer et al, 2004) and 0.1-10% of  ${}^4\text{He}$  could be attributed to  ${}^{147}\text{Sm}$  decay (Belton et al, 2004b). In this case, the most likely explanations to the erroneously large ages has come from 1) non-broken inclusions contributing excess trapped mantle helium to the analysed radiogenic helium and 2) helium implantation of surrounding groundmass and mineral grains with higher U and Th concentrations. Constraining accurate eruption ages are important when understanding their relationship with glacial unloading, volcanic output and mantle melting. Exploiting this process can help investigating the essential aspects of mantle melting.

## 9.2 Further Work

1. Future research using Icelandic olivine for U-Th/He dating should ensure that geochemical analyses of the surrounding groundmass is carried out; as well as taking note of any minerals that are in close proximity to the analysed grain that could cause significant  ${}^4\text{He}$  implantation into the analysed mineral. Concentrations of U-Th in the groundmass surrounding the olivines could be analysed to determine accurately the implantation effect, specifically on Icelandic basaltic olivines. As well as verifying any U-Th rich or alpha-particle ejection preventing minerals in close proximity to the analysed olivines. Both of these factors contribute to an overestimate in eruption age (Fitzgerald 2006). Whole rock basaltic samples may provide some mileage to U-Th/He dating in Iceland, given the evidence of the 1000 times higher U-Th concentration found (Kokfelt et al., 2003). The caveat with whole rock samples, however, is the introduction of problems related to the fine-grain sized minerals and heterogeneity of the groundmass. A multitude of various fine-grain sized minerals would make it impossible to: determine what exactly is being analysed, apply the various corrections previously discussed to be applied and calculate an accurate eruption age.
2. A more effective and complete method of crushing a large ( $\geq 1$  gram) sample size would help ensure that the majority of trapped mantle helium held within inclusions would be released before fusion. As long as care was taken to ensure no radiogenic  ${}^4\text{He}$  was also released through crushing. If this were possible then perhaps a larger sample size ( $> 1$  gram) would enable U-Th isotopic ratios to be analysed and determine more accurate and reliable eruption ages. In this case, if employing the same method of fusion with a resistance furnace, aliquots would need be made for separate U-Th and He concentration analyses. This is due to the small capacity of the crucibles and Pt foil used in the resistance furnace. Heterogeneity of U and Th concentrations between aliquots were minimal when comparing concentrations measured of two samples acquired from the same edifice (Table 8.1). It was impossible to determine whether this is the same case for helium, due to the additional trapped mantle helium analysed. If a more

effective heating method for larger sample sizes were established then it is arguable that accurate eruption ages could still be determined on Icelandic subglacial basalts using U-Th/He dating.

3. Geochemical analyses on the subglacial edifices that tie in with specific geomorphological features could be determined. This could be additional data to include on previously published research on the effects of deglaciation being seen in the geochemistry of mineral grains in subglacial edifices before the ice had fully retreated.
4. The U-Th/He dating technique may be more widely applicable for dating subglacial volcanoes elsewhere in the world. Areas with similar subglacial volcanic edifices include, the Stikine Volcanic Belt in British Columbia, Canada (Hickson et al., 1995; Moore et al, 1995; Dixon et al., 2002; Edwards et al, 2011), the Alaskan Peninsula (Wood and Kienle, 1992) in USA and the Antarctic Peninsula (Smellie and Skilling, 1994). However, data has not been published on the U-Th contents of olivine minerals found within these subglacial volcanoes. Whole rock analyses of U-Th was carried out on the Caribou Tuya Center in British Columbia, Canada (Abraham et al, 2005). These samples had 2.8-3.54 ppm and 0.79-0.98 ppm of Th and U respectively whereas Icelandic olivine samples presented here only contained 1-22 ppb and 0.5-5 ppb Th and U respectively. As this analysis occurred on whole rock, it is hard to know whether the U-Th/He dating technique would be successfully applied on suitable minerals separated from the whole rock that was analysed. There is a distinct lack of U-Th data published on olivine mineral grains (GEOROC database) and so perhaps the best route for further work could start by producing a general survey of U-Th measurements on olivines to identify suitable candidates or applying U-Th/He on a different mineral, such as apatite (Zeitler et al, 1987; Wolf et al, 1998; Ehlers and Farley 2003), garnet (Dunai and Roselieb 1996; Aciego et al, 2003), amphibole (Lippolt and Weigel 1988), magnetite (Fanale and Kulp 1962; Blackburn et al, 2007), allanite (Wolf 1997; Cox et al, 2012), hematite (Wernicke and Lippolt 1994a,b; Bähr et al, 1994), non-metamict titanite (Hurley 1952; Reiners and Farley 1999; Stockli and Farley

2004) non-metamict zircon (Hurley 1952; Damon and Kulp 1957; Farley et al, 2002; Reiners et al, 2004; Reiners 2005; Reich et al, 2007; Guenthner et al, 2013) and goethite (Shuster et al, 2005; Monteiro et al, 2014; Riffel et al, 2016).

## Appendix A - Error Propagation

The volume of each noble gas was obtained by using a linear fit regression through each point of measurement back to time zero, which is the intercept. This regression is essential in determining the original concentration at the time the gas entered the mass spectrometer (Fig. A1).

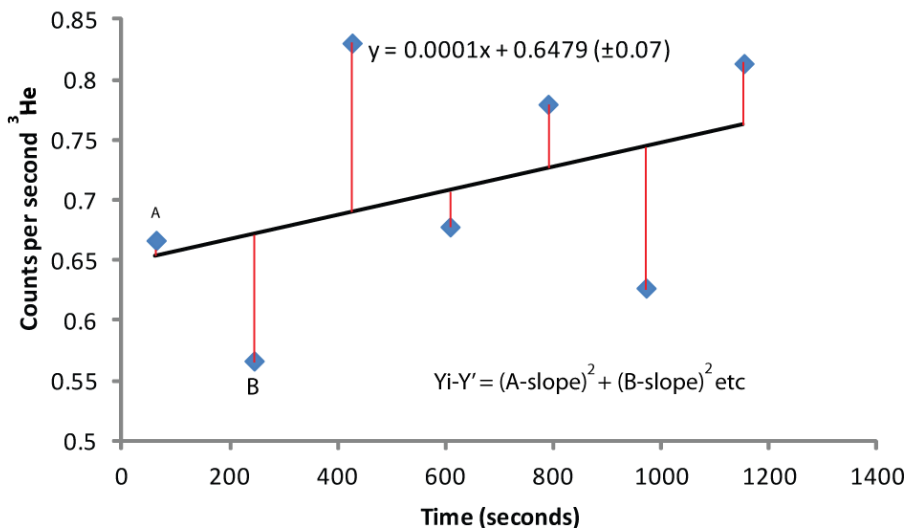


**Figure A1:** Linear regression through six individual  ${}^3\text{He}$  measurements taken from the analysis of 104A (50 crushes).

Depending on the regression to determine the intercept therefore means the quality of the regression controls the final intercept value. The line of regression is fitted through each measured point and calculated through minimizing the sum of the squares ( $Y_i - Y'$ ) of each points vertical deviation from the regression line, then dividing by the amount of data points (N) subtracted by 2 as there are two parameters that are being estimated (intercept and slope; Equation A1, Figure A1).

$$S_s = \sqrt{\frac{\sum(Y_i - Y')}{N-2}} \quad \text{Equation A1}$$

$S_s$  represents the regression's standard error. Each individual measurement does not have an error connected with the intercept and so the initial noble gas concentration is determined from the fit of the regression line (Equation A1). The regression's standard error is then used to determine the standard error connected with the intercept ( $S_i$ ; Equation A2):

$$Ss = Ss \sqrt{\frac{1}{N} \frac{(x)^2}{(xi - \bar{x})^2}}$$

Equation A2

The error connected with the slope of the regression and such the error of the intercept are affected by certain factors including the mass spectrometer stability (collectors and ion source), gas volume being analysed and the background level inside the spectrometer itself.

The main error source in noble gas measurements are due to low volumes of sample gas released into the spectrometer for analyses. This issue has created fairly large errors on measurements presented here due to the low volumes of helium released throughout crushing and heating of olivine phenocrysts (see Table 6.1, Table 7.1 and Table 8.1). Isotopes with higher abundances ( $^{40}\text{Ar}$  isotopes) are usually measured at concentrations well above the limit of detection for the collectors and so small decreases in gas from ionisation are quantified easily. In the case of isotopes like helium for samples presented here, the low abundances mean the collectors operate close to their detection limit. The collectors are then more vulnerable to interference and signal noise and can increase each relative error. This can be seen when comparing Figure A1 to Figure A2. Figure A2 shows the regression on a highly abundant Argon isotope,  $^{40}\text{Ar}$ . The fit of the  $^{40}\text{Ar}$  regression is better than the fit of  $^3\text{He}$ , which is less abundant and therefore the percentage error linked to the signal is greater for  $^3\text{He}$  (0.15% error for  $^{40}\text{Ar}$  and 11.5% error for  $^3\text{He}$ ).

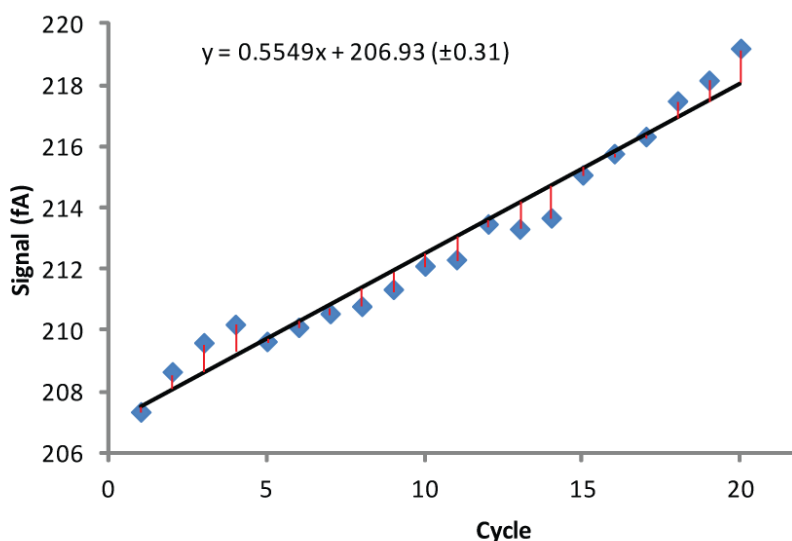


**Figure A2:** Linear regression through twenty individual  $^{40}\text{Ar}$  measurements taken from the analysis of 104A (50 crushes)

## Appendix B - Sampling Context

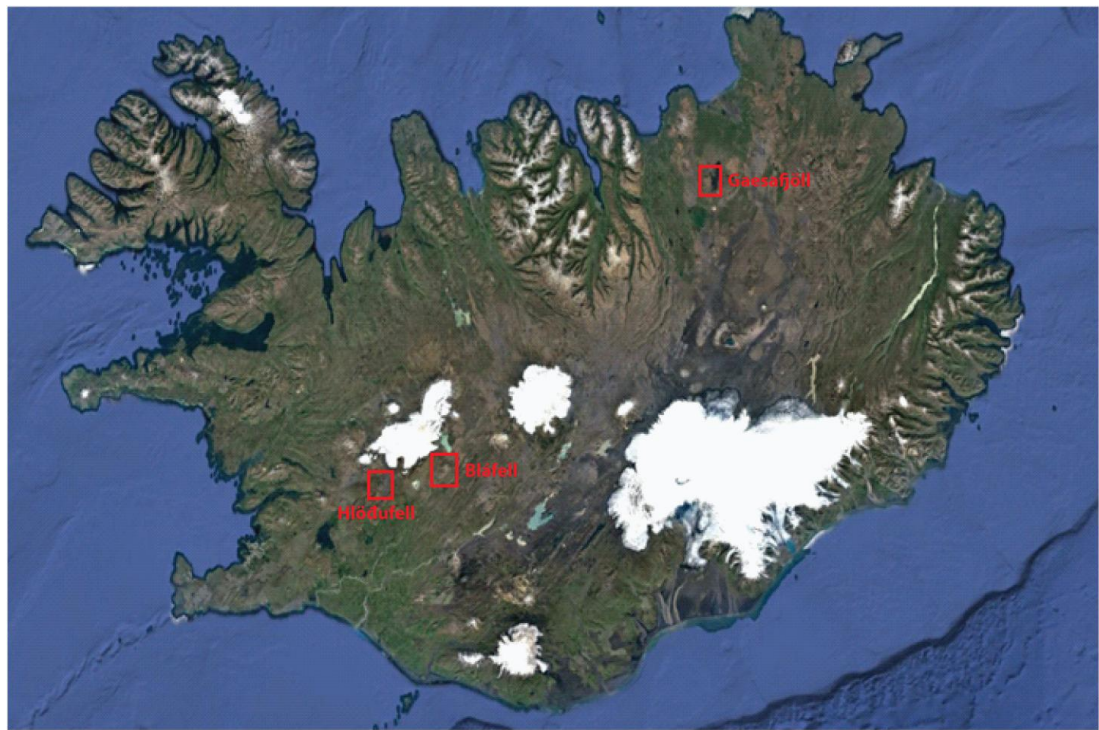
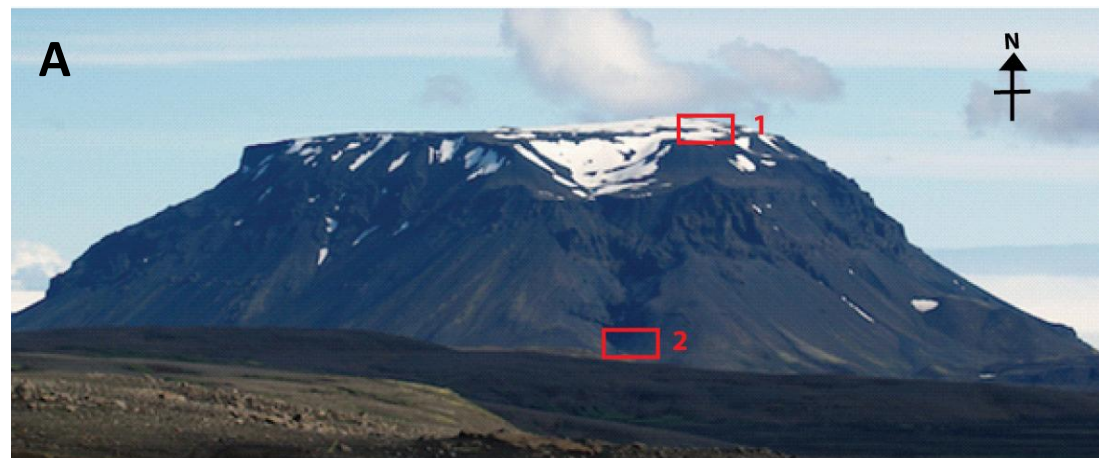


Figure B: Map showing where tuyas Hlöðufell, Bláfell and Gaesafjöll are located in Iceland. Further detailed images on each tuya are shown below.

### B1: Hlöðufell (KS88A, KS88B and KS97)





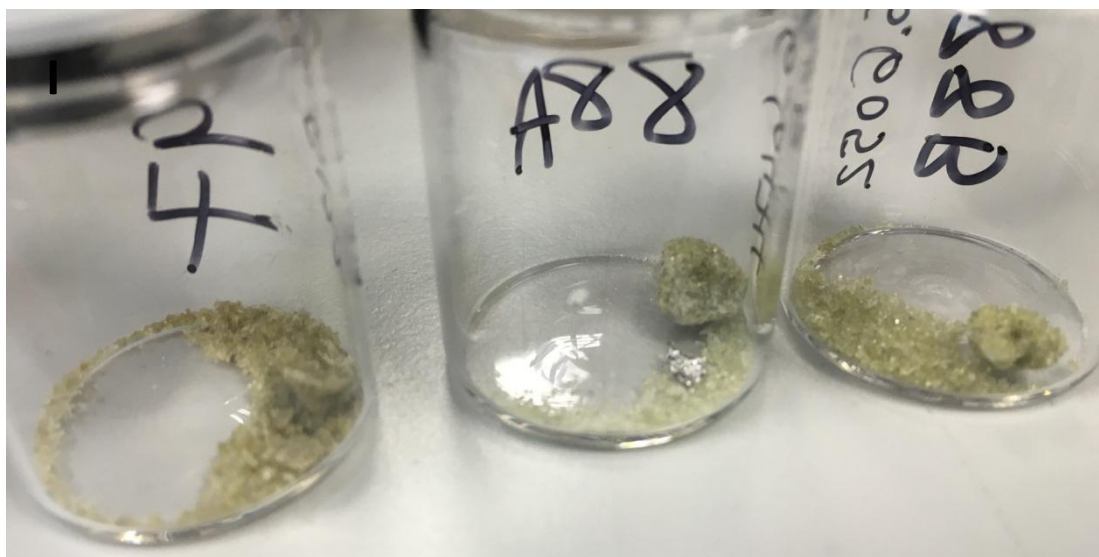
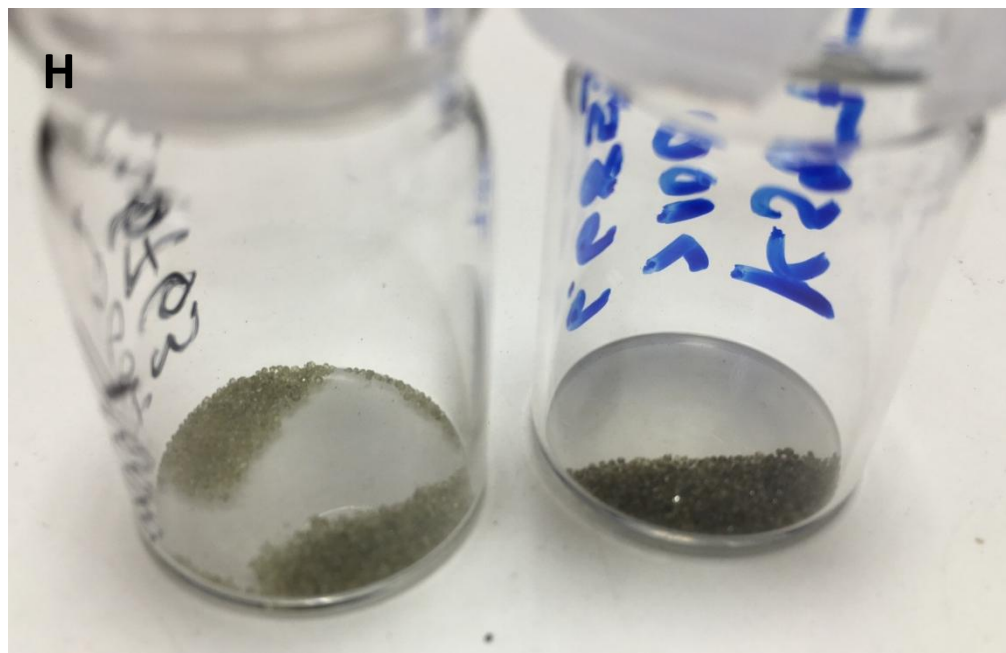
D



E

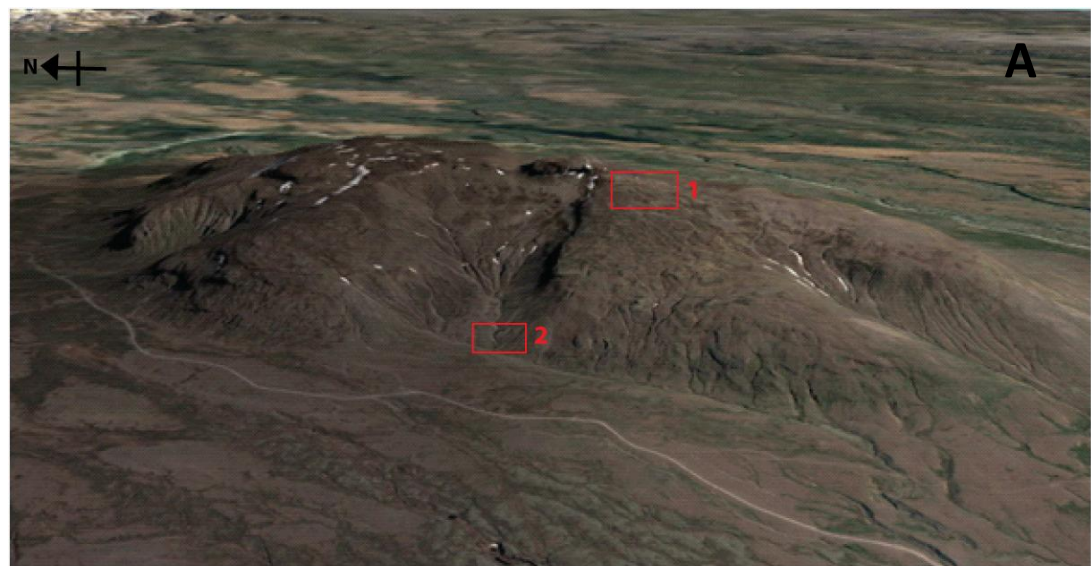




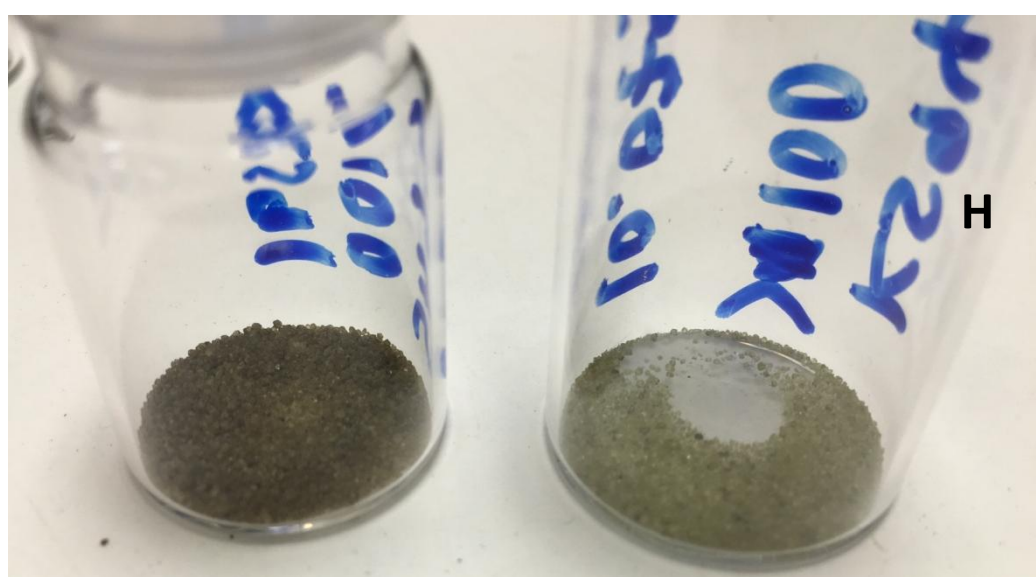
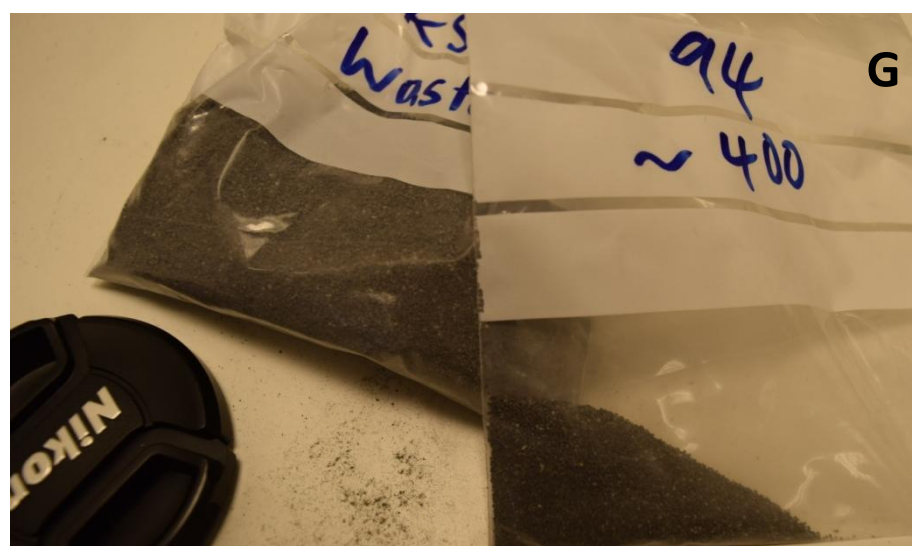


**Figure B1:** Sample context for Hlöðufell. **A:** Overview of Hlöðufell facing North showing both sampling areas. Box 1 shows cosmogenic eruption age sample (Photo B) and box 2 shows basal pillow lava sampling for eruption age dating (Photos C-F). **B:** Surface exposure sample showing visible ropey pahoehoe textures still remain with minimal erosion occurring (Surface Category 2 and Sample KS97). **C:** Meltwater gully used to acquire shielded pillow samples. Red box indicates where in the gully the sample was taken, facing North/North West into the gully. **D:** Photo showing sampling occurring facing South/South East out of the gully. **E:** Sampled pillow basalts in shielded gully. **F:** Pillow basalts after having been excised to ensure total shielding has occurred from all sides (Samples KS88A and KS88B). **G:** Bulk sample chopped into blocks and then crushed into various sized sections for picking. **H:** Picked olivine phenocrysts from KS88B and KS97. **I:** Samples of olivines after being heated in the furnace (KS97, KS88A and KS88B).

**B2: Bláfell (KS91 and KS94)**







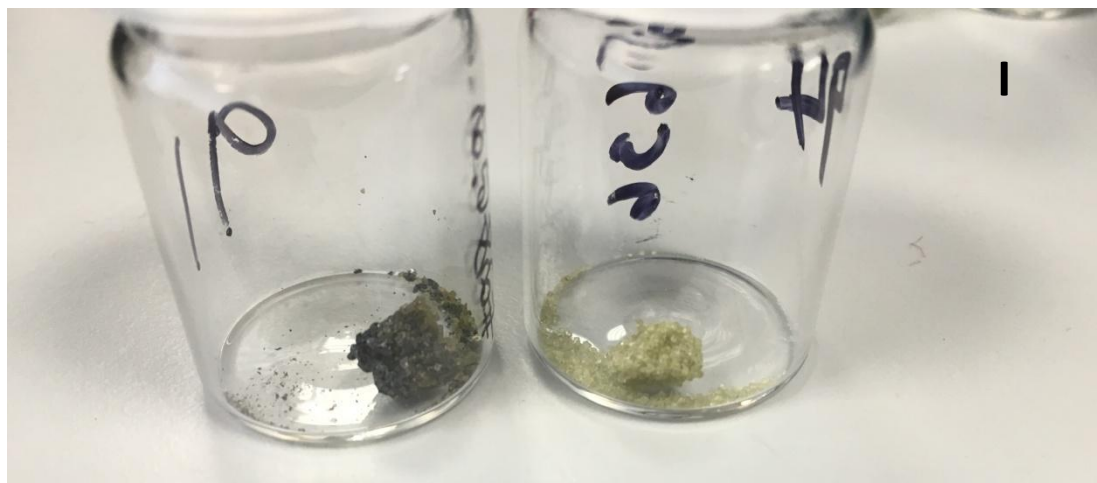


**Figure B2:** Sample context for Bláfell. **A:** Overview of Bláfell taken from Google Earth facing East showing points of sampling. Box 1 shows the location where the cosmogenic exposure age sample was taken (photos B - D) and box 2 shows where the basal pillow lavas for eruption age dating (photo E) was taken. **B:** Panoramic photo of the summit of Bláfell taken by author facing South-East. Note the very eroded blocky glaciated surface (Surface Category 4). **C:** Closer look of the glaciated blocky textures on the summit of Bláfell facing South. Cosmogenic exposure sample was taken from this exposure. **D:** Closer image of sampled block/boulder on summit of Bláfell for sample KS91. **E:** Basal pillow sample taken from slightly excised meltwater stream. Can see where starting to remove top layer of basalt to acquire shielded sample (Sample KS94). **F:** Bulk sample of KS94, with visible olivines. **G:** Different sections of sieving sample KS94. **H:** Olivine phenocrysts picked from samples KS91 and KS94. **I:** Olivine phenocrysts after being heated in the furnace.

### B3: Gaesafjöll (KS104 and KS106)





C



D



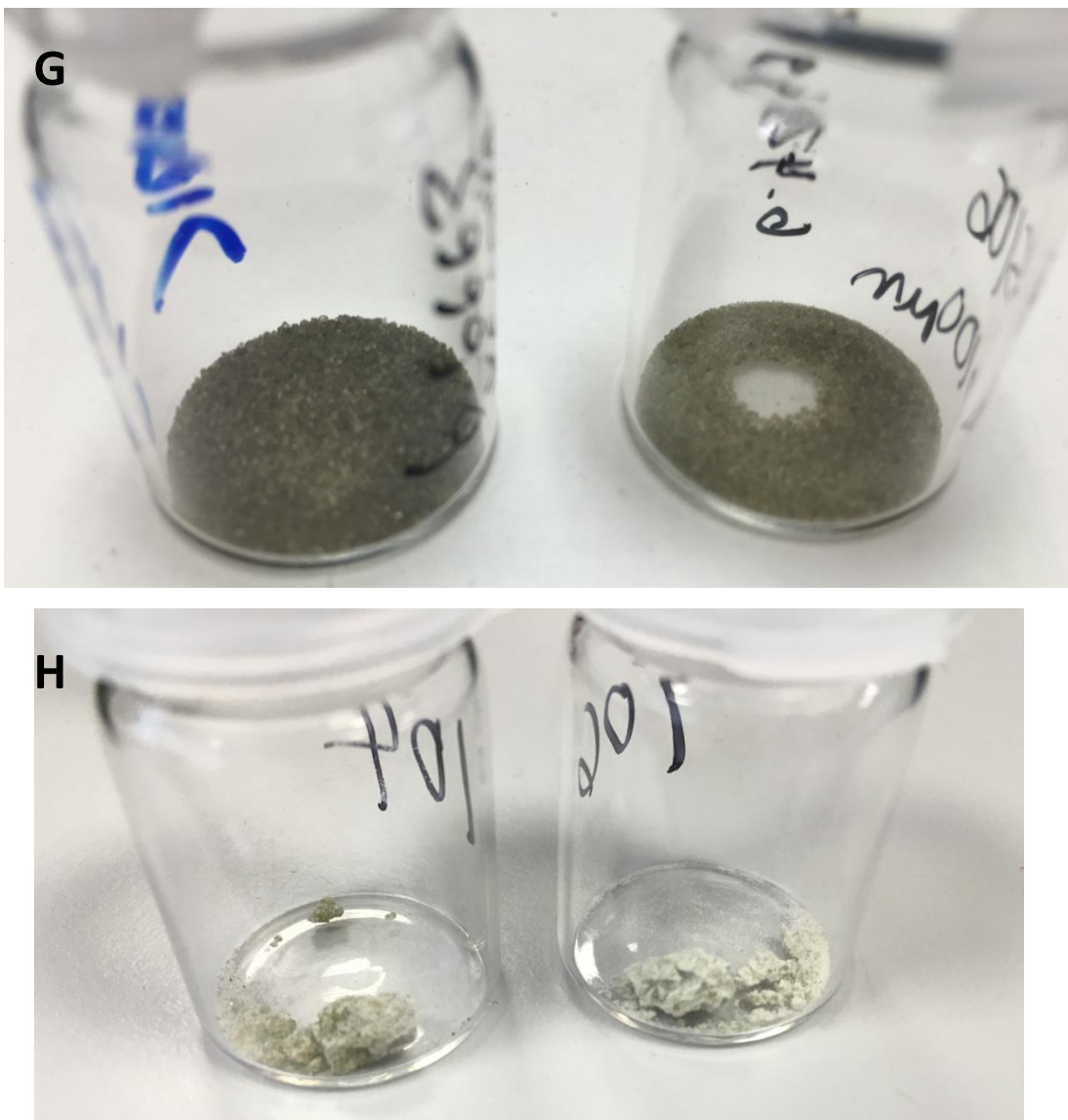


**Figure B3:** Sampling context for Gaesafjöll. **A:** Overview of Gaesafjöll showing sampling locations taken from Google Earth. Box 1 indicates where the cosmogenic exposure age sample was acquired (Photo B-C) and box 2 indicates where the basal pillow samples were taken for eruption age dating (Photo D-E). **B:** Photo of Dr. Dave McGarvie indicating the exposure sample location (Surface Category 2). **C:** Evidence of remaining pahoehoe textures with minimal erosion and excised sample spot (Sample KS104). **D:** Looking out of meltwater gully facing West. **E:** Pillow lavas within the meltwater gully with overhanging section above providing even more shielding (Sample KS106). **F:** Bag of bulk sample of KS106 and separate sections from sieving. **G:** Olivine phenocryst separates from picking. **H:** Olivine phenocryst once melted in the furnace.

## References

- ARAHAM, A. C., FRANCIS, D., & POLVÉ, M. 2005. Origin of Recent alkaline lavas by lithospheric thinning beneath the northern Canadian Cordillera. *Canadian Journal of Earth Sciences*, 42(6), 1073-1095.
- ACIEGO, S., KENNEDY, B., DEPAOLO, D. J., CHRISTENSEN, J. N. & HUTCHEON, I. 2003. U-Th/He age of phenocrystic garnet from the 79 AD eruption of Mt. Vesuvius. *Earth and Planetary Science Letters*, 216, 209-219.
- ACIEGO, S. M., DEPAOLO, D. J., KENNEDY, B. M., LAMB, M. P., SIMS, K. W. W. & DIETRICH, W. E. 2007. Combining He-3 cosmogenic dating with U-Th/He eruption ages using olivine in basalt. *Earth and Planetary Science Letters*, 254, 288-302.
- ACKERMANN, M., AJELLO, M., ALLAFORT, A., BALDINI, L., BALLET, J., BARBIELLINI, G., BARING, M. G., BASTIERI, D., BECHTOL, K., BELLAZZINI, R., BLANDFORD, R. D., BLOOM, E. D., BONAMENTE, E., BORGLAND, A. W., BOTTACINI, E., BRANDT, T. J., BREGEON, J., BRIGIDA, M., BRUEL, P., BUEHLER, R., BUSETTO, G., BUSON, S., CALIANDRO, G. A., CAMERON, R. A., CARAVEO, P. A., CASANDJIAN, J. M., CECCHI, C., ÇELIK, Ö., CHARLES, E., CHATY, S., CHAVES, R. C. G., CHEKHTMAN, A., CHEUNG, C. C., CHIANG, J., CHIARO, G., CILLIS, A. N., CIPRINI, S., CLAUS, R., COHEN-TANUGI, J., COMINSKY, L. R., CONRAD, J., CORBEL, S., CUTINI, S., D'AMMANDO, F., DE ANGELIS, A., DE PALMA, F., DERMER, C. D., DO COUTO E SILVA, E., DRELL, P. S., DRLICA-WAGNER, A., FALLETTI, L., FAVUZZI, C., FERRARA, E. C., FRANCKOWIAK, A., FUKAZAWA, Y., FUNK, S., FUSCO, P., GARGANO, F., GERMANI, S., GIGLIETTO, N., GIOMMI, P., GIORDANO, F., GIROLETTI, M., GLANZMAN, T., GODFREY, G., GRENIER, I. A., GRONDIN, M.-H., GROVE, J. E., GUIRIC, S., HADASCH, D., HANABATA, Y., HARDING, A. K., HAYASHIDA, M., HAYASHI, K., HAYS, E., HEWITT, J. W., HILL, A. B., HUGHES, R. E., JACKSON, M. S., JOGLER, T., JÓHANNESSON, G., JOHNSON, A. S., KAMAE, T., KATAOKA, J., KATSUTA, J., KNÖDLSEDER, J., KUSS, M., LANDE, J., LARSSON, S., LATRONICO, L., LEMOINE-GOUMARD, M., LONGO, F., LOPARCO, F., LOVELLETTE, M. N., LUBRANO, P., MADEJSKI, G. M., MASSARO, F., MAYER, M., MAZZIOTTA, M. N., MCENERY, J. E., et al. 2013. Detection of the Characteristic Pion-Decay Signature in Supernova Remnants. *Science*, 339, 807-811.
- ACKERT JR, R. P., SINGER, B. S., GUILLOU, H., KAPLAN, M. R. & KURZ, M. D. 2003. Long-term cosmogenic  $^3\text{He}$  production rates from  $^{40}\text{Ar}/^{39}\text{Ar}$  and K-Ar dated Patagonian lava flows at 47°S. *Earth and Planetary Science Letters*, 210, 119-136.
- ALBINO, F., PINEL, V., & SIGMUNDSSON, F. 2010. Influence of surface load variations on eruption likelihood: application to two Icelandic subglacial volcanoes, Grímsvötn and Katla. *Geophysical journal international*, 181(3), 1510-1524.
- ALLEGRE, C. J., T. STAUDACHER, P. SARDA, and M. KURZ. 1983, Constraints on evolution of Earth mantle from rare gas systematics, *Nature*, 303(5920), 762-766.

- ALLEGRE, C.-J., P. SARDA, and T. STAUDACHER. 1993, Speculations about the cosmic origin of He and Ne in the interior of the Earth, *Earth and Planetary Science Letters*, 117(1-2), 229-233.
- ALLEGRE, C. J., T. STAUDACHER, and P. SARDA. 1994, Speculations about the cosmic origin of He and Ne in the interior of the Earth; reply, *Earth and Planetary Science Letters*, 122(1-2), 249-250.
- ALLEN, C. C. 1979. Volcano-ice interactions on Mars. *Journal of Geophysical Research: Solid Earth (1978–2012)*, 84, 8048-8059.
- ALLEN, C. C. 1980. Icelandic subglacial volcanism: thermal and physical studies. *The Journal of Geology*, 108-117.
- ANDERSON, D. L. 1998, A model to explain the various paradoxes associated with mantle noble gas geochemistry, *Proceedings of the National Academy of Sciences of the United States of America*, 96(16), 9087-9092.
- BÄHR, R., LIPPOLT, H. J., & WERNICKE, R. S. 1994. Temperature-induced  $^4\text{He}$  degassing of specularite and botryoidal hematite: A  $^4\text{He}$  retentivity study. *Journal of Geophysical Research: Solid Earth*, 99(B9), 17695-17707.
- BALLENTINE, C. J., and G. HOLLAND. 2008, What  $\text{CO}_2$  well gases tell us about the origin of noble gases in the mantle and their relationship to the atmosphere, *Philosophical transactions. Series A, Mathematical, physical, and engineering sciences*, 366(1883), 4183-4203.
- BALCO, G., STONE, J. O., LIFTON, N. A. & DUNAI, T. J. 2008. A complete and easily accessible means of calculating surface exposure ages or erosion rates from  $^{10}\text{Be}$  and  $^{26}\text{Al}$  measurements. *Quaternary Geochronology*, 3, 174-195.
- BALLENTINE, C. J. & BURNARD, P. G. 2002. Production, Release and Transport of Noble Gases in the Continental Crust. *Reviews in Mineralogy and Geochemistry*, 47, 481-538.
- BELL, R. E. 2008. The role of subglacial water in ice-sheet mass balance. *Nature Geoscience*, 1(5), 297-304.
- BELTON, D.X., KOHN, B.P., GLEADOW, A.J.W., 2004a. Quantifying bexcess heliumQ: some of the issues and assumptions in combined (U-Th)/He and fission track analysis. In: Andressien, P. (Ed.), 10th International Fission track Dating Conference. Amsterdam, pp. 18.
- BELTON, D.X., LORENCAK, M., CARTER, T.J., NORMAN, M., KOHN, B.P., GLEADOW, A.J.W., 2004b. Samarium in apatite: contributions to radiogenic helium and the effect on (U-Th)/He thermochronology. In: Andressien, P. (Ed.), 10th International Fission track Dating Conference. Amsterdam, pp. 40.
- BEST, M. G. 2009. *Igneous and metamorphic petrology*, Wiley-Blackwell.
- BJÖRNSSON, H. & EINARSSON, P. 1990. Volcanoes beneath Vatnajökull, Iceland: Evidence from radio echo-sounding, earthquakes and jökulhlaups. *Jökull*, 147-168.
- BJÖRNSSON, H. 2003. Subglacial lakes and jökulhlaups in Iceland. *Global and Planetary Change*, 35, 255-271.
- BLACKBURN, T. J., STOCKLI, D. F. & WALKER, J. D. 2007. Magnetite (U-Th)/He dating and its application to the geochronology of intermediate to mafic volcanic rocks. *Earth and Planetary Science Letters*, 259, 360-371.
- BLARD, P. H., PIK, R., LAVÉ, J., BOURLÈS, D., BURNARD, P. G., YOKOCHI, R., MARTY, B. & TRUSDELL, F. 2006. Cosmogenic  $^3\text{He}$

- production rates revisited from evidences of grain size dependent release of matrix-sited helium. *Earth and Planetary Science Letters*, 247, 222-234.
- BLARD, P. H., PUCHOL, N. & FARLEY, K. A. 2008. Constraints on the loss of matrix-sited helium during vacuum crushing of mafic phenocrysts. *Geochimica et Cosmochimica Acta*, 72, 3788-3803.
- BLARD, P.-H. & FARLEY, K. 2008. The influence of radiogenic  ${}^4\text{He}$  on cosmogenic  ${}^3\text{He}$  determinations in volcanic olivine and pyroxene. *Earth and Planetary Science Letters*, 276, 20-29.
- BOURDON, B., ZINDLER, A., ELLIOTT, T. & LANGMUIR, C. 1996. Constraints on mantle melting at mid-ocean ridges from global  ${}^{238}\text{U}$ - ${}^{230}\text{Th}$  disequilibrium data.
- BOURDON, B., TURNER, S., HENDERSON, G. M. & LUNDSTROM, C. C. 2003. Introduction to U-series geochemistry. *Reviews in mineralogy and geochemistry*, 52, 1-21.
- BOURGEOIS, O., DAUTEUIL, O. & VAN VLIET-LANOUE, B. 1998. Pleistocene subglacial volcanism in Iceland: tectonic implications. *Earth and Planetary Science Letters*, 164, 165-178.
- BOURGEOIS, O., DAUTEUIL, O. & VAN VLIET-LANOUE, B. 2000. Geothermal control on flow patterns in the last glacial maximum ice sheet of Iceland. *Earth Surface Processes and Landforms*, 25, 59-76.
- BRADWELL, T. (2001). A new lichenometric dating curve for southeast Iceland. *Geografiska Annaler: Series A, Physical Geography*, 83(3), 91-101.
- BROWN, E. T., BROOK, E. J. & RAISBECKL, G. M. 1992. EFFECTIVE ATTENUATION LENGTHS OF COSMIC RAYS PRODUCING. *Geophysical Research Letters*, 19, 369-372.
- BURNARD, P. G., STUART, F. M., TURNER, G., & OSKARSSON, N. 1994. Air contamination of basaltic magmas: implications for high  ${}^3\text{He}/{}^4\text{He}$  mantle Ar isotopic composition. *Journal of Geophysical Research: Solid Earth*, 99(B9), 17709-17715.
- BURNARD, P., D. GRAHAM, and G. TURNER. 1997, Vesicle-specific noble gas analyses of "popping rock"; implications for primordial noble gases in Earth, *Science*, 276(5312), 568-571.
- BURNARD, P., and D. HARRISON. 2005, Argon isotope constraints on modification of oxygen isotopes in Iceland Basalts by surficial processes, *Chemical Geology*, 216(1-2), 143-156.
- CAPRA, L., ROVERATO, M., GROPPELLI, G., CABALLERO, L., SULPIZIO, R., & NORINI, G. 2015. Glacier melting during lava dome growth at Nevado de Toluca volcano (Mexico): Evidences of a major threat before main eruptive phases at ice-capped volcanoes. *Journal of Volcanology and Geothermal Research*, 294, 1-10.
- CARRIVICK, J. L., RUSSELL, A. J., RUSHMER, E. L., TWEED, F. S., MARREN, P. M., DEEMING, H. & LOWE, O. J. 2009. Geomorphological evidence towards a de- glacial control on volcanism. *Earth Surface Processes and Landforms*, 34, 1164-1178.
- CERLING, T. 1990. Dating geomorphologic surfaces using cosmogenic  ${}^3\text{He}$ . *Quaternary Research*, 33, 148-156.
- CERLING, T. E. & CRAIG, H. 1994. Cosmogenic  ${}^3\text{He}$  production rates from  $39^\circ\text{N}$  to  $46^\circ\text{N}$  latitude, western USA and France. *Geochimica et Cosmochimica Acta*, 58, 249-255.

- CHAPMAN, M. G., TANAKA, K. L. 2001. The interior trough deposits on Mars: sub-ice volcanoes? *J. Geophys. Res.*, 106, 10087-10100.
- CHAPMAN, M.G., SMELLIE, J. L. 2007. Mars interior layered deposits and terrestrial sub-ice volcanoes compared: observations and interpretations of similar geomorphic characteristics. *The Geology of Mars: Evidence from Earth-based analogues*. Cambridge University Press, Cambridge. 178-210
- CLARKE, G. K., CROSS, G. M., & BENSON, C. S. 1989. Radar imaging of glaciovolcanic stratigraphy, Mount Wrangell caldera, Alaska: interpretation model and results. *Journal of Geophysical Research: Solid Earth*, 94(B6), 7237-7249.
- COMPTON, A. H. & TURNER, R. N. 1937. Cosmic Rays on the Pacific Ocean. *Physical Review*, 52, 799-814.
- CONDOMINES, M., GRÖNVOLD, K., HOOKER, P. J., MUEHLENBACHS, K., O'NIONS, R. K., OSKARSSON, N., & OXBURGH, E. R. 1983. Helium, oxygen, strontium and neodymium isotopic relationships in Icelandic volcanics. *Earth and Planetary Science Letters*, 66, 125-136.
- COX, S. E., FARLEY, K. A., & HEMMING, S. R. 2012. Insights into the age of the Mono Lake Excursion and magmatic crystal residence time from (U-Th)/He and  $^{230}\text{Th}$  dating of volcanic allanite. *Earth and Planetary Science Letters*, 319, 178-184.
- CRAIG, H., and J. E. LUPTON. 1976, Primordial neon, helium, and hydrogen in oceanic basalts, *Earth and Planetary Science Letters*, 31(3), 369-385.
- DAMON, P. E. 1957. Determination of radiogenic helium in zircon by stable isotope dilution technique. *Eos, Transactions American Geophysical Union*, 38(6), 945-953.
- DEMETS, C., GORDON, R. G., ARGUS, D. F. & STEIN, S. 1994. Effect of recent revisions to the geomagnetic reversal time scale on estimates of current plate motions. *Geophysical research letters*, 21, 2191-2194.
- DESILETS, D. & ZREDA, M. 2003. Spatial and temporal distribution of secondary cosmic-ray nucleon intensities and applications to in situ cosmogenic dating. *Earth and Planetary Science Letters*, 206, 21-42.
- DESILETS, D., ZREDA, M. & PRABU, T. 2006. Extended scaling factors for in situ cosmogenic nuclides: New measurements at low latitude. *Earth and Planetary Science Letters*, 246, 265-276.
- DIXON, E. T., M. HONDA, I. MCDOUGALL, I. H. CAMPBELL, and I. SIGURDSSON. 2000, Preservation of near-solar neon isotopic ratios in Icelandic basalts, *Earth and Planetary Science Letters*, 180(3-4), 309-324.
- DIXON, J. E., Filiberto, J. R., Moore, J. G., & Hickson, C. J. 2002. Volatiles in basaltic glasses from a subglacial volcano in northern British Columbia (Canada): implications for ice sheet thickness and mantle volatiles. *Geological Society, London, Special Publications*, 202(1), 255-271.
- DIXON, E. T. 2003, Interpretation of helium and neon isotopic heterogeneity in Icelandic basalts, *Earth and Planetary Science Letters*, 206(1-2), 83-99.
- DUGMORE, A. J., COOK, G., SHORE, J., NEWTON, A. J., EDWARDS, K. J. & LARSEN, G. 2006. Radiocarbon dating tephra layers in Britain and Iceland. *Radiocarbon*, 37, 379-388.
- DUNAI, T. J., & ROSELIEB, K. 1996. Sorption and diffusion of helium in garnet: implications for volatile tracing and dating. *Earth and planetary science letters*, 139(3), 411-421.

- DUNAI, T. J. 2000. Scaling factors for production rates of in situ produced cosmogenic nuclides: a critical reevaluation. *Earth and Planetary Science Letters*, 176, 157-169.
- DUNAI, T. J. & WIJBRANS, J. R. 2000. Long-term cosmogenic  $^{3}\text{He}$  production rates (152 ka–1.35 Ma) from  $^{40}\text{Ar}/^{39}\text{Ar}$  dated basalt flows at 29°N latitude. *Earth and Planetary Science Letters*, 176, 147-156.
- DUNAI, T. J. 2001a. Influence of secular variation of the geomagnetic field on production rates of in situ produced cosmogenic nuclides. *Earth and Planetary Science Letters*, 193, 197-212.
- DUNAI, T. J. 2001b. Reply to comment onScaling factors for production rates of in situ produced cosmogenic nuclides: a critical reevaluation'by Darin Desilets, Marek Zreda and Nathaniel Lifton. *Earth and Planetary Science Letters*, 188, 298.
- DUNAI, T. J., STUART, F. M., PIK, R., BURNARD, P. & GAYER, E. 2007. Production of $<\sup>3</sup>$  He in crustal rocks by cosmogenic thermal neutrons. *Earth and Planetary Science Letters*, 258, 228-236.
- DUNAI, T. 2010. Cosmogenic Nuclides: Principles. *Concepts and Applications in the Earth*.
- DUNCAN, R. & HOGAN, L. 1994. Radiometric dating of young MORB using the  $^{40}\text{Ar}-^{39}\text{Ar}$  incremental heating method. *Geophysical Research Letters*, 21, 1927-1930.
- EASON, D. E., & SINTON, J. M. 2009. Lava shields and fissure eruptions of the Western Volcanic Zone, Iceland: Evidence for magma chambers and crustal interaction. *Journal of Volcanology and Geothermal Research*, 186(3), 331-348.
- EASON, D.E., SINTON, J.M., GRÖNVOLD, K., KURZ, M.D., Effects of deglaciation on the petrology and eruptive history of the Western Volcanic Zone, Iceland. 2015. *Bull Volcanol*, 77:47
- EDWARDS, R. R., RUSSELL, J. K. 2002. Glacial influence on the morphology and eruption products of Hoodoo Mountain volcano, northwestern British Columbia, in: J.L. Smellie, M.G. Chapman (Eds), *Volcano-ice Interaction on Earth and Mars*, Geological Society of London Special Publication 202, 179-194
- EDWARDS, B. R., TUFFEN, H., SKILLING, I., WILSON, L. 2009. Introduction to special issue on volcano-ice interactions on Earth and Mars: the state of the science. *J. Volcanol. Geotherm. Res.*, 185, 247-250.
- EDWARDS, B. R., RUSSELL, J. K., SIMPSON, K. 2011. Volcanology and petrology of Mathews Tuya, northern British Columbia, Canada: glaciovolcanic constraints on interpretations of the 0.730 Ma Cordilleran paleoclimate, *Bull Volcanol.*, 73, 479-496.
- EHLERS, T. A. & FARLEY, K. A. 2003. Apatite (U-Th)/He thermochronometry: methods and applications to problems in tectonic and surface processes. *Earth and Planetary Science Letters*, 206, 1-14.
- EIDELMAN, S., HAYES, K. G., OLIVE, K. A., AGUILAR-BENITEZ, M., AMSLER, C., ASNER, D., BABU, K. S., BARNETT, R. M., BERINGER, J., BURCHAT, P. R., CARONE, C. D., CASO, S., CONFORTO, G., DAHL, O., D'AMBROSIO, G., DOSER, M., FENG, J. L., GHERGHETTA, T., GIBBONS, L., GOODMAN, M., GRAB, C., GROOM, D. E., GURTU, A., HAGIWARA, K., HERNÁNDEZ-REY, J. J., HIKASA, K., HONSCHIED, K., JAWAHERY, H., KOLDA, C., KWON,

- Y., MANGANO, M. L., MANOHAR, A. V., MARCH-RUSSELL, J., MASONI, A., MIQUEL, R., MÖNIG, K., MURAYAMA, H., NAKAMURA, K., NAVAS, S., PAPE, L., PATRIGNANI, C., PIEPK, A., RAFFELT, G., ROOS, M., TANABASHI, M., TERNING, J., TÖRNQVIST, N. A., TRIPPE, T. G., VOGEL, P., WOHL, C. G., WORKMAN, R. L., YAO, W. M., ZYLA, P. A., ARMSTRONG, B., GEE, P. S., HARPER, G., LUGOVSKY, K. S., LUGOVSKY, S. B., LUGOVSKY, V. S., ROM, A., ARTUSO, M., BARBERIO, E., BATTAGLIA, M., BICHSEL, H., BIEBEL, O., BLOCH, P., CAHN, R. N., CASPER, D., CATTAI, A., CHIVUKULA, R. S., COWAN, G., DAMOUR, T., DESLER, K., DOBBS, M. A., DREES, M., EDWARDS, A., EDWARDS, D. A., ELVIRA, V. D., ERLER, J., EZHELA, V. V., FETSCHER, W., FIELDS, B. D., FOSTER, B., FROIDEVAUX, D., FUKUGITA, M., GAISSER, T. K., GARREN, L., GERBER, H. J., GERBIER, G., GILMAN, F. J., HABER, H. E., HAGMANN, C., HEWETT, J., HINCHLIFFE, I., HOGAN, C. J., HÖHLER, G., IGO-KEMENES, P., JACKSON, J. D., JOHNSON, K. F., KARLEN, D., et al. 2004. Review of Particle Physics. *Physics Letters B*, 592, 1-5.
- EINARSSON, M. A. 1988. Precipitation in southwestern Iceland. *Jokull*, 38, 61-67.
- EINARSSON, T. & ALBERTSSON, K. J. 1988. The glacial history of Iceland during the past three million years. *Philosophical Transactions of the Royal Society of London. B, Biological Sciences*, 318, 637-644.
- ELSASSER, W. & WINCKLER, E. N. J. 1956. Cosmic-ray intensity and geomagnetism.
- EYSTEINSSON, H. & GUNNARSSON, K. 1995. Maps of gravity, bathymetry and magnetics for Iceland and surroundings. *Orkustofnun*.
- FANALE, F. P., & KULP, J. L. 1962. The helium method and the age of the Cornwall, Pennsylvania magnetite ore. *Economic Geology*, 57(5), 735-746.
- FARLEY, K. A., WOLF, R. A. & SILVER, L. T. 1996. The effects of long alpha-stopping distances on (U-Th)/He ages. *Geochimica et Cosmochimica Acta*, 60, 4223-4229.
- FARLEY, K. A. 2002. (U-Th)/He dating: Techniques, calibrations, and applications. In: PORCELLI, D., BALLENTINE, C. J. & WIELER, R. (eds.) *Noble Gases in Geochemistry and Cosmochemistry*.
- FARLEY, K. A., & STOCKLI, D. F. 2002. (U-Th)/He dating of phosphates: Apatite, monazite, and xenotime. *Reviews in mineralogy and geochemistry*, 48(1), 559-577.
- FARLEY, K., KOHN, B. & PILLANS, B. 2002. The effects of secular disequilibrium on (U-Th)/He systematics and dating of Quaternary volcanic zircon and apatite. *Earth and Planetary Science Letters*, 201, 117-125.
- FISHER, R. V. & SCHMINCKE, H. U. 1985. R. V. Fisher & H.-U. Schmincke 1984. *Pyroclastic Rocks*. xiv + 472 pp. Berlin, Heidelberg, New York, Tokyo: Springer-Verlag. ISBN 3 540 12756 9. *Geological Magazine*, 122, 216-216.
- FITZGERALD, P. G., BALDWIN, S. L., WEBB, L. E., & O'SULLIVAN, P. B. 2006. Interpretation of (U-Th)/He single grain ages from slowly cooled crustal terranes: a case study from the Transantarctic Mountains of southern Victoria Land. *Chemical Geology*, 225(1), 91-120.

- FLOWERS, G.E., BJÖRNSSON, H., GEIRSDÓTTIR, Á., MILLER, G.H., BLACK, J.L., CLARKE, G.K.C. 2008. Holocene climate conditions and glacier variation in central Iceland from physical modelling and empirical evidence. *Quat Sci Rev*, 27:797-813.
- FLUDE, S., MCGARVIE, D. W., BURGESS, R. & TINDLE, A. G. 2010. Rhyolites at Kerlingarfjöll, Iceland: the evolution and lifespan of silicic central volcanoes. *Bulletin of Volcanology*, 72, 523-538.
- FOULGER, G. R. 2002. Plumes, or plate tectonic processes? *Astronomy & Geophysics*, 43, 6.19-6.24.
- FOULGER, G. 2006. Older crust underlies Iceland. *Geophysical Journal International*, 165, 672-676.
- FRIEDLANDER, M. W. 1989. Cosmic rays.
- FÜRI, E., HILTON, D. R., HALLDÓRSSON, S. A., BARRY, P. H., HAHM, D., FISCHER, T. P., & GRÖNVOLD, K. 2010. Apparent decoupling of the He and Ne isotope systematics of the Icelandic mantle: the role of He depletion, melt mixing, degassing fractionation and air interaction. *Geochimica et cosmochimica acta*, 74(11), 3307-3332.
- FURMAN, T., FREY, F., & PARK, K. H. 1995. The scale of source heterogeneity beneath the Eastern neovolcanic zone, Iceland. *Journal of the Geological Society*, 152(6), 997-1002.
- GAYER, E., MUKHOPADHYAY, S. & MEADE, B. J. 2008. Spatial variability of erosion rates inferred from the frequency distribution of cosmogenic  $^{3}\text{He}$  in olivines from Hawaiian river sediments. *Earth and Planetary Science Letters*, 266, 303-315.
- GEE, M. M., TAYLOR, R. N., THIRLWALL, M. F., & MURTON, B. J. 1998. Glacioisostacy controls chemical and isotopic characteristics of tholeiites from the Reykjanes Peninsula, SW Iceland. *Earth and Planetary Science Letters*, 164(1), 1-5.
- GEIRSDÓTTIR, Á., HARDARDÓTTIR, J., & ANDREWS, J. T. 2000. Late-Holocene terrestrial glacial history of Miki and IC Jacobsen fjords, East Greenland. *The Holocene*, 10(1), 123-134.
- GEIRSDÓTTIR, Á., MILLER, G. H., & ANDREWS, J. T. 2007. Glaciation, erosion, and landscape evolution of Iceland. *Journal of Geodynamics*, 43(1), 170-186.
- GEMSOORRM, A. & EIRIKSSON, J. 1994. Growth of an intermittent ice sheet in Iceland during the late Pliocene and early Pleistocene. *Quaternary research*, 42, 115-130.
- GHATAN, G. J., HEAD, I. I. I. J. W. 2002. Candidate subglacial volcanoes in the south polar region of Mars: morphometry and eruption conditions, *J. Geophys. Res.* 107, E7.
- GIBBARD, P. & COHEN, K. M. 2008. Global chronostratigraphical correlation table for the last 2.7 million years. *Episodes*, 31, 243.
- GOEHRING, B. M., KURZ, M. D., BALCO, G., SCHAEFER, J. M., LICCIARDI, J. & LIFTON, N. 2010. A reevaluation of *in situ* cosmogenic  $^{3}\text{He}$  production rates. *Quaternary Geochronology*, 5, 410-418.
- GOODFELLOW, B.W. 2007. Relict non-glacial surfaces in formerly glaciated landscapes. *Earth-Sci Rev.* 80:47-73.
- GOSSE, J. C. & PHILLIPS, F. M. 2001. Terrestrial *in situ* cosmogenic nuclides: theory and application. *Quaternary Science Reviews*, 20, 1475-1560.

- GRAHAM, D. W., LARSEN, L. M., HANAN, B. B., STOREY, M., PEDERSEN, A. K., & LUPTON, J. E. 1998. Helium isotope composition of the early Iceland mantle plume inferred from the Tertiary picrites of West Greenland. *Earth and Planetary Science Letters*, 160.3, 241-255
- GRAHAM, D. W. 2002, Noble gas isotope geochemistry of mid-ocean ridge and ocean island basalts; characterization of mantle source reservoirs, *Reviews in Mineralogy and Geochemistry*, 47, 247-317.
- GRAHAM, D. W., HANAN, B. B., HÉMOND, C., BLICHER-TофT, J., & ALBARÈDE, F. 2014. Helium isotopic textures in Earth's upper mantle. *Geochemistry, Geophysics, Geosystems*, 15(5), 2048-2074.
- GROOM, D. E., MOKHOV, N. V. & STRIGANOV, S. I. 2001. MUON STOPPING POWER AND RANGE TABLES 10 MeV–100 TeV. *Atomic Data and Nuclear Data Tables*, 78, 183-356.
- GROVE, E. W. 1974. Deglaciation - A possible triggering mechanism for recent volcanism. *Proceedings of the Symposium on Andean and Antarctic Volcanology Problems, Rome: IAVCEI*. 88-97.
- GUDMUNDSSON, A. 1986. Mechanical aspects of postglacial volcanism and tectonics of the Reykjanes Peninsula, southwest Iceland. *Journal of Geophysical Research: Solid Earth (1978–2012)*, 91, 12711-12721.
- GUDMUNDSSON, M. T., SIGMUNDSSON, F. & BJORNSSON, H. 1997. Ice-volcano interaction of the 1996 Gjálp subglacial eruption, Vatnajökull, Iceland. *Nature*, 389, 954-957.
- GUDMUNDSSON, M., PÁLSSON, F., BJÖRNSSON, H. & HÖGNADÓTTIR, H. 2002. The hyaloclastite ridge formed in the subglacial 1996 eruption in Gjálp, Vatnajökull, Iceland: present day shape and future preservation. *Geological Society, London, Special Publications*, 202, 319-335.
- GUDMUNDSSON, M. T., PEDERSEN, R., VOGFJÖRD, K., THORBJARNARDÓTTIR, B., JAKOBSDÓTTIR, S. & ROBERTS, M. J. 2010. Eruptions of Eyjafjallajökull Volcano, Iceland. *Eos, Transactions American Geophysical Union*, 91, 190-191.
- GUENTHNER, W. R., REINERS, P. W., KETCHAM, R. A., NASDALA, L., & GIESTER, G. 2013. Helium diffusion in natural zircon: Radiation damage, anisotropy, and the interpretation of zircon (U-Th)/He thermochronology. *American Journal of Science*, 313(3), 145-198.
- HAFLIDASON, H., EIRIKSSON, J., & KREVELD, S. V. (2000). INVITED CONTRIBUTION-The tephrochronology of Iceland and the North Atlantic region during the Middle and Late Quaternary: A review. *Journal of Quaternary Science*, 15(1), 3-22.
- HALL, K. 1982. Rapid deglaciation as an initiator of volcanic activity: an hypothesis. *Earth Surface Processes and Landforms*, 7, 45-51.
- HARDARSON, B., FITTON, J., ELLAM, R. & PRINGLE, M. 1997. Rift relocation—a geochemical and geochronological investigation of a palaeorift in northwest Iceland. *Earth and Planetary Science Letters*, 153, 181-196.
- HARRISON, D., BURNARD, P. and TURNER, G. 1999, Noble gas behaviour and composition in the mantle: constraints from the Iceland Plume, *Earth and Planetary Science Letters*, 171(2), 199-207.
- HARROP, P. J. 1996. Dating recent surface processes using cosmic ray generated  ${}^3\text{He}$  in rocks. Doctor of Philosophy. University of Manchester

- HART, S. R. 1984. He diffusion in olivine. *Earth and Planetary Science Letters*, 70, 297-302.
- HART, J. K. 1995. Subglacial erosion, deposition and deformation associated with deformable beds. *Progress in Physical Geography*, 19(2), 173-191.
- HAWKESWORTH, C., and SCHERSTÉN, A. 2007, Mantle plumes and geochemistry, *Chemical Geology*, 241(3-4), 319-331.
- HEISINGER, B., LAL, D., JULL, A., KUBIK, P., IVY-OCHS, S., KNIE, K. & NOLTE, E. 2002a. Production of selected cosmogenic radionuclides by muons: 2. Capture of negative muons. *Earth and Planetary Science Letters*, 200, 357-369.
- HEISINGER, B., LAL, D., JULL, A., KUBIK, P., IVY-OCHS, S., NEUMAIER, S., KNIE, K., LAZAREV, V. & NOLTE, E. 2002b. Production of selected cosmogenic radionuclides by muons: 1. Fast muons. *Earth and Planetary Science Letters*, 200, 345-355.
- HELGASON, J. 1984. Frequent shifts of the volcanic zone in Iceland. *Geology*, 12, 212-216.
- HELGASON, J., and DUNCAN, R. A. 2001. Glacial-interglacial history of the Skaftafell region, southeast Iceland, 0–5 Ma. *Geology*, 29(2), 179-182.
- HELMBERGER, D. V., WEN, L. and DING, X. 1998, Seismic evidence that the source of the Iceland hotspot lies at the core-mantle boundary, *Nature* (London), 396(6708), 251-255.
- HICKSON, C. J., MOORE, J. G., CALK, L. & METCALFE, P. 1995. Intraglacial volcanism in the Wells Gray-Clearwater volcanic field, east-central British Columbia, Canada. *Canadian Journal of Earth Sciences*, 32, 838-851.
- HILTON, D. R., GRONVOLD, K., O'NIIONS, R. K., and OXBURGH, E. R. 1990, Regional distribution of super  $^3\text{He}$  anomalies in the Icelandic crust, *Chemical Geology*, 88(1-2), 53-67.
- HILTON, D. R., HAMMERSCHMIDT, K., LOOCK, G., & FRIEDRICHSEN, H. 1993. Helium and argon isotope systematics of the central Lau Basin and Valu Fa Ridge: Evidence of crust/mantle interactions in a back-arc basin. *Geochimica et Cosmochimica Acta* 57.12: 2819-2841
- HILTON, D. R., K. GRONVOLD, C. G. MACPHERSON, and P. R. CASTILLO. 1999, Extreme super  $^3\text{He}$ /super  $^4\text{He}$  ratios in Northwest Iceland; constraining the common component in mantle plumes, *Earth and Planetary Science Letters*, 173(1-2), 53-60.
- HIYAGON, H., OZIMA, M., MARTY, B., ZASHU, S., & SAKAI, H. 1992. Noble gases in submarine glasses from mid-oceanic ridges and Loihi seamount: constraints on the early history of the Earth. *Geochimica et Cosmochimica Acta*, 56(3), 1301-1316.
- HJARTARSON, A. 1988. The Thjorsa lava the largest Holocene lava flow on earth. *Naturufraedgurinn*, 58, 116.
- HOFMANN, A. W., Farnetani C. G., Spiegelman M., and Class G. 2011, Displaced helium and carbon in the Hawaiian plume, *Earth and Planetary Science Letters*, 312(1-2), 226-236.
- HOPPE, G. 1968. Grimsey and the maximum extent of the last glaciation of Iceland. *Geografiska Annaler. Series A. Physical Geography*, 16-24.
- HÖSKULDSSON, A., SPARKS, R. S. & CARROLL, M. R. 2006. Constraints on the dynamics of subglacial basalt eruptions from geological and

- geochemical observations at Kverkfjöll, NE-Iceland. *Bulletin of volcanology*, 68, 689-701.
- HOUSE, M. A., WERNICKE, B. P., FARLEY, K. A., & DUMITRU, T. A. (1997). Cenozoic thermal evolution of the central Sierra Nevada, California, from (U Th)/He thermochronometry. *Earth and Planetary Science Letters*, 151(3), 167-179.
- HOUSE, M. A., WERNICKE, B. P. & FARLEY, K. A. 1998. Dating topography of the Sierra Nevada, California, using apatite (U-Th)/He ages. *Nature*, 396, 66-69.
- HUBBARD, A., SUGDEN, D., DUGMORE, A., NORDDAHL, H. & PÉTURSSON, H. G. 2006. A modelling insight into the Icelandic Last Glacial Maximum ice sheet. *Quaternary Science Reviews*, 25, 2283-2296.
- HURLEY, P. M. 1952. Alpha ionization damage as a cause of low helium ratios. *Eos, Transactions American Geophysical Union*, 33(2), 174-183.
- HYUYBERS, P., & LANGMUIR, C. 2009. Feedback between deglaciation, volcanism, and atmospheric CO<sub>2</sub>. *Earth and Planetary Science Letters*, 286(3), 479-491.
- IMBRIE, J., HAYES, J. D., MARTINSON, D. G., MCINTYRE, A., MIX, A. C., MORLEY, J. J., PISIAS, N. G., PRELL, W. L. & SHACKLETON, N. J. 1984. The orbital theory of Pleistocene climate: support from a revised chronology of the marine d<sub>18</sub>O record. *Milankovitch and climate. Proc. NATO workshop, Palisades, 1982. Vol. 1*, 269-305.
- INGÓLFSSON, Ó. (ed.) 1991. *A review of the Late Weichselian and early Holocene glacial and environmental history of Iceland*, in: (eds.), Dordrecht: Kluwer.
- INGÓLFSSON, Ó., NORDDAHL, H. & HAFLIDASON, H. 1995. Rapid isostatic rebound in southwestern Iceland at the end of the last glaciation. *Boreas*, 24, 245-259.
- INGÓLFSSON, Ó. & NORDDAHL, H. 2001. High relative sea level during the Bolling Interstadial in western Iceland: A reflection of ice-sheet collapse and extremely rapid glacial unloading. *Arctic, Antarctic, and Alpine Research*, 231-243.
- JAKOBSSON, S. P. 1979. 8. *Outline of the Petrology of Iceland*, Museum of Natural History, Department of Geology and Geography.
- JAKOBSSON, S. P. & GUDMUNDSSON, M. T. 2008. Subglacial and intraglacial volcanic formations in Iceland. *Jokull*, 58, 179-196.
- JAKOBSSON, S. P., JONASSON, K. & SIGURDSSON, I. A. 2008. The three igneous rock series of Iceland. *Jokull*, 58, 117-138.
- JAKOBSSON, S. P. & JOHNSON, G. L. 2012. Intraglacial volcanism in the Western Volcanic Zone, Iceland. *Bulletin of Volcanology*, 74, 1141-1160.
- JAMBON, A., WEBER, H. W., and BEGEMANN, F. 1985, Helium and argon from an Atlantic MORB glass; concentration, distribution and isotopic composition, *Earth and Planetary Science Letters*, 73(2-4), 255-268.
- JÓHANNESSON, H. & SÆMUNDSSON, K. 1998. Geological map of Iceland. 1: 500 000. *Tectonics, Icelandic Inst. of Nat. Hist., Reykjavík*.
- JOKIPII, J. & MARTI, K. Temporal variations of cosmic rays over a variety of time scales. *The Galaxy and the Solar System*, 1986. 116-128.
- JÓNASSON, K. 2007. Silicic volcanism in Iceland: Composition and distribution within the active volcanic zones. *Journal of Geodynamics*, 43, 101-117.

- JONES, J. G. 1968a. Intraglacial volcanoes of the Laugarvatn region, south-west Iceland --I. *Quarterly Journal of the Geological Society*, 124, 197-211.
- JONES, J. G. 1968b. Intraglacial volcanoes of the Laugarvatn region, south-west Iceland—II. *Quarterly Journal of the Geological Society*, 124, 197-211.
- JONES, J. & NELSON, P. 1970. The flow of basalt lava from air into water—its structural expression and stratigraphic significance. *Geological Magazine*, 107, 13-19.
- JULL, M., & MCKENZIE, D. 1996. The effect of deglaciation on mantle melting beneath Iceland. *Journal of Geophysical Research: Solid Earth*, 101(B10), 21815-21828.
- KIRKBRIDE, M. P. & DUGMORE, A. J. 2001. Timing and significance of mid-Holocene glacier advances in northern and central Iceland. *Journal of Quaternary Science*, 16, 145-153.
- KJARTANSSON, G. 1943. Arnesingasaga: The geology of Árnessýsla. Reykjavík.
- KOKFELT, T. F., HOERNLE, K., & HAUFF, F. 2003. Upwelling and melting of the Iceland plume from radial variation of  $^{238}\text{U}$ - $^{230}\text{Th}$  disequilibria in postglacial volcanic rocks. *Earth and Planetary Science Letters*, 214(1), 167-186.
- KURZ, M. D., JENKINS W. J., and HART S. R. 1982. Helium isotopic systematics of oceanic islands and mantle heterogeneity, *Nature (London)*, 297(5861), 43-47.
- KURZ, M. D., MEYER P. S., and SIGURDSSON H. 1985. Helium isotopic systematics within the neovolcanic zones of Iceland, *Earth and Planetary Science Letters*, 74(4), 291-305.
- KURZ, M. D. 1986. *In situ* production of terrestrial cosmogenic helium and some applications to geochronology. *Geochimica et Cosmochimica Acta*, 50, 2855-2862.
- KURZ, M. D., COLODNER, D., TRULL, T. W., MOORE, R. B. & O'BRIEN, K. 1990. Cosmic ray exposure dating with *in situ* produced cosmogenic  $^3\text{He}$ : Results from young Hawaiian lava flows. *Earth and Planetary Science Letters*, 97, 177-189.
- LAL, D. & PETERS, B. 1967. Cosmic Ray Produced Radioactivity on Earth. In: S. Flugg, (Ed). *Handbook of Physics*, 46/2, 551-612.
- LAL, D. 1987. Production of  $^3\text{He}$  in terrestrial rocks. *Chemical Geology: Isotope Geoscience section*, 66, 89-98.
- LAL, D. 1988. *In situ*-produced cosmogenic isotopes in terrestrial rocks. *Annual Review of Earth and Planetary Sciences*, 16, 355-388.
- LAL, D. 1989. An important source of  $^4\text{He}$  (and  $^3\text{He}$ ) in diamonds. *Earth and planetary science letters*, 96, 1-7.
- LAL, D. 1991. Cosmic ray labeling of erosion surfaces: *in situ* nuclide production rates and erosion models. *Earth and Planetary Science Letters*, 104, 424-439.
- LARSEN, G., & EIRIKSSON, J. (2008). Late Quaternary terrestrial tephrochronology of Iceland—frequency of explosive eruptions, type and volume of tephra deposits. *Journal of Quaternary Science*, 23(2), 109-120.
- LEE, J.-Y., K. MARTI, J. P. SEVERINGHAUS, K. KAWAMURA, H.-S. YOO, J. B. LEE, and J. S. KIM. 2006, A redetermination of the isotopic abundances of atmospheric Ar, *Geochem. Cosmochim. Acta*, 70, 4507–4512

- LEYA, I., BUSEMANN, H., BAUR, H., WIELER, R., GLORIS, M., NEUMANN, S., MICHEL, R., SUDBROCK, F. & HERPERS, U. 1998. Cross sections for the proton-induced production of He and Ne isotopes from magnesium, aluminum, and silicon. *Nuclear Instruments and Methods in Physics Research Section B: Beam Interactions with Materials and Atoms*, 145, 449-458.
- LICCIARDI, J., KURZ, M., CLARK, P. & BROOK, E. 1999. Calibration of cosmogenic  $^3\text{He}$  production rates from Holocene lava flows in Oregon, USA, and effects of the Earth's magnetic field. *Earth and Planetary Science Letters*, 172, 261-271.
- LICCIARDI, J., KURZ, M. & CURTICE, J. 2006. Cosmogenic  $^3\text{He}$  production rates from Holocene lava flows in Iceland. *Earth and Planetary Science Letters*, 246, 251-264.
- LICCIARDI, J. M., KURZ, M. D. & CURTICE, J. M. 2007. Glacial and volcanic history of Icelandic table mountains from cosmogenic He-3 exposure ages. *Quaternary Science Reviews*, 26, 1529-1546.
- LIFTON, N. A., BIEBER, J. W., CLEM, J. M., DULDIG, M. L., EVENSON, P., HUMBLE, J. E. & PYLE, R. 2005. Addressing solar modulation and long-term uncertainties in scaling secondary cosmic rays for in situ cosmogenic nuclide applications. *Earth and Planetary Science Letters*, 239, 140-161.
- LIPPOLT, H. J., & WEIGEL, E. (1988).  $^4\text{He}$  diffusion in  $^{40}\text{Ar}$ -retentive minerals. *Geochimica et Cosmochimica Acta*, 52(6), 1449-1458.
- LIPPOLT, H. J., LEITZ, M., WERNICKE, R. S., & HAGEDOM, B. 1994. (Uranium+ thorium)/helium dating of apatite: experience with samples from different geochemical environments. *Chemical Geology*, 112(1), 179-191.
- LOWE, J. J. & WALKER, M. J. 1997. *Reconstructing quaternary environments*, Longman Harlow.
- LUPTON, J. E., and H. CRAIG. 1975, Excess (super 3) He in oceanic basalts; evidence for terrestrial primordial helium, *Earth and Planetary Science Letters*, 26(2), 133-139.
- MACLENNAN, J., MCKENZIE, D., & GRONVOLD, K. 2001. Plume-driven upwelling under central Iceland. *Earth and Planetary Science Letters*, 194(1), 67-82.
- MACLENNAN, J., JULL, M., MCKENZIE, D., SLATER, L. & GRÖNVOLD, K. 2002. The link between volcanism and deglaciation in Iceland. *Geochemistry, Geophysics, Geosystems*, 3, 1-25.
- MACPHERSON, C. G., D. R. HILTON, J. M. SINTON, R. J. POREDA, and H. CRAIG 1998, High  $^3\text{He}/^4\text{He}$  ratios in the Manus backarc basin: Implications for mantle mixing and the origin of plumes in the western Pacific Ocean, *Geology*, 26(11), 1007.
- MAMYRIN, B. A., I. N. TOLSTIKHIN, G. S. ANUFRIYEV, and I. L. KAMENSKIY. 1969, Anomalous isotopic composition of helium in volcanic gases, *Anomal'nyy izotopnyy sostav gelya vulkanicheskikh gazakh*, Doklady Akademii Nauk SSSR, 184(5), 1197-1199.
- MAMYRIN, B., ANUFRIEV, G., KAMENSKII, I. & TOLSTIKHIN, I. 1970. DETERMINATION OF THE ISOTOPIC COMPOSITION OF ATMOSPHERIC HELIUM. All-Union Petroleum Geology Exploration Inst., Moscow. Inst. of Precambrian Geology and Geochronology, Leningrad.

- MARTEL, D., O'NIONS, R., HILTON, D. & OXBURGH, E. 1990. The role of element distribution in production and release of radiogenic helium: The Carnmenellis Granite, southwest England. *Chemical geology*, 88, 207-221.
- MARTY, B., APPORA, I., BARRAT, J. A. A., DENIEL, C., VELLUTINI, P., & VIDAL, P. 1993. He, Ar, Sr, Nd and Pb isotopes in volcanic rocks from Afar: Evidence for a primitive mantle component and constraints on magmatic sources. *Geochemical Journal*, 27(4/5), 219-228.
- MARTY, B., TOLSTIKHIN, I., KAMENSKY, I. L., NIVIN, V., BALAGANSKAYA, E., & ZIMMERMANN, J. L. 1998. Plume-derived rare gases in 380 Ma carbonatites from the Kola region (Russia) and the argon isotopic composition in the deep mantle. *Earth and Planetary Science Letters*, 164(1), 179-192.
- MASARIK, J. & REEDY, R. C. 1994. Effects of bulk composition on nuclide production processes in meteorites. *Geochimica et Cosmochimica Acta*, 58, 5307-5317.
- MASARIK, J. & REEDY, R. C. 1995. Terrestrial cosmogenic-nuclide production systematics calculated from numerical simulations. *Earth and Planetary Science Letters*, 136, 381-395.
- MASARIK, J. & REEDY, R. C. 1996. Monte Carlo simulation of the in-situ-produced cosmogenic nuclides. *Radiocarbon*, 38, 163-164.
- MASARIK, J. & BEER, J. 1999. Simulation of particle fluxes and cosmogenic nuclide production in the Earth's atmosphere. *Journal of Geophysical Research*, 104, 12,099-112.
- MATHEWS, W. H. 1947. "Tuyas," flat-topped volcanoes in northern British Columbia. *American Journal of Science*, 245, 560-570.
- MATSUDA, J. I., & MARTY, B. 1995. The  $^{40}\text{Ar}/^{36}\text{Ar}$  ratio of the undepleted mantle; a reevaluation. *Geophysical research letters*, 22(15), 1937-1940.
- MATSUMOTO, T., Y. ORIHASHI, J.-i. MATSUDA, and K. YAMAMOTO. 2008, Argon isotope ratio of the plume-source deduced from high-resolution stepwise crushing extraction, *Geochemical Journal*, 42(1), 39-49.
- MATTHEWS, J. A. (1994). Lichenometric dating: a review with particular reference to 'Little Ice Age' moraines in southern Norway. *Dating in Exposed and Surface Contexts*. University of New Mexico Press, Albuquerque, 185-212.
- MCELHINNY, M. & SENANAYAKE, W. 1982. Variations in the geomagnetic dipole. I-The past 50,000 years. *Journal of Geomagnetism and Geoelectricity*, 34, 39-51.
- MCGARVIE, D. W., BURGESS, R., TINDLE, A. G., TUFFEN, H. & STEVENSON, J. A. 2006. Pleistocene rhyolitic volcanism at Torfajökull, Iceland: eruption ages, glaciovolcanism, and geochemical evolution. *Jokull*, 56, 57-75.
- MCGARVIE, D. W., STEVENSON, J. A., BURGESS, R., TUFFEN, H., & TINDLE, A. G. 2007. Volcano–ice interactions at Prestahnúkur, Iceland: rhyolite eruption during the last interglacial–glacial transition. *Annals of Glaciology*, 45(1), 38-47.
- MCGARVIE, D. 2009. Rhyolitic volcano–ice interactions in Iceland. *Journal of Volcanology and Geothermal Research*, 185, 367-389.
- MEE, K., TUFFEN, H., & GILBERT, J. S. 2006. Snow-contact volcanic facies and their use in determining past eruptive environments at Nevados de Chillán volcano, Chile. *Bulletin of volcanology*, 68(4), 363-376.

- MEESTERS, A. G. C. A., & DUNAI, T. J. 2005. A noniterative solution of the (U-Th)/He age equation. *Geochemistry, Geophysics, Geosystems*, 6.4.
- MERRILL, R. T., MCELHINNY, M. W., & MCFADDEN, P. L. 1996. The magnetic field of the Earth: Paleomagnetism, the Core, and the Deep Mantle. *International Geophysics Series*, 63. Academic Press, San Diego, 531 pp.
- MICHEL, R., LEYA, I. & BORGES, L. 1996. Production of cosmogenic nuclides in meteoroids: accelerator experiments and model calculations to decipher the cosmic ray record in extraterrestrial matter. *Nuclear Instruments and Methods in Physics Research Section B: Beam Interactions with Materials and Atoms*, 113, 434-444.
- MIN, K., REINERS, P. W., WOLFF, J. A., MUNDIL, R., WINTERS, R. L. 2006. (U-Th)/He dating of volcanic phenocrysts with high U-Th inclusions, Jemez Volcanic Field, New Mexico. *Chemical Geology*, 227, 223-235.
- MOLNAR, P., & STOCK, J. 1987. Relative motions of hotspots in the Pacific, Atlantic and Indian Oceans since late Cretaceous time. *Nature*, 327(6123), 587-591.
- MONTEIRO, H. S., VASCONCELOS, P. M., FARLEY, K. A., SPIER, C. A., & MELLO, C. L. 2014. (U-Th)/He geochronology of goethite and the origin and evolution of cangas. *Geochimica et Cosmochimica Acta*, 131, 267-289.
- MOORE, J. G., & CALK, L. C. 1991. Degassing and differentiation in subglacial volcanoes, Iceland. *Journal of Volcanology and Geothermal Research*, 46(1-2), 157-180.
- MOORE, J. G., HICKSON, C. J., & CALK, L. C. 1995. Tholeiitic-alkalic transition at subglacial volcanoes, Tuya region, British Columbia, Canada. *Journal of Geophysical Research: Solid Earth*, 100(B12), 24577-24592.
- MOREIRA, M., K. BREDDAM, J. CURTICE, and M. D. KURZ. 2001, Solar neon in the Icelandic mantle: new evidence for an undegassed lower mantle, *Earth and Planetary Science Letters*, 185(1-2), 15-23.
- MOREIRA, M., and MADUREIRA, P. 2005. Cosmogenic helium and neon in 11 Myr old ultramafic xenoliths: consequences for mantle signatures in old samples. *Geochemistry, Geophysics, Geosystems* 6.8.
- MORGAN, W. J. 1972. Deep mantle convection plumes and plate motions. *AAPG bulletin*, 56(2), 203-213.
- MORRISON, P. & PINE, J. 1955. Radiogenic origin of the helium isotopes in rock. *Annals of the New York Academy of Sciences*, 62, 71-92.
- MOURÃO, C., M. MOREIRA, J. MATA, A. RAQUIN, and J. MADEIRA. 2012, Primary and secondary processes constraining the noble gas isotopic signatures of carbonatites and silicate rocks from Brava Island: Evidence for a lower mantle origin of the Cape Verde plume, *Contributions to Mineralogy and Petrology*, 163(6), 995-1009.
- MUKHOPADHYAY, S. 2012, Early differentiation and volatile accretion recorded in deep-mantle neon and xenon, *Nature*, 486(7401), 101-104.
- NICHOLS, A. R. L., CARROL, M. R., & HÖSKULDSSON, A. 2002. Is the Iceland hot spot also wet? Evidence from the water contents of undegassed submarine and subglacial pillow basalts. *Earth and Planetary Science Letters*, 202(1), 77-87.
- NICHOLSON, H., CONDOMINES, M., FITTON, J. G., FALLICK, A. E., GRÖNVOLD, K., & ROGERS, G. 1991. Geochemical and isotopic

- evidence for crustal assimilation beneath Krafla, Iceland. *Journal of Petrology*, 32(5), 1005-1020.
- NICHOLSON, H., & LATIN, D. 1992. Olivine tholeiites from Krafla, Iceland: evidence for variations in melt fraction within a plume. *Journal of Petrology*, 33(5), 1105-1124.
- NIEDERMANN, S. 2002. Cosmic-ray-produced noble gases in terrestrial rocks: dating tools for surface processes. *Reviews in mineralogy and geochemistry*, 47, 731-784.
- NISHIZUMI, K., WINTERER, E., KOHL, C., KLEIN, J., MIDDLETON, R., LAL, D. & ARNOLD, J. 1989. Cosmic ray production rates of  $^{10}\text{Be}$  and  $^{26}\text{Al}$  in quartz from glacially polished rocks. *Journal of Geophysical Research*, 94, 17907-17,915.
- NISHIZUMI, K., WELTEN, K., MATSUMURA, H., CAFFEE, M., NINOMIYA, K., OMOTO, T., NAKAGAKI, R., SHIMA, T., TAKAHASHI, N. & SEKIMOTO, S. 2009. Measurements of high-energy neutron cross sections for accurate cosmogenic nuclide production rates.
- NORÐDAHL, H. 1991. A review of the glaciation maximum concept and the deglaciation of Eyjafjördur, North Iceland. *Environmental change in Iceland: past and present*. Springer.
- NORÐDAHL, H. & PÉTURSSON, H. G. 2005. 3. Relative sea-level changes in Iceland: new aspects of the Weichselian deglaciation of Iceland. *Developments in Quaternary Sciences*, 5, 25-78.
- NORÐDAHL, H., INGÓLFSSON, Ó., PÉTURSSON, H. & HALLSDÓTTIR, M. 2008. Late Weichselian and Holocene environmental history of Iceland. *Jökull*, 58, 343-364.
- NYE, J. 1951. The flow of glaciers and ice-sheets as a problem in plasticity. *Proceedings of the Royal Society of London. Series A. Mathematical and Physical Sciences*, 207, 554-572.
- OHNO, M., & HAMANO, Y. 1992. Geomagnetic poles over the past 10,000 years. *Geophysical Research Letters*, 19(16), 1715-1718.
- OSKARSSON, N., STEINTHORSSON, S. & SIGVALDASON, G. 1985. Iceland geochemical anomaly: origin, volcanotectonics, chemical fractionation and isotope evolution of the crust. *Journal of Geophysical Research*, 90, 10011-10,025.
- OWEN, J., TUFFEN, H., & MCGARVIE, D. W. 2012. Using dissolved H<sub>2</sub>O in rhyolitic glasses to estimate palaeo-ice thickness during a subglacial eruption at Bláhnúkur (Torfajökull, Iceland). *Bulletin of volcanology*, 74(6), 1355-1378.
- OZIMA, M. & PODOSEK, F. 1983. Noble gas geochemistry. Cambridge Univ. Press.
- PEATE, D. W., K. BREDDAM, J. A. BAKER, M. D. KURZ A. K. BARKER, T. PRESTVIK, N. GRASSINEAU, and A. C. SKOVGAARD. 2010, Compositional Characteristics and Spatial Distribution of Enriched Icelandic Mantle Components, *Journal of Petrology*, 51(7), 1447-1475.
- PHILLIPS, F. M. & PLUMMER, M. A. 1996. CHLOE: A program for interpreting in-situ cosmogenic nuclide data for surface exposure dating and erosion studies. *Radiocarbon*, 38, 98-99.
- PHILLIPS, F. M., STONE, W. D. & FABRYKA-MARTIN, J. T. 2001. An improved approach to calculating low-energy cosmic-ray neutron fluxes near the land/atmosphere interface. *Chemical Geology*, 175, 689-701.

- PHILLIPS, F.M., ARGENTO, D.C., BALCO, G., CAFFEE, M.W., CLEM, J., DUNAI, T.J., FINKEL, R., GOEHRING, B., GOSSE, J.C., HUDSON, A.M. and JULL, A.T., 2016. The CRONUS-Earth project: a synthesis. *Quaternary Geochronology*, 31, pp.119-154.
- PORCELLI, D. & BALLENTINE, C. J. 2002. Models for Distribution of Terrestrial Noble Gases and Evolution of the Atmosphere. *Reviews in Mineralogy and Geochemistry*, 47, 411-480.
- POREDA, R. J. & CERLING, T. E. 1992. Cosmogenic neon in recent lavas from the western United States. *Geophysical Research Letters*, 19, 1863-1866.
- POWELL, C. F., FOWLER, P. H. & PERKINS, D. H. 1959. *The Study of Elementary Particles by the Photographic Method: An Account of the Principal Techniques and Discoveries*.
- REEDY, R. C., ARNOLD, J. R. & LAL, D. 1983. Cosmic-Ray Record in Solar System Matter. *Science*, 219, 127-135.
- REICH, M., EWING, R. C., EHLERS, T. A., & BECKER, U. 2007. Low-temperature anisotropic diffusion of helium in zircon: implications for zircon (U-Th)/He thermochronometry. *Geochimica et Cosmochimica Acta*, 71(12), 3119-3130.
- REINERS, P. W., & FARLEY, K. A. 1999. Helium diffusion and (U-Th)/He thermochronometry of titanite. *Geochimica et Cosmochimica Acta*, 63(22), 3845-3859.
- REINERS, P. W., SPELL, T. L., NICOLESCU, S., & ZANETTI, K. A. 2004. Zircon (U-Th)/He thermochronometry: He diffusion and comparisons with 40 Ar/39 Ar dating. *Geochimica et cosmochimica acta*, 68(8), 1857-1887.
- REINERS, P. W. 2005. Zircon (U-Th)/He thermochronometry. *Reviews in Mineralogy and Geochemistry*, 58(1), 151-179.
- RIFFEL, S. B., VASCONCELOS, P. M., CARMO, I. O., & FARLEY, K. A. 2016. Goethite (U-Th)/He geochronology and precipitation mechanisms during weathering of basalts. *Chemical Geology*.
- ROSI, M., VEZZOLI, L., ALEOTTI, P., & DE CENSI, M. 1996. Interaction between caldera collapse and eruptive dynamics during the Campanian Ignimbrite eruption, Phlegraean Fields, Italy. *Bulletin of Volcanology*, 57(7), 541-554.
- RUSSELL, J. K., EDWARDS, B. R., PORRITT, L. A. 2013. Pyroclastic passage zones in glaciovolcanic sequences. *Nat. Commun.* 4, 1788.
- RUSSELL, J. K., EDWARDS, B. R., PORRITT, L., RYANE, C. 2014. Tuyas: A descriptive genetic classification. *Quaternary Science Reviews* 87, 70-81.
- SÆMUNDSSON, K. 1978. Fissure swarms and central volcanoes of the neovolcanic zones of Iceland. *Geol. J. Spec. Issue*, 10, 415-432.
- SÆMUNDSSON, K. 1979. Outline of the geology of Iceland.
- SCHOPKA, H. H., GUDMUNDSSON, M. T. & TUFFEN, H. 2006. The formation of Helgafell, southwest Iceland, a monogenetic subglacial hyaloclastite ridge: sedimentology, hydrology and volcano–ice interaction. *Journal of volcanology and geothermal research*, 152, 359-377.
- SHEA, M. & SMART, D. Vertical cutoff rigidities for cosmic ray stations since 1955. International Cosmic Ray Conference, 2001. 4063.
- SHEN, Y., S. C. SOLOMON, I. T. BJARNASSON, and C. J. WOLFE. 1998, Seismic evidence for a lower-mantle origin of the Iceland plume, *Nature*, 395(6697), 62-65.

- SHEN, Y., SOLOMON, S. C., BJARNASSON, I. T., NOLET, G., MORGAN, W. J., ALLEN, R. M., VOGFJÖRD K., JAKOBSDÓTTIR S, STEFÁNSSON R, JULIAN BR. 2002. Seismic evidence for a tilted mantle plume and north-south mantle flow beneath Iceland. *Earth and Planetary Science Letters*, 197(3), 261-272.
- SHUSTER, D. L., FARLEY, K. A., SISTERSON, J. M., BURNETT, D. S. 2003. Quantifying the diffusion kinetics and spatial distribution of radiogenic  ${}^4\text{He}$  in minerals containing proton-induced  ${}^3\text{He}$ . *Earth Planet Sci. Lett*, 217, 19-32.
- SHUSTER, D. L., VASCONCELOS, P. M., HEIM, J. A., & FARLEY, K. A. 2005. Weathering geochronology by (U-Th)/He dating of goethite. *Geochimica et Cosmochimica Acta*, 69(3), 659-673.
- SIGMARSSON, O., and S. STEINHÓRSSON. 2007, Origin of Icelandic basalts: A review of their petrology and geochemistry, *Journal of Geodynamics*, 43(1), 87-100.
- SIGMUNDSSON, F., HREINSDÓTTIR, S., HOOPER, A., ÁRNADÓTTIR, T., PEDERSEN, R., ROBERTS, M. J., ÓSKARSSON, N., AURIAC, A., DECRIEM, J. & EINARSSON, P. 2010. Intrusion triggering of the 2010 Eyjafjallajokull explosive eruption. *Nature*, 468, 426-430.
- SIGMUNDSSON, F., PINEL, V., LUND, B., ALBINO, F., PAGLI, C., GEIRSSON, H., STURKELL, E. 2010. Climate effects on volcanism: influence on magmatic systems of loading and unloading from ice mass variations, with examples from Iceland. *Phil. Trans. R. Soc. A: Mathematical, Physical and Engineering Sciences* 368. 1919, 2519-2534.
- SIMPSON, J. A. & FAGOT, W. C. 1953. Properties of the Low Energy Nucleonic Component at Large Atmospheric Depths. *Physical Review*, 90, 1068-1072.
- SIMPSON, J. A. 1983. Elemental and Isotopic Composition of the Galactic Cosmic Rays. *Annual Review of Nuclear and Particle Science*, 33, 323-382.
- SIMS, K. W., MACLENNAN, J., BLICHERT-TOFT, J., MERVINE, E. M., BLUSZTAJN, J., & GRÖNVOLD, K. 2013. Short length scale mantle heterogeneity beneath Iceland probed by glacial modulation of melting. *Earth and Planetary Science Letters*, 379, 146-157.
- SINTON, J. M., GRÖNVOLD, K., SAEMUNDSSON, K. 2005. Postglacial eruptive history of the Western Volcanic Zone, Iceland. *Geochem, Geophys, Geosyst*, 6:Q12009. doi:10.1029/2005GC001021
- SKILLING, I. P. 2002. Basaltic pahoehoe lava-fed deltas: large-scale characteristics, clast generation, emplacement processes and environmental discrimination. *Geological Society, London, Special Publications*, 202, 91-113.
- SKILLING, I. P. 2009. Subglacial to emergent basaltic volcanism at Hlooufell, south-west Iceland: A history of ice-confinement. *Journal of Volcanology and Geothermal Research*, 185, 276-289.
- SLATER, L. 1996. Melt generation beneath Iceland (*Doctoral dissertation, University of Cambridge*).
- SLATER, L., JULL, M., MCKENZIE, D., & GRÖNVÖLD, K. 1998. Deglaciation effects on mantle melting under Iceland: results from the northern volcanic zone. *Earth and Planetary Science Letters*, 164(1), 151-164.

- SLEEP, N. H. 1990. Hotspots and mantle plumes: Some phenomenology. *Journal of Geophysical Research: Solid Earth*, 95(B5), 6715-6736.
- SMART, D. & SHEA, M. 2005. A review of geomagnetic cutoff rigidities for earth-orbiting spacecraft. *Advances in Space Research*, 36, 2012-2020.
- SMART, D. & SHEA, M. World grid of calculated cosmic ray vertical cutoff rigidities for epoch 2000.0. Proceedings of the 30th International Cosmic Ray Conference, 2008. 737-740.
- SMART, D. F. & SHEA, M. A. 1994. Geomagnetic cutoffs: A review for space dosimetry applications. *Advances in Space Research*, 14, 787-796.
- SMART, D., SHEA, M. & FLÜCKIGER, E. 2000. Magnetospheric models and trajectory computations. *Space Science Reviews*, 93, 305-333.
- SMELLIE, J. L. & SKILLING, I. P. 1994. Products of Subglacial Volcanic-Eruptions under Different Ice Thicknesses - 2 Examples from Antarctica. *Sedimentary Geology*, 91, 115-129.
- SMELLIE, J. & HOLE, M. 1997. Products and processes in Pliocene–Recent, subaqueous to emergent volcanism in the Antarctic Peninsula: examples of englacial Surtseyan volcano construction. *Bulletin of Volcanology*, 58, 628-646.
- SMELLIE, J. L. 2000. Subglacial eruptions. In: H. Sigurdsson, B. Houghton, S.R. McNutt, H. Rymer, J. Stix (Eds.) *Encyclopedia of Volcanoes*, Academic Press, London. 403-418.
- SMELLIE, J. L. 2001. Lithofacies architecture and construction of volcanoes in englacial lakes: icefall Nunatak, Mount Murphy, eastern Marie Byrd Land, Antarctica. *Special Publication J. D. L. White, N. Riggs (Eds.), Lacustrine volcaniclastic sedimentation, International Association of Sedimentologists*, vol 30, 73-98.
- SMELLIE, J. L. 2006. The relative importance of supraglacial versus subglacial meltwater escape in basaltic subglacial tuya eruptions: An important unresolved conundrum. *Earth-Science Reviews*, 74, 241-268.
- SMELLIE J. L., JOHNSON, J. S., MCINTOSH, W. C., ESSER, R., GUDMUNDSSON, M. T., HAMBREY, M. J., VAN WYK DE VRIES, B. 2008. Six million years of glacial history recorded in volcanic lithofacies of the James Ross Island Volcanic Group, Antarctic Peninsula, *Palaeogeogr. Palaeoclimatol. Palaeoecol.*, 260, 122-148.
- SMELLIE, J. L. 2009. Terrestrial sub-ice volcanism: landform morphology, sequence characteristics and environmental influences and implications for candidate Mars examples, in: M.G. Chapman, L. Leszthely (Eds.), *Preservation of Random Mega-Scale Events on Mars and Earth: Influence on Geological History*, Geological Society of America Special Papers. 55-76.
- SMELLIE, J. L., and EDWARDS, B. R. 2016. Glaciovolcanism on Earth and Mars. Cambridge University Press.
- SMYTH, J. R., FROST, D. J., NESTOLA, F., HOLL, C. M., & BROMILEY, G. 2006. Olivine hydration in the deep upper mantle: effects of temperature and silica activity. *Geophysical Research Letters*, 33(15).
- SPENCER, A.S., KOHN, B.P., GLEADOW, A.J.W., NORMAN, M., BELTON, D.X., CARTER, T.J. 2004. The importance of residing in a good neighbourhood: rechecking the rules of the game for apatite (U– Th)/He thermochronology. In: Andressien, P. (Ed.), 10th International Fission track Dating Conference. Amsterdam, pp. 20

- SPÖRLI, K. B., & ROWLAND, J. V. 2006. 'Column on column' structures as indicators of lava/ice interaction, Ruapehu andesite volcano, New Zealand. *Journal of Volcanology and Geothermal Research*, 157(4), 294-310.
- STEINBERGER, B. 2000. Plumes in a convecting mantle: Models and observations for individual hotspots. *Journal of Geophysical Research: Solid Earth*, 105(B5), 11127-11152.
- STEVENSON, J. A., SMELLIE, J. L., MCGARVIE, D. W., GILBERT, J. S., & CAMERON, B. I. 2009. Subglacial intermediate volcanism at Kerlingarfjöll, Iceland: magma–water interactions beneath thick ice. *Journal of Volcanology and Geothermal Research*, 185(4), 337-351.
- STEVENSON, J. A., GILBERT, J. S., MCGARVIE, D. W. & SMELLIE, J. L. 2011. Explosive rhyolite tuya formation: classic examples from Kerlingarfjöll, Iceland. *Quaternary Science Reviews*, 30, 192-209.
- STOCKLI, D. F., & FARLEY, K. A. 2004. Empirical constraints on the titanite (U-Th)/He partial retention zone from the KTB drill hole. *Chemical Geology*, 207(3), 223-236.
- STONE, J. O. 2000. Air pressure and cosmogenic isotope production. *Journal of Geophysical Research*, 105, 23753-23,759.
- STØRMER, C. 1955. *The polar aurora*, Clarendon Press.
- STUART, F. M. 1994, Speculations about the cosmic origin of He and Ne in the interior of the Earth; discussion, *Earth and Planetary Science Letters*, 122(1-2), 245-247.
- STUART, F. M., TURNER, G., DUCKWORTH, R. C., & FALLICK, A. E. 1994. Helium isotopes as tracers of trapped hydrothermal fluids in ocean-floor sulfides." *Geology*, 22.9. 823-826
- STUART, F. M., S. LASS-EVANS, J. G. FRITTON, and R. M. ELLAM. 2003, High (<sup>3</sup>He) / (<sup>4</sup>He) ratios in picritic basalts from Baffin Island and the role of a mixed reservoir in mantle plumes, *Nature (London)*, 424(6944), 57-59.
- STRUXTT, R. J. 1905. On the radio-active minerals. *Proceedings of the Royal Society of London. Series A*, 76, 88-101.
- SUMINO, H., NAGAO, K., and NoTSU, K. 2001. Highly Sensitive and Precise Measurement of Helium Isotopes Using a Mass Spectrometer with Double Collector System. *Journal of the Mass Spectrometry Society of Japan* 49.2 61-68
- THORDARSSON, T. & HOSKULDSSON, A. 2002. *Iceland*, Harpenden, Terra Publishing.
- THORARINSSON, S. (1981). The application of tephrochronology in Iceland. In *Tephra studies* (pp. 109-134). Springer Netherlands.
- TOLSTIKHIN, I. N. 1975, Helium isotopes in the earth's interior and in the atmosphere: a degassing model of the earth, *Earth and Planetary Science Letters*, 26(1), 88-96.
- TRULL, T. W. & KURZ, M. D. 1993. Experimental measurements of <sup>3</sup>He and <sup>4</sup>He mobility in olivine and clinopyroxene at magmatic temperatures. *Geochimica et Cosmochimica Acta*, 57, 1313-1324.
- TRULL, T. W., KURZ, M. D. & JENKINS, W. J. 1991. Diffusion of cosmogenic <sup>3</sup>He in olivine and quartz: implications for surface exposure dating. *Earth and Planetary Science Letters*, 103, 241-256.

- TUFFEN, H., GILBERT, J. & MCGARVIE, D. 2001. Products of an effusive subglacial rhyolite eruption: Bláhnúkur, Torfajökull, Iceland. *Bulletin of volcanology*, 63, 179-190.
- TUFFEN, H., PINKERTON, H., MCGARVIE, D. & GILBERT, J. 2002. Melting of the glacier base during a small-volume subglacial rhyolite eruption: evidence from Bláhnúkur, Iceland. *Sedimentary Geology*, 149, 183-198.
- TUFFEN, H. 2007. Models of ice melting and edifice growth at the onset of subglacial basaltic eruptions. *J. Geophys. Res.*, 112, B03203.
- TUFFEN, H., & CASTRO, J. M. 2009. The emplacement of an obsidian dyke through thin ice: Hrafntinnuhryggur, Krafla Iceland. *Journal of Volcanology and Geothermal Research*, 185(4), 352-366.
- TUFFEN, H. 2010. How will melting of ice affect volcanic hazards in the twenty-first century?. *Philosophical Transactions of the Royal Society of London A: Mathematical, Physical and Engineering Sciences*, 368(1919), 2535-2558.
- TUFFEN, H., BETTS, R. 2010. Volcanism and climate: chicken and egg (or vice versa)? *Philos. Trans. R. Soc. Lond. Ser.*, 368, 2585-2588.
- TUFFEN, H., OWEN, J., DENTON, J. 2010. Magma degassing during subglacial eruptions and its use to reconstruct palaeo-ice thicknesses. *Earth-Sci. Rev.*, 99, 1-18.
- TUSHINGHAM, A. M. & PELTIER, W. 1991. Ice- 3G: A new global model of late Pleistocene deglaciation based upon geophysical predictions of post- glacial relative sea level change. *Journal of Geophysical Research: Solid Earth (1978–2012)*, 96, 4497-4523.
- VAN KEKEN, P. E., and C. J. BALLENTINE. 1998. Whole-mantle versus layered mantle convection and the role of a high-viscosity lower mantle in terrestrial volatile evolution, *Earth and Planetary Science Letters*, 156(1-2), 19-32.
- VERMEESCH, P. 2008. Three new ways to calculate average (U-Th)/He ages. *Chemical Geology*, 249.3, 339-347
- VERMEESCH, P., BAUR, H., HEBER, V. S., KOBER, F., OBERHOLZER, P., SCHAEFER, J. M., SCHLÜCHTER, C., STRASKY, S. & WIELER, R. 2009. Cosmogenic  $^{3}\text{He}$  and  $^{21}\text{Ne}$  measured in quartz targets after one year of exposure in the Swiss Alps. *Earth and Planetary Science Letters*, 284, 417-425.
- WALKER, A. J. 2011. *Rhyolite Volcanism At Öraefajökull Volcano, S.E. Iceland - A Window On Quaternary Climate Change*. PhD, University of Manchester.
- WALKER, G. P. L. 1965. *Some aspects of Quaternary volcanism in Iceland*.
- WALKER, G. P. L. 1966. Acid volcanic rocks in Iceland. *Bulletin Volcanologique*, 29, 375-402.
- WERNER, R., SCHMINCKE, H.-U. & SIGVALDASON, G. 1996. A new model for the evolution of table mountains: volcanological and petrological evidence from Herdubreid and Herdubreidartögl volcanoes (Iceland). *Geologische Rundschau*, 85, 390-397.
- WERNER, R. & SCHMINCKE, H.-U. 1999. Englacial vs lacustrine origin of volcanic table mountains: evidence from Iceland. *Bulletin of volcanology*, 60, 335-354.

- WERNICKE, R. S., & LIPPOLT, H. J. 1994a.  $^4\text{He}$  age discordance and release behavior of a double shell botryoidal hematite from the Schwarzwald, Germany. *Geochimica et cosmochimica acta*, 58(1), 421-429.
- WERNICKE, R. S., & LIPPOLT, H. J. 1994b. Dating of vein Specularite using internal ( $\text{U} + \text{Th}$ )/ $^4\text{He}$  isochrons. *Geophysical Research Letters*, 21(5), 345-347.
- WESTON, B. M. 2012. *Noble Gases and Halogens in Icelandic Basalts*. Doctor of Philosophy, University of Manchester.
- WESTON, B., BURGESS, R., & BALLENTINE, C. J. 2015. Disequilibrium degassing model determination of the  $^3\text{He}$  concentration and  $^3\text{He}/^{22}\text{Ne}$  of the MORB and OIB mantle sources. *Earth and Planetary Science Letters*, 410, 128-139.
- WOLF, R. A., FARLEY, K. A. & SILVER, L. T. 1996. Helium diffusion and low-temperature thermochronometry of apatite. *Geochimica et Cosmochimica Acta*, 60, 4231-4240.
- WOLF, R. A. 1997. The development of the (U-Th)/He thermochronometer (Doctoral dissertation, California Institute of Technology).
- WOLF, R. A., FARLEY, K. A., & KASS, D. M. 1998. Modeling of the temperature sensitivity of the apatite (U-Th)/He thermochronometer. *Chemical Geology*, 148(1), 105-114.
- WOLFE, C. J., BJARNASON, I. T., VANDECAR, J. C. & SOLOMON, S. C. 1997. Seismic structure of the Iceland mantle plume. *Nature*, 385, 245-247.
- WOOD, B. J., BLUNDY, J. D. & ROBINSON, J. A. C. 1999. The role of clinopyroxene in generating U-series disequilibrium during mantle melting. *Geochimica et Cosmochimica Acta*, 63, 1613-1620.
- WOOD, C. A. & KIENLE, J. 1992. *Volcanoes of North America: The United States and Canada*, Cambridge University Press.
- YOKOYAMA, Y., REYSS, J.-L. & GUICHARD, F. 1977. Production of radionuclides by cosmic rays at mountain altitudes. *Earth and Planetary Science Letters*, 36, 44-50.
- ZEITLER, P. K., HERCZEG, A. L., MCDOUGALL, I. & HONDA, M. 1987. U-Th-He dating of apatite: A potential thermochronometer. *Geochimica et Cosmochimica Acta*, 51, 2865-2868.
- ZIEGLER, J. F. 1977. *Helium: stopping powers and ranges in all elemental matter*, Pergamon Press New York.
- ZINDLER, A., HART, S. R., FREY, F. A., & JAKOBSSON, S. P. 1979. Nd and Sr isotope ratios and rare earth element abundances in Reykjanes Peninsula basalts evidence for mantle heterogeneity beneath Iceland. *Earth and Planetary Science Letters*, 45(2), 249-262.